Universidad del País VascoEuskal Herriko Unibertsitatea

Facultad de QuímicaKimika Fakultatea

Departamento de Ciencia y Tecnología de PolímerosPolimeroen Zientzia eta Teknologia Departamentua

Alkali Metal Salts Based on Novel Anions for Solid Polymer Electrolytes

By

Lixin Qiao

Thesis supervisors:

Prof. Michel Armand

Dr. Heng Zhang

Donostia, 2021

Acknowledgements

First of all, I would like to deliver my deepest appreciation to my superiors, Prof. Michel Armand and Dr. Heng Zhang for their kind guidance, encouragement and support during my PhD period. Michel, thank you for giving me this chance to work with you. Your innovative ideas and skilful guidance encourage and help me a lot to finish this thesis. I also would like to appreciate your kindness, understanding and patience, giving me a huge confidence to improve myself. Tough we don't have enough chances to have talks in person, I learned a lot from you in our fruitful online meetings. Heng, thank you very much for your constant and significant support since I applied for the scholarship. Your "crazy" and supper good ideas and attitude to science are always inspiring, surprising and motivating me to be a better researcher. Thank you for your patience and guidance you have shown to my lab and computer works. I also would like to convey my appreciation to my tutor Marilo and Miren for your help to guide me to finish this thesis.

I would to like to take this opportunity to say thanks to my group members and colleagues. María Martinez, thanks for your continuous help and support from the begging of my PhD, I still remembered you picked me up at the Vitoria bus station when I came here three years ago. I really appreciate your help during the three years. You are the one who always support and encourage me. Muchas gracias. I also want to give acknowledgements to cariño Itziar Aldalur. Thank you for helping me to deal with everything regarding to UPV and giving me a Basque name 'Ekaitz'. Thanks Xabier Judez and Alex Alexander Santiago for teaching me a lot of super good Spanish vocabularies, we are Máquinas, hope you can go to China for a visit

in future, I will be your tour guide. Uxue Oteo, thank you for helping to get used to the labs at the begging of my PhD. It is very happy to work with you in labs, hope we have chance to work with each other in future and I am looking forward to hear your voice “give me five”. Eduardo Sanchez-Diez, thank you for your help and accompany in Lab 6. I remembered the sentences you taught me, ‘Don’t be panic, it’s organic chemistry’ and ‘Thanks god, today is Friday’. It is a good memory to work with you in Lab 6. Leire Meabe, thanks for you to help me to do synthesis and cell tests in labs, it is pleasant to work with you. Elias Lobato and Ander Celaya, thank you both for teaching me Spanish and your support during my stay in CIC. I also would like to acknowledge other colleges in CIC, Yan, Chunmei, Lian, Oihane, Amaia S., Julen Castillo, Maddalen, Asier F., Julen Etxabe, Jose, Silvia, Sona, Ram, Yang Wang, Marta Cabello, Roshan, Catarina, Pierre, Ander O., Fred, Nicola, Simon and Brigette, thanks for their help in my work and in my daily life.

I am grateful to thank the financial support from Chinese Scholarship Council (no.201808370162) and CIC/UPV for their support to let me stay here to do my thesis. I also want to convey my appreciation to the technicians and collaborators, Rosalia, Javi, Yan, Sergio, Maria E, thanks for them to help me publish some papers.

I would like to thank my Chinese friends in Europe and China, 曲红涛，刘元鑫，鲁承龙，王龙龙，李杰东，崔涛，张聪聪，崔艳艳，董甜甜，谢凯楠，吴俊，汪慧怡，感谢他们三年以来的照顾和关心。尤其感谢曲红涛‘院士’夫妇，谢谢你们三年以来对我的陪伴，期待回国后能够在同一城市工作。

Finally and most importantly，my deepest gratitude and love go to my family, my parents, my grandparents, brothers and sisters. I love you. 最后，我想感谢我的爸爸妈妈，感谢他们一直以来对我的支持和理解，感谢爷爷奶奶，感谢乔木，乔臻，王英杰，三姨一家，二哥及三哥一家，大姐及小玲姐一家，我爱你们！！！我也想感谢苏老师，谢谢你的陪伴，未来可期！加油!

Thanks to CIC, Vitoria and everyone. MUCHAS GRACIAS !!!

Abstract

Developing and exploiting environmentally renewable and sustainable energy resources (e.g., solar, tidal and wind energy) the has been considered as the most feasible way to solve the environmental pollution and global warning issues generated from the over-consumption of the fossil fuels. However, most of these renewable and sustainable energy sources are typically periodic or intermittent and unevenly distributed in nature. Therefore, reliable and large-scale energy storage systems with high efficiency have been regarded as the most promising method to store and accumulate the energy produced from these noncontinuous energy resources, and could transform the energy back at peak times when needed.

Among all the existing technologies, rechargeable lithium-ion batteries (LIBs) have become the most dominant power source for portable electronic, and have become attractive for electrical vehicles (EVs) and stationary energy storage systems due to their higher energy density and efficiency. However, conventional LIBs containing organic liquid electrolytes suffer from safety concerns such as flammability, thermal runaway and even explosion under abusive conditions. In addition, LIBs composed of graphite anodes and lithium transition metal oxide cathodes have more or less reached their theoretical limits in terms of specific and gravimetric energy densities.

Solid polymer electrolytes (SPEs) with high safety have attracted great attention in the development of practical lithium batteries ever since the perceptive proposal of using SPEs for rechargeable batteries by Armand in 1978. More importantly, lithium metal (Li°) could be used as anode material in SPEs-based batteries because of the good interfacial compatibility between Li° and SPEs, which might enhance the energy density of current LIBs. Amongst the various polymer matrices suggested, poly(ethylene oxide) (PEO) possesses flexibility, processability, and excellent solvating ability toward a wide variety of salts, and has therefore been abundantly used as host material. The technological feasibility of PEO-based SPEs has been demonstrated by the implementation of Bluecar® and Bluebus® powered by Li° | SPEs | $LiFePO_4$ batteries in different cities and countries (*i.e.* Lyon, Bordeaux, Indianapolis, and Singapore).

Indeed, the chemistry of the lithium salt employed plays a pivotal role in dictating the physico-chemical and electrochemical performance of any SPE, and thus also influences the performance of solid-state lithium metal batteries (SSLMBs). The lithium bis(trifluoromethanesulfonyl)imide (LiTFSI) salt, first suggested as salt for SPEs in 1986, possesses low lattice energy and the $TFSI^-$ anion has a large structural flexibility, both due to the anion's highly delocalized negative charge and flexible center [*e.g.*, $–SO_2–N^{(-)}–SO_2–$] and has therefore been commonly used for SPE-based SSLMBs. However, low lithium-ion transference number (T_{Li^+}) and poor solid electrolyte interphase (SEI) creating

properties result in severe cell polarization and simultaneously notorious dendritic growth on the Li° anode.

Therefore, in this thesis, several novel lithium salts were designed and synthesized to suppress anionic mobility and enhance T_{Li^+}, but without sacrificing significantly the ionic conductivity, and simultaneously with the aim of forming excellent SEI layers at the Li° anode to improve interfacial compatibility and stability towards Li° anode.

In the first work of this thesis, a trifluoromethyl-free anion, bis(difluoromethanesulfonyl)imide ($DFSI^-$), as an environmentally benign and interfacially favorable anion for high-performance SSLMB is reported. In contrast to LiTFSI, the $–CHF_2$ moieties of LiDFSI-based salt shows a more rapid chemical degradation under a mild basic solution. In addition, a high lithium-ion transference number resulted from H-bonding interactions between $–CF_2H$ moieties and EO units as well as the better SEI layers formed by the decomposition of $DFSI^-$ synergistically enhanced stability against Li° electrode, showing a better cell performance of SSRLMB batteries.

In another work, a benzene-based salt, lithium benzenesulfonyl(trifluoromethanesulfonyl)imide (LiBTFSI), was synthesized for high-performance PEO-based SPE with aim of further improving the lithium-ion conductivity. In contrast to the abundantly used LiTFSI-based SPEs, the LiBTFSI-based SPEs exhibited extremely high lithium-ion transference

number due to the intermolecular interactions (e.g., π-π stacking bonds) among the benzene-based anions, which was demonstrated by computational calculations. In addition, the $LiFePO_4$ || Li° cells assembled with the LiBTFSI-based SPEs showed a superior long-term cyclability with excellent Coulombic efficiencies as well as high discharge capacities.

In the last work, we reported a new type of chiral salts built from commercially available camphorsulfonic acid and their use as electrolyte salts for PEO-based SPEs. We demonstrated that the resulting SPEs exhibited decent ionic conductivities (ca. 10^{-4} S cm^{-1}) accompanied by high cation transference numbers (ca. 0.5) at 70 °C. Whether either the R or the S enantiomers were used the ion transport properties were the same, as expected, but rather surprisingly the artificial racemic mixture was within the errors of the measurements just as conductive.

All these results demonstrate the importance of the molecular structure of anions in SPEs and shed light on ways for future anion design to advance and develop high-performance SPEs-based SSLMBs.

Resumen

El desarrollo y la explotación de recursos energéticos sostenibles y renovables para el medio ambiente (tales como, energía solar, mareomotriz y eólica) se considera la forma más factible de resolver la contaminación ambiental y los problemas de calentamiento global generados por el excesivo consumo de combustibles fósiles. Sin embargo, la mayoría de estas fuentes de energía renovables y sostenibles suelen ser periódicas o intermitentes y están distribuidas de manera irregular en la naturaleza. Por lo tanto, los sistemas de almacenamiento energético con alta eficiencia y a gran escala se han considerado como el método más prometedor para almacenar y acumular la energía producida a partir de estos recursos energéticos intermitentes, ya que podrían transformar la energía en las horas de mayor demanda cuando sea necesario.

De todas las tecnologías existentes, las baterías recargables de iones de litio (LIB, por sus siglas en inglés) se han convertido en la fuente de energía más empleada en los dispositivos electrónicos portátiles y se han comenzado a aplicar en los vehículos eléctricos y los sistemas de almacenamiento de energía estacionarios debido a su mayor densidad y eficiencia energética. Sin embargo, las LIB convencionales que contienen electrolitos líquidos orgánicos presentan problemas de seguridad tales como inflamabilidad, fugas e incluso explosión en condiciones extremas. Además, las LIB compuestos por ánodos de grafito y cátodos de óxido de metal de transición de litio están cercanas a alcanzar sus

límites teóricos en términos de densidad de energía específica y gravimétrica, sin llegar a alcanzar los rendimientos deseables.

Los electrolitos poliméricos sólidos (SPEs, por sus siglas en inglés), presentan mayor seguridad que los electrolitos líquidos, y han obtenido especial atención en el desarrollo de LIB desde la propuesta de Armand en 1978 de usar SPEs en baterías recargables. Más importante aún, el litio metálico (Li °) podría usarse como ánodo en baterías basadas en SPEs debido a la buena compatibilidad interfacial existente entre Li ° y SPEs, lo que podría mejorar la densidad energética de los LIBs actuales. Entre las diversas matrices poliméricas sugeridas, el óxido de polietileno (PEO, por sus siglas en ingés) posee gran flexibilidad, buena procesabilidad y excelente capacidad de solvatación hacia una amplia variedad de sales y, por lo tanto, ha sido ampliamente utilizado como material huésped. La viabilidad tecnológica de las SPEs basadas en PEO se ha podido demostrar al implementarlas en los coches y autobuses Bluecar® y Bluebus® que emplean baterías con tecnología Li ° | SPEs | $LiFePO_4$ en diferentes ciudades y países (tales como, Lyon, Burdeos, Indianápolis y Singapur).

La química de la sal de litio juega un papel crucial dictando las propiedades fisicoquimicas y electroquímicas en cualquier SPE y, en consecuencia, también tiene una gran influencia en el rendimiento de las baterías de litio metal en estado sólido (SSLMB, por sus siglas en inglés). De entre todas las sales de litio empleadas en los electrolitos sólidos destaca el bis (trifluorometano)

sulfonamida de litio (LiTFSI), sal sugerida por primera vez en 1986, debido a poseer una baja energía de disociación. Además, el anión $TFSI^-$ se caracteriza por una gran flexibilidad estructural principalmente debido al centro flexible [–SO_2–$N^{(-)}$–SO_2–] y a la deslocalización de la carga negativa por su estructura. Por todo ello, esta sal ha sido ampliamente utilizada para las baterías poliméricas en estado sólido. Sin embargo, el bajo número de transferencia del ion litio (T_{Li^+}) y la pobre intercara creada entre el electrolito sólido y el ánodo (capa SEI, por sus siglas en inglés) resulta en la polarización del sistema y simultáneamente en la generación y crecimiento de incontroladas dendritas de litio en el ánodo que pueden revertir en la muerte de la batería.

Por todo ello, y con el fin de mejorar las prestaciones obtenidas por la sal anteriormente mencionada, en esta tesis, diferentes sales de litio han sido diseñadas y sintetizadas. Los objetivos de estas nuevas sales son tratar de suprimir la movilidad aniónica y aumentar el T_{Li^+} sin con ello sacrificar significativamente la conductividad iónica del sistema. Simultáneamente, estas sales también tienen como objetivo formar SEI protectoras en el ánodo de Liº de mayor calidad que las generadas por la sal de referencia para mejorar la compatibilidad interfacial y la estabilidad del electrolito frente al ánodo de litio.

En el primer capítulo experimental de esta tesis se presenta la síntesis y caracterización una nueva sal formada por un anión libre de grupos trifluorometanos, denominada bis (difluorometano) sulfonamida de litio (LiDFSI). Este anión se considera medioambientalmente benigno y favorable

para baterías en estado sólido de alto rendimiento. En contraposición con el LiTFSI, las unidades $–CHF_2$ del LiDFSI muestran una mayor y más veloz degradación química bajo un medio ligeramente básico. Además, el estudio sobre esta nueva sal reporta un mayor valor de T_{Li^+} como resultado de las interacciones de los enlaces H en las unidades $–CHF_2$ y los grupos EO. Por último, también se ha observado que la SEI protectora formada por la descomposición de esta sal (LiDFSI) tiene una gran estabilidad frente al ánodo de litio. Todo esto deriva en un rendimiento en celda muy destacado para tecnologías de baterías en estado sólido.

En otro capítulo, una sal basada en benceno, la sal de bencenosulfonil(trifluorometanosulfonil)imida de litio (LiBTFI), fue sintetizada para SPEs basados en PEO de alto con el objetivo de mejorar la conductividad de iones de litio. En contraste con los SPEs comúnmente basados en LiTFSI, los SPEs basados en LiBTFSI poseían un T_{Li^+} extraordinariamente elevado debido a las interacciones intermoleculares (enlace π-π) entre los aniones basados en benceno, lo cual se demostró mediante cálculos computacionales. Además, las celdas $LiFePO_4$ || Li° que contienen los SPEs basados en LiBTFSI demostraron una mejor ciclabilidad a largo plazo, con una excelente eficiencia coulómbica, así como una alta capacidad de descarga.

En el capítulo final, reportamos una nueva sal de tipo quiral sintetizada mediante el reactivo comercial de ácido canforsulfónico y su uso para SPEs

basados en PEO. Así mismo, demostramos que los SPEs obtenidos presentaban conductividades iónicas moderadas (ca. 10^{-4} S cm^{-1}) a la vez que un alto número de transferencia de cationes (ca. $T_{Li}{}^{+} = 0.5$) a 70 ºC. Independientemente de usar los enantiomeros R o S, las propiedades de transporte fueron las mismas, como cabía esperar. De la misma manera los valores obtenidos con la muestra racémica se situaban dentro del margen de error.

Todos estos resultados demuestran la importancia de la estructura molecular de los aniones en los SPE y arrojaron luz sobre las posibles futuras direcciones para el diseño de aniones para el desarrollo de SSLMBs de alto rendimiento basadas en SPEs.

Chapter 1:
Introduction

Chapter 2:
Experimental section

Chapter 4:
A benzene-conjugated anion for all-solid-state lithium-metal batteries

Appendix:

Chapter 1

Introduction

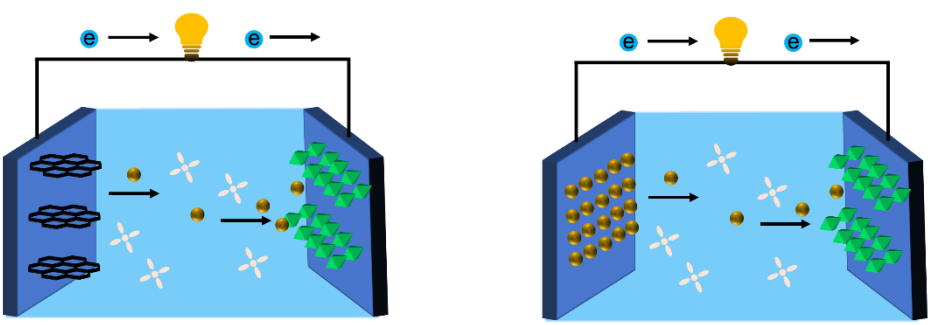

Chapter 1:

Introduction

1.1. Energy overview

The development of society in the past few decades has mainly relied on the consumption of non-renewable energy, such as oil, natural gas and coal.[1-2] With the development and prosperity of economy, along with the expansion of human population, the energy demand will be continuously increased. As shown in **Figure 1.1**, the global energy consumption is expected to increase to more than 700 exajoules (1 exajoule = 10^{18} joule) by 2050, which will definitely accelerate the consumption of non-renewable energy although renewable energy consumption is expected to increase and will reach about 170 exajoules.[3]

Indeed, the over-exploitation and consumption of the non-renewable energy will not only cause the continuous depletion of resources, but also significantly cause serious environmental problems due to the harmful emissions of greenhouse gases [such as carbon dioxide, sulfur species sulfides (SO_x) and nitrogen oxides (NO_x)] generated from the combustion of these fossil fuels, which adversely hurts human health and results in global warming.[2, 4-5] Hence, developing and exploiting environmentally renewable and sustainable energy resources, e.g., solar, tidal, wind, biomass, geothermal and hydroelectric energy, are of significant importance and a need. However, most of these renewable and sustainable energy sources are typically periodic or intermittent and unevenly distributed on earth/Nature.[6] Therefore, reliable and large-scale energy storage systems with high efficiencies have been regarded as the most promising method to store and accumulate the energy produced from these non-continuous energy resources, and could restore the energy back at peak times when needed.[7]

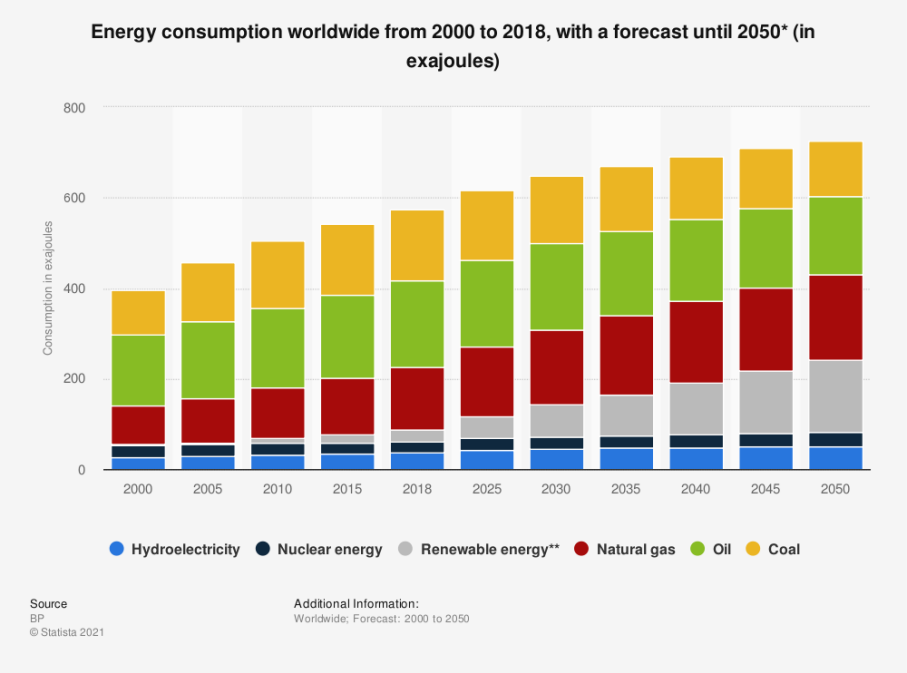

Figure 1.1. Energy consumption worldwide from 2000 to 2018, with a forecast until 2050. Reproduced with permission from Ref. [3].

1.2. Energy storage systems

The widely used energy storage systems worldwide could be divided into several categories, including: 1) magnetic energy storage systems, i.e., superconducting magnetic coils, 2) reversible dams, i.e., pumped hydro, 3) pneumatic energy storage systems, i.e., air compressors, 4) mechanical energy storage systems, i.e., flywheels, 5) thermal energy storage systems, i.e., geothermal energy and 6) electrochemical energy storage systems, i.e., capacitors, fuel cells and batteries, according to different energy storage mechanisms and distinct properties such as different energy densities, charge/discharge rates, storage time, cost and efficiencies.[8]

Among these different energy storage systems, the electrochemical energy storage systems, which store energy under a chemical way, play an important role in storing and accumulating sustainable and renewable energy. This storage technique benefits from the fact that both electrical and chemical energy shares the same carriers and the electrons. Based on the working principles controlled by different electrochemical reactions, charge/discharge mechanisms, chemistry as well as energy and power densities, the electrochemical energy storage systems could be classified as capacitors, fuel cells and batteries,[9] as mentioned above. The systematic classification of electrochemical energy storage and conversion systems is shown in **Figure 1.2**.[10]

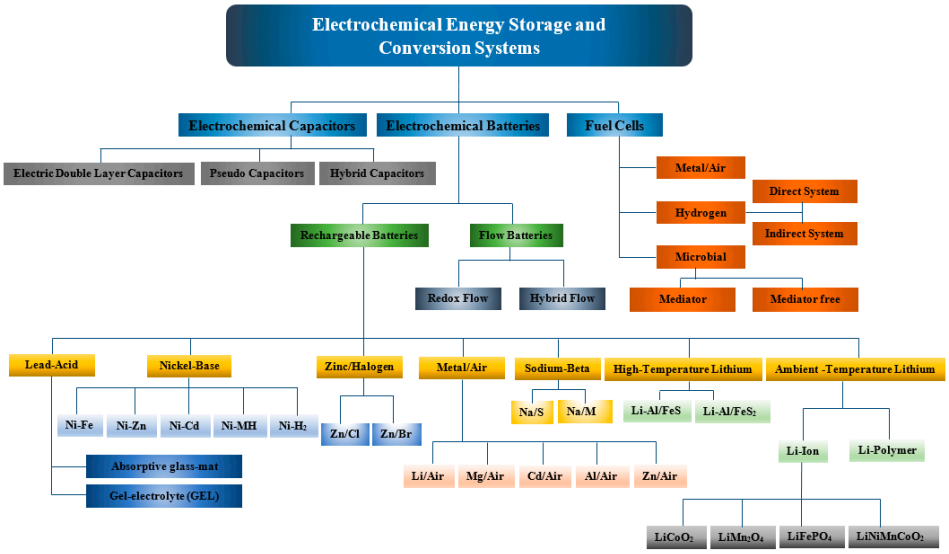

Figure 1.2. The classification of electrochemical energy storage and conversion systems. Reproduced with permission from Ref. [[10]].

Figure 1.3 presents the comparison of these three electrochemical energy storage systems, showing their specific energy and specific power

energies. Electrochemical capacitors or supercapacitors have been known as one of the electrochemical energy storage devices owing to their high power density, long cycle-time and good capacity retention.[11-12] Nevertheless, supercapacitors suffer from a lower energy density compared batteries and fuel cells (**Figure 1.3**), which limits their applications in some scenarios where higher energy density is needed.[13-14] According to their different working principles, electrochemical capacitors are mainly divided into three categories: 1) electric double layer capacitors (EDLCs), 2) hybrid capacitors (HCs) and 3) pseudo-capacitors (PCs).[10]

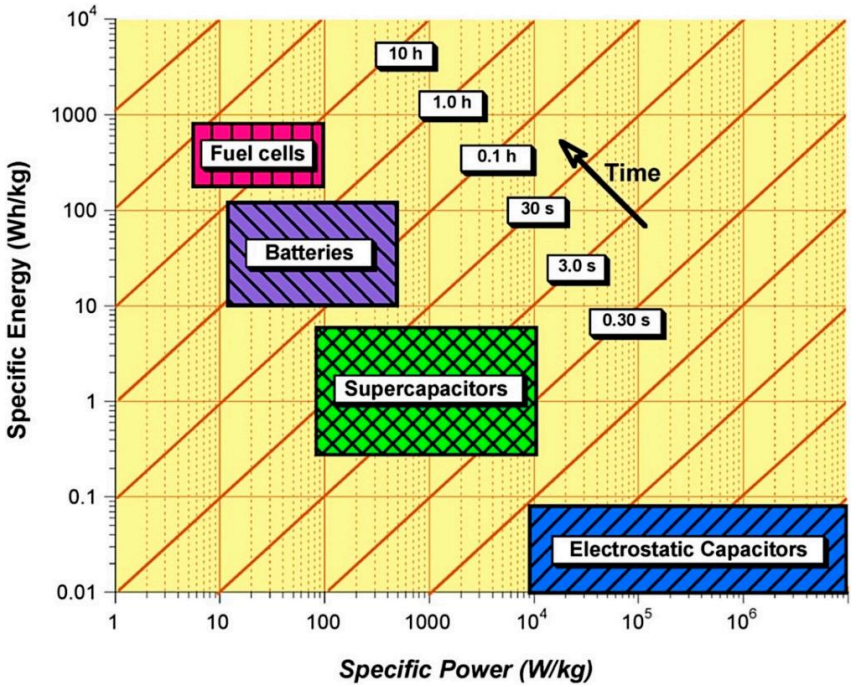

Figure 1.3. Comparison of the different electrochemical energy storage systems. Reproduced with permission from Ref. [10].

A fuel cell is mainly composed of a fuel (e.g., hydrogen) and an oxidizing agent (e.g., oxygen), which can transform the chemical energy of these two components into electricity though a pair of redox reactions.[15] As shown in **Figure 1.4**, electricity is created once the two chemical reactions occur at the interfaces of the anode, electrolytes and cathode components.[16] Fuel cells differ from batteries that they require a continuous source of fuel and oxygen/air to sustain the chemical redox reactions, while for batteries, all the active materials/ions are contained in the housing. However, fuel cells can produce electricity continuously as long as fuel and oxygen are fully added.[17] Compared with batteries and supercapacitors, fuel cells deliver the highest energy density, but much lower power density (as shown in **Figure 1.3**). Besides, the expensive catalyst/hydrogen, the lack of charging infrastructure and immature technologies for now hinder their large-scale application.

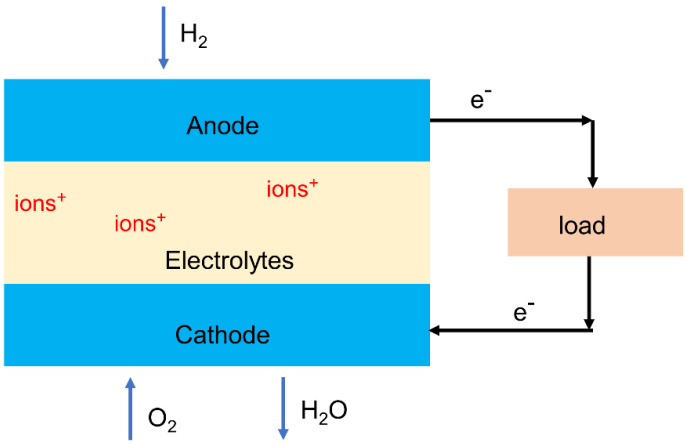

Figure 1.4. Schematic diagram of a fuel cell.

Batteries with high energy density and decent power density have been widely employed as energy storage devices in portable electronics (such as laptops, mobile phone and cameras) and electric vehicles (such as Tesla electric vehicles) as well as stationary energy storage systems. A conventional battery or a cell is made up of anode materials, cathode materials and electrolytes, except for flow batteries. To prevent short-circuits of batteries, separators immersed in electrolytes are used in liquid-based batteries. A battery could convert chemical energy into electric energy though the reactions occur at the interfaces of positive and negative sides.[18-20] The wider discussion of different batteries, especially lithium batteries, are detailed in the following section.

1.3. Rechargeable batteries

1.3.1. Classification of batteries

Batteries are generally classified as two categories, 1) primary batteries (i.e., single-use or "disposable" batteries) and 2) secondary batteries. Primary batteries are able to discharge only one time and a primary battery will be discarded once the discharge process is finished because the electrode materials are irreversibly changed/damaged and are not capable of being recharged. Hence, the primary batteries cannot be used as electrochemical energy storage systems/devices to power 3C electronics and electric vehicles, and to store the energy generated from the sustainable energy resources.[21]

Secondary batteries, also known as rechargeable batteries, could be charged/discharged reversibly and repeatedly. Upon the charging process, cations are extracted from the positive materials and transported through the

electrolytes to the negative electrode side. Inversely, during the discharge process, the cations will migrate from the negative material and return back to the positive electrode material, and the corresponding electrons transfer from cathode sides to anode sides in external circuit. Rechargeable batteries are produced in many different shapes and sizes, ranging from miniature button cells to megawatt systems connected to stabilize an electrical distribution network.[22] Several different rechargeable batteries are commercial and widely used in our social life, including lead-acid batteries, nickel-cadmium batteries (Ni-Cd), nickel-metal hybrid batteries (Ni-MH) as well as lithium-ion batteries (LIBs). Among these options, LIBs with high energy density (**Figure 1.5**), long cycle life, fast charge and discharge rates as well flexible and lightweight design are considered as one of the most promising electrochemical energy storage system.[22]

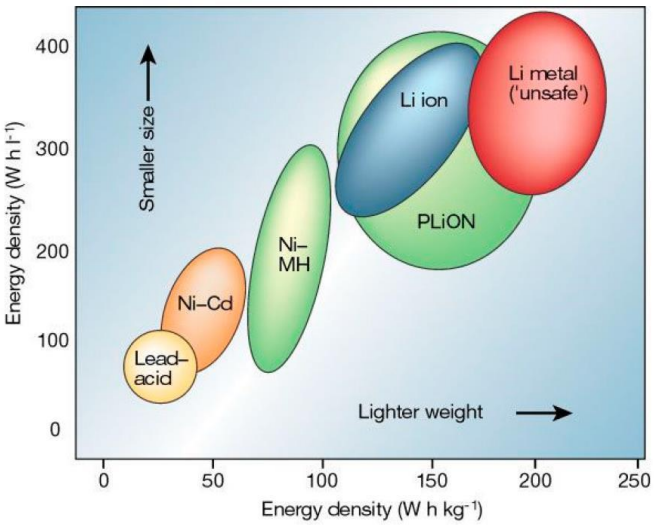

Figure 1.5. Comparison of the different rechargeable battery technologies in terms of volumetric and gravimetric energy density. Reproduced with permission from Ref. [22].

1.3.2. Rechargeable lithium-ion batteries (LIBs)

The research of lithium batteries has gone through a process from the lithium metal (Li°) batteries (LMBs) with a Li° metal anode in the 1970-80's to LIBs using graphite as anodes material, and returns to revive the LMBs due to their higher energy density compared to LIBs,[23] and a discussion of LMBs will be presented in the following section of **1.4**. The electrochemical reduction potential of lithium was firstly explored by Kahlenberg in 1899 and then following by Lewis in 1912.[24] Latterly, Rüdorff, Rouxel and co-workers firstly revealed that the alkali metals could be chemically and rapidly intercalated between the S-Ti-S slabs in a liquid ammonia solution.[25-26] The dichalcogenide battery was then patented by Whittingham who also firstly demonstrated battery performance of the Li° || TiS_2 cells in 1976.[27] This kind of cells were then commercialized by Exxon and exhibited at an electric vehicle (EV) show in 1977.[28] However, the high reactivity of Li° and lithium dendrites growth in the flammable liquid electrolytes triggered off repulsive safety issues (e.g., fire or even explosion), which inspired researchers to explore safer electrode materials.

In 1979, Armand creatively proposed a novel battery design, 'rocking chair battery', which was composed of two intercalation electrodes with potential difference, allowing lithium ions forth and back reversibly between these two electrodes.[29] Based on this prospective seminal concept, applicable intercalated electrodes such as lithium cobalt oxide ($LiCoO_2$)[30] cathode and carbonaceous anodes were revealed in 1980s, and the first commercial LIB was successfully launched by Sony in 1991. After then, other high voltage/capacity intercalated cathodes [e.g., ternary layered oxide $LiNi_{1-x-}$

$_yCo_xMn_yO_2$ (NCM)], conversion-type electrodes [e.g., sulfur (S) and O_2] as well as environmentally friendly organic electrodes were also discovered and exhibited excellent battery performance.[29, 31]

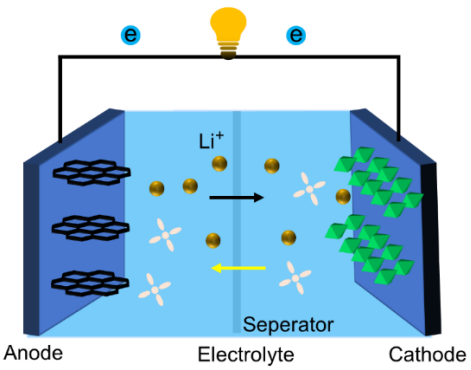

Figure 1.6. Schematic diagram of a rechargeable lithium-ion battery.

A commercially rechargeable LIB is mainly made up of an anode material (e.g., graphite), electrolyte comprising a lithium salt [e.g., lithium hexafluorophosphate ($LiPF_6$)] and organic solvents (e.g., carbonates), a separator (e.g., polyolefin) and a cathode material (e.g., $LiCoO_2$). **Figure 1.6** shows the schematic diagram of a rechargeable LIB, during the charge step, Li^+ is extracted from the cathode, and is embedded into the graphite electrode through the electrolyte, separator and solid electrolyte interface layer (SEI layer) on the surface of the graphite. Meanwhile, the electron follows through external circuit into the anode side. During the discharge process, an inverse behavior is observed.[32]

The electrolyte, as an indispensable component of LIBs, plays an important role in determining the working temperature, capacity, and cycle performance, power density, energy density and safety performance of LIBs.

To fulfill the practical application, an electrolyte in a rechargeable LIB should necessarily meets several requirements, including: 1) excellent thermal and chemical stability, 2) superior compatibility with both anode and cathode, 3) high ionic conductivity, 4) wide electrochemical window, 5) facile preparation and low cost and 6) environmental benignity, etc. Electrolytes for lithium batteries are currently mainly divided into liquid electrolytes and solid electrolytes.[18-19]

Organic liquid electrolytes consisting of lithium salts that are dissolved in organic carbonate solvents [ethylene carbonate (EC), ethyl methyl carbonate (EMC) and vinylene carbonate (VC)] have been abundantly used in currently state-of-the-art LIBs owing to their high ionic conductivity and excellent compatibility towards electrodes. Lithium salts are of importance to dictate the properties of organic liquid electrolytes, for example, the cathodic stability at anode side at low potential depends importantly on the choice of the cation, while the stability of liquid electrolytes at high potentials is mainly determined by the oxidation stability of anions.[33] The ion mobility and dissociation are highly dependent primarily on the delocalization of the anion. Currently, $LiPF_6$ is the dominant lithium salt used in commercially graphite anode-based rechargeable LIBs because $LiPF_6$-based electrolyte has high ionic conductivities and good electrochemical stability. In addition, the $LiPF_6$-based electrolyte could protect the positive electrode Al° current collector against corrosion, and simultaneously could form an excellent SEI on the surface of graphite.[33-34] Yet, $LiPF_6$ is not the ideal lithium salt for every LIBs due to its lower thermal stability even at a moderate temperature (e.g., 60 °C) and its moisture sensitivity.[35-38]

These limitations and drawbacks of $LiPF_6$ salt have motivated extensive research on other salts. Early studies have found that lithium hexafluoroarsenate ($LiAsF_6$), lithium perchlorate ($LiClO_4$), lithium tetrafluoroborate ($LiBF_4$) and lithium trifluoromethanesulfonate ($LiCF_3SO_3$) are good candidates for LIBs.[39-42] Yet, further studies demonstrate that $LiAsF_6$ and $LiClO_4$ are inappropriate for commercial LIBs owing to their toxicity and explosion proneness, respectively. The choice narrows further as $LiCF_3SO_3$ and $LiBF_4$-based electrolytes exhibit relatively low conductivities at room temperature, rendering these salts less popular.[34]

Many other lithium salts are also considered, such as fluorinated sulfonimide salts [lithium bis(trifluoromethanesulfonyl)imide (LiTFSI) and lithium bis(fluorosulfonyl)imide (LiFSI)] and lithium borate salts [lithium bis(oxalato)borate (LiBOB)[43-44] and lithium difluoro(oxalato)borate (LiDFOB)]. Fluorinated sulfonimide salts including a highly conjugated anionic center [i.e., —SO_2—N(−)—SO_2—] are generally well dissociated and soluble in carbonate solvents, presenting decent ionic conductivities and thermal stability. The most popular sulfonimide salt, LiTFSI, is thermally stable up to 380 °C, resistant towards hydrolysis, and conductive in carbonates; yet, the LiTFSI-based carbonate electrolytes are corrosive towards Al° current collector at a potential of > 3.8 V vs. Li/Li^+,[42, 45-46] which is a common issue for these sulfonimide salts, but a proper electrolyte solvent/additive or anions redesign can be facilitated to alleviate or even eliminate the corrosion problem. The popular borate salts, LiBOB and LiDFOB, which promote the formation of stable SEI/cathode electrode interface (CEI) layers on electrodes have been investigated.[47] However, these salts are extremely sensitive to water and undergo hydrolysis at

ambient temperature, and being less soluble, provide insufficient ionic conductivities (e.g., 4×10^{-3} S cm^{-1} at 20 ℃ for 0.7 M LiBOB in EC/EMC).

Apart from the liquid electrolytes-based LIBs, solid-state electrolytes (SSEs) have attracted extensively attention owing to their intrinsic safer feature and better mechanical stability compared with liquid ones. Moreover, SSEs could couple with high-capacity Li° anode and definitely enhance the energy density of LIBs which are suffering from the so-called of 'range anxiety' issue currently,[48] the details regarding to solid electrolytes, especially solid polymer electrolytes (SPEs), will be discussed in section **1.4**.

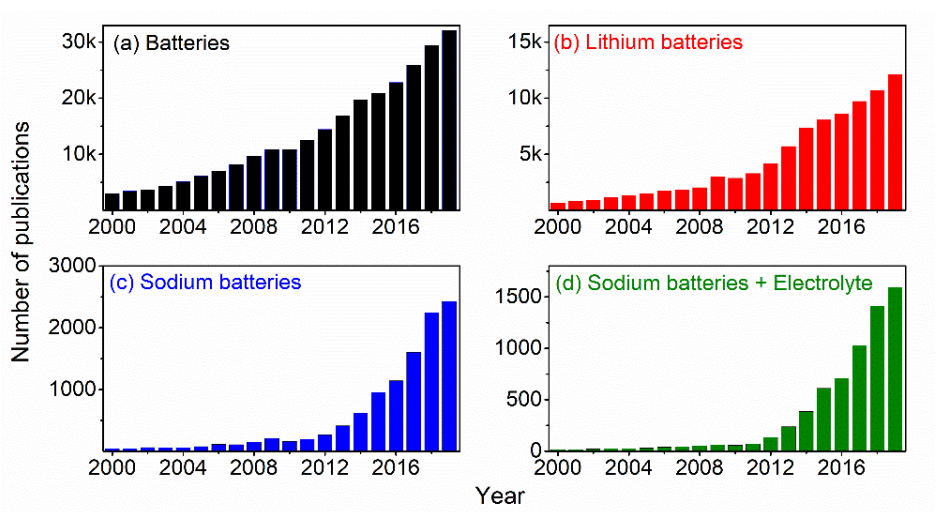

Figure 1.7. Evolution of research interest in batteries (i.e., number of publications) over the past 20 years. The numbers were obtained by searching the key words i.e., (a) "Batteries"; (b) "Lithium batteries"; (c) "Sodium batteries" and (d) "Sodium batteries + Electrolyte" in Scopus database (last updated on the 13th February 2020). Reproduced with permission from Ref. [49].

1.3.3. Beyond LIBs

As mentioned above, rechargeable LIBs have become one of the most important power sources for a wide palette of energy storage scenarios, e.g., portable electronics, electric vehicles (EVs), stationary applications, etc.…[32] [50] However, the LIBs technology built on the reversible intercalation of Li^+ in the two electrodes has reached a global production of 316 gigawatt-hours (GWh) in 2019 and is projected to be > 1200 GWh by 2025 due to the ever-growing market of EVs and stationary energy storage.[51] However, such colossal production of LIBs faces tremendous challenges caused by the shortage of lithium and cobalt sources. As an analogue of the widely known LIBs, sodium batteries have captured intense attention from both academia and industry owing to the higher natural abundance of sodium vs. lithium sources [2.4×10^4 ppm (Na) vs. 20 ppm (Li) in crust and 1.8×10^4 ppm (Na) vs. 180 ppb (Li) in ocean[49]].[52-68] As seen in **Figure 1.7**, the number of publications per year related to sodium batteries has been increasing dramatically in the past 10 years. In recent years, several innovative companies dedicated to sodium battery technologies (e.g., HiNa battery,[69] [70] Faradion,[71] and Tiamat[72]) have been founded, and in particular, sodium-ion batteries (SIBs) have been successfully implemented as power sources for low-speed EVs and a 500 kWh grid energy storage,[69] [70] strongly manifesting the technological feasibility of sodium batteries.

To clarify the technical feasibility of sodium batteries, energy densities of sodium and lithium batteries were estimated in terms of liquid electrolytes (LEs) and SPEs, respectively. As seen in **Figure 1.8**, several interesting conclusions could be drawn:

1) The energy density of sodium-based cells is quite decent even with ~500 mV difference at the anode side, and this is certainly in favor of achieving low cost for storing every kilo-watt-hour (kWh) of energy.

2) The incorporation of SE increases slightly the energy density (~10% in gravimetric values), SPEs are the best candidate compared to glassy and ceramic electrolytes due to the lower specific gravity of the former.

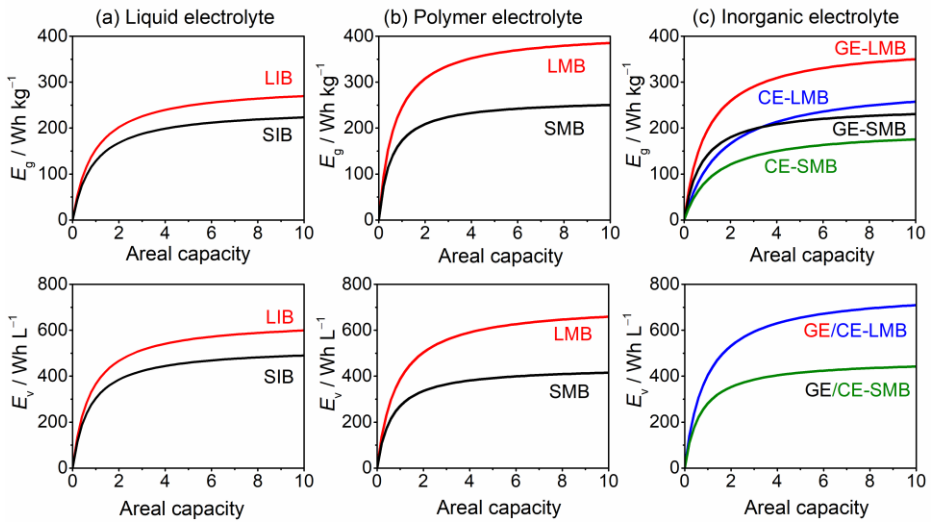

Figure 1.8. Estimated gravimetric (E_g) and volumetric (E_v) energy densities of lithium and sodium batteries with various kinds of electrolytes: (a) liquid electrolyte; (b) polymer electrolyte; (c) inorganic electrolyte. Graphite | LE | $LiFePO_4$ and hard carbon | LE | $NaFePO_4$ cells are denoted as LIB and SIB, respectively. Li° | SPE | $LiFePO_4$ and Na° | SPE | $NaFePO_4$ are cells denoted as LMB and SMB, respectively. Li° | glassy electrolyte (GE) or ceramic electrolyte (CE) | $LiFePO_4$ and Na° | GE or CE | $NaFePO_4$ cells are denoted as GE (CE)-LMB and GE (CE)-SMB, respectively. Noteworthily that the volumetric energy densities of glassy and ceramic electrolyte-based cells are superimposed in Figure 1.8c. Reproduced with permission from Ref. [49].

3) The difference between sodium metal (Na°) anode and hard carbon is not as obvious as Li° electrode vs. graphite anode, e.g., 350 Wh kg^{-1} for Li° | SPE | $LiFePO_4$ cell vs. 250 Wh kg^{-1} for graphite | LE | $LiFePO_4$ cell at an areal capacity of 4 mAh cm^{-2} (40% increase); 220 Wh kg^{-1} for Na° | SPE | $NaFePO_4$ cell vs. 200 Wh kg^{-1} for hard carbon | LE | $NaFePO_4$ cell at an areal capacity of 4 mAh cm^{-2} (~10% increase). Hence, low negative positive (N/P) capacity ratio for Na°-based solid sodium batteries is of vital importance for attaining sufficient energy density.[49]

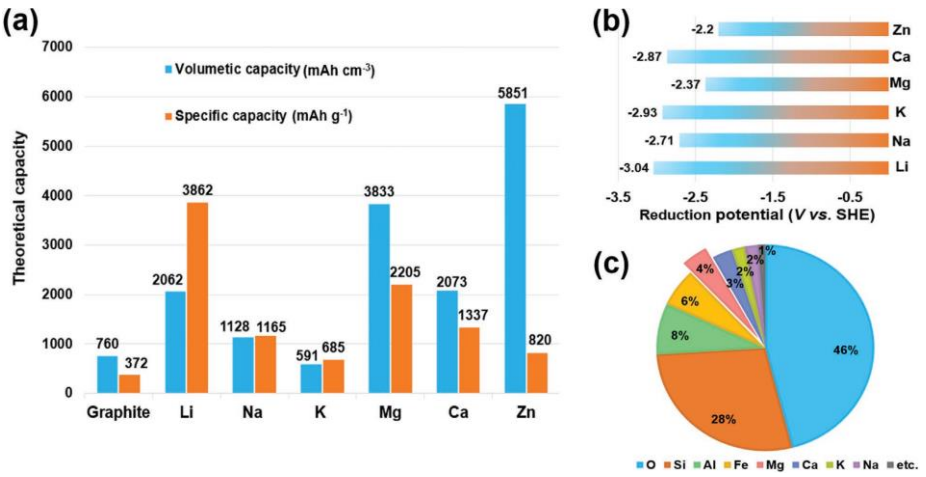

Figure 1.9. (a) The theoretical capacity of graphite and various metal anodes. (b) Reduction potential of various metal anodes. (c) The elemental abundance in earth crust. Reproduced with permission from Ref. [73].

Similar to sodium batteries, potassium batteries are also attracting intense attention in scientific research due to its higher elemental abundance, comparable reduction potential (see **Figure 1.9**) and lower cost of electrodes materials compared with those of lithium. It is reported that the world resource of potassium is about 250 billion tons, and in a sharp contrast to

lithium, potassium resources are available all over the world. Furthermore, it is well known that intercalation of K^+ cations into graphite electrode is successfully feasible, whereas intercalation of Na^+ cations is not achieved. In addition, aluminum foils can be employed as current collectors in potassium batteries because potassium is not capable to form alloys with aluminum, which can significantly decrease the cost and weight of potassium batteries. However, with lower reversible capacity and rate performance as well as inferior cyclability, potassium batteries necessitate much improvement.[74-83]

Except for the monovalent cation's batteries (Li, Na, K), multivalent batteries have an advantage with respect to volumetric energy density compared to LIBs (see **Figure 1.9a**), are regarded as promising alternatives to monovalent batteries. Although it is unachievable to compete with the gravimetric energy density of lithium metal batteries due to the lowest weight of lithium, the gravimetric energy density of multivalent batteries is much higher than that of the LIBs where graphite is used as anode material, as shown in **Figure 1.9a**. Several multivalent rechargeable batteries, e.g., Mg, Ca, Zn and even Al batteries, have been studied over the past decades;[84-87] however, all these multivalent batteries are beyond the scope of this thesis and are not discussed here.

1.4. Rechargeable lithium metal batteries (RLMBs)

1.4.1. Challenges of lithium metal (Li°) anode

Since the inauguration in commodity market in the early 1990s, LIBs have become the most dominant power source for portable electronics, and have become attractive for electrical vehicles (EVs) and stationary energy

storage systems which are of supreme importance to enable greener and more sustainable societies. Differing from the evolution of computer science where the memory of chips doubles every 18 months as indicated by Moore's law, the energy density of LIBs has been increasing in a low growth rate in the last 60 years (ca. 3% per year),[88] which would not fulfil the stringent requirements of next-generation rechargeable batteries for emerging applications, in particular EVs which requires a driving range comparable to petrol-fuelled vehicles.

However, the actual energy density of state-of-the-art LIBs using graphite as anode is gradually approaching its theoretical limit value due to the lower capacity of graphite (372 mAh g^{-1} based on LiC_6). With the extra-high specific capacity (3860 $mAhg^{-1}$) and the lowest negative electrochemical potential (−3.040 V vs. the standard hydrogen electrode), Li° has been considered as the "Holy Grail" electrode for batteries and received extensive research attention. The replacement of conventional graphite anode with higher capacity anodes is regarded as one of the most viable approaches to tackle the "driving range anxiety".[89-92]

Lithium, 'lithion/lithina', with the symbol of '*Li*' is located in IA group in periodic table and atomic number is 3, is a soft, silvery-white and the lightest alkali metal. It was firstly detected by Arfwedson and Berzelius in 1817 when they were analyzing petalite ore ($LiAlSi_4O_{10}$).[93-94] In 1821, it was isolated by Brande via the electrolysis of lithium oxide (Li_2O), and the commercial production of lithium was launched in 1923 by the German company Metallgesellschaft AG, which performed an electrolysis of a liquid mixture of lithium chloride (LiCl) and potassium chloride (KCl).[24] Li° is one

of the most favored anode choices for next-generation lithium batteries, especially lithium–sulfur and lithium–air batteries. After falling into oblivion for several decades owing to its safety issues (as mentioned in section **1.3.2** in this chapter), Li° is now ready for a revival, thanks to the development of investigative tools and other modification strategies and methodologies.[23]

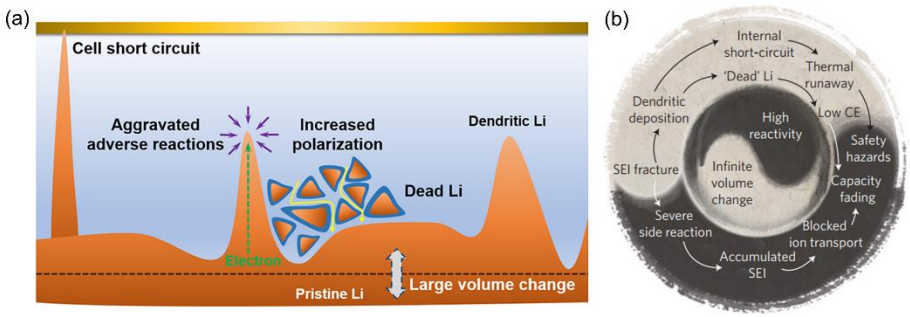

Figure 1.10. (a) Scheme of dilemma for Li° anode in rechargeable batteries Reproduced with permission from Ref. [95]. (b). Correlations among the different challenges in the Li° anode, originating from high reactivity and infinite relative volume change. Reproduced with permission from Ref. [23].

Similar to other alkali metals, lithium is a highly reactive metal that tends to react with commonly used electrolytes such as carbonate solvents and lithium salts in LMBs to form the SEI due to its low electrochemical potential. It has been reported that the SEI is made up of a dual-layer structure with an inner inorganic layer and an outer organic layer, which could enable the LMBs with good cyclability and high Coulombic efficiency.[96-99] However, the mechanically fragile and unstable SEI breaks and regenerates during operation process, resulting in the consumption of electrolytes as well as Li° anode, and thereby causing the premature failure of LMBs. An ideal SEI for a safe and high-performance rechargeable LMB

should possess the following properties: 1) proper thickness, 2) high ionic conductivity and electron-insulating features, 3) strong mechanical toughness, and 4) superior structural stability during long-term cycling.[100-107]

Notoriously, lithium ions tend to deposit in a dendritic morphology and the uncontrollable Li dendrites caused by uneven deposition of lithium may detach from the lithium substrate to form "dead lithium' or pierce the separator, eventually resulting in short circuits of batteries, overheat and even fires (see **Figure 1.10a**).[95] In addition, the infinite volume change of Li° anode is another challenge that prevents the achievement of long-term cycling performance of LMBs compared with the conventional graphite anode, whose volume change is about 10% during cycling processes. Differing from the graphite anode, Li° anode is "hostless", and the volume change is almost infinite in theory during the charge and discharge operation processes. The large volume change may easily destroy mechanically fragile and unstable SEI, and thus forming holes or cracks on the surface of Li° anode (see **Figure 1.10b**).[23] In this case, the liquid electrolytes might go through those cracks and react with the fresh lithium underneath to form new SEI. The repeated destruction and repair of the SEI can endlessly consume active lithium and liquid electrolytes, which can form a thick passivation layer on the surface of Li° anode and thus significantly increase the overpotential of the batteries.[23, 108-118]

In order to overcome above challenges of Li° anode to suppress lithium dendrites for a safe Li° anode and achieve a high-performance of RLMB, multiple strategies and methodologies have been proposed and employed, including: 1) introducing functional electrolyte additives (e.g., functional

salts or solvents), 2) constructing an artificial SEI through electrochemical, chemical or physical treatments, 3) utilizing a highly-concentrated/locally high-concentrated or nanostructured electrolytes, 4) using solid state electrolytes (e.g., SPEs, inorganic electrolytes or composite polymer electrolytes), 4) designing structured anodes (e.g., 3D anodes), 5) modifying separators and 6) optimizing cell operation programs through the Battery Management System (BMS), etc.[95, 119-126] Amongst all the strategies, the solid polymer, ceramic and their intermediate composite solid-state electrolytes are expected to provide a desirable mechanical property (high shear modulus) that could efficiently suppress lithium dendrites growth. More importantly, replacing the flammable organic liquid electrolytes with solid-state electrolytes could significantly alleviate the safety issues of RLMB such as leakage and fires, thus drastically enhancing the safety performance of LMBs.[107, 127-130]

1.4.2. Polymer electrolytes for RLMBs

As mentioned above, apart from the widely used organic liquid electrolytes, solid-state electrolytes with high safety and intrinsic feature of lithium dendrites suppression have attracted extensively attention. The research of solid ion conductor could be traced back to 1834 when Faraday proposed the first example of Ag_2S and PbF_2. As early as 1957, Masdupuy discovered a lithium ion conductor Li_3N with a high conductivity of 10^{-3} S cm^{-1}.[131] Two decades later, in 1976, Hong reported the synthesis and characterization of $Na_{1+x}Zr_2P_{3-x}Si_xO_{12}$ ($0 < x < 3$) compounds (known as NASICON), of which the Na^+ could be ion-exchanged with Li^+ to prepare LISICON.[132] In 1993, Chen et al.[133] showed that the perovskite-type lithium

ion conductor $Li_{0.34}La_{0.51}TiO_{2.94}$ (LLTO), exhibiting a high ionic conductivity (σ_{total}) of 2×10^{-5} S cm^{-1} at room temperature, indicating that this conductor had a large amount of equivalent sites for Li^+ to occupy and freely transport. Later, Murugan et al.[134] revealed a garnet-like inorganic conductor $Li_7La_3Zr_2O_{12}$ which showed a high ionic conductivity (3.0×10^{-4} S cm^{-1} at 25 °C) as well as good thermal and chemical stabilities, enabling it as a promising SSE for all-solid-state rechargeable lithium batteries. In 2011, Kanno et al.[135] originally developed a three-dimensional-framework-structure lithium superionic conductor, $Li_{10}GeP_2S_{12}$, which exhibited the highest ionic conductivity of 1.2×10^{-2} S cm^{-1} at RT compared with those inorganic SSEs reported from previous literature. After that, more conductive inorganic solid-state electrolytes such as $Li_7P_3S_{11}$ ($\sigma = 1.7 \times 10^{-2}$ S cm^{-1} at RT)[136], $Li_{9.54}Si_{1.74}P_{1.44}S_{11.7}Cl_{0.3}$ ($\sigma = 2.5 \times 10^{-2}$ S cm^{-1} at RT)[137] were reported, but nonetheless, the poor interface stability and compatibility as well as the brittleness of inorganic solid-state electrolytes should be improved to meet the requirements of lithium batteries for large-format application.[138-140 141]

In contrast to inorganic solid-state electrolytes, polymer electrolytes are more flexible, processable, and possess superior interfacial compatibility as well as stability towards electrodes, especially Li° anode.[142] In addition, the molecular structures, mechanical properties, and ion transport of polymer electrolytes could be finely designed and tuned to advance and improve battery performance. In principle, polymer electrolytes for Li° batteries can be divided into three major categories: dry SPEs, gel polymer electrolytes (GPEs), and their hybrids with ceramic as composite polymer electrolytes (CPEs). The protocol of solid polymetric ion conductor could be traced back

to early 1970s when Wright et al. found that the poly(ethylene oxide) (PEO) was a good conductive matrix for alkali-metal-ions, and simultaneously they also found that the ionic conductivity of PEO/KSCN could be enhanced significantly at high temperatures.[143] Inspired by this work, Armand proposed the employment of these ionic conductive materials as SPEs for rechargeable lithium batteries. However, SPEs-based batteries suffer from low ionic conductivity at RT, which hinders their application areas. Therefore, considerable strategies and approaches have been developed, such as polymeric matrix modifications, incorporation of inorganic fillers/electrolytes to form composite electrolytes, novel lithium salts design and doping with additives etc. to enhance the ionic conductivity of SPEs.[144] The practical feasibility of SPEs-based RLBs are testified by the worldwide implementation of Bluecars® and Bluebuses® commercialized by the Bolloré Group since 2011 **(Figure 1.11**). After that, new polymers and salts have been designed and synthesized to further enhance the room-temperature ionic conductivity and lithium-ion transference number (T_{Li^+}), which will be presented in the following sections.[127]

An ideal polymer electrolyte used in a high-performance lithium metal battery ought to fulfill following some requirements.[128-130, 145-146]

1) Mechanical stability. As polymer electrolytes serve both as electrolyte and separator in lithium metal batteries, polymer electrolytes need to be able to deform elastically stable and relax when stress is applied in the process of manufacture, cell assembly and operation process. More significantly, a polymer electrolyte with high mechanical stability will inhibit or suppress lithium dendrites.

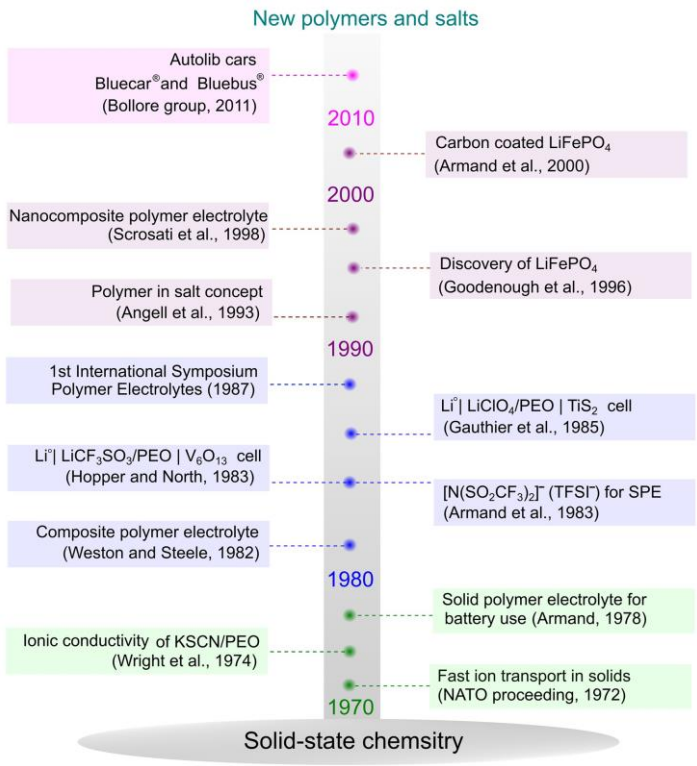

Figure 1.11. Historical overview on the development of solid polymer electrolytes (SPEs)-based solid-state lithium metal batteries. Reproduced with permission from Ref. [127].

2) High ionic conductivity. Ionic conductivity is a standard for measuring the certain ability of ions conduction in electrolyte systems and also a determining factor to dictate the electrochemical performance of lithium metal batteries. Superior ionic conduction and electronic insulation are needed for polymer electrolytes to achieve a rapid charge/discharge of cells.

3) High chemical and thermal stability. The polymer electrolytes for lithium metal batteries should be inert and unreactive towards electrodes

(especially Li° anode) and other cell components when contact with them even at high temperature. In addition, a high thermal stability of electrolyte components is of vital importance to enable scalable processing of polymer electrolytes, e.g., extrusion process, without detrimental decomposition.

4) Wide electrochemical window. The electrochemical window of one electrolyte is the potential domain within which the material is stable, i.e., does not undergo destructive reduction or oxidation. The oxidation potential SPEs for lithium metal batteries nominally should be higher than the operating potential of the cathode and the corresponding reduction potential must be lower than that of the Li° anode. To meet the practical application, the polymer electrolytes for lithium metal batteries should possess a high oxidation potential at least > 4.0 V vs. Li/Li^+ to appropriately and compatibly incorporate with high-voltage cathode materials.

5) High lithium-ion transference number (T_{Li^+}). A high T_{Li^+} is prone to reduce the salt concentration gradients and concentration polarization during cell operation, which is beneficial to obtain higher power density and reduce the nucleation reaction of dendrites.

6) Facile preparation and low cost. The methodologies to prepare polymer electrolytes for lithium metal batteries are supposed to be as simple as possible to reduce the preparation cost.

7) Environmental benignity. The elements and materials for the preparation of polymer electrolytes should be non-toxic and sustainable. Those materials possessing better chemical and biochemical degradability are desirable to avoid the potential risks to environment and human health

once the electrolytes or their decomposition products leak out of the battery packs.

1.4.2.1 Solid polymer electrolytes (SPEs)

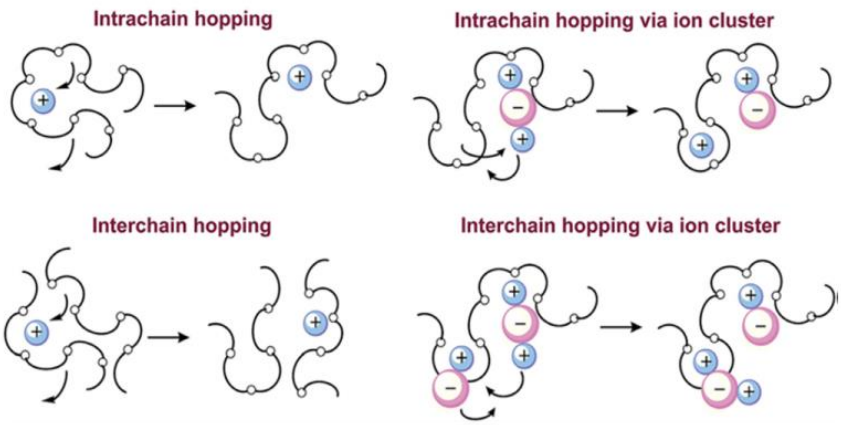

Figure 1.12. Mechanism of ion transport in PEO-based polymers. Reproduced with permission from Ref. [128].

Solid polymer electrolytes (SPEs) are made up of polymer matrices and lithium salts as solutes without any plasticizers (e.g., liquid solvents/electrolytes or ceramic particles), which can be facilely prepared by conventional casting and hot high-press process. In SPEs, the lithium ions are generally solvated and complexed by the polar functional group, e.g., –O–, –S–, –N–, –P–, C=O and C≡N, in the backbone of the matrices.[129] Indeed, ionic conductivity is proportional to the effective number of mobile charge carries, multiplied by the ions mobility and the elementary electric charge. Hence, the polymer matrices with high solvation power and dielectric constant could enable the dissociation of lithium salts in SPEs, and thereby enhance the ionic conductivity. Taking into consideration the ability

to dissolve lithium salts, polyether appears to be the one of the best candidates for serving as polymer matrices because of the good solvation/complex between the ether oxygens and lithium ions.[129] Among these, PEO is the earliest studied and most applied polymer matrix due to its high donor number (ca. 22) and superior Li^+ solvation generated from its flexible ethylene oxide segments and ether oxygen atoms.[92]

In PEO-based SPEs, Li^+ ions transfer in the PEO matrix adopts a commonly accepted mechanism. It was generally believed that ion transport in PEO-based SPEs occurs only in amorphous regions above their glass transition temperature (T_g). As shown in **Figure 1.12**, Li^+ ions are coordinated by the ether oxygen atoms on the PEO chain. The local segmental motion of the polymer chains stemmed from conformational change of polymer segments leads to the appearance of free volume. With the processes of breaking/forming lithium–oxygen (Li–O) bonds, lithium ions transport by intrachain or interchain hopping in the PEO-based electrolytes facilitated by a segmental motion of the PEO chains.[128]

However, PEO-based SPEs present a low ionic conductivity at temperatures below the melting point due to the semi-crystalline nature of the PEO chains. Furthermore, the PEO-based SPEs also show a low anodic stability (ca. 4.0 V Li/Li^+), limiting their utilization as electrolytes in high voltage lithium metal batteries [e.g., lithium cobalt oxide (LCO)-based cell)]. Therefore, other polymer matrices with specific properties have also been investigated, including polycarbonates,[147] polyesters[148] and polysiloxane,[130] showing promise for lithium metal batteries. Recently, our group developed a new family of comb-like polymer matrices comprising commercial

polyetheramines (Jeffamine®) as side moiety and poly(ethylene-altmaleimide) as backbone, showing nearly total amorphicity with a low glass transition temperature and emerging as an appealing candidate for building robust SPEs with high ionic conductivity at ambient temperatures.[92]

1.4.2.2 Composite polymer electrolytes (CPEs)

As mentioned above, SPEs have been considered as one of the most promising candidates for high safe lithium batteries due to their shape versatility, flexibility and thermodynamic stability. However, the low mobility of cations in SPEs (e.g., PEO) at ambient temperature limits their practical applications.[142] Introducing inorganic fillers into polymer matrices is treated as an elegant approach to enhance the ionic conductivity of electrolytes for batteries considering that: 1) the crystallinity and glass transition temperature (T_g) can be reduced after the addition of inorganic fillers;[149] and 2) the surface groups of inorganic fillers can interact with polymer chains and salts, and that could facilitate faster ion conduction throughout the conductive pathways on the inorganic surfaces.[150-154] In addition, the inorganic fillers could also help to enhance the mechanical stability of the SPEs.

The inorganic filles are generally divided as two categories: 1) passive inorganic fillers and 2) active fillers. The passive fillers are not ionically conductive and different types of fillers have been studied and employed in SPEs, such as ceramic oxides (e.g., Al_2O_3,[155-156] SiO_2,[157-160] TiO_2,[161-162] ZrO_2,[163-164] Y_2O_3,[165] $LiAlO_2$,[166] and $Mg_2B_2O_5$[167]), ferroelectric ceramic fillers (e.g., $BaTiO_3$, $PbTiO_3$, $LiNbO_3$)[168-170] and clays.[171] For this kind of CPE, the Li^+ ion transportation mainly occurs both in the amorphous phase

of polymers (**Figure 1.13a**) and the interfacial phase (**Figure 1.13b**). In contrast to the passive filler, active filles like garnet-based[172-174] perovskite-structured-based,[175-177] NASICON-based[178-179] and LISICON-based[180-181] inorganic solid electrolytes are Li^+ ion conductive. When the content of these active fillers exceeds a threshold (i.e., > 50 wt%), the active fillers can form an ionic conduction pathway to enhance the ionic conductivity of the CPEs (**Figure 1.13c**).[182-183]

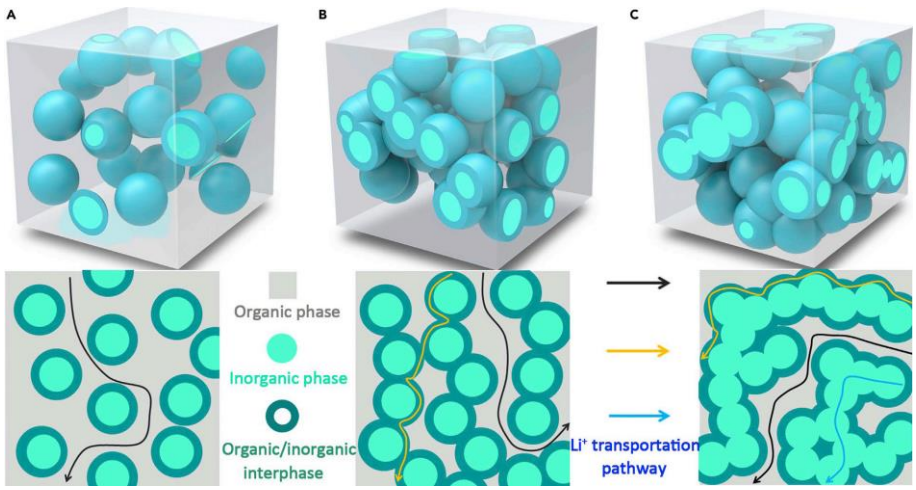

Figure 1.13. Schematic view of organic/inorganic composites with different microstructures and various Li^+ transportation pathways. Reproduced with permission from Ref. [183].

1.4.2.3 Gel polymer electrolytes (GPEs)

SPEs and CPEs are promising alternatives of conventional liquid electrolytes for highly safe and structurally flexible lithium metal batteries; however, their utilization in practical cells/batteries is hindered by the still low room-temperature ionic conductivity and unsatisfactory interfacial compatibility with electrodes (in particular, when no liquid solvent is added

in CPEs). In this regard, GPEs, containing a fraction of liquid phases/ plasticizers (normally the content of liquid phase/plasticizers exceeds 50 wt%), have attracted increasing attention owing to their higher ionic conductivity, better interfacial contact with the electrodes, etc. Therefore, flammable or volatile liquids, such as ether solvents and carbonate solvents were introduced into SPEs or CPEs to enhance the performance of lithium metal batteries despite a possible loss in safety. Besides, non-flammable and less-volatile ionic liquids (ILs) were also investigated as plasticizers for lithium metal batteries.[109, 184-185]

In the GPEs, Li^+ ions are mainly transported in the liquid plasticizers containing dissolved lithium salts, and the plasticizers also react with electrodes to form SEI and CEI films.[148] Several polymer matrices such as PEO,[186] poly(vinyl chloride) (PVC),[187-188] poly(acrylonitrile) (PAN),[189-190] poly(vinylidene fluoride) (PVDF)[191] and poly(vinylidene fluoride-co-hexafluoropropylene) (PVDF-HFP)[192] have been extensively used in GPEs and provided the GPEs with mechanical strength. The introduction of liquid phases into polymer electrolytes might reduce mechanical stability of GPEs membranes, thus supporting materials such as glass fibers, polymers or non-woven fibers including cellulose were applied as scaffolds to reinforce mechanical strength of GPEs.[193-195]

1.5. Lithium salts for SPEs

The anion chemistry of lithium salts plays a pivotal role in dictating the physicochemical and electrochemical performance of SPEs, thereby influencing the cyclability of all-solid-state RLMBs. In addition, tuning the chemical structures of salt anions could regulate the reduction potential of

the salts and the SEI components as well, hence, the choice of the salt is very crucial to achieving a high-performance SPEs-based RLMBs. To realize these good properties, several criteria need to be considered for screening suitable lithium salts for SPEs-based RLMBs: 1) weak interaction between lithium cation and anion, which is beneficial for dissociation and dissolution of lithium salts in SPEs; 2) superior anionic flexibility with sufficient plasticizing effect, which is of significance to lower the glass transition temperatures and decrease the crystallinity of polymer matrices; 3) high anodic stability, which is critical for SPEs to be coupled with high-voltage cathode materials; 4) excellent SEI formation ability, which could facilitate to prevent the SPEs from excess consumption and 5) low reactivity against other electro-active species in order to minimize degradation processes.[196] In the early stages of SPEs-based lithium metal batteries, several lithium salts such as, lithium bis(trifluoromethanesulfonyl)imide (LiTFSI),[197] lithium thiocyanate (LiSCN),[198-199] lithium perchlorate ($LiClO_4$),[200-204] lithium hexafluoroarsenate ($LiAsF_6$),[205-207] lithium hexafluoroantimonate ($LiSbF_6$),[205] lithium tetrafluoroborate ($LiBF_4$),[208-209] and lithium trifluoromethanesulfonate (LiTf)[200, 204, 208-215] were studied with the aim of completely dissociating the salts in polymer matrices and studying the complex/solvation between Li^+ and polymer matrices as well as the Li^+ transport in SPEs, thus realizing high Li^+ availability and ionic conductivity. To date, various lithium salts have been investigated for SPEs-based lithium batteries, according to the structures of the salt anions, the lithium salts are generally classified into several categories in this chapter, including 1) lithium borates, 2) lithium phosphates, 3) lithium sulfonates, 4) lithium imides and 5) other promising lithium salts. The chemical structures of the lithium salts for SPEs are summarized in **Scheme 1.1**. It should be noted that

the polymeric lithium salts (e.g., single-ion conducting lithium salts) have also been well studied and have attracted significant attention due to their several excellent properties such as super high T_{Li^+},[142, 216] but those salts are not included here because this thesis is focusing on the lithium salts with simple anionic structures and small molecule weight.

1.5.1. Lithium borates

For lithium borate-based polymer electrolytes, the $LiBF_4$ salt featured with a good thermal stability, low sensitivity towards environmental moisture,[217] low lattice energy is widely used as conducting lithium salt in different polymer matrices in the early days, like PEO,[218] poly(vinyl alcohol) (PVA)[219] and blended PVC/poly(methylmethacrylate) (PMMA),[209] etc.[220] However, the electrolytes consisted of $LiBF_4$ show a relatively low ionic conductivity and the it is unable to form a stable SEI layer at anode side.[221] Lithium bis(oxalato) borate (LiBOB) has been in the spotlight owing to its good thermal stability (200 °C), no risk of production of harmful gases, low cost, and ability to form stable and protective SEI layers on graphite electrodes since Xu et al. introduced it as a lithium conductive salt for LIBs in 2002.[44, 124, 222-223] Later, Scrosati et al. introduced LiBOB into PEO-based SPEs and expected that the large BOB^- anion could interfere with the crystallization process of the PEO chains, possibly resulting in an increase of its amorphous regions and improving lithium-ion transport throughout the electrolyte. As a result, the LiBOB/PEO showed conductivity values varying from 10^{-5} to 10^{-3} S cm^{-1} in a temperature range from 30 to 80 °C and T_{Li^+} values ranging from 0.25 to 0.30.[224] Recent studies have demonstrated that the ionic conductivities of the LiBOB-based electrolytes were able to be

enhanced by introduction of plasticizes and/or inorganic fillers, e.g., succinonitrile,[225] glutaronitrile[226] and SiO_2.[227]

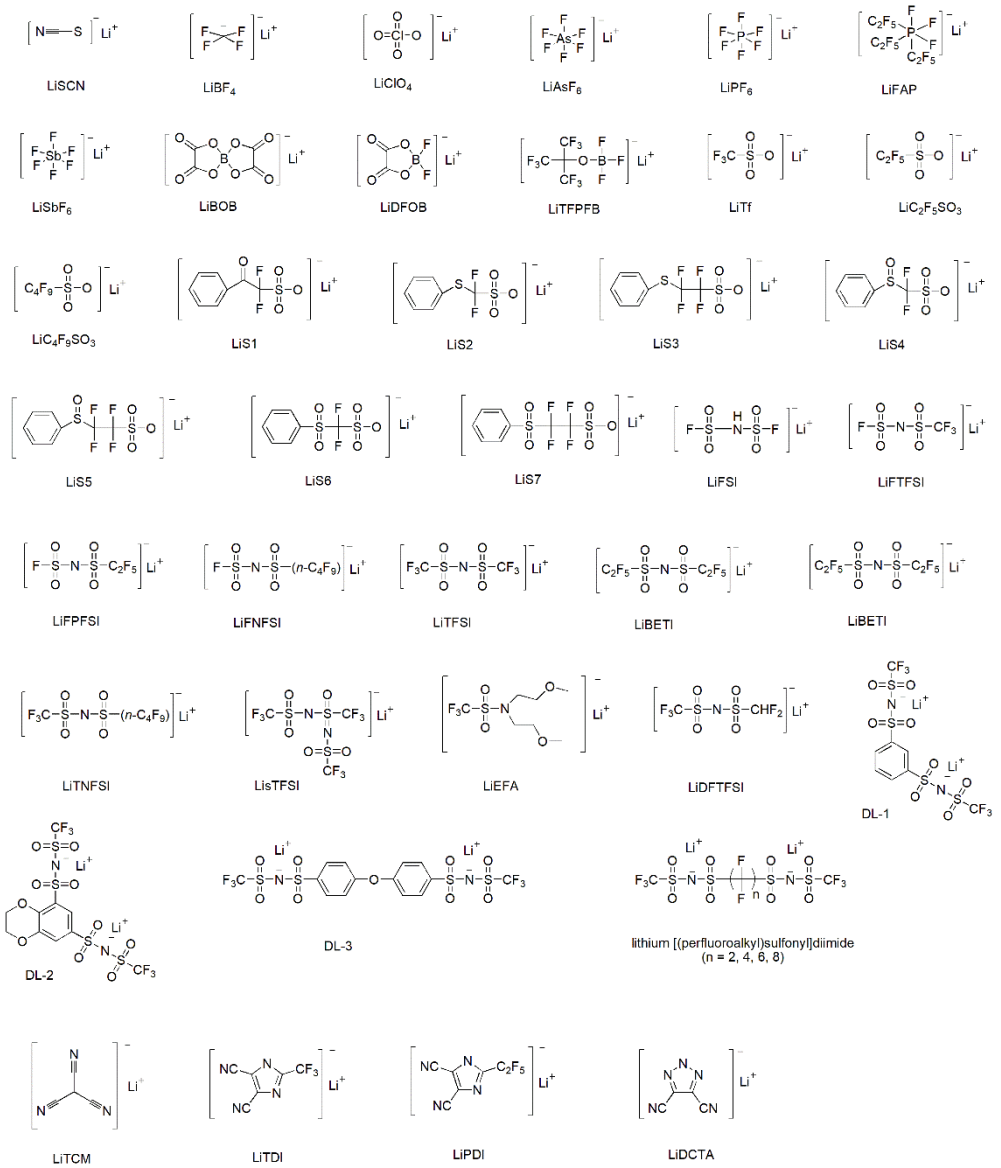

Scheme 1.1. Structures of the lithium salts for polymer electrolytes.

Another lithium borate, lithium difluoro(oxalato)borate (LiDFOB), combining advantages of LiBOB and the low temperature performance of $LiBF_4$ because its structure is made up of half LiBOB and half $LiBF_4$, exhibiting better performances than the other two lithium borate salts.[228] The PEO-based SPEs complexed LiDFOB demonstrated an ionic conductivity of 3.2×10^{-5} S cm^{-1} at room temperature (23 °C) attributed to decrease in the degree of crystallinity and increase of amorphous region of the PEO chains.[229] Very recently, Cui et al. reported a SPE comprising a novel highly-fluorinated-anion based lithium salt, lithium trifluoro(perfluoro-tertbutyloxyl)borate (LiTFPFB), and an amorphous comb polymer of poly[propylene oxide-co-2-(2-methoxyethoxy)ethyl glycidyl ether] [P(PO/EM)], showing a high T_{Li^+} of 0.59 due to the supramolecular interaction between the highly fluorinated LiTFPFB and polymeric skeleton of P(PO/EM).[230]

1.5.2. Lithium phosphates

As mentioned above, it is generally accepted that $LiPF_6$ is the largely used lithium salt in commercially graphite anode-based rechargeable LIBs due to its high ionic conductivity, good electrochemical stability, Al° corrosion inhibition and good SEI formation property.[33-34] Yet, $LiPF_6$ displays lower thermal stability even at a moderate temperature (e.g., 60 °C), which excluding its utilization in PEO-based SPEs where a high operation temperature of 70 °C is needed. As an alternative to $LiPF_6$, lithium tris(perfluoroethyl)trifluorophosphate (LiFAP) has been proposed by Schmidt et al. through a partial replacement of the fluorine atoms in $LiPF_6$ by perfluoroalkyl groups. The electron-withdrawing and hydrophobic nature

of the perfluoroalkyl groups not only improve the stability towards hydrolysis but also delocalize of the negative charge, leading to a weak coordination between the Li^+ and FAP^- anion.[231-232] In 2008, the LiFAP salt was incorporated in a PVDF-HFP based polymer electrolyte, which exhibited an ionic conductivity of 6.7×10^{-5} at room temperature, though EC and diethyl carbonate (DEC) were also introduced in that electrolyte as plasticizers.[129, 231, 233]

1.5.3. Lithium sulfonates

Lithium sulfonates are another type of salts that are applied in SPEs in the early stage, LiTf was widely used in different polymer matrices, e.g., PEO,[200, 208, 210-212] polyacrylonitrile (PAN),[213-214] PVC[234] and blended PVC/PMMA.[209] The replacement of CF_3– group with longer perfluorinated alkyl chains might not only effectively enhance the solvating and/or plasticizing effect of the salts but also may result in a good combination of ionic conductivity and T_{Li}^+. Hence, some other lithium sulfonates, lithium perfluoroethanesulfonate ($LiC_2F_5SO_3$), lithium perfluorobutanesulfonate ($LiC_4F_9SO_3$) and a family of aryl-substituted lithium perfluorosulfonates (LiS1-S7; see **Scheme 1.1**) have been proposed and used as electrolytes salts in polymer electrolytes, exhibiting high anodic stability and thermal stability.[235-238] Unfortunately, those lithium sulfonates-based SPEs show poor ionic conductivities, which impedes their application.[129]

1.5.4. Lithium sulfonimides

Significant advancements and developments have been achieved by designing lithium sulfonimides salts with expected low dissociation energy,

high dissolution capability and superior oxidation stability. LiTFSI with excellent physicochemical/electrochemical properties and good plasticizing effect generated from its outstanding anionic flexibility has been regarded as the dominate salt to be used in SPEs and ionic liquids filed since Armand introduced it into SPEs in 1989.[197] Yet, the LiTFSI-based SPEs suffer from a low T_{Li^+}, which could lead to the concentration gradient issue and further increase cell overpotentials or even premature of lithium cells.[239] In addition, the SEI formed at Li° anode in LiTFSI/PEO-based electrolytes is not stable enough to inhibit lithium dendrites growth, and this phenomenon is much more serious when high current densities or high areal capacity of cathodes are performed. As an alternative salt to LiTFSI, LiFSI was incorporated into the PEO-based SPEs by Zhou et al.,[240] it shows superior electrochemical performance compared with the LiTFSI-based counterpart in both Li° || Li° and Li° || $LiFePO_4$ cells because a more stable LiF-rich SEI film could be formed at Li° anode, which benefits from the relatively easier cleavage of S–F bond than the C–F bond in LiTFSI. Nevertheless, the extremely thick SEI generated from LiFSI decomposition may unfortunately cause a high resistance of the SEI because of the low ionic conductivity of the LiF species, resulting in a high overpotential and fast capacity decay.[92, 241-242] Another lithium sulfonimide salt, lithium (fluorosulfonyl)(trifluoromethanesulfonyl)imide (LiFTFSI) (see **Scheme 1.1**), combining the advantages of LiTFSI and LiFSI, was investigated in PEO-based Li-S cells, showing the best interfacial compatibility with Li° anode and cyclability profited from the balanced mechanical stability and interfacial resistance of the SEI.[243] Recently, Zhou et al.[244] investigated the impact of anionic structure of lithium salt on the performances of PEO-based RLMBs through a comparison of their fundamental physical properties,

including ionic conductivity, anodic stability and electrochemical performances utilizing LiTFSI, LiFSI, LiFTFSI, lithium (fluorosulfonyl)(pentafluoroethanesulfonyl)imide (LiFPFSI),[244-245] and lithium (fluorosulfonyl)(*n*-nonafluorobutanesulfonyl)imide (LiFNFSI)[246-248] as conducting salts (see **Scheme 1.1**). Specifically, LiFNFSI-based Li° || Li° and Li || $LiFePO_4$ cells display the best electrochemical performance, which could be explained by the best Li° anode compatibility due to the formation of insoluble organofluoride species at Li° anode and displaying strongest anodic stability of LiFNFSI.

Indeed, it is generally known that replacing the $–CF_3$ moiety with perfluorinated alkyl chains in $TFSI^–$ anion could not only enhance anionic flexibility, anodic stability and T_{Li^+} but also enable to protect Al° current collector from corrosion.[249] Hence, several lithium analogues with longer perfluorinated alkyl chains were proposed, like lithium bis (perfluoroethanesulfonyl)imide (LiBETI),[250-253] lithium (trifluoromethanesulfonyl)(*n*-nonafluorobutanesulfonyl)imide (LiTNFSI)[254] and lithium [trifluoromethane(*S*-trifluoromethanesulfonylimino)sulfonyl]-(trifluoromethanesulfonyl)imide (LisTFSI),[255] showing promising application in PEO-based RLMBs. For example, the LisTFSI/PEO-based SPE exhibited a higher T_{Li^+} (0.29) and lithium-ion only conductivity (σ_{Li^+}; $\sigma_{Li^+} = 2.5 \times 10^{-4}$ S cm^{-1}) compared to the LiTFSI-based one ($T_{Li^+} = 0.14$ and $\sigma_{Li^+} = 2.0 \times 10^{-4}$ S cm^{-1}) at 80 °C.

Apart from introducing the perfluorinated alkyl group to enhance T_{Li^+}, our group suggested an ether-functionalized anion (EFA; see in **Scheme 1.1**) to be used as a counter-charge in a lithium salt, achieving a low anionic

diffusivity but sufficient σ_{Li^+}. The ethylene oxide (EO) unit in EFA anion endows nanosized self-agglomeration of anions and dipole–dipole trapping interactions between the anions and PEO matrix, hindering the mobility of negative charges.[144] In another work, one of the $–CF_3$ moiety in LiTFSI was substituted by a $–CF_2H$ moiety to obtain the lithium (difluoromethanesulfonyl)(trifluoromethanesulfonyl)imide (LiDFTFSI), benefiting from the strong electron-withdrawing ability of F atoms and SO_2 group, the H hydrogen atom in $–CF_2H$ moiety showed a good H-donicity, enabling to form strong H–O bonds between LiDFTFSI and PEO, thus, giving a high T_{Li^+} of 0.35 at 70 °C. Moreover, SEM and XPS results indicated that a homogenous SEI composed of mechanically stable LiF and ionically conductive LiH was formed at Li anode, leading to an enhanced interfacial stability between the SPE and Li° anode.[239, 256]

In addition to the single-lithium salts, di-lithium salts that possess two lithium ions per molecule were also studied as conducting salt for SPEs but using low concentration of salts.[129] Similar to LiTFSI where the negative charges on the nitrogen atom are delocalized by the $–CF_3$ moiety and two sulfonyl groups, the interaction between the anion and lithium cation of the di-lithium sulfonimides is expected to be not high. PEO-based SPEs with a kind of di-lithium salts (DL-1, DL-2 and DL-3; see **Scheme 1.1**) were reported by Chakrabarti et al.,[257] but showed decent ionic conductivities (e.g., 2.19×10^{-6} S cm^{-1} at 30 °C for the DL-1/PEO-based SPE). Creager et al.[258-260] demonstrated a series of di-lithium sulfonimides salts with the structure of [(perfluoroalkyl)sulfonyl]diimide dianions [$CF_3SO_2N(Li)SO_2(CF_2)_nSO_2N(Li)SO_2CF_3$, n = 2, 4, 6, 8]. However, the

super long length of the perfluoroalkylene exhibited a low transportation kinetics, decreasing the total ionic conductivity of the PEO-based SPEs.[129]

1.5.5. Other promising lithium salts

A designer salt anion should possess the ability to form a robust SEI and CEI layers at the anode and cathodes, respectively, facilitating to a better electrode wettability and acting as an important component to get a high ionic conductivity, as mentioned above. The aforementioned fluorinated salt anion may lead to a robust and efficient SEI layer benefited from the formation of LiF as SEI-building material. However, the LiF is a two-sided sword, when becoming a thick layer at Li° electrode, the SEI film is prone to be more resistive because of the low Li^+ conductivity of LiF (about 10^{-31} S cm^{-1}).[261] Hence, a fluorine-free noble salt lithium tricyanomethanide (LiTCM) with a fairly stable structure of a triple C ≡ N group was investigated in our group in PEO-based SPEs. The Li_3N-rich SEI layer with a high σ_{Li^+} generated from the reduction of C≡N group imparts the Li° || Li° cell an extremely low overpotential of 10 mV at 0.2 mAh cm^{-2} at 70 °C.[262] Further research demonstrated that the introduction of a small fraction of LiTCM into the LiFSI or LiTFSI-based SPEs could synergistically form a homogeneous and stable SEI layer, endowing the Li-S cells with superior cyclability.[263-264]

Other salts, such as lithium 2-trifluoromethyl-4,5-dicyanoimidazolate (LiTDI), lithium-4,5-dicyano-2-(pentafluoroethyl)imidazole (LiPDI) and lithium-4,5-dicyano-1,2,3-triazolate (LiDCTA) have been studied in PEO-based SPEs, but with a main focus on their physicochemical properties, such as ionic conductivities rather than electrochemical performance.[33, 128, 265-266]

1.6. Objectives of this thesis

Solid-state based RLMBs (SSRLMBs) are considered as the most promising alternatives to improve the energy density and safety of state-of-the-art liquid-based LIBs. SPEs have been investigated as important candidates for enhancing the energy density and safety of the next-generation rechargeable batteries, due to their good flexibility, no-leakage, less-flammability, light weight, and good compatibility with Li° electrode. PEO chains containing ether oxygen coordination sites show a superior salt dissociation capability, which have been widely used as polymer matrices in SPEs.

It is generally accepted that the chemistry of lithium salts plays a pivotal role in dictating the physicochemical and electrochemical performance of SPEs, thus influencing the cyclability of SSRLMBs. To date, LiTFSI has attracted the most attention among all the lithium salts evaluated for SSLSBs due to its good thermal and chemical stability, structural flexibility, and plasticizing effect when coupled with the PEO matrix. However, the LiTFSI/PEO based SPEs suffer from low lithium-ion transference number (i.e., T_{Li^+}= 0.2) and poor SEI creating properties, resulting in severe cell polarization and simultaneously notorious dendritic growth at the Li° anode at 70 °C.

Within this scope, the main objective of this work is to design and synthesize new lithium salts with suppressed anionic mobility to enhance lithium-ion transference number (T_{Li^+}) without sacrificing significantly the ionic conductivity, and simultaneously with the aim of forming excellent SEI

layers at the Li° anode to improve interfacial compatibility and stability towards Li° anode.

In **Chapter 3**, a trifluoromethyl-free anion, bis(difluoromethanesulfonyl)imide ($DFSI^-$), as an environmentally benign and interfacially favorable anion for high-performance SSRLMB is reported. The widely used LiTFSI salt generally contains the trifluoromethyl ($–CF_3$) group which has very low chemical and biochemical degradability, despite its strong electron-withdrawing ability which is essential for the dissolution and transport of ions in SPEs. In contrast to LiTFSI, the $–CHF_2$ moieties of LiDFSI-based salt shows a more rapid chemical degradation under a mild basic solution. In addition, a high lithium-ion transference number (T_{Li^+}) resulted from H-bonding interactions between $–CF_2H$ moieties and EO units as well as the better SEI layers formed by the decomposition of $DFSI^-$ synergistically enhanced stability against Li° electrode, showing a better cell performance of SSRLMB batteries.

In **Chapter 4**, a benzene-based salt, lithium benzenesulfonyl(trifluoromethanesulfonyl)imide (LiBTFSI), was synthesized for high-performance PEO-based SPE with aim of further improving the lithium-ion conductivity. In contrast to the abundantly used LiTFSI-based SPEs, the LiBTFSI-based SPEs exhibited extremely high lithium-ion transference number (T_{Li^+}) due to the intermolecular interactions (e.g., π-π stacking bonds) among the benzene-based anions, which was demonstrated by computational calculations. In addition, the $LiFePO_4$ || Li° cells assembled with the LiBTFSI-based SPEs showed a superior long-term cyclability with excellent Coulombic efficiencies as well as high discharge

capacities. These results demonstrate the importance of the molecular structure of anions in SPEs and shed light on a way for future advancement and development high-performance SPEs-based LMBs.

In **Chapter 5**, we report a new type of chiral salts built from commercially available camphorsulfonic acid and their use as electrolyte salts for PEO-based SPEs. The fundamental properties of the neat salts and PEO-based electrolytes are comprehensively characterized, in terms of surface morphology, thermal stability, phase transition, ionic conductivity, and electrochemical stability... We demonstrate that the resulting SPEs exhibit decent ionic conductivities (ca. 10^{-4} S cm^{-1}) accompanied by high cation transference numbers (ca. 0.5) at 70 °C. Whether either the R or the S enantiomers are used the ion transport properties are the same, as expected, but rather surprisingly the artificial racemic mixture is within the errors of the measurements just as conductive. The role of chirality on the properties of the PEO-based electrolytes is thus intensively revealed. We discuss how this opens a new avenue to design novel salts for reaching high-performance SSRLMBs.

1.7. References

1. Zou, C.; Zhao, Q.; Zhang, G.; Xiong, B., Energy revolution: From a fossil energy era to a new energy era. *Natural Gas Industry B* **2016,** *3* (1), 1-11.

2. Chu, S.; Cui, Y.; Liu, N., The path towards sustainable energy. *Nature Materials* **2017,** *16* (1), 16-22.

3. https://www.statista.com/statistics/222066/projected-global-energy-consumption-by-source/.

4. Wuebbles, D. J.; Jain, A. K., Concerns about climate change and the role of fossil fuel use. *Fuel processing technology* **2001,** *71* (1-3), 99-119.

5. Jacobson, M. Z., Review of solutions to global warming, air pollution, and energy security. *Energy & Environmental Science* **2009,** *2* (2), 148-173.

6. Fridleifsson, I. B., Status of geothermal energy amongst the world's energy sources. *Geothermics* **2003,** *32* (4-6), 379-388.

7. Gür, T. M., Review of electrical energy storage technologies, materials and systems: challenges and prospects for large-scale grid storage. *Energy & Environmental Science* **2018,** *11* (10), 2696-2767.

8. Olabi, A. G., Renewable energy and energy storage systems. *Energy* **2017,** *136*, 1-6.

9. Winter, M.; Brodd, R. J., What are batteries, fuel cells, and supercapacitors? *Chemical reviews* **2004,** *104* (10), 4245-4270.

10. Abbas, Q.; Mirzaeian, M.; Hunt, M. R. C.; Hall, P.; Raza, R., Current State and Future Prospects for Electrochemical Energy Storage and Conversion Systems. *Energies* **2020,** *13* (21).

11. Simon, P.; Gogotsi, Y., Perspectives for electrochemical capacitors and related devices. *Nature Materials* **2020,** *19* (11), 1151-1163.

12. Kurzweil, P.; Schottenbauer, J.; Schell, C., Past, present and future of electrochemical capacitors: pseudocapacitance, aging mechanisms and service life estimation. *Journal of Energy Storage* **2021**, 102311.

13. Wang, Y.; Song, Y.; Xia, Y., Electrochemical capacitors: mechanism, materials, systems, characterization and applications. *Chemical Society Reviews* **2016,** *45* (21), 5925-5950.

14. Kötz, R.; Carlen, M., Principles and applications of electrochemical capacitors. *Electrochimica acta* **2000,** *45* (15-16), 2483-2498.

15. Saikia, K.; Kakati, B. K.; Boro, B.; Verma, A., Current Advances and Applications of Fuel Cell Technologies. In *Recent Advancements in Biofuels and Bioenergy Utilization*, Sarangi, P. K.; Nanda, S.; Mohanty, P., Eds. Springer Singapore: Singapore, 2018; pp 303-337.

16. Raza, R.; Akram, N.; Javed, M. S.; Rafique, A.; Ullah, K.; Ali, A.; Saleem, M.; Ahmed, R., Fuel cell technology for sustainable development in Pakistan–An over-view. *Renewable and Sustainable Energy Reviews* **2016,** *53*, 450-461.

17. Schmidt-Rohr, K., How Batteries Store and Release Energy: Explaining Basic Electrochemistry. *Journal of Chemical Education* **2018,** *95* (10), 1801-1810.

18. Xu, K., Electrolytes and Interphases in Li-Ion Batteries and Beyond. *Chemical Reviews* **2014,** *114* (23), 11503-11618.

19. Xu, K., Nonaqueous Liquid Electrolytes for Lithium-Based Rechargeable Batteries. *Chemical Reviews* **2004,** *104* (10), 4303-4418.

20. Li, M.; Wang, C.; Chen, Z.; Xu, K.; Lu, J., New concepts in electrolytes. *Chemical reviews* **2020,** *120* (14), 6783-6819.

21. https://en.wikipedia.org/wiki/Electric_battery.

22. Tarascon, J. M.; Armand, M., Issues and challenges facing rechargeable lithium batteries. *Nature* **2001,** *414* (6861), 359-367.

23. Lin, D.; Liu, Y.; Cui, Y., Reviving the lithium metal anode for high-energy batteries. *Nature nanotechnology* **2017,** *12* (3), 194.

24. Reddy, M. V.; Mauger, A.; Julien, C. M.; Paolella, A.; Zaghib, K., Brief History of Early Lithium-Battery Development. *Materials* **2020,** *13* (8).

25. Rouxel, J.; Danot, M.; Bichon, M., Les composites intercalaires NaxTiS2. Etude gènérale des phases NaxTiS2 et KxTiS2. *Bull. Soc. Chim* **1971,** *11*, 3930-3936.

26. Rudorff, W., Inclusion of base metals in graphite and in metallic chalcogenides of the type MeX 2. *Chimia* **1965,** *19* (9), 489-499.

27. Whittingham, M. S., Lithium titanium disulfide cathodes. *Nature Energy* **2021,** *6* (2), 214-214.

28. Whittingham, M. S., History, evolution, and future status of energy storage. *Proceedings of the IEEE* **2012,** *100* (Special Centennial Issue), 1518-1534.

29. Zhang, H.; Li, C.; Eshetu, G. G.; Laruelle, S.; Grugeon, S.; Zaghib, K.; Julien, C.; Mauger, A.; Guyomard, D.; Rojo, T., From Solid‐Solution Electrodes and the Rocking‐Chair Concept to Today's Batteries. *Angewandte Chemie* **2020,** *132* (2), 542-546.

30. Mizushima, K.; Jones, P. C.; Wiseman, P. J.; Goodenough, J. B., LixCoO2 (0< x<-1): A new cathode material for batteries of high energy density. *Materials Research Bulletin* **1980,** *15* (6), 783-789.

31. Judez, X.; Eshetu, G. G.; Li, C.; Rodriguez-Martinez, L. M.; Zhang, H.; Armand, M., Opportunities for Rechargeable Solid-State Batteries Based on Li-Intercalation Cathodes. *Joule* **2018,** *2* (11), 2208-2224.

32. Armand, M.; Tarascon, J. M., Building better batteries. *Nature* **2008,** *451* (7179), 652-657.

33. Mauger, A.; Julien, C. M.; Paolella, A.; Armand, M.; Zaghib, K., A comprehensive review of lithium salts and beyond for rechargeable batteries: Progress and perspectives. *Materials Science and Engineering: R: Reports* **2018,** *134*, 1-21.

34. Younesi, R.; Veith, G. M.; Johansson, P.; Edström, K.; Vegge, T., Lithium salts for advanced lithium batteries: Li–metal, Li–O2, and Li–S. *Energy & Environmental Science* **2015,** *8* (7), 1905-1922.

35. Plakhotnyk, A. V.; Ernst, L.; Schmutzler, R., Hydrolysis in the system LiPF6—propylene carbonate—dimethyl carbonate—H2O. *Journal of Fluorine Chemistry* **2005,** *126* (1), 27-31.

36. Tasaki, K.; Kanda, K.; Nakamura, S.; Ue, M., Decomposition of LiPF6and Stability of PF 5 in Li-Ion Battery Electrolytes: Density Functional Theory and Molecular Dynamics Studies. *Journal of the Electrochemical Society* **2003,** *150* (12), A1628.

37. Heider, U.; Oesten, R.; Jungnitz, M., Challenge in manufacturing electrolyte solutions for lithium and lithium ion batteries quality control and minimizing contamination level. *Journal of Power Sources* **1999,** *81*, 119-122.

38. Gnanaraj, J. S.; Zinigrad, E.; Asraf, L.; Gottlieb, H. E.; Sprecher, M.; Schmidt, M.; Geissler, W.; Aurbach, D., A detailed investigation of the thermal reactions of LiPF6 solution in organic carbonates using ARC and DSC. *Journal of the Electrochemical Society* **2003,** *150* (11), A1533.

39. Besenhard, J. O.; Eichinger, G., High energy density lithium cells: Part I. Electrolytes and anodes. *Journal of Electroanalytical Chemistry and Interfacial Electrochemistry* **1976,** *68* (1), 1-18.

40. Desjardins, C. D.; Cadger, T. G.; Salter, R. S.; Donaldson, G.; Casey, E. J., Lithium Cycling Performance in Improved Lithium Hexafluoroarsenate/2 - Methyl Tetrahydrofuran Electrolytes. *Journal of The Electrochemical Society* **1985,** *132* (3), 529-533.

41. Koch, V. R., Status of the secondary lithium electrode. *Journal of Power Sources* **1981,** *6* (4), 357-370.

42. Krause, L. J.; Lamanna, W.; Summerfield, J.; Engle, M.; Korba, G.; Loch, R.; Atanasoski, R., Corrosion of aluminum at high voltages in non-aqueous electrolytes containing perfluoroalkylsulfonyl imides; new lithium salts for lithium-ion cells. *Journal of Power Sources* **1997,** *68* (2), 320-325.

43. Xu, K.; Zhang, S. S.; Lee, U.; Allen, J. L.; Jow, T. R., LiBOB: Is it an alternative salt for lithium ion chemistry? *Journal of Power Sources* **2005,** *146* (1-2), 79-85.

44. Xu, K.; Zhang, S.; Jow, T. R.; Xu, W.; Angell, C. A., LiBOB as salt for lithium-ion batteries: a possible solution for high temperature operation. *Electrochemical and Solid State Letters* **2001,** *5* (1), A26.

45. Qiao, L.; Cui, Z.; Chen, B.; Xu, G.; Zhang, Z.; Ma, J.; Du, H.; Liu, X.; Huang, S.; Tang, K.; Dong, S.; Zhou, X.; Cui, G., A promising bulky anion based lithium borate salt for lithium metal batteries. *Chemical Science* **2018,** *9* (14), 3451-3458.

46. Meister, P.; Qi, X.; Kloepsch, R.; Krämer, E.; Streipert, B.; Winter, M.; Placke, T., Anodic Behavior of the Aluminum Current Collector in Imide - Based Electrolytes: Influence of Solvent, Operating Temperature, and Native Oxide - Layer Thickness. *ChemSusChem* **2017,** *10* (4), 804-814.

47. Wang, S.; Qiu, W.; Guan, Y.; Yu, B.; Zhao, H.; Liu, W., Electrochemical characteristics of LiMxFe1−xPO4 cathode with LiBOB based electrolytes. *Electrochimica Acta* **2007,** *52* (15), 4907-4910.

48. Zhang, H.; Armand, M., History of Solid Polymer Electrolyte ‐ Based Solid ‐ State Lithium Metal Batteries: A Personal Account. *Israel Journal of Chemistry* **2021,** *61* (1-2), 94-100.

49. Qiao, L.; Judez, X.; Rojo, T.; Armand, M.; Zhang, H., Review—Polymer Electrolytes for Sodium Batteries. *Journal of The Electrochemical Society* **2020,** *167* (7), 070534.

50. Dunn, B.; Kamath, H.; Tarascon, J.-M., Electrical energy storage for the grid: a battery of choices. *Science* **2011,** *334* (6058), 928-935.

51. https://www.forbes.com/sites/rrapier/2019/08/04/why-china-is-dominating-lithium-ion-battery-production/?sh=714d5b453786#cae4c5b37867.

52. Saurel, D.; Orayech, B.; Xiao, B.; Carriazo, D.; Li, X.; Rojo, T., From Charge Storage Mechanism to Performance: A Roadmap toward High Specific Energy Sodium-Ion Batteries through Carbon Anode Optimization. *Advanced Energy Materials* **2018,** *8* (17), 1703268.

53. Hu, Y.-S.; Lu, Y., 2019 Nobel prize for the Li-ion batteries and new opportunities and challenges in Na-ion batteries. ACS Publications: 2019.

54. Zhang, H.; Armand, M.; Rojo, T., Review—Innovative polymeric materials for better rechargeable batteries: strategies from CIC Energigune. *Journal of The Electrochemical Society* **2019,** *166* (4), A679.

55. Vaalma, C.; Buchholz, D.; Weil, M.; Passerini, S., A cost and resource analysis of sodium-ion batteries. *Nature reviews materials* **2018,** *3* (4), 1-11.

56. Ortiz-Vitoriano, N.; Drewett, N. E.; Gonzalo, E.; Rojo, T., High performance manganese-based layered oxide cathodes: overcoming the challenges of sodium ion batteries. *Energy & Environmental Science* **2017,** *10* (5), 1051-1074.

57. Hwang, J.-Y.; Myung, S.-T.; Sun, Y.-K., Sodium-ion batteries: present and future. *Chemical Society Reviews* **2017,** *46* (12), 3529-3614.

58. Hueso, K. B.; Palomares, V.; Armand, M.; Rojo, T., Challenges and perspectives on high and intermediate-temperature sodium batteries. *Nano Research* **2017,** *10* (12), 4082-4114.

59. Landa-Medrano, I.; Li, C.; Ortiz-Vitoriano, N.; Ruiz de Larramendi, I.; Carrasco, J.; Rojo, T. f., Sodium–oxygen battery: steps toward reality. *The journal of physical chemistry letters* **2016,** *7* (7), 1161-1166.

60. Blomgren, G. E., The development and future of lithium ion batteries. *Journal of The Electrochemical Society* **2016,** *164* (1), A5019.

61. Kang, H.; Liu, Y.; Cao, K.; Zhao, Y.; Jiao, L.; Wang, Y.; Yuan, H., Update on anode materials for Na-ion batteries. *Journal of Materials Chemistry A* **2015,** *3* (35), 17899-17913.

62. Manthiram, A.; Yu, X., Ambient temperature sodium–sulfur batteries. *Small* **2015,** *11* (18), 2108-2114.

63. Han, M. H.; Gonzalo, E.; Singh, G.; Rojo, T., A comprehensive review of sodium layered oxides: powerful cathodes for Na-ion batteries. *Energy & Environmental Science* **2015,** *8* (1), 81-102.

64. Slater, M. D.; Kim, D.; Lee, E.; Johnson, C. S., Sodium‐ion batteries. *Advanced Functional Materials* **2013,** *23* (8), 947-958.

65. Pan, H.; Hu, Y.-S.; Chen, L., Room-temperature stationary sodium-ion batteries for large-scale electric energy storage. *Energy & Environmental Science* **2013,** *6* (8), 2338-2360.

66. Palomares, V.; Casas-Cabanas, M.; Castillo-Martínez, E.; Han, M. H.; Rojo, T., Update on Na-based battery materials. A growing research path. *Energy & Environmental Science* **2013,** *6* (8), 2312-2337.

67. Hueso, K. B.; Armand, M.; Rojo, T., High temperature sodium batteries: status, challenges and future trends. *Energy & Environmental Science* **2013,** *6* (3), 734-749.

68. Palomares, V.; Serras, P.; Villaluenga, I.; Hueso, K. B.; Carretero-González, J.; Rojo, T., Na-ion batteries, recent advances and present challenges to become low cost energy storage systems. *Energy & Environmental Science* **2012,** *5* (3), 5884-5901.

69. http://wls.iphy.ac.cn/emagazine/news.php?id=25141.

70. http://www.hinabattery.com/en/index.php?catid=15.

71. https://www.faradion.co.uk/.

72. http://www.tiamat-energy.com/.

73. Liu, F.; Wang, T.; Liu, X.; Fan, L.-Z., Challenges and Recent Progress on Key Materials for Rechargeable Magnesium Batteries. *Advanced Energy Materials* **2020,** *n/a* (n/a), 2000787.

74. Liu, Y.; Gao, C.; Dai, L.; Deng, Q.; Wang, L.; Luo, J.; Liu, S.; Hu, N., The Features and Progress of Electrolyte for Potassium Ion Batteries. *Small* **2020,** *n/a* (n/a), 2004096.

75. Zhou, M.; Bai, P.; Ji, X.; Yang, J.; Wang, C.; Xu, Y., Electrolytes and Interphases in Potassium Ion Batteries. *Advanced Materials* **2021,** *n/a* (n/a), 2003741.

76. Zhou, L.; Cao, Z.; Zhang, J.; Cheng, H.; Liu, G.; Park, G.-T.; Cavallo, L.; Wang, L.; Alshareef, H. N.; Sun, Y.-K.; Ming, J., Electrolyte-Mediated Stabilization of High-Capacity Micro-Sized Antimony Anodes for Potassium-Ion Batteries. *Advanced Materials* **2021,** *n/a* (n/a), 2005993.

77. Zheng, J.; Wu, Y.; Sun, Y.; Rong, J.; Li, H.; Niu, L., Advanced Anode Materials of Potassium Ion Batteries: from Zero Dimension to Three Dimensions. *Nano-Micro Letters* **2020,** *13* (1), 12.

78. Zhao, X.; Lu, Y.; Qian, Z.; Wang, R.; Guo, Z., Potassium-sulfur batteries: Status and perspectives. *EcoMat* **2020,** *2* (3), e12038.

79. Sheng, C.; Yu, F.; Li, C.; Zhang, H.; Huang, J.; Wu, Y.; Armand, M.; Chen, Y., Diagnosing the SEI Layer in a Potassium Ion Battery Using Distribution of Relaxation Time. *The Journal of Physical Chemistry Letters* **2021,** *12* (8), 2064-2071.

80. Min, X.; Xiao, J.; Fang, M.; Wang, W.; Zhao, Y.; Liu, Y.; Abdelkader, A. M.; Xi, K.; Kumar, R. V.; Huang, Z., Potassium-ion batteries: outlook on present and future technologies. *Energy & Environmental Science* **2021**.

81. Ma, Y.; Ma, Y.; Euchner, H.; Liu, X.; Zhang, H.; Qin, B.; Geiger, D.; Biskupek, J.; Carlsson, A.; Kaiser, U.; Groß, A.; Indris, S.; Passerini, S.; Bresser, D., An Alternative Charge-Storage Mechanism for High-Performance Sodium-Ion and Potassium-Ion Anodes. *ACS Energy Letters* **2021**, 915-924.

82. Wu, C.; Lai, W.-H.; Cai, X.; Chou, S.-L.; Liu, H.-K.; Wang, Y.-X.; Dou, S.-X., Carbonaceous Hosts for Sulfur Cathode in Alkali-Metal/S (Alkali Metal = Lithium, Sodium, Potassium) Batteries. *Small* **2021,** *n/a* (n/a), 2006504.

83. Huang, X. L.; Guo, Z.; Dou, S. X.; Wang, Z. M., Rechargeable Potassium–Selenium Batteries. *Advanced Functional Materials* **2021,** *n/a* (n/a), 2102326.

84. An, S. Y.; Schon, T. B.; McAllister, B. T.; Seferos, D. S., Design strategies for organic carbonyl materials for energy storage: Small molecules, oligomers, polymers and supramolecular structures. *EcoMat* **2020,** *2* (4), e12055.

85. Liang, Y.; Dong, H.; Aurbach, D.; Yao, Y., Current status and future directions of multivalent metal-ion batteries. *Nature Energy* **2020**.

86. Tian, Y.; Zeng, G.; Rutt, A.; Shi, T.; Kim, H.; Wang, J.; Koettgen, J.; Sun, Y.; Ouyang, B.; Chen, T.; Lun, Z.; Rong, Z.; Persson, K.; Ceder, G., Promises and Challenges of Next-Generation "Beyond Li-ion" Batteries for Electric Vehicles and Grid Decarbonization. *Chemical Reviews* **2020**.

87. Pan, Z.; Liu, X.; Yang, J.; Li, X.; Liu, Z.; Loh, X.; Wang, J., Aqueous Rechargeable Multivalent Metal-Ion Batteries: Advances and Challenges. *Advanced Energy Materials* **2021,** *n/a* (n/a), 2100608.

88. Zu, C.-X.; Li, H., Thermodynamic analysis on energy densities of batteries. *Energy & Environmental Science* **2011,** *4* (8), 2614-2624.

89. Aslam, M. K.; Niu, Y.; Hussain, T.; Tabassum, H.; Tang, W.; Xu, M.; Ahuja, R., How to avoid dendrite formation in metal batteries: Innovative strategies for dendrite suppression. *Nano Energy* **2021,** *86*, 106142.

90. Um, J. H.; Yu, S.-H., Unraveling the Mechanisms of Lithium Metal Plating/Stripping via In Situ/Operando Analytical Techniques. *Advanced Energy Materials* **2020,** *n/a* (n/a), 2003004.

91. Li, J.; Cai, Y.; Wu, H.; Yu, Z.; Yan, X.; Zhang, Q.; Gao, T. Z.; Liu, K.; Jia, X.; Bao, Z., Polymers in Lithium-Ion and Lithium Metal Batteries. *Advanced Energy Materials* **2021,** *n/a* (n/a), 2003239.

92. Zhang, H.; Chen, Y.; Li, C.; Armand, M., Electrolyte and anode-electrolyte interphase in solid-state lithium metal polymer batteries: A perspective. *SusMat* **2021,** *n/a* (n/a).

93. Shen, X.; Cheng, X.; Shi, P.; Huang, J.; Zhang, X.; Yan, C.; Li, T.; Zhang, Q., Lithium–matrix composite anode protected by a solid electrolyte layer for stable lithium metal batteries. *Journal of Energy Chemistry* **2019,** *37*, 29-34.

94. Xu, K., A Long Journey of Lithium: From the Big Bang to Our Smartphones. *Energy & Environmental Materials* **2019,** *2* (4), 229-233.

95. Cheng, X.-B.; Zhang, R.; Zhao, C.-Z.; Zhang, Q., Toward safe lithium metal anode in rechargeable batteries: a review. *Chemical reviews* **2017,** *117* (15), 10403-10473.

96. Wu, H.; Jia, H.; Wang, C.; Zhang, J.-G.; Xu, W., Recent Progress in Understanding Solid Electrolyte Interphase on Lithium Metal Anodes. *Advanced Energy Materials* **2021,** *11* (5), 2003092.

97. Wei, C.; Zhang, Y.; Tian, Y.; Tan, L.; An, Y.; Qian, Y.; Xi, B.; Xiong, S.; Feng, J.; Qian, Y., Design of safe, long-cycling and high-energy lithium metal anodes in all working conditions: progress, challenges and perspectives. *Energy Storage Materials* **2021**.

98. Qin, K.; Holguin, K.; Mohammadiroudbari, M.; Huang, J.; Kim, E. Y. S.; Hall, R.; Luo, C., Strategies in Structure and Electrolyte Design for High-Performance Lithium Metal Batteries. *Advanced Functional Materials* **2021,** *n/a* (n/a), 2009694.

99. Han, Z.; Zhang, C.; Lin, Q.; Zhang, Y.; Deng, Y.; Han, J.; Wu, D.; Kang, F.; Yang, Q.-H.; Lv, W., A Protective Layer for Lithium Metal Anode: Why and How. *Small Methods* **2021,** *n/a* (n/a), 2001035.

100. Zou, P.; Sui, Y.; Zhan, H.; Wang, C.; Xin, H. L.; Cheng, H.-M.; Kang, F.; Yang, C., Polymorph Evolution Mechanisms and Regulation Strategies of Lithium Metal Anode under Multiphysical Fields. *Chemical Reviews* **2021**.

101. Yu, Q.; Jiang, K.; Yu, C.; Chen, X.; Zhang, C.; Yao, Y.; Jiang, B.; Long, H., Recent progress of composite solid polymer electrolytes for all-solid-state lithium metal batteries. *Chinese Chemical Letters* **2021**.

102. Li, Y.-N.; Wang, C.-Y.; Gao, R.-M.; Cao, F.-F.; Ye, H., Recent Smart Lithium Anode Configurations for High-Energy Lithium Metal Batteries. *Energy Storage Materials* **2021**.

103. Wang, R.; Cui, W.; Chu, F.; Wu, F., Lithium metal anodes: Present and future. *Journal of Energy Chemistry* **2020,** *48*, 145-159.

104. Wang, H.; Zhu, J.; Su, Y.; Gong, Z.; Yang, Y., Interfacial compatibility issues in rechargeable solid-state lithium metal batteries: a review. *Science China Chemistry* **2021**.

105. Ma, L.; Lv, Y.; Wu, J.; Chen, Y.; Jin, Z., Recent Advances in Emerging Non-Lithium Metal–Sulfur Batteries: A Review. *Advanced Energy Materials* **2021,** *n/a* (n/a), 2100770.

106. Hou, L.-P.; Zhang, X.-Q.; Li, B.-Q.; Zhang, Q., Challenges and promises of lithium metal anode by soluble polysulfides in practical lithium–sulfur batteries. *Materials Today* **2021**.

107. Hatzell, K. B.; Chen, X. C.; Cobb, C. L.; Dasgupta, N. P.; Dixit, M. B.; Marbella, L. E.; McDowell, M. T.; Mukherjee, P. P.; Verma, A.; Viswanathan, V.; Westover, A. S.; Zeier, W. G., Challenges in Lithium Metal Anodes for Solid-State Batteries. *ACS Energy Letters* **2020,** *5* (3), 922-934.

108. Han, Y.; Liu, B.; Xiao, Z.; Zhang, W.; Wang, X.; Pan, G.; Xia, Y.; Xia, X.; Tu, J., Interface issues of lithium metal anode for high-energy batteries: Challenges, strategies, and perspectives. *InfoMat* **2021,** *3* (2), 155-174.

109. Fu, S.; Zuo, L.-L.; Zhou, P.-S.; Liu, X.-J.; Ma, Q.; Chen, M.-J.; Yue, J.; Wu, X.; Deng, Q., Recent Advancements of Functional Gel Polymer Electrolytes for Rechargeable Lithium Metal Batteries. *Materials Chemistry Frontiers* **2021**.

110. Zhang, X.; Wang, A.; Liu, X.; Luo, J., Dendrites in Lithium Metal Anodes: Suppression, Regulation, and Elimination. *Accounts of Chemical Research* **2019**.

111. Wang, H.; Liu, Y.; Li, Y.; Cui, Y., Lithium Metal Anode Materials Design: Interphase and Host. *Electrochemical Energy Reviews* **2019,** *2* (4), 509-517.

112. Yang, H.; Li, J.; Sun, Z.; Fang, R.; Wang, D.-W.; He, K.; Cheng, H.-M.; Li, F., Reliable liquid electrolytes for lithium metal batteries. *Energy Storage Materials* **2020**.

113. Xu, W.; Wang, J.; Ding, F.; Chen, X.; Nasybulin, E.; Zhang, Y.; Zhang, J.-G., Lithium metal anodes for rechargeable batteries. *Energy & Environmental Science* **2014,** *7* (2), 513-537.

114. Wang, S.; Xiong, P.; Zhang, J.; Wang, G., Recent progress on flexible lithium metal batteries: Composite lithium metal anodes and solid-state electrolytes. *Energy Storage Materials* **2020**.

115. Park, S.; Lee, J.-I.; Song, G.; Cho, S.; Han, D.-Y., Lithium Metal Interface Modification for High-Energy Batteries: Approaches and Characterization. *Batteries & Supercaps* **2020,** *n/a* (n/a).

116. Li, S.; Luo, Z.; Li, L.; Hu, J.; Zou, G.; Hou, H.; Ji, X., Recent progress on electrolyte additives for stable lithium metal anode. *Energy Storage Materials* **2020**.

117. Li, G., Regulating Mass Transport Behavior for High-Performance Lithium Metal Batteries and Fast-Charging Lithium-Ion Batteries. *Advanced Energy Materials* **2021,** *n/a* (n/a), 2002891.

118. Chen, S.; Dai, F.; Cai, M., Opportunities and Challenges of High-Energy Lithium Metal Batteries for Electric Vehicle Applications. *ACS Energy Letters* **2020**, 3140-3151.

119. Varzi, A.; Raccichini, R.; Passerini, S.; Scrosati, B., Challenges and prospects of the role of solid electrolytes in the revitalization of lithium metal batteries. *Journal of Materials Chemistry A* **2016,** *4* (44), 17251-17259.

120. Li, L.; Dai, H.; Wang, C., Electrolyte additives: Adding the stability of lithium metal anodes. *Nano Select* **2020,** *n/a* (n/a).

121. Zhang, J.-G.; Xu, W.; Xiao, J.; Cao, X.; Liu, J., Lithium Metal Anodes with Nonaqueous Electrolytes. *Chemical Reviews* **2020**.

122. Xu, L.; Lu, Y.; Zhao, C.-Z.; Yuan, H.; Zhu, G.-L.; Hou, L.-P.; Zhang, Q.; Huang, J.-Q., Toward the Scale-Up of Solid-State Lithium Metal Batteries: The Gaps between Lab-Level Cells and Practical Large-Format Batteries. *Advanced Energy Materials* **2020,** *n/a* (n/a), 2002360.

123. Subramanian, K.; Alexander, G. V.; Karthik, K.; Patra, S.; Indu, M. S.; Sreejith, O. V.; Viswanathan, R.; Narayanasamy, J.; Murugan, R., A brief review of recent advances in garnet structured solid electrolyte based lithium metal batteries. *Journal of Energy Storage* **2021,** *33*, 102157.

124. Zhang, H.; Eshetu, G. G.; Judez, X.; Li, C.; Rodriguez-Martínez, L. M.; Armand, M., Electrolyte Additives for Lithium Metal Anodes and Rechargeable Lithium Metal Batteries: Progress and Perspectives. *Angewandte Chemie International Edition* **2018,** *57* (46), 15002-15027.

125. Xie, Z.; Wu, Z.; An, X.; Yue, X.; Wang, J.; Abudula, A.; Guan, G., Anode-free rechargeable lithium metal batteries: Progress and prospects. *Energy Storage Materials* **2020**.

126. Wu, M.; Li, Y.; Liu, X.; Yang, S.; Ma, J.; Dou, S., Perspective on solid-electrolyte interphase regulation for lithium metal batteries. *SmartMat* **2020,** *n/a* (n/a).

127. Zhang, H.; Armand, M., History of Solid Polymer Electrolyte-based Solid-state Lithium Metal Batteries: A Personal Account. *Israel Journal of Chemistry* **2020,** *n/a* (n/a).

128. Xue, Z.; He, D.; Xie, X., Poly(ethylene oxide)-based electrolytes for lithium-ion batteries. *Journal of Materials Chemistry A* **2015,** *3* (38), 19218-19253.

129. Long, L.; Wang, S.; Xiao, M.; Meng, Y., Polymer electrolytes for lithium polymer batteries. *Journal of Materials Chemistry A* **2016,** *4* (26), 10038-10069.

130. Wang, Q.; Zhang, H.; Cui, Z.; Zhou, Q.; Shangguan, X.; Tian, S.; Zhou, X.; Cui, G., Siloxane-based polymer electrolytes for solid-state lithium batteries. *Energy Storage Materials* **2019**.

131. Masdupuy, E., *Ann. Chim. (Paris)* **1957,** *13* (2 Ser.), 527.

132. Hong, H. Y. P., Crystal structures and crystal chemistry in the system Na1+xZr2SixP3−xO12. *Materials Research Bulletin* **1976,** *11* (2), 173-182.

133. Inaguma, Y.; Liquan, C.; Itoh, M.; Nakamura, T.; Uchida, T.; Ikuta, H.; Wakihara, M., High ionic conductivity in lithium lanthanum titanate. *Solid State Communications* **1993,** *86* (10), 689-693.

134. Murugan, R.; Thangadurai, V.; Weppner, W., Fast lithium ion conduction in garnet-type Li(7)La(3)Zr(2)O(12). *Angew Chem Int Ed Engl* **2007,** *46* (41), 7778-81.

135. Kamaya, N.; Homma, K.; Yamakawa, Y.; Hirayama, M.; Kanno, R.; Yonemura, M.; Kamiyama, T.; Kato, Y.; Hama, S.; Kawamoto, K.; Mitsui, A., A lithium superionic conductor. *Nature Materials* **2011,** *10* (9), 682-686.

136. Seino, Y.; Ota, T.; Takada, K.; Hayashi, A.; Tatsumisago, M., A sulphide lithium super ion conductor is superior to liquid ion conductors for use in rechargeable batteries. *Energy & Environmental Science* **2014,** *7* (2), 627-631.

137. Kato, Y.; Hori, S.; Saito, T.; Suzuki, K.; Hirayama, M.; Mitsui, A.; Yonemura, M.; Iba, H.; Kanno, R., High-power all-solid-state batteries using sulfide superionic conductors. *Nature Energy* **2016,** *1* (4), 16030.

138. Xia, S.; Wu, X.; Zhang, Z.; Cui, Y.; Liu, W., Practical challenges and future perspectives of all-solid-state lithium-metal batteries. *Chem* **2019,** *5* (4), 753-785.

139. Banerjee, A.; Wang, X.; Fang, C.; Wu, E. A.; Meng, Y. S., Interfaces and Interphases in All-Solid-State Batteries with Inorganic Solid Electrolytes. *Chemical Reviews* **2020**.

140. Zhao, Q.; Stalin, S.; Zhao, C.-Z.; Archer, L. A., Designing solid-state electrolytes for safe, energy-dense batteries. *Nature Reviews Materials* **2020**.

141. Xiao, Y.; Wang, Y.; Bo, S.-H.; Kim, J. C.; Miara, L. J.; Ceder, G., Understanding interface stability in solid-state batteries. *Nature Reviews Materials* **2019**.

142. Zhang, H.; Li, C.; Piszcz, M.; Coya, E.; Rojo, T.; Rodriguez-Martinez, L. M.; Armand, M.; Zhou, Z., Single lithium-ion conducting solid polymer electrolytes: advances and perspectives. *Chemical Society Reviews* **2017,** *46* (3), 797-815.

143. Fenton, D. E.; Parker, J. M.; Wright, P. V., Complexes of alkali metal ions with poly(ethylene oxide). *Polymer* **1973,** *14* (11), 589.

144. Zhang, H.; Chen, F.; Lakuntza, O.; Oteo, U.; Qiao, L.; Martinez-Ibañez, M.; Zhu, H.; Carrasco, J.; Forsyth, M.; Armand, M., Suppressed Mobility of Negative Charges in Polymer Electrolytes with an Ether-Functionalized Anion. *Angewandte Chemie International Edition* **2019,** *58* (35), 12070-12075.

145. Xi, G.; Xiao, M.; Wang, S.; Han, D.; Li, Y.; Meng, Y., Polymer-Based Solid Electrolytes: Material Selection, Design, and Application. *Advanced Functional Materials* **2020,** *n/a* (n/a), 2007598.

146. Wang, H.; Sheng, L.; Yasin, G.; Wang, L.; Xu, H.; He, X., Reviewing the current status and development of polymer electrolytes for solid-state lithium batteries. *Energy Storage Materials* **2020,** *33*, 188-215.

147. Sun, B.; Mindemark, J.; Edström, K.; Brandell, D., Polycarbonate-based solid polymer electrolytes for Li-ion batteries. *Solid State Ionics* **2014,** *262*, 738-742.

148. Zhou, D.; Shanmukaraj, D.; Tkacheva, A.; Armand, M.; Wang, G., Polymer Electrolytes for Lithium-Based Batteries: Advances and Prospects. *Chem* **2019**.

149. Capuano, F.; Croce, F.; Scrosati, B., Composite polymer electrolytes. *Journal of the Electrochemical Society* **1991,** *138* (7), 1918.

150. Wieczorek, W.; Florjanczyk, Z.; Stevens, J. R., Composite polyether based solid electrolytes. *Electrochimica Acta* **1995,** *40* (13), 2251-2258.

151. Lago, N.; Garcia-Calvo, O.; Lopez del Amo, J. M.; Rojo, T.; Armand, M., All-Solid-State Lithium-Ion Batteries with Grafted Ceramic Nanoparticles Dispersed in Solid Polymer Electrolytes. *ChemSusChem* **2015,** *8* (18), 3039-3043.

152. Lin, D.; Liu, W.; Liu, Y.; Lee, H. R.; Hsu, P.-C.; Liu, K.; Cui, Y., High Ionic Conductivity of Composite Solid Polymer Electrolyte via In Situ Synthesis of

Monodispersed SiO2 Nanospheres in Poly(ethylene oxide). *Nano Letters* **2016,** *16* (1), 459-465.

153. Liu, W.; Lee, S. W.; Lin, D.; Shi, F.; Wang, S.; Sendek, A. D.; Cui, Y., Enhancing ionic conductivity in composite polymer electrolytes with well-aligned ceramic nanowires. *Nature Energy* **2017,** *2* (5), 17035.

154. Boaretto, N.; Meabe, L.; Martinez-Ibañez, M.; Armand, M.; Zhang, H., Review—Polymer Electrolytes for Rechargeable Batteries: From Nanocomposite to Nanohybrid. *Journal of The Electrochemical Society* **2020,** *167* (7), 070524.

155. Jayathilaka, P. A. R. D.; Dissanayake, M. A. K. L.; Albinsson, I.; Mellander, B. E., Effect of nano-porous Al2O3 on thermal, dielectric and transport properties of the (PEO)9LiTFSI polymer electrolyte system. *Electrochimica Acta* **2002,** *47* (20), 3257-3268.

156. Kwon, S. J.; Jung, B. M.; Kim, T.; Byun, J.; Lee, J.; Lee, S. B.; Choi, U. H., Influence of Al2O3 nanowires on ion transport in nanocomposite solid polymer electrolytes. *Macromolecules* **2018,** *51* (24), 10194-10201.

157. Capiglia, C.; Mustarelli, P.; Quartarone, E.; Tomasi, C.; Magistris, A., Effects of nanoscale SiO2 on the thermal and transport properties of solvent-free, poly(ethylene oxide) (PEO)-based polymer electrolytes. *Solid State Ionics* **1999,** *118* (1), 73-79.

158. Zhu, Y.; Cao, J.; Chen, H.; Yu, Q.; Li, B., High electrochemical stability of a 3D cross-linked network PEO@nano-SiO2 composite polymer electrolyte for lithium metal batteries. *Journal of Materials Chemistry A* **2019,** *7* (12), 6832-6839.

159. Zhou, D.; Liu, R.; He, Y.-B.; Li, F.; Liu, M.; Li, B.; Yang, Q.-H.; Cai, Q.; Kang, F., SiO2 Hollow Nanosphere-Based Composite Solid Electrolyte for Lithium Metal Batteries to Suppress Lithium Dendrite Growth and Enhance Cycle Life. *Advanced Energy Materials* **2016,** *6* (7), 1502214.

160. Xu, Z.; Yang, T.; Chu, X.; Su, H.; Wang, Z.; Chen, N.; Gu, B.; Zhang, H.; Deng, W.; Zhang, H., Strong Lewis Acid–Base and Weak Hydrogen Bond Synergistically Enhancing Ionic Conductivity of Poly (ethylene oxide)@ SiO2 Electrolytes for a High Rate Capability Li-Metal Battery. *ACS applied materials & interfaces* **2020,** *12* (9), 10341-10349.

161. Adebahr, J.; Best, A. S.; Byrne, N.; Jacobsson, P.; Macfarlane, D. R.; Forsyth, M., Ion transport in polymer electrolytes containing nanoparticulate TiO 2: The influence of polymer morphology. *Physical chemistry chemical physics* **2003,** *5* (4), 720-725.

162. Ketabi, S.; Lian, K., The effects of SiO2 and TiO2 nanofillers on structural and electrochemical properties of poly (ethylene oxide)–EMIHSO4 electrolytes. *Electrochimica Acta* **2015,** *154*, 404-412.

163. Croce, F.; Settimi, L.; Scrosati, B., Superacid ZrO2-added, composite polymer electrolytes with improved transport properties. *Electrochemistry Communications* **2006,** *8* (2), 364-368.

164. Solarajan, A. K.; Murugadoss, V.; Angaiah, S., Dimensional stability and electrochemical behaviour of ZrO2 incorporated electrospun PVdF-HFP based nanocomposite polymer membrane electrolyte for Li-ion capacitors. *Scientific Reports* **2017,** *7* (1), 45390.

165. Liu, W.; Lin, D.; Sun, J.; Zhou, G.; Cui, Y., Improved lithium ionic conductivity in composite polymer electrolytes with oxide-ion conducting nanowires. *ACS nano* **2016,** *10* (12), 11407-11413.

166. Mastragostino, M.; Soavi, F.; Zanelli, A., Improved composite materials for rechargeable lithium metal polymer batteries. *Journal of power sources* **1999,** *81*, 729-733.

167. Sheng, O.; Jin, C.; Luo, J.; Yuan, H.; Huang, H.; Gan, Y.; Zhang, J.; Xia, Y.; Liang, C.; Zhang, W., Mg2B2O5 nanowire enabled multifunctional solid-state electrolytes with high ionic conductivity, excellent mechanical properties, and flame-retardant performance. *Nano letters* **2018,** *18* (5), 3104-3112.

168. Sun, H. Y.; Takeda, Y.; Imanishi, N.; Yamamoto, O.; Sohn, H. J., Ferroelectric materials as a ceramic filler in solid composite polyethylene oxide‐based electrolytes. *Journal of The Electrochemical Society* **2000,** *147* (7), 2462.

169. Shanmukaraj, D.; Murugan, R., Characterization of PEG: LiClO4+ SrBi4Ti4O15 nanocomposite polymer electrolytes for lithium secondary batteries. *Journal of power sources* **2005,** *149*, 90-95.

170. Shanmukaraj, D.; Wang, G. X.; Murugan, R.; Liu, H.-K., Ionic conductivity and electrochemical stability of poly (methylmethacrylate)–poly (ethylene oxide) blend-ceramic fillers composites. *Journal of Physics and Chemistry of Solids* **2008,** *69* (1), 243-248.

171. Zhang, Y.; Zhao, Y.; Gosselink, D.; Chen, P., Synthesis of poly (ethylene-oxide)/nanoclay solid polymer electrolyte for all solid-state lithium/sulfur battery. *Ionics* **2015,** *21* (2), 381-385.

172. Li, Y.; Xu, B.; Xu, H.; Duan, H.; Lü, X.; Xin, S.; Zhou, W.; Xue, L.; Fu, G.; Manthiram, A., Hybrid polymer/garnet electrolyte with a small interfacial resistance for lithium‐ion batteries. *Angewandte Chemie International Edition* **2017,** *56* (3), 753-756.

173. Chen, L.; Li, Y.; Li, S.-P.; Fan, L.-Z.; Nan, C.-W.; Goodenough, J. B., PEO/garnet composite electrolytes for solid-state lithium batteries: From "ceramic-in-polymer" to "polymer-in-ceramic". *Nano Energy* **2018,** *46*, 176-184.

174. Gao, M.; Li, H.; Xu, L.; Xue, Q.; Wang, X.; Bai, Y.; Wu, C., Lithium metal batteries for high energy density: Fundamental electrochemistry and challenges. *Journal of Energy Chemistry* **2021,** *59*, 666-687.

175. Bae, J.; Li, Y.; Zhang, J.; Zhou, X.; Zhao, F.; Shi, Y.; Goodenough, J. B.; Yu, G., A 3D nanostructured hydrogel‐framework‐derived high‐performance composite polymer lithium‐ion electrolyte. *Angewandte Chemie International Edition* **2018,** *57* (8), 2096-2100.

176. Li, B.; Su, Q.; Yu, L.; Wang, D.; Ding, S.; Zhang, M.; Du, G.; Xu, B., Li0. 35La0. 55TiO3 nanofibers enhanced poly (vinylidene fluoride)-based composite polymer electrolytes for all-solid-state batteries. *ACS applied materials & interfaces* **2019,** *11* (45), 42206-42213.

177. Xu, H.; Chien, P.-H.; Shi, J.; Li, Y.; Wu, N.; Liu, Y.; Hu, Y.-Y.; Goodenough, J. B., High-performance all-solid-state batteries enabled by salt bonding to perovskite in poly (ethylene oxide). *Proceedings of the National Academy of Sciences* **2019,** *116* (38), 18815-18821.

178. Zhai, H.; Xu, P.; Ning, M.; Cheng, Q.; Mandal, J.; Yang, Y., A flexible solid composite electrolyte with vertically aligned and connected ion-conducting nanoparticles for lithium batteries. *Nano letters* **2017,** *17* (5), 3182-3187.

179. Wang, X.; Zhai, H.; Qie, B.; Cheng, Q.; Li, A.; Borovilas, J.; Xu, B.; Shi, C.; Jin, T.; Liao, X., Rechargeable solid-state lithium metal batteries with vertically aligned ceramic nanoparticle/polymer composite electrolyte. *Nano Energy* **2019,** *60*, 205-212.

180. Chen, B.; Huang, Z.; Chen, X.; Zhao, Y.; Xu, Q.; Long, P.; Chen, S.; Xu, X., A new composite solid electrolyte PEO/Li10GeP2S12/SN for all-solid-state lithium battery. *Electrochimica Acta* **2016,** *210*, 905-914.

181. Zhao, Y.; Wu, C.; Peng, G.; Chen, X.; Yao, X.; Bai, Y.; Wu, F.; Chen, S.; Xu, X., A new solid polymer electrolyte incorporating Li10GeP2S12 into a

polyethylene oxide matrix for all-solid-state lithium batteries. *Journal of Power Sources* **2016,** *301*, 47-53.

182. Fan, P.; Liu, H.; Marosz, V.; Samuels, N. T.; Suib, S. L.; Sun, L.; Liao, L., High Performance Composite Polymer Electrolytes for Lithium-Ion Batteries. *Advanced Functional Materials* **2021,** *n/a* (n/a), 2101380.

183. Cui, G., Reasonable Design of High-Energy-Density Solid-State Lithium-Metal Batteries. *Matter* **2020,** *2* (4), 805-815.

184. Qiao, L.; Judez, X.; Rojo, T.; Armand, M.; Zhang, H., Polymer Electrolytes for Sodium Batteries. *Journal of The Electrochemical Society* **2020,** *167* (7), 070534.

185. Qian, J.; Jin, B.; Li, Y.; Zhan, X.; Hou, Y.; Zhang, Q., Research progress on gel polymer electrolytes for lithium-sulfur batteries. *Journal of Energy Chemistry* **2021,** *56*, 420-437.

186. Kim, Y.-T.; Smotkin, E. S., The effect of plasticizers on transport and electrochemical properties of PEO-based electrolytes for lithium rechargeable batteries. *Solid State Ionics* **2002,** *149* (1-2), 29-37.

187. Vickraman, P.; Ramamurthy, S., A study on the blending effect of PVDF in the ionic transport mechanism of plasticized PVC–LiBF4 polymer electrolyte. *Materials Letters* **2006,** *60* (28), 3431-3436.

188. Rajendran, S.; Babu, R.; Sivakumar, P., Optimization of PVC–PAN ‐ based polymer electrolytes. *Journal of applied polymer science* **2009,** *113* (3), 1651-1656.

189. Carol, P.; Ramakrishnan, P.; John, B.; Cheruvally, G., Preparation and characterization of electrospun poly (acrylonitrile) fibrous membrane based gel polymer electrolytes for lithium-ion batteries. *Journal of Power Sources* **2011,** *196* (23), 10156-10162.

190. Min, H.-S.; Ko, J.-M.; Kim, D.-W., Preparation and characterization of porous polyacrylonitrile membranes for lithium-ion polymer batteries. *Journal of power sources* **2003,** *119*, 469-472.

191. Wang, X.; Gong, C.; He, D.; Xue, Z.; Chen, C.; Liao, Y.; Xie, X., Gelled microporous polymer electrolyte with low liquid leakage for lithium-ion batteries. *Journal of membrane science* **2014,** *454*, 298-304.

192. Li, Z. H.; Cheng, C.; Zhan, X. Y.; Wu, Y. P.; Zhou, X. D., A foaming process to prepare porous polymer membrane for lithium ion batteries. *Electrochimica Acta* **2009,** *54* (18), 4403-4407.

193. Du, A.; Zhang, Z.; Qu, H.; Cui, Z.; Qiao, L.; Wang, L.; Chai, J.; Lu, T.; Dong, S.; Dong, T.; Xu, H.; Zhou, X.; Cui, G., An efficient organic magnesium borate-based electrolyte with non-nucleophilic characteristics for magnesium–sulfur battery. *Energy & Environmental Science* **2017,** *10* (12), 2616-2625.

194. Kim, H.; Oh, B.; Kang, Y., Preparation and electrochemical properties of nonwoven reinforced solid polymer electrolytes. *Polymer Bulletin* **2000,** *44* (5), 509-515.

195. Liang, S.; Yan, W.; Wu, X.; Zhang, Y.; Zhu, Y.; Wang, H.; Wu, Y., Gel polymer electrolytes for lithium ion batteries: Fabrication, characterization and performance. *Solid State Ionics* **2018,** *318*, 2-18.

196. Zhang, H.; Chen, F.; Carrasco, J., Nanoscale modelling of polymer electrolytes for rechargeable batteries. *Energy Storage Materials* **2020**.

197. M. Armand; W. Gorecki; R. Andreani, Proceedings of the 2nd International Meeting on Polymer Electrolytes (Ed.: B. Scrosati). *Elsevier, London* **1989**, p. 91.

198. Weston, J. E.; Steele, B. C. H., Thermal history-conductivity relationship in lithium salt-poly(ethylene oxide) complex polymer electrolytes. *Solid State Ionics* **1981,** *2* (4), 347-54.

199. Ravn Sørensen, P.; Jacobsen, T., Conductivity, charge transfer and transport number—an ac-investigation of the polymer electrolyte LiSCN-poly(ethyleneoxide). *Electrochimica Acta* **1982,** *27* (12), 1671-1675.

200. Yang, L.; Zhang, A.; Qiu, B.; Yin, J.; Liu, Q., Effects of thermal history on lithium salt-poly(ethylene oxide) complex polymer electrolytes. *Solid State Ionics* **1988,** *28-30* (Pt. 2), 1029-31.

201. Schantz, S., On the ion association at low salt concentrations in polymer electrolytes; a Raman study of sodium triflate (NaCF3SO3) and lithium perchlorate dissolved in poly(propylene oxide). *J. Chem. Phys.* **1991,** *94* (9), 6296-306.

202. Kim, D. W.; Ryoo, B. K.; Park, J. K.; Maeng, K. S.; Hwang, T. S., Study on the ionic conductivity and mobility of liquid polymer electrolytes containing lithium salts. *Polym. J. (Tokyo)* **1992,** *24* (6), 509-18.

203. Benrabah, D.; Baril, D.; Sanchez, J.-Y.; Armand, M.; Gard, G. G., Comparative electrochemical study of new poly(oxyethylene)–Li salt complexes. *Journal of the Chemical Society, Faraday Transactions* **1993,** *89* (2), 355-359.

204. Besner, S.; Vallée, A.; Bouchard, G.; Prud'Homme, J., Effect of anion polarization on conductivity behavior of poly (ethylene oxide) complexed with alkali salts. *Macromolecules* **1992,** *25* (24), 6480-6488.

205. Gadjourova, Z.; Marero, D. M. y.; Andersen, K. H.; Andreev, Y. G.; Bruce, P. G., Structures of the Polymer Electrolyte Complexes PEO6:LiXF6 (X = P, Sb), Determined from Neutron Powder Diffraction Data. *Chem. Mater.* **2001,** *13* (4), 1282-1285.

206. Zhang, C.; Ainsworth, D.; Andreev, Y. G.; Bruce, P. G., Ionic Conductivity in the Solid Glyme Complexes [CH3O(CH2CH2O)nCH3]:LiAsF6 (n = 3,4). *J. Am. Chem. Soc.* **2007,** *129* (28), 8700-8701.

207. Gadjourova, Z.; Andreev, Y. G.; Tunstall, D. P.; Bruce, P. G., Ionic conductivity in crystalline polymer electrolytes. *Nature* **2001,** *412* (6846), 520-523.

208. Appetecchi, G. B.; Croce, F.; Dautzenberg, G.; Mastragostino, M.; Ronci, F.; Scrosati, B.; Soavi, F.; Zanelli, A.; Alessandrini, F.; Prosini, P. P., Composite polymer electrolytes with improved lithium metal electrode interfacial properties: I. Electrochemical properties of dry PEO-LiX systems. *J. Electrochem. Soc.* **1998,** *145* (12), 4126-4132.

209. Stephan, A. M.; Renganathan, N. G.; Kumar, T. P.; Thirunakaran, R.; Pitchumani, S.; Shrisudersan, J.; Muniyandi, N., Ionic conductivity studies on plasticized PVC/PMMA blend polymer electrolyte containing LiBF4 and LiCF3SO3. *Solid State Ionics* **2000,** *130* (1,2), 123-132.

210. Sequeira, C. A. C.; North, J. M.; Hooper, A., Stability domain of a complexed lithium salt-polyethylene oxide polymer electrolyte. *Solid State Ionics* **1984,** *13* (2), 175-9.

211. Bonino, F.; Scrosati, B.; Selvaggi, A., The lithium-polymer electrolyte interface. I. Lithium cyclability. *Solid State Ionics* **1986,** *18-19*, 1050-1053.

212. Vallée, A.; Besner, S.; Prud'Homme, J., Comparative study of poly (ethylene oxide) electrolytes made with LiN (CF3SO2) 2, LiCF3SO3 and LiClO4: Thermal properties and conductivity behaviour. *Electrochimica acta* **1992,** *37* (9), 1579-1583.

213. Ferry, A.; Edman, L.; Forsyth, M.; MacFarlane, D. R.; Sun, J., Connectivity, ionic interactions, and migration in a fast-ion-conducting polymer-in-salt electrolyte based on poly(acrylonitrile) and LiCF3SO3. *J. Appl. Phys.* **1999,** *86* (4), 2346-2348.

214. Ferry, A.; Edman, L.; Forsyth, M.; MacFarlane, D. R.; Sun, J., NMR and Raman studies of a novel fast-ion-conducting polymer-in-salt electrolyte based on LiCF3SO3 and PAN. *Electrochim. Acta* **2000,** *45* (8-9), 1237-1242.

215. Yoshizawa, M.; Marwanta, E.; Ohno, H., Preparation and characteristics of natural rubber/poly(ethylene oxide) salt hybrid mixtures as novel polymer electrolytes. *Polymer* **2000,** *41* (26), 9049-9053.

216. Zhu, J.; Zhang, Z.; Zhao, S.; Westover, A. S.; Belharouak, I.; Cao, P.-F., Single-Ion Conducting Polymer Electrolytes for Solid-State Lithium–Metal Batteries: Design, Performance, and Challenges. *Advanced Energy Materials* **2021,** *n/a* (n/a), 2003836.

217. Osman, Z.; Mohd Ghazali, M. I.; Othman, L.; Md Isa, K. B., AC ionic conductivity and DC polarization method of lithium ion transport in PMMA–LiBF4 gel polymer electrolytes. *Results in Physics* **2012,** *2*, 1-4.

218. Kalita, M.; Bukat, M.; Ciosek, M.; Siekierski, M.; Chung, S. H.; Rodríguez, T.; Greenbaum, S. G.; Kovarsky, R.; Golodnitsky, D.; Peled, E.; Zane, D.; Scrosati, B.; Wieczorek, W., Effect of calixpyrrole in PEO–LiBF4 polymer electrolytes. *Electrochimica Acta* **2005,** *50* (19), 3942-3948.

219. Rajendran, S.; Sivakumar, M.; Subadevi, R., Effect of salt concentration in poly(vinyl alcohol)-based solid polymer electrolytes. *Journal of Power Sources* **2003,** *124* (1), 225-230.

220. Ulaganathan, M.; Rajendran, S., Effect of different salts on PVAc/PVdF-co-HFP based polymer blend electrolytes. *Journal of Applied Polymer Science* **2010,** *118* (2), 646-651.

221. Zhang, S. S.; Xu, K.; Jow, T. R., Study of LiBF[sub 4] as an Electrolyte Salt for a Li-Ion Battery. *Journal of The Electrochemical Society* **2002,** *149* (5), A586.

222. Abraham, D. P.; Furczon, M. M.; Kang, S. H.; Dees, D. W.; Jansen, A. N., Effect of electrolyte composition on initial cycling and impedance characteristics of lithium-ion cells. *Journal of Power Sources* **2008,** *180* (1), 612-620.

223. Xu, G.; Shangguan, X.; Dong, S.; Zhou, X.; Cui, G., Key Scientific Issues in Formulating Blended Lithium Salts Electrolyte for Lithium Batteries. *Angewandte Chemie International Edition* **2019,** *0* (ja).

224. Appetecchi, G. B.; Zane, D.; Scrosati, B., PEO-Based Electrolyte Membranes Based on LiBC4O8 Salt. *J. Electrochem. Soc.* **2004,** *151* (9), A1369-A1374.

225. Wu, X.-L.; Xin, S.; Seo, H.-H.; Kim, J.; Guo, Y.-G.; Lee, J.-S., Enhanced Li+ conductivity in PEO-LiBOB polymer electrolytes by using succinonitrile as a plasticizer. *Solid State Ionics* **2011,** *186* (1), 1-6.

226. Li, S.; Chen, Y.-M.; Liang, W.; Shao, Y.; Liu, K.; Nikolov, Z.; Zhu, Y., A Superionic Conductive, Electrochemically Stable Dual-Salt Polymer Electrolyte. *Joule* **2018,** *2* (9), 1838-1856.

227. Huang, K.-C.; Li, H.-H.; Fan, H.-H.; Guo, J.-Z.; Xing, Y.-M.; Hu, Y.-P.; Wu, X.-L.; Zhang, J.-P., An In Situ-Fabricated Composite Polymer Electrolyte Containing Large-Anion Lithium Salt for All-Solid-State LiFePO4/Li Batteries. *ChemElectroChem* **2017,** *4* (9), 2293-2299.

228. Zhang, S. S., An unique lithium salt for the improved electrolyte of Li-ion battery. *Electrochemistry communications* **2006,** *8* (9), 1423-1428.

229. Polu, A. R.; Kim, D. K.; Rhee, H.-W., Poly(ethylene oxide)-lithium difluoro(oxalato)borate new solid polymer electrolytes: ion-polymer interaction, structural, thermal, and ionic conductivity studies. *Ionics* **2015,** *21* (10), 2771-2780.

230. Wang, Q.; Cui, Z.; Zhou, Q.; Shangguan, X.; Du, X.; Dong, S.; Qiao, L.; Huang, S.; Liu, X.; Tang, K., A supramolecular interaction strategy enabling high-performance all solid state electrolyte of lithium metal batteries. *Energy Storage Materials* **2020,** *25*, 756-763.

231. Schmidt, M.; Heider, U.; Kuehner, A.; Oesten, R.; Jungnitz, M.; Ignat'Ev, N.; Sartori, P., Lithium fluoroalkylphosphates: a new class of conducting salts for electrolytes for high energy lithium-ion batteries. *Journal of power sources* **2001,** *97*, 557-560.

232. Aravindan, V.; Gnanaraj, J.; Madhavi, S.; Liu, H. K., Lithium‐ion conducting electrolyte salts for lithium batteries. *Chemistry–A European Journal* **2011,** *17* (51), 14326-14346.

233. Aravindan, V.; Vickraman, P., Polyvinylidenefluoride–hexafluoropropylene based nanocomposite polymer electrolytes (NCPE) complexed with LiPF3 (CF3CF2) 3. *European Polymer Journal* **2007,** *43* (12), 5121-5127.

234. Nik Zulkepeli, N. A. S.; Winie, T.; Subban, R. H. Y., Electrical and structural properties of PVC-LiCF3SO3 polymer electrolyte. *Solid State Sci. Technol.* **2016,** *24* (1), 70-75.

235. Ue, M.; Takeda, M.; Takehara, M.; Mori, S., Electrochemical Properties of Quaternary Ammonium Salts for Electrochemical Capacitors. *Journal of The Electrochemical Society* **1997,** *144* (8), 2684-2688.

236. Ue, M.; Murakami, A.; Nakamura, S., Anodic stability of several anions examined by ab initio molecular orbital and density functional theories. *Journal of the Electrochemical Society* **2002,** *149* (12), A1572.

237. Paillard, E.; Toulgoat, F.; Sanchez, J. Y.; Médebielle, M.; Iojoiu, C.; Alloin, F.; Langlois, B., Electrochemical investigation of polymer electrolytes based on lithium 2-(phenylsulfanyl)-1,1,2,2-tetrafluoro-ethansulfonate. *Electrochimica Acta* **2007,** *53* (4), 1439-1443.

238. Paillard, E.; Toulgoat, F.; Iojoiu, C.; Alloin, F.; Guindet, J.; Medebielle, M.; Langlois, B.; Sanchez, J. Y., Polymer electrolytes based on new aryl-containing lithium perfluorosulfonates. *Journal of Fluorine Chemistry* **2012,** *134*, 72-76.

239. Zhang, H.; Oteo, U.; Zhu, H.; Judez, X.; Martinez-Ibañez, M.; Aldalur, I.; Sanchez-Diez, E.; Li, C.; Carrasco, J.; Forsyth, M., Enhanced Li ‐ ion conductivity of polymer electrolytes with selective introduction of hydrogen in the anion. *Angewandte Chemie* **2019**.

240. Zhang, H.; Liu, C.; Zheng, L.; Xu, F.; Feng, W.; Li, H.; Huang, X.; Armand, M.; Nie, J.; Zhou, Z., Lithium bis (fluorosulfonyl) imide/poly (ethylene oxide) polymer electrolyte. *Electrochimica Acta* **2014,** *133*, 529-538.

241. Judez, X.; Zhang, H.; Li, C.; Eshetu, G. G.; Zhang, Y.; González-Marcos, J. A.; Armand, M.; Rodriguez-Martinez, L. M., Polymer-Rich Composite Electrolytes for All-Solid-State Li–S Cells. *The Journal of Physical Chemistry Letters* **2017,** *8* (15), 3473-3477.

242. Judez, X.; Zhang, H.; Li, C.; González-Marcos, J. A.; Zhou, Z.; Armand, M.; Rodriguez-Martinez, L. M., Lithium Bis(fluorosulfonyl)imide/Poly(ethylene oxide) Polymer Electrolyte for All Solid-State Li–S Cell. *The Journal of Physical Chemistry Letters* **2017,** *8* (9), 1956-1960.

243. Eshetu, G. G.; Judez, X.; Li, C.; Martinez-Ibanez, M.; Gracia, I.; Bondarchuk, O.; Carrasco, J.; Rodriguez-Martinez, L. M.; Zhang, H.; Armand, M., Ultrahigh Performance All Solid-State Lithium Sulfur Batteries: Salt Anion's Chemistry-Induced Anomalous Synergistic Effect. *J. Am. Chem. Soc.* **2018,** *140* (31), 9921-9933.

244. Tong, B.; Wang, P.; Ma, Q.; Wan, H.; Zhang, H.; Huang, X.; Armand, M.; Feng, W.; Nie, J.; Zhou, Z., Lithium fluorinated sulfonimide-based solid polymer electrolytes for Li || LiFePO4 cell: The impact of anionic structure. *Solid State Ionics* **2020,** *358*, 115519.

245. Deng, P.; Zhang, H.; Feng, W.; Zhou, Z.; Armand, M.; Nie, J., Lithium (fluorosulfonyl)(pentafluoroethylsulfonyl)imide/poly (ethylene oxide) polymer electrolyte: Physical and electrochemical properties. *Solid State Ionics* **2019,** *338*, 161-167.

246. Han, H.; Guo, J.; Zhang, D.; Feng, S.; Feng, W.; Nie, J.; Zhou, Z., Lithium (fluorosulfonyl)(nonafluorobutanesulfonyl)imide (LiFNFSI) as conducting salt to improve the high-temperature resilience of lithium-ion cells. *Electrochemistry Communications* **2011,** *13* (3), 265-268.

247. Fang, Z.; Ma, Q.; Liu, P.; Ma, J.; Hu, Y.-S.; Zhou, Z.; Li, H.; Huang, X.; Chen, L., Novel Concentrated Li[(FSO2)(n-C4F9SO2)N]-Based Ether Electrolyte for Superior Stability of Metallic Lithium Anode. *ACS Applied Materials & Interfaces* **2017,** *9* (5), 4282-4289.

248. Ma, Q.; Song, Z.; Liu, J.; Zheng, L.; Zhang, H.; Huang, X.; Armand, M.; Feng, W.; Nie, J.; Zhou, Z., Li[(FSO2)(n-C4F9SO2)N]: a difunctional salt for ethylene carbonate- and additive-free electrolyte for Li-ion cells. *ChemElectroChem* **2021,** *n/a* (n/a).

249. Gorecki, W.; Roux, C.; Clémancey, M.; Armand, M.; Belorizky, E., NMR and Conductivity Study of Polymer Electrolytes in the Imide Family: P(EO)/Li[N(SO2CnF2n+1)(SO2CmF2m+1)]. *ChemPhysChem* **2002,** *3* (7), 620-625.

250. Appetecchi, G. B.; Henderson, W.; Villano, P.; Berrettoni, M.; Passerini, S., PEO-LiN (SO 2 CF 2 CF 3) 2 Polymer Electrolytes: I. XRD, DSC, and Ionic Conductivity Characterization. *Journal of the Electrochemical Society* **2001,** *148* (10), A1171.

251. Appetecchi, G. B.; Passerini, S., Poly (ethylene oxide)-LiN (SO 2 CF 2 CF 3) 2 Polymer Electrolytes: II. Characterization of the Interface with Lithium. *Journal of The Electrochemical Society* **2002,** *149* (7), A891.

252. Villano, P.; Carewska, M.; Appetecchi, G. B.; Passerini, S., PEO LiN (SO 2 CF 2 CF 3) 2 Polymer Electrolytes: III. Test in Batteries. *Journal of the Electrochemical Society* **2002,** *149* (10), A1282.

253. Capiglia, C.; Imanishi, N.; Takeda, Y.; Henderson, W. A.; Passerini, S., Poly (ethylene oxide) LiN (SO 2 CF 2 CF 3) 2 Polymer Electrolytes: IV. Raman Characterization. *Journal of the Electrochemical Society* **2003,** *150* (4), A525.

254. Ma, Q.; Qi, X.; Tong, B.; Zheng, Y.; Feng, W.; Nie, J.; Hu, Y.-S.; Li, H.; Huang, X.; Chen, L.; Zhou, Z., Novel Li[(CF3SO2)(n-C4F9SO2)N]-Based Polymer Electrolytes for Solid-State Lithium Batteries with Superior Electrochemical Performance. *ACS Applied Materials & Interfaces* **2016,** *8* (43), 29705-29712.

255. Zhang, H.; Song, Z.; Yuan, W.; Feng, W.; Nie, J.; Armand, M.; Huang, X.; Zhou, Z., Impact of negative charge delocalization on the properties of solid polymer electrolytes. *ChemElectroChem* **2021,** *n/a* (n/a).

256. Zhang, H.; Oteo, U.; Judez, X.; Eshetu, G. G.; Martinez-Ibañez, M.; Carrasco, J.; Li, C.; Armand, M., Designer Anion Enabling Solid-State Lithium-Sulfur Batteries. *Joule* **2019**.

257. Chakrabarti, A.; Filler, R.; Mandal, B. K., Synthesis and properties of a new class of fluorine-containing dilithium salts for lithium-ion batteries. *Solid State Ionics* **2010,** *180* (40), 1640-1645.

258. Geiculescu, O. E.; Yang, J.; Blau, H.; Bailey-Walsh, R.; Creager, S. E.; Pennington, W. T.; DesMarteau, D. D., Solid polymer electrolytes from dilithium salts based on new bis [(perfluoroalkyl) sulfonyl] diimide dianions. Preparation and electrical characterization. *Solid state ionics* **2002,** *148* (1-2), 173-183.

259. Geiculescu, O. E.; Xie, Y.; Rajagopal, R.; Creager, S. E.; DesMarteau, D. D., Dilithium bis [(perfluoroalkyl) sulfonyl] diimide salts as electrolytes for rechargeable lithium batteries. *Journal of fluorine chemistry* **2004,** *125* (8), 1179-1185.

260. Geiculescu, O. E.; Rajagopal, R. V.; Mladin, E. C.; Creager, S. E.; Desmarteau, D. D., Solid Polymer Electrolytes from Crosslinked PEG and Dilithium N, N'-Bis (trifluoromethanesulfonyl) perfluoroalkane-1, ω-disulfonamide and Lithium Bis (trifluoromethanesulfonyl) imide Salts. *Collection of Czechoslovak Chemical Communications* **2008,** *73* (12), 1777-1798.

261. Zhang, Q.; Pan, J.; Lu, P.; Liu, Z.; Verbrugge, M. W.; Sheldon, B. W.; Cheng, Y.-T.; Qi, Y.; Xiao, X., Synergetic effects of inorganic components in solid

electrolyte interphase on high cycle efficiency of lithium ion batteries. *Nano letters* **2016,** *16* (3), 2011-2016.

262. Zhang, H.; Judez, X.; Santiago, A.; Martinez-Ibanez, M.; Munoz-Marquez, M. A.; Carrasco, J.; Li, C.; Eshetu, G. G.; Armand, M., Fluorine-Free Noble Salt Anion for High-Performance All-Solid-State Lithium-Sulfur Batteries. *Adv. Energy Mater*. **2019,** *9* (25), n/a.

263. Santiago, A.; Judez, X.; Castillo, J.; Garbayo, I.; Sáenz de Buruaga, A.; Qiao, L.; Baraldi, G.; Coca-Clemente, J. A.; Armand, M.; Li, C.; Zhang, H., Improvement of Lithium Metal Polymer Batteries through a Small Dose of Fluorinated Salt. *The Journal of Physical Chemistry Letters* **2020**, 6133-6138.

264. Santiago, A.; Castillo, J.; Garbayo, I.; Saenz de Buruaga, A.; Coca Clemente, J. A.; Qiao, L.; Cid Barreno, R.; Martinez-Ibañez, M.; Armand, M.; Zhang, H.; Li, C., Salt Additives for Improving Cyclability of Polymer-Based All-Solid-State Lithium–Sulfur Batteries. *ACS Applied Energy Materials* **2021**.

265. Niedzicki, L.; Grugeon, S.; Laruelle, S.; Judeinstein, P.; Bukowska, M.; Prejzner, J.; Szczecinski, P.; Wieczorek, W.; Armand, M., New covalent salts of the 4+ V class for Li batteries. *Journal of Power Sources* **2011,** *196* (20), 8696-8700.

266. Niedzicki, L.; Kasprzyk, M.; Kuziak, K.; Żukowska, G. Z.; Armand, M.; Bukowska, M.; Marcinek, M.; Szczeciński, P.; Wieczorek, W., Modern generation of polymer electrolytes based on lithium conductive imidazole salts. *Journal of Power Sources* **2009,** *192* (2), 612-617.

Chapter 2

Experimental section

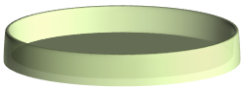

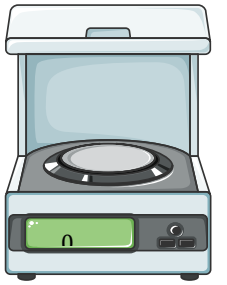

Chapter 2:

Experimental section

2.1. Introduction

The proposal of this chapter is to detail the experimental techniques, samples preparation and characterization as well the cell assembly, characterization that have been used for this thesis work. Firstly, the characterization techniques for the synthesized neat salts including nuclear magnetic resonance spectroscopy (NMR), Fourier-transform infrared spectroscopy (FTIR) and Raman spectroscopy are briefly provided. Yet, the experimental details for the synthesis of the neat salts are not included in this chapter and those will be discussed in their respective chapters.

Secondly, the preparation process of the solid polymer electrolytes (SPEs) for their use in batteries, especially the characterization of the SPEs is emphasized in this part. At first, a description of the chemical, morphological techniques that allow for providing the chemical stability, phase behaviours (e.g., glass transition temperature, crystallinity) as well as the morphological properties of the SPEs are presented. And, then, the techniques required for showing the physicochemical properties in terms of ionic conductivities and lithium-ion transference number of the SPEs are given. Finally, electrochemical methodologies such as linear sweeping voltammogram (LSV), cyclic voltammogram (CV) for measuring the anodic and cathodic stability of the electrolytes are described.

Thirdly, the $LiFePO_4$ electrodes preparation, cell assembly and cells testing are detailed presented with respect to different cell configurations, e.g., Li° || Li°, Li° || Cu° and Li° || $LiFePO_4$ cells.

2.2. Structural characterization of the synthesized salts

2.2.1. Nuclear magnetic resonance spectroscopy (NMR)

To confirm the successful synthesis of the targeted salts in this thesis, nuclear magnetic resonance spectroscopy [NMR, Bruker 300 Ultrashield (300 MHz for ^{1}H, 75.5 MHz for ^{13}C, and 283 MHz for ^{19}F)] is used to characterize the chemical structure of synthesized salts. NMR is known as a spectroscopic technique to probe local magnetic fields around atomic nuclei, such as proton (^{1}H), carbon (^{13}C) and fluorine (^{19}F). The sample is sealed in an NMR tube and placed in a magnetic field and the NMR signal is produced by excitation of the nuclei sample with radio frequency waves into nuclear magnetic resonance, which is detected with sensitive radio receivers. The different intra-molecular magnetic fields around an atom in a molecule could change the resonance frequencies, thereby giving information about of the electronic structure of a molecule and its functional groups.[1]

To further detail the structures of the synthesized salts, correlation spectroscopy heteronuclear single quantum coherence spectroscopy (HSQC) is also employed in this thesis. The obtained spectrum from the HSQC experiments is two-dimensional (2D) with one axis for proton (^{1}H, horizontal axis) and the other for a ^{13}C (vertical axis), which provides more information of the synthesized salts.

2.2.2. Fourier-transform infrared spectroscopy (FTIR)

Except for the NMR technique, Fourier-transform infrared spectroscopy (FTIR, Bruker vertex 70) is used to clarify the structures of the synthesized salts. This is a technique that used to obtain an infrared spectrum of absorption or emission of a solid, liquid or even gas, which could identify the

presence of organic and inorganic information in the sample.[2] During the measurements, the equipment releases a beam containing many frequencies of light at once and measures how much of that beam is absorbed by the sample. Afterwards, a computer not only takes all this data and works backward to infer what the absorption is at each wavelength but also makes the Fourier transform algorithm to translate the raw data to spectra.[3] In addition to the synthesized salts, the FTIR was also used to characterize the SPEs with different salts, which will be discussed in Chapter 5.

2.2.3. Raman spectroscopy

Raman spectroscopy is a non-destructive chemical analysis technique based also on interaction of light with the chemical bonds within a material. An incident beam is shifted in wavelength through inelastic scattering. This technique is used to determine vibrational, rotational and other low-frequency modes of molecules, which provides detailed information about chemical structure, phase and polymorphism, crystallinity and molecular interactions.[4] Raman spectra feature a number of peaks showing the intensity and wavelength positions, which are related to the specific molecular bond vibrations, including individual bonds such as C-C, C=C, N=O, C-H, O=S=O and C-F etc., and groups of bonds such as benzene ring breathing mode, polymer chain vibrations, lattice modes, etc.[5] In this thesis, Raman spectroscopy was employed as complementary technique to characterize the salts as well as the SPEs. Raman spectra of the salts or SPEs were recorded with a Renishaw inVia confocal Raman spectrometer (serial number 16H981). Incident laser has wavelength of 532 nm and microscope configurations were typically used with a 50×/0.75 focusing objective. The

laser spot size is about 0.8 μm and spatial resolution is around 0.4 μm. In an argon-filled glovebox, the sample was sealed in a home-made cell with a Raman-inactive glass window for avoiding the direct contact between the sample and air/moisture.

2.3. SPEs preparation and characterization

2.3.1. SPEs preparation

SPEs comprising of the synthesized salts and poly (ethylene oxide) (PEO) matrix were prepared by the conventional solvent casting method using acetonitrile (ACN) as secondary solvent. After solvent evaporation, membranes were prepared by hot-pressing (high temperature film maker controller, Specac®) with a final average thickness of 70 μm. The preparation process for SPEs is schematically shown **Figure 2.1**. SPEs with different EO/Li^+ ratios, e.g., EO/Li^+ = 64, 32, 20, 12 and 8, were prepared, respectively.

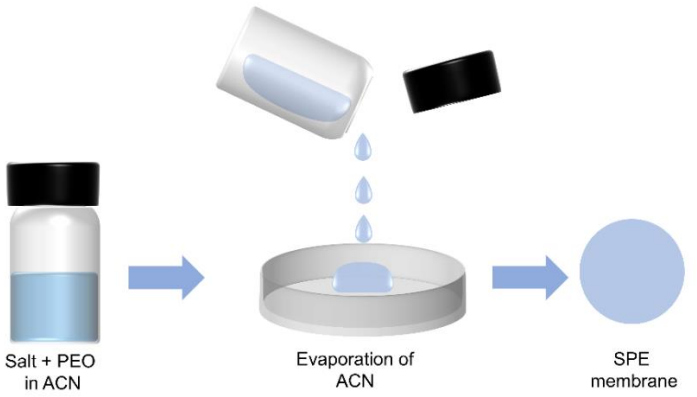

Figure 2.1. Schematic illustration of SPEs preparation by conventional solvent casting method.

2.3.2. Thermogravimetric analysis (TGA)

Thermogravimetric analysis (TGA) is a method of thermal analysis where the mass of a sample is measured as the temperature changes over time. The mass changes of the samples are measured by TGA while its temperature is increasing. There will be no observed mass change if a species is thermally stable.[6] In this thesis, thermal stabilities of the salts and SPEs were measured using a TGA 209 F1 Libra (Netzsch) equipment. The samples were heated from room temperature (RT) to 600 ^{o}C at a heating rate of 10 ^{o}C min^{-1} under Argon flow and the decomposition temperatures (T_d) are defined as 5wt% mass loss.

2.3.3. Differential scanning calorimetry (DSC)

Differential scanning calorimetry (DSC) is a widely used thermo-analytical technique, which in our case we use to examine polymeric materials to determine their thermal transitions, e.g., glass transition temperature (T_g), crystallization temperature (T_c), and melting temperature (T_m).[7] The neat salts and the SPEs obtained in this thesis are carefully tested by DSC instrument (Q2000, TA Instruments) in different temperature range (e.g., –80 °C to 300 °C for neat salts; –80 °C to 150 °C for SPEs). Samples were hermetically sealed in an aluminum pan in an argon-filled glovebox (the content of O_2 and H_2O is less than 0.1 ppm) with an average mass of ca. 10–15 mg. Each sample was measured for two consecutive scans at a cooling and heating process at a rate of 10 °C min^{-1}. The T_g (onset of the heat capacity change), T_m (maximum of the endothermic peak) as well as melting enthalpy (ΔH_m, area below the endothermic peak) are taken from the first heating scan for the neat salts and second heating scan for the SPEs,

respectively. The crystalline fraction (χ_c) of the SPEs was calculated by Equation [2.1]:

$$\chi_c = \frac{\Delta H_m}{\Delta H_{PEO} \times f_{PEO}} \qquad [2.1]$$

where ΔH_m is the melting enthalpy of electrolyte, ΔH_{PEO} is the value of 196.4 J g^{-1} for PEO perfect crystals reported in literature[8] for the melting enthalpy of 100% crystalline PEO, and f_{PEO} is the PEO weight fraction in the electrolyte.

2.3.4. X-ray diffraction analysis

X-Ray diffraction (XRD) is a rapid analytical technique widely used for phase and molecular structure identification of a crystalline material, which allows to provide information on unit cell dimensions.[9] In addition, XRD is also a fundamental tool to ascertain the crystallinity of crystalline polymers.[10] In this regard, XRD (Bruker D8 Discover X-ray diffractometer was used in this thesis to characterize the prepared SPEs suing $\lambda_{Cu\text{-}K\alpha}$ = 1.54056 Å radiation in the 2θ range from 2° to 80° with a step width of 0.0198°. Samples were assembled inside an argon-filled glovebox into a sensitive sample holder to avoid contact with moisture.

2.3.5. Morphological characterization of SPEs

The optical microscope is a type of microscope that commonly utilizes visible light and a system of lenses to generate magnified images of small samples. Atomic force microscopy (AFM) consisting of a cantilever with a sharp tip (probe) at its end is a powerful tool that allows a variety of surfaces to be imaged and characterized at the atomic level.[11] A scanning electron

microscope (SEM) is another surface morphology characterization technique that generates images of a sample by scanning the surface with a focused beam of electrons. The electrons interact with atoms in the sample surface, producing various signals that contain information about the surface topography of the sample. The surface morphologies of the SPEs prepared in this thesis are observed by AFM (AFM, Agilent 5500), optical microscope (Micro Scope Axio Carl Zeiss) and SEM (SEM, Quanta 200 FEG, FEI), respectively.

2.3.6. Ionic conductivity

The ionic conductivities of the as-prepared SPEs were obtained by electrochemical impedance spectroscopy (EIS) on a VMP3 potentiostat (Biologic). CR2032 type coin cells (SS | SPEs | SS) comprising two stainless steel (SS) blocking electrodes and Teflon O-ring (see **Figure 2.2** for schematic illustration) were assembled in an argon filled glovebox (M Braun, H_2O < 0.1 ppm, O_2 < 0.1 ppm) for ionic conductivity tests. The cells were subjected to EIS in a frequency range 10^4 to 10^{-1} Hz from 30 to 100 °C and the temperature was controlled by using an electro-thermostatic oven (± 1 °C, Lan Technics, Model DHG). The ionic conductivities were obtained by Equation [2.2]:

$$\sigma_{\text{total}} = \frac{L}{S \times R_{\text{bulk}}} \qquad [2.2]$$

wherein, σ_{total} (in S cm^{-1}) is the total ionic conductivity of the SPE, L (in cm) is the thickness of the SPE, S (in cm^2) is the contact area between the SPE and the electrode and R_{bulk} (in Ω) is the bulk resistance of the SPE.

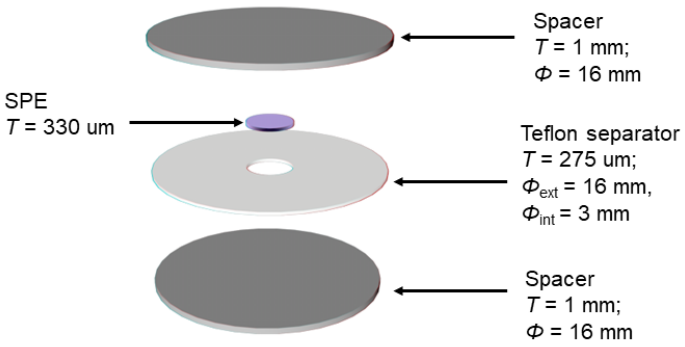

Figure 2.2. Schematic illustration of the coin cell used for ionic conductivity measurements.

2.3.7. Lithium-ion transference number

Electrochemical lithium-ion transference numbers (T_{Li}^{+}, dimensionless) of the SPEs were obtained using a VMP3 potentiostat (Biologic) and a combination of alternating-current (AC) EIS and direct-current (DC) polarization methods suggested by Hu *et al.*[12] First, AC EIS was used to determine the total resistance (R_{cell}, in Ω) of the symmetric Li° | SPEs | Li° cells. Subsequently, DC polarization was performed using a polarization voltage of 10 mV (V_{DC}, in mV) to obtain the stable current (I_{DC}, in mA). The T_{Li}^{+} were calculated by Equation [2.3]:

$$T_{Li}^{+} = \frac{V_{DC}}{I_{DC} \times R_{cell}} \qquad [2.3]$$

The temperature was accurately controlled and set to 70 °C (± 1 °C) for all measurements using an electro-thermostatic oven (Lan technics, Model DHG).

2.3.8. Lithium-ion conductivity

The lithium-ion conductivity ($\sigma_{Li}{}^{+}$) of PEO-based SPEs was calculated by the measured total conductivity and lithium-ion transference number followed by Equation [2.4]:

$$\sigma_{Li}^{+} = \sigma_{total} \times T_{Li}^{+} \qquad [2.4]$$

As mentioned above, the $\sigma_{Li}{}^{+}$, σ_{total}, and $T_{Li}{}^{+}$ are the lithium-ion conductivity, total ionic conductivity and lithium-ion transference number of a SPE, respectively.

2.3.9. Electrochemical stability

Anodic stability: anodic stability of the electrolytes in this thesis was determined by linear sweep voltammogram (LSV) measurement using a VMP3 potentiostat (Biologic). To determine the anodic stability of the salts, LSV experiments were performed in both liquid-based electrolyte at 25 ºC and PEO-based electrolytes at 70 ºC. For the liquid electrolytes of 0.1 M lithium salts in propylene carbonate (PC), a three-electrode cell with platinum (surface area: 0.0314 cm^{-2}) as working electrode, Li° disks as both counter and reference electrodes were used. For PEO-based SPEs, a two-electrode cell using Li° | SPEs | SS (surface area: 0.0707 cm^{-2}) was adopted. All the LSV measurements were performed between the open circuit potential (OCP) and 6.5 V vs. Li/Li^{+} at a scan rate of 1 mV s^{-1}.

Cathodic Stability: Electrochemical cathodic stability of the SPEs was determined by cyclic voltammetry (CV) in a VMP3 potentiostat (Biologic). A CR2032 type Li ||° Cu coin cell was used comprising copper disk (surface area: 0.0707 cm^{-2}) as working electrode and Li° disk as both counter and

reference electrodes. All the CV measurements were performed between the open-circuit voltage and −0.2 V vs. Li/Li^+ at a scan rate of 1 mV s^{-1} at 70 °C.

2.4. Cell preparation and characterization

2.4.1. Electrode preparation

$LiFePO_4$ (LFP) cathodes comprising 63 wt% active material, 7 wt% C65 conductive carbon and 30 wt% polymer binders (i.e., Li salt/PEO at EO/Li^+ = 20) are prepared by conventional casting method using doctor-blade, and the areal loading of active material was ca. 4.0 mg cm^{-2}. To enhance the electronic of the LFP cathodes, carbon-coated aluminum current collector is used for the cathode preparation.

2.4.2. Li° || Li° cells

For the SPEs-based Li° || Li° cells, galvanostatic cycling of Li° symmetrical cells (areal of Li° disk: 1.54 cm^{-2}) are carried out using Neware® battery testers at a current density of 0.1 mA cm^{-2}. The duration of each half-cycle is 3 h for the measurement. Electrochemical impedance spectra (EIS) of the cells are recorded before and after cycling in the range from 10^6 to 10^{-2} Hz at 70 °C. 1,2-dimethoxyethane (DME) was used as the solvent to prepare the liquid electrolytes and cycling tests of liquid-based Li° || Li° cells are performed using the same program for the SPEs-based cells at room temperature.

2.4.3. Li° || Cu cells

To explore the different surface morphologies, microstructures and components of the Li° deposits in different salt electrolytes, Li° deposits are obtained by the galvanostatic deposition of Li° on Cu substrates using Li° || Cu cells with DME-based liquid electrolyte at a current density of 0.1 mA cm^{-2} for 25 h. Afterwards, the surface morphologies and microstructures of the Li deposits are observed by SEM (Quanta 200 FEG, FEI), and the chemical composition of the surface layer is measured by a Phoibos 150 XPS with a non-monochromatic Mg K_α source ($h\nu$ = 1253.6 eV) and Raman spectra. The XPS spectra were recorded with high resolution scans at low power (100 W, 20 eV pass energy, and 0.1 eV energy step). The Ar^+ sputtering process was carried out using ion energy of 1 keV (Ar partial pressure: 10−8 Torr; ion beam current density: 1 mA mm^{-2}). The calibration of the binding energy was performed taking into account as reference the Auger parameter of LiF at 1340 eV.[13] The samples for the SEM, XPS and Raman measurements were gently rinsed with DME and dried thoroughly under vacuum before being transferred to the corresponding equipments.

2.4.4. Li° || LFP cells

All the Li° || LFP cells are assembled in an argon-filled glovebox. Afterwards, these cells are subjected to three formation cycles at a rate of C/5 and then charged and discharged with a constant *C*-rate of C/3 for constant cycling, and the corresponding charge/discharge voltage range is between 2.5 and 3.7 V. EIS of the cells are recorded before and after cycling by using a VMP3 potentiostat (Biologic) in the range from 10^6 to 10^{-2} Hz.

2.5. References

1. https://en.wikipedia.org/wiki/Nuclear_magnetic_resonance_spectroscopy.

2. Griffiths, P. R.; De Haseth, J. A., *Fourier transform infrared spectrometry*. John Wiley & Sons: 2007; Vol. 171.

3. Mohamed Shameer, P.; Mohamed Nishath, P., Chapter 8 - Exploration and enhancement on fuel stability of biodiesel: A step forward in the track of global commercialization. In *Advanced Biofuels*, Azad, A. K.; Rasul, M., Eds. Woodhead Publishing: 2019; pp 181-213.

4. Graves, P.; Gardiner, D., Practical raman spectroscopy. *Springer* **1989**.

5. https://www.horiba.com/en_en/raman-imaging-and-spectroscopy/.

6. Prime, R. B.; Bair, H. E.; Vyazovkin, S.; Gallagher, P. K.; Riga, A., Thermogravimetric analysis (TGA). *Thermal analysis of polymers: Fundamentals and applications* **2009**, 241-317.

7. Schick, C., Differential scanning calorimetry (DSC) of semicrystalline polymers. *Analytical and bioanalytical chemistry* **2009,** *395* (6), 1589-1611.

8. Stolwijk, N. A.; Heddier, C.; Reschke, M.; Wiencierz, M.; Bokeloh, J.; Wilde, G., Salt-concentration dependence of the glass transition temperature in PEO–NaI and PEO–LiTFSI polymer electrolytes. *Macromolecules* **2013,** *46* (21), 8580-8588.

9. Vishwakarma, V.; Uthaman, S., 9 - Environmental impact of sustainable green concrete. In *Smart Nanoconcretes and Cement-Based Materials*, Liew, M. S.; Nguyen-Tri, P.; Nguyen, T. A.; Kakooei, S., Eds. Elsevier: 2020; pp 241-255.

10. Rajeswari, A.; Jackcina Stobel Christy, E.; Gopi, S.; Jayaraj, K.; Pius, A., 9 - Characterization studies of polymer-based composites related to functionalized filler-matrix interface. In *Interfaces in Particle and Fibre Reinforced Composites*, Goh, K. L.; M.K, A.; De Silva, R. T.; Thomas, S., Eds. Woodhead Publishing: 2020; pp 219-250.

11. Blanchard, C. R., Atomic force microscopy. *The chemical educator* **1996,** *1* (5), 1-8.

12. Suo, L.; Hu, Y.-S.; Li, H.; Armand, M.; Chen, L., A new class of solvent-in-salt electrolyte for high-energy rechargeable metallic lithium batteries. *Nature communications* **2013,** *4* (1), 1-9.

13. Qiao, L.; Oteo, U.; Zhang, Y.; Peña, S. R.; Martínez-Ibañez, M.; Santiago, A.; Cid, R.; Meabe, L.; Manzano, H.; Carrasco, J.; Zhang, H.; Armand, M., Trifluoromethyl-free anion for highly stable lithium metal polymer batteries. *Energy Storage Materials* **2020,** *32*, 225-233.

Chapter 3

Trifluoromethyl-free anion for highly stable lithium metal polymer batteries

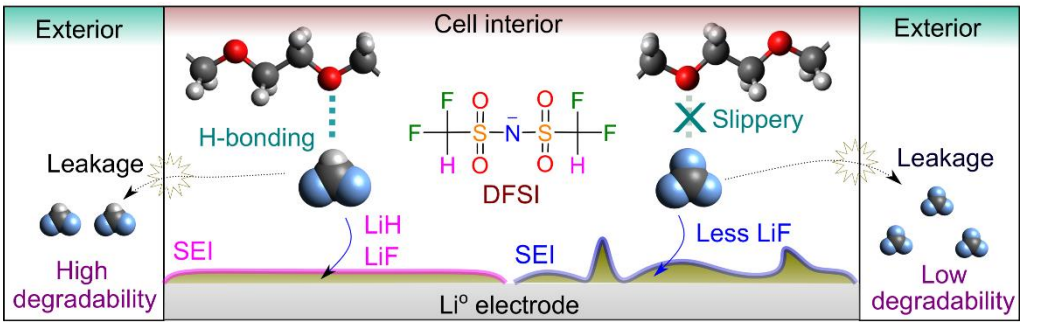

Chapter 3:

Trifluoromethyl-free anion for highly stable lithium metal polymer batteries

Chapter 3

3.1. Introduction

Stemming from the solid-solution electrodes and rocking-chair battery concepts conceived in the 1970s,[1-2] lithium-ion batteries (LIBs) have become one of the most representative life-impacting technologies, powering a wide gallery of energy-related applications, from untethered internet of things (IoTs) devices, to e-mobility (electric vehicles, EVs), and grid energy storage.[3] Conventional LIBs encompass two intercalation electrodes with different redox potentials [i.e., graphitized carbon (0.05 V vs. Li/Li^+) and layered oxide materials (4.1 V vs. Li/Li^+) as the respective negative and positive electrodes] and a Li-ion conducting liquid electrolyte (LE) of lithium hexafluorophosphate ($LiPF_6$) dissolved in a mixture of linear and cyclic carbonate solvents [e.g., dimethyl carbonate (DMC), ethyl methyl carbonate (EMC), ethylene carbonate (EC), etc…].[4-5] The four-volt class LIBs provide now gravimetric and volumetric energy densities of ~250 Wh kg^{-1} and ~700 Wh L^{-1}, respectively, outperforming traditional battery technologies such as lead-acid battery (~40 Wh kg^{-1} and ~90 Wh L^{-1}) or, nickel metal hydride battery (~80 Wh kg^{-1} and ~300 Wh L^{-1}).[6]

With a high ionic conductivity of ~10^{-2} S cm^{-1} at room temperature, good electrochemical stability against electrodes and current collectors, and excellent wettability, the commercial LE 1 M $LiPF_6$-EC/EMC (30/70, by volume), confers on the liquid LIBs good rate-capability (> 2C) and acceptable calendar life (≥ 5 years).[4] However, the flammability, the ease of leakage of LEs, and the plating of lithium dendrite on charging arise due safety concerns (e.g., cascading thermal runaway), handicapping the massive deployment of current LIB technology in the application domains where large-format batteries [e.g., EVs or grid storage (GS)] are required.[7-8] More

than a dozen of 1 MWh-class GS containers were destroyed by spontaneous fire in the last two years, in USA and South Korea. Moreover, the high chemical reactivity of carbonate solvents further amplifies the potential risks when replacing the state-of-the-art graphite electrode with the "holy grail" lithium metal electrode which has lower redox potential [−3.04 V (Li°) vs. −2.84 V (graphite) vs. standard hydrogen electrode (SHE)] and a remarkably higher capacity [3860 mAh g^{-1} (Li°) vs. 372 mAh g^{-1} (graphite)].[9-10] Hence, moving from liquid to full solid battery is essential for enhancing the inherent safety and energy density of rechargeable batteries. Solid polymer electrolytes (SPEs), which simply comprise a lithium salt and an elastic polymer matrix, are solid-state Li-ion conductors with excellent structural conformability, processability, and cost-effectiveness.[11-14] Since the early findings of the ionic transport behaviour in salt/poly(ethylene oxide) (PEO) complexes by Wright et al.[15] and the perceptive suggestions of their use in solid-state batteries (SSBs) by Armand in the 1970s,[16] SPEs have been long deemed as a promising solution to safe and high-performance rechargeable batteries and their technological effectiveness has been testified by the successful implementation of lithium metal polymer (LMP) batteries as power sources for commercial EVs (Bluecar® and Bluebus®) by Bollore group.[17]

Though SPEs are generally less reactive towards Li° compared to LEs, notorious "dead Li°" and "dendritic Li°" have also been observed in LMP batteries, accounting for the low cycling efficiency and abrupt cell failure.[18-19] The regulation of electrolyte recipes including the polymer matrix, salt, and electrolyte additives has proven to be effective. For example, incorporating rigid polystyrene (PS) blocks in PEO[20-21] or using porous and

high modulus polyimide (PI) substrates[18] could enhance the mechanical strength of SPEs, thereby suppressing the growth of dendritic Li°. Adding inorganic fillers, in particular, nano-sized particles[22] or well-aligned nanowires[23-24] could largely promote the Li-ion transport in electrolyte bulk and decrease the resistance of Li° electrode/SPE interphase, leading to an improved cycle life of the Li° electrode. Affixing the salt anion to a polymer or inorganic particle restricts the mobility of anionic species and avoids the concentration gradient appearing during the charge/discharge process, preventing the anion depletion at the vicinity of Li° electrode and the formation of dendritic Li°. Nevertheless, long-term cycling of Li° by modifying single electrolyte component, being of prime importance to understand the intertwined chemistry behind cell performance, has yet to be demonstrated.

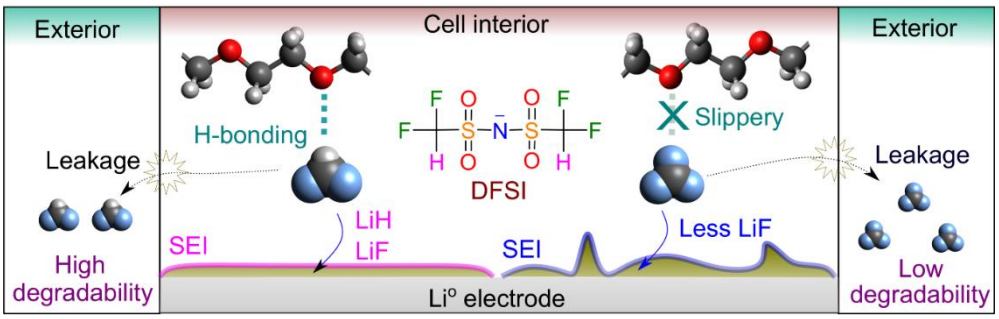

Figure 3.1. Comparison between the chemistry of CF_2H- and CF_3-containing compounds inside and outside a lithium metal cell. The light grey, grey, red, and light blue balls represent H, C, O, and F atoms, respectively. Reproduced with permission from Ref. [25].

The bis(trifluoromethanesulfonyl)imide anion {$[N(SO_2CF_3)_2]^-$, $TFSI^-$} was firstly brought into SPEs by Armand et al.[26] in 1986 and soon became

the most popular anion during the past 35 years in light of its intrinsic flexibility and low binding energy attributed to strong delocalization of the negative charge via the sulfonimide center and electron-withdrawing trifluoromethyl (—CF_3) group. $TFSI^-$ has then been widely used as the anionic component of alkali metal salts and ionic liquids. Recently, we demonstrated that replacing $TFSI^-$ with a hydrogen-containing anion, (difluoromethanesulfonyl)-(trifluoromethanesulfonyl)imide {$[N(SO_2CF_2H)(SO_2CF_3)]^-$, $DFTFSI^-$} anion, could sufficiently improve the Li-ion conductivity (σ_{Li^+}) of the classic PEO-based SPEs via hydrogen bonding interaction with the backbone and the interfacial stability of Li° electrode/SPE due to the formation of solid-electrolyte-interphase (SEI) building species (e.g., LiF, LiH, see **Figure 3.1**), enabling a prolonged cycling of solid-state lithium sulfur cells.[27] However, CF_3-containing substances are known to be resistive towards chemical and biochemical degradation.[28-29] For instance, Neumann et al.[28] observed a negligible concentration loss of LiTFSI in a biologically active inoculum over 58 days. This raises considerable risks to environment and human health once the salts or their decomposition products leak out of the battery pack or are poorly disposed of. However, in addition to the aforementioned advantageous electrochemical properties of —CF_2H vs. —CF_3 group, the de-fluorinated —CF_2H moieties generally possess better chemical and biochemical degradability.[30] Hence, we herein propose a CF_3-free anion, bis(difluoromethanesulfonyl)imide {$[N(SO_2CF_2H)_2]^-$, $DFSI^-$, **Figure 3.1**} as an environmentally benign and SEI-favourable anion for high-performance solid-state lithium metal batteries (SSLMBs). With a wide palette of characterization techniques, the fundamental chemical, physical, and

electrochemical properties of the neat salt and LiDFSI/PEO SPEs are examined and intensively discussed, in hope of shedding light on the peculiar properties of the DFSI-based electrolyte such higher Li-ion conductivity, largely enhanced stability against Li° electrode, and better cell performance of LMP batteries.

3.2. Experimental

3.2.1 Materials

Potassium hydroxide (KOH, Scharlab), poly(ethylene oxide) (PEO, M_w = 5 × 10^6 g mol^{-1}, Sigma-Aldrich), propylene carbonate (anhydrous, 99.7%, Sigma-Aldrich), *tert*-butyl methyl ether (TBME, anhydrous, 99.8%, Sigma-Aldrich), deuterium oxide (D_2O, Eurisotop, 99.9% D) and deuterated acetone (acetone-d_6, Eurisotop, 99.8% D) were used as purchased. Lithium perchlorate ($LiClO_4$, Sigma-Aldrich), lithium hydroxide (LiOH, Sigma-Aldrich), and lithium bis(trifluoromethanesulfonyl)imide (LiTFSI, battery grade, Sigma-Aldrich) were dried before use. Difluoromethanesulfonamide ($CF_2HSO_2NH_2$) and difluoromethanesulfonyl chloride (CF_2HSO_2Cl) were generous gifts from Solvay.

3.2.2 Theoretical approaches

The Fritz Haber Institute *ab* initio molecular simulations (FHI-aims) software[31-32] was used for DFT calculations. The Becke's three parameters (B3) exchange functional together with the Lee–Yang–Parr (LYP) nonlocal correlation functional (B3LYP)[33-34] was adopted with the "tier2" standard basis set in the FHI-aims code. The optimized geometries of $DFSI^-$ and $TFSI^-$ were taken from our previous calculations.[35] The highest occupied

molecular orbital (HOMO) and the lowest unoccupied molecular orbital (LUMO) obtained from frontier molecular orbital theory for both anions and their reduced form were computed by FHI-aims and visualized by VESTA (visualization for electronic and structural analysis) software.[36] Molecular dynamic simulations were conducted on LiDFSI/PEO and LiTFSI/PEO systems using Gromacs.[37] The simulation box consisted of 40 PEO chains with 20 repeat EO units in each chain, and 40 LiDFSI or LiTFSI ion pairs. The initial configuration of these molecules box was generated randomly by Gromacs, using large simulation cubic box (6 nm × 6 nm × 6 nm) with a low density. The structure was then compressed at 10 K under hydrostatic pressure of 10 atm until reaching a value close to the experimental density (3.28 g cm^{-3}) and a box size of 3.99 nm × 3.99 nm × 3.99 nm for LiDFSI/PEO and 4.03 nm × 4.03 nm × 4.03 nm for LiTFSI/PEO. The motion equations were integrated in steps of 1fs using a leap-frog algorithm, together with a Berendsen thermostat and a Parrinello-Rahman barostat (relaxation times of 1.0 ps for both). Then the system was heated up gradually to 343 K and 1 atm at a rate of 5 K ps^{-1} (with relaxation times of 20.0 ps). The final structure was further equilibrated during 1 ns at the same temperature and pressure. The production simulation was carried out for 200 ns in the NVT ensemble to ensure that the system reached diffusion regime. The cutoffs for van der Waals force and the real space of Ewald summation were 10 Å. The fast smooth Particle-Mesh Ewald (PME) electrostatics method was used to treat Coulomb interaction in the periodic system. The energy potential of PEO, $TFSI^-$, $DFSI^-$, and Li^+ was described by the OPLS_AA force field.[38-44] The charges were obtained from DFT calculations of isolated ions with the electro-static potential (ESP) method, and a uniform

factor of 0.7 was applied to scale down all the atomic charges during the molecular dynamics simulation.

3.2.3. Structural characterization

(a) Nuclear magnetic resonance spectroscopy [NMR, Bruker 300 Ultrashield (300 MHz for ^{1}H, 75.5 MHz for ^{13}C, and 283 MHz for ^{19}F)] was used to characterize the chemical structure of synthetized salts. Chemical shifts (δ) are reported in ppm relative to residual solvent signals (acetone-d_6, 2.05 ppm for ^{1}H-NMR). (b) Raman spectra of samples were recorded with a Renishaw inVia confocal Raman spectrometer (serial number 16H981). Incident laser has wavelength of 532 nm and microscope configurations were typically used with a 50X/0.75 focusing objective. Standard procedures of the measurements described in our previous work were followed.[45]

3.2.4. Synthesis and characterization of the neat salt

Potassium difluoromethanesulfonamide (CF_2HSO_2NHK) was synthesized by equivalent reaction between KOH and $CF_2HSO_2NH_2$ in H_2O. To a solution of imidazole (27.2 g, 400 mmol) and CF_2HSO_2NHK (33.8 g, 200 mmol) in 150 mL acetonitrile, a solution of CF_2HSO_2Cl (30.1 g, 200 mmol) in 50 mL acetonitrile was added dropwise at 0 ºC and then heated at reflux temperature for 24 h. The precipitates were filtered off and the solvent in the liquid phase was removed using rotary evaporator. Bis(difluoromethanesulfonyl)imide acid {$H[N(SO_2CF_2H)_2]$, HDFSI} was easily obtained by the acidification of the above residue and subsequent extraction with TBME. Then, KOH (1 eq., 7.9 g, 140 mmol) was used to neutralize HDFSI in H_2O, and a yellowish solid was obtained after removal

of solvent under reduced pressure. Recrystallization of the crude from ethanol/toluene (1/1, vol/vol) gave potassium bis(difluoromethanesulfonyl)imide (KDFSI) as a white powder (19.0 g, yield: 34%).[1]H NMR (300 MHz, acetone-d_6, TMS, ppm): δ = 6.41 (t, J = 54.8 Hz, 1H). ^{19}F NMR (282 MHz, acetone-d_6, CCl_3F, ppm): δ = –125.63 (d, J = 53.4 Hz, 2F).

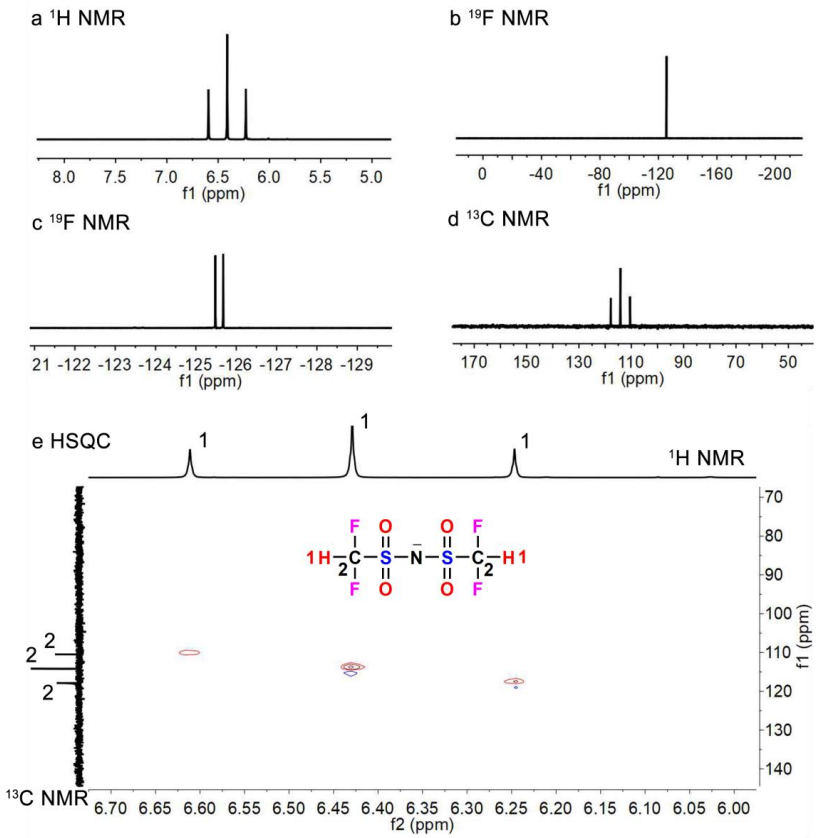

Figure. 3.2. NMR spectra of the as-prepared LiDFSI salt: (a) ^{1}H NMR, (b) ^{19}F NMR without decoupling, (c) ^{19}F NMR decoupling, (d) ^{13}C NMR, and (e) edited 2D correlation heteronuclear single quantum coherence spectroscopy (HSQC). Reproduced with permission from Ref. [25].

LiDFSI was prepared by the cation exchange of KDFSI (19.0 g, 67 mmol) with $LiClO_4$ (7.1 g, 67 mmol) in anhydrous acetonitrile as described in our previous work.[35] As a result, 11.8 g (yield: 70%) of LiDFSI as a white powder was obtained. ^{1}H NMR (300 MHz, acetone-d_6, TMS, ppm): δ = 6.41 (t, J = 54.7 Hz, 1H). ^{13}C NMR (75 MHz, acetone-d_6, TMS, ppm): δ = 115.05 (t, J = 277.2 Hz). ^{19}F NMR (282 MHz, acetone-d_6, CCl_3F, ppm): δ = –125.58 (d, J = 54.7 Hz, 2F). The NMR and Raman spectra of LiDFSI are shown respectively in **Figures 3.2** and **3.3**, the corresponding assignment of typical Raman peaks is shown in **Table 3.1**.

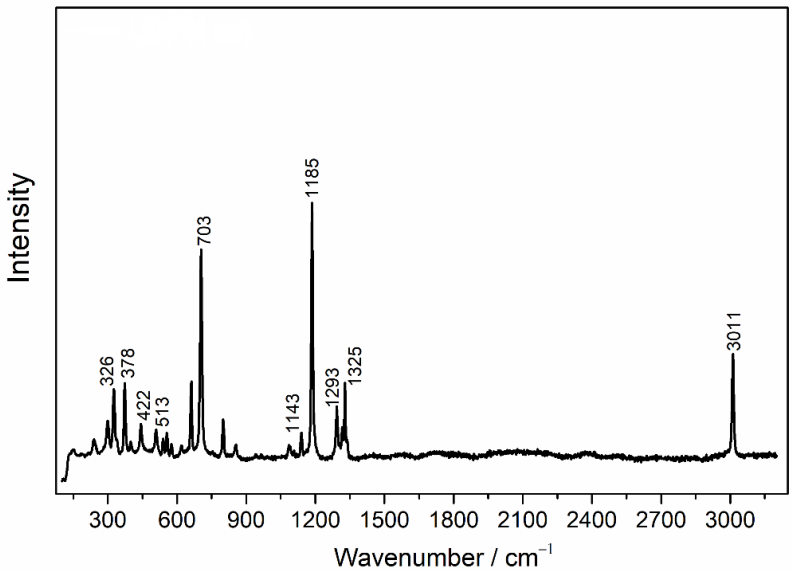

Figure 3.3. Raman spectrum of the LiDFSI salt. Reproduced with permission from Ref. [25].

3.2.5. Chemical degradability

The solutions of 0.02 M LiX (X = DFSI or TFSI) with or without 0.1 M LiOH were prepared in D_2O to screen the chemical degradability of the salts.

The hydrolysis evolution of the salts over time from 0 h to 30 days was monitored by NMR spectra. Chemical shifts (δ) are reported in ppm relative to deuterated solvent (e.g., D_2O, 4.80 ppm for ^{1}H-NMR).

Table 3.1. Assignment of typical peaks observed in Raman spectrum of the LiDFSI salt. Reproduced with permission from Ref. [25].

Raman shift / cm^{-1}	Assignment
326	CF_2 rocking vibration
378	SO_2 rocking vibration
422	SO_2 wagging vibration
513	SO_2 bending vibration
703	S–N–S bending vibration
1143	CF_2 anti-symmetrical stretching vibration
1185	CF_2 symmetrical stretching vibration
1293	SO_2 out-of-phase rocking vibration
1325	SO_2 in-phase rocking vibration
3011	C–H stretching vibration

3.2.6. Chemical reduction of lithium salts

The stability of salt anion towards chemical reduction was performed in an argon-filled glovebox. The experimental details are available in our previous work.[46] In brief, the naphthalene radical was prepared by reacting Li° with naphthalene in dry tetrahydrofuran (THF) solution. Afterwards, LiDFSI or LiTFSI was added to the naphthalene radical solution and the colour change was monitored.

3.3. Results and discussion

3.3.1 Hydrolysis of LiDFSI and LiTFSI

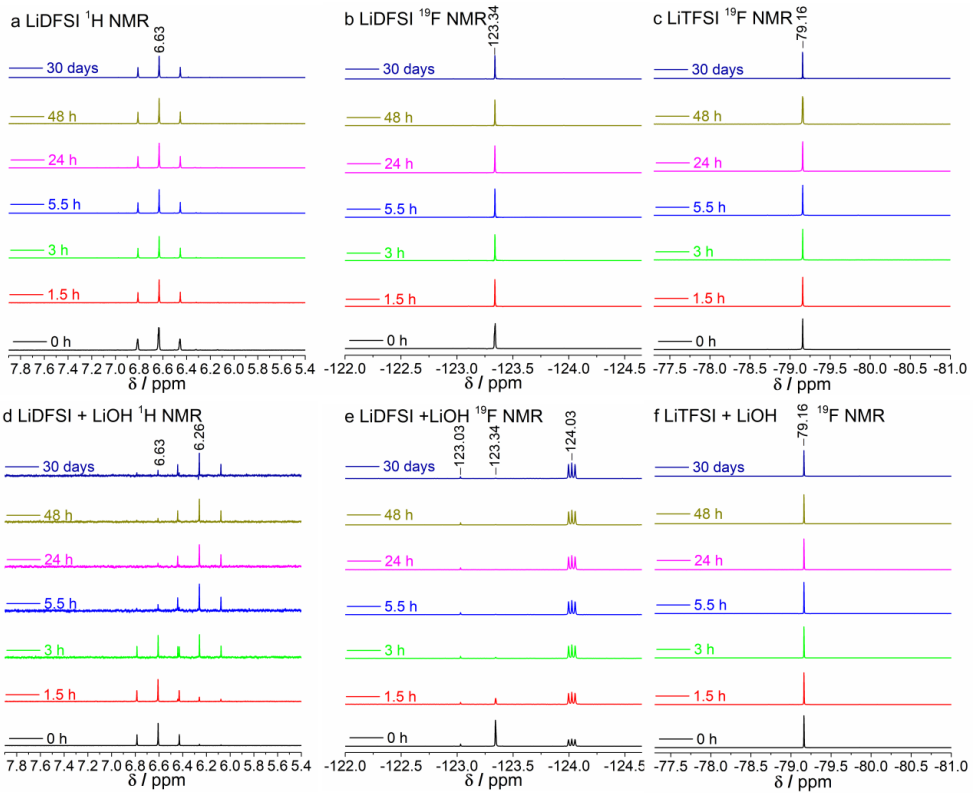

Figure 3.4. Hydrolysis tests of the lithium salts. (a) ^{1}H NMR and (b) ^{19}F NMR spectra of LiDFSI/D_2O, and (c) ^{19}F NMR spectra of LiTFSI/D_2O after different storage times under neutral condition. (d) ^{1}H NMR and (e) ^{19}F NMR spectra of LiDFSI/D_2O, and (f) ^{19}F NMR spectra of LiTFSI/D_2O after different storage times under basic condition. Reproduced with permission from Ref. [25].

The CF_3-free lithium salt LiDFSI is prepared via the cation exchange of the corresponding potassium salt [i.e., potassium bis(difluoro methanesulfonyl) imide, KDFSI] with a stoichiometric amount of lithium perchlorate ($LiClO_4$) in an argon-filled glovebox [see experimental section

for more details and nuclear magnetic resonance (NMR) (**Figure 3.2**) and Raman (**Figure 3.3**, **Table 3.1**) characterizations].

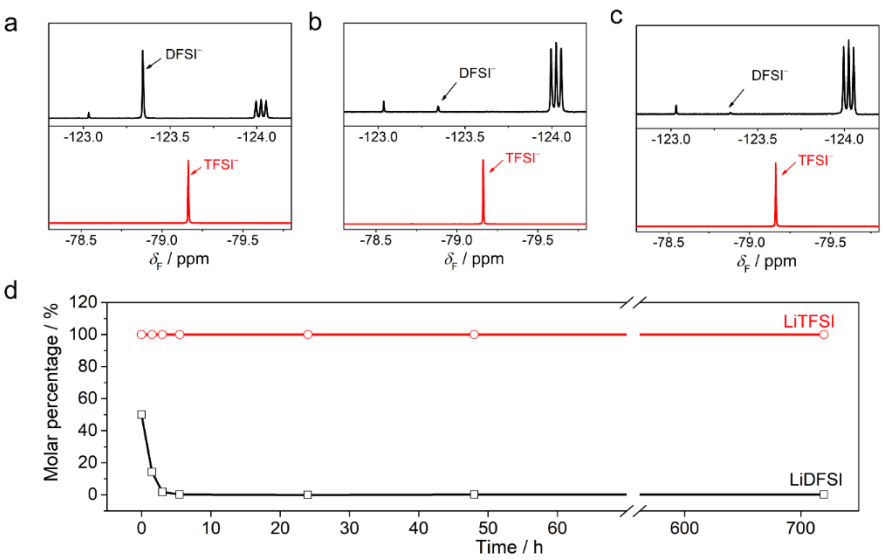

Figure 3.5. Hydrolysis of lithium salts under basic condition. (a-c) ^{19}F NMR spectra of LiDFSI/D_2O and LiTFSI/D_2O: (a) 0 h, (b) 3 h, and (c) 720 h. (d) Molar percentage of residual lithium salt vs. storage time. Reproduced with permission from Ref. [25].

To mimic chemical degradation of lithium salts when the electrolyte leaks out of the cells during thermal runaway, hydrolysis tests of LiDFSI and LiTFSI in aqueous solution under neutral and basic condition were performed. As seen in **Figure 3.4a** and **b**, under neutral condition, the LiDFSI-based solution shows only a triplet at ~6.63 ppm (CF_2H, $DFSI^-$) in ^{1}H NMR spectra and a singlet at −123.34 ppm (CF_2H, $DFSI^-$) in ^{19}F NMR spectra (H-decoupled), irrespective of the variation of storage time. Similarly, in **Figure 3.4c**, the ^{19}F NMR spectra of the LiTFSI-based solution retain the single peak at −79.16 ppm assigned to the —CF_3 moieties over 30 days.

These clearly indicate that LiDFSI and LiTFSI remain chemically stable in neutral aqueous solutions, which is beneficial for the electrolyte preparation, processing, and recycling.

Notably, a distinct difference between two salts occurs when adjusting the aqueous solution to a mild basic condition. In **Figure 3.4d**, ^{1}H NMR spectra of the newly prepared LiDFSI-based solution which was kept at pH = 13 (i.e., 0.1 M LiOH/D_2O) for less than 10 minutes shows a minor triplet at ~6.26 ppm in addition to the main peak assigned to the CF_2H moiety at ~6.63 ppm (CF_2*H*, $DFSI^-$). This foreign peak at ~6.26 ppm becomes more pronounced when extending the storage time to 1.5 h and finally predominates over the peak at ~6.63 ppm (i.e., CF_2*H* in $DFSI^-$) after 3 h of storage under basic condition, indicating the formation of other CF_2H-containing compounds (e.g., CF_2HSO_2Li, CF_2HSO_2NHLi) originated from the chemical decomposition of $DFSI^-$. More evidently, as seen in **Figure 3.5**, associated with the changes in ^{1}H NMR spectra, new peaks at −123.03 ppm and −124.03 ppm are observed in ^{19}F NMR spectra (**Figure 3.5a-c**, **Figure 3.4e**), and the peak at −123.34 ppm (CF_2H, $DFSI^-$) fully disappears after 3 h. The triplet at −124.03 ppm might be associated with the deprotonation of CF_2H moiety via the strong base OH^-. In **Figure 3.5d**, the molar percentage of LiDFSI dramatically decreases to nearly zero after few hours, suggesting that LiDFSI could be easily hydrolyzed under a mild basic condition. In stark contrast, LiTFSI remains intact under the same condition and no extra peaks are observable in ^{19}F NMR spectra (see **Figure 3.4f**). All these experimental proofs reinforce our central hypothesis that the LiDFSI is significantly more degradable compared to LiTFSI, which corroborates well the previous studies on the degradation of CF_3-based salts or ionic liquids.[28]

3.3.2 Physical and electrochemical properties of SPEs

In the first place, the fundamental physical and electrochemical properties of LiX/PEO (X = DFSI or TFSI) are characterized in terms of surface morphology, phase identification and thermal transition, and ion transport behaviour. At a molar ratio of ethylene oxide/Li = 20, the electrolytes of LiDFSI/PEO and LiTFSI/PEO obtained via solvent-casting/hot-pressing techniques are self-standing and ductile membranes (ca. 70 μm in thickness, as shown in **Figure 3.6a** and **b**). However, a polymer electrolyte with sticky property was obtained when increased the salt concentration to $EO/Li^+ = 8$, see **Figure 3.6e**.

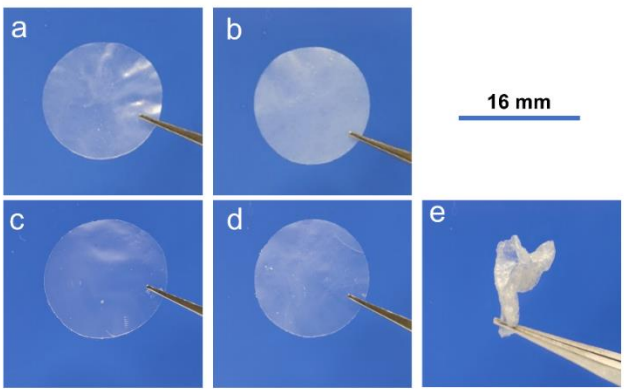

Figure 3.6. The digital camera images (scale bar: 16 mm) of LiDFSI/PEO and LiTFSI/PEO electrolytes. (a) LiDFSI/PEO ($EO/Li^+ = 20$), (b) LiTFSI/PEO ($EO/Li^+ = 20$), (c) LiDFSI/PEO ($EO/Li^+ = 64$), (d) LiDFSI/PEO ($EO/Li^+ = 32$) and (e) LiDFSI/PEO ($EO/Li^+ = 8$). Reproduced with permission from Ref. [25].

In addition, scanning electron microscopy (SEM) and optical microscope images show that all of the SPE membranes are uniform and homogenous at the micro-scale (see **Figure 3.7**), indicating the absence of

salt precipitation and the good solubility of the partially H-substituted imide salt. When shifting from micro to nano-scale, atomic force microscopy (AFM) phase images (**Figure 3.8a** and **b**) and topography images (**Figure 3.8c** and **d**) show that the outermost surface of both membranes are sculptured with fiber-like textures, which belong to the crystalline PEO phase in the electrolytes.[47] It is interesting to note that the average widths of those 'fibers' are thinner for LiDFSI/PEO than those for LiTFSI/PEO (e.g., ~100 nm vs. ~130 nm; **Figure 3.9**), suggesting the presence of larger crystal size in the latter electrolyte.

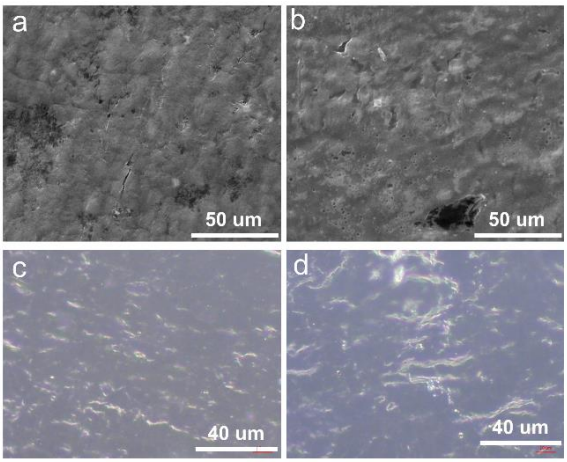

Figure 3.7. Scanning electron microscopy (SEM) and optical microscope images of the (a,c) LiDFSI/PEO (EO/Li^+ = 20), and (b,d) LiTFSI/PEO (EO/Li^+ = 20) electrolytes. (a,b) SEM images and (c,d) optical microscope images. Reproduced with permission from Ref. [25].

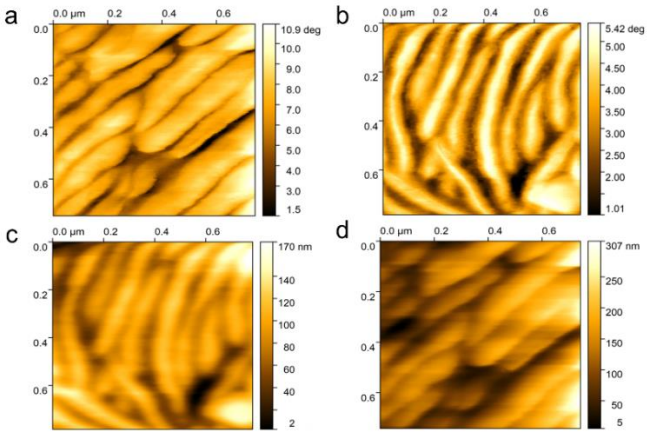

Figure 3.8. Atomic force microscopy (AFM) images of the (a,c) LiDFSI/PEO and (b,d) LiTFSI/PEO electrolytes. (a,b) phase images and (c,d) topography images. (EO/Li^+ = 20). Reproduced with permission from Ref. [25].

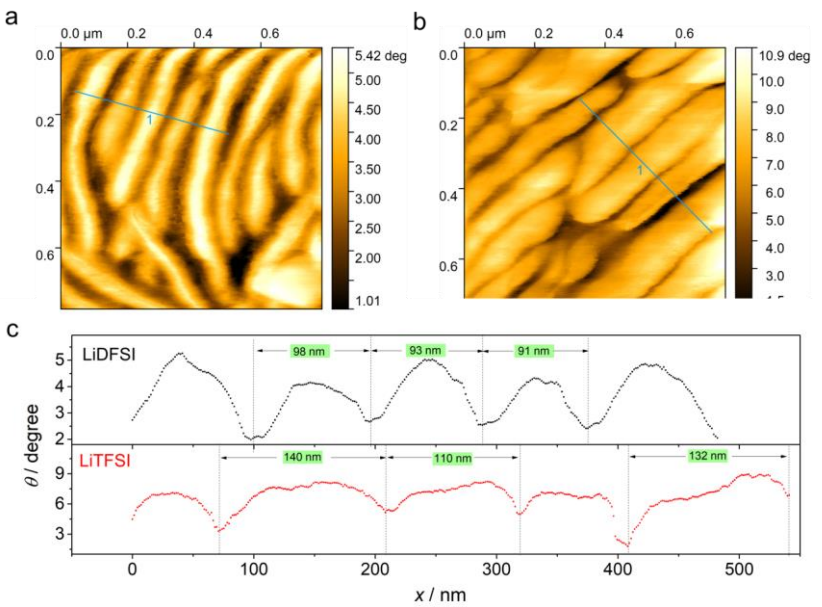

Figure 3.9. AFM phase images of the (a) LiDFSI/PEO and (b) LiTFSI/PEO electrolytes, as well as (c) the dependence of phase on a given axis indicated by cyan lines. EO/Li^+ = 20. Reproduced with permission from Ref. [25].

The neat salt LiDFSI shows significantly lower melting point (T_m) and decomposition temperature (T_d) as compared to LiTFSI (**Figure 3.10**), e.g., T_m = 117 °C (LiDFSI) vs. T_m = 233 °C (LiTFSI),[48] and T_d = 273 °C (LiDFSI) vs. T_d = 384 °C (LiTFSI),[48] indicating that the partial replacement of fluorine atoms in $TFSI^-$ with hydrogen atoms increases the asymmetry of the sulfonimide and thereby decreases the lattice energy, but, meanwhile, the newly introduced C—H bond tends to be more thermally fragile (i.e., bond energy: 431 kJ mol^{-1} for C—H vs. 483 kJ mol^{-1} for C—F). However, after dissolving LiDFSI in PEO, the T_d value increases substantially from 273 °C to 327 °C (see **Figure 3.10c** for TGA traces) due to the solvation and stabilization of hard Lewis acid lithium cation (Li^+) in the presence of electron-donating EO group though slightly lower than that of the LiTFSI-based one (T_d = 381 °C). Both electrolytes show T_d values higher than 300 °C, which are well acceptable for all LMP batteries since the lithium anode melts at 180 °C.[49] Industrial preparation of membranes by extrusion, used with LiTFSI by Blue Solutions®, remains possible, what provides a major technological advantage.

At a standard EO/Li^+ molar ratio of 20, the glass transition temperature (T_g) of the LiDFSI-based SPE is slightly higher than that of the LiTFSI-based one [i.e., T_g = −27 °C (LiDFSI/PEO) vs. T_g = −35 °C (LiTFSI/PEO), see **Figure 3.11a** for differential scanning calorimeter (DSC) traces], attributed to stronger inter/intra-molecular interactions via the hydrogen bonds formed between acidic H atoms of the anion and Lewis base O atoms of either salt or polymer matrix. However, the melting transitions and the crystallinities (χ_c) of both electrolytes are quite comparable and lower than other PEO electrolytes using small inorganic anions (e.g., $LiPF_6$).[50] This

implies that $DFSI^-$ and $TFSI^-$ possess similar structural flexibility and sulfonimide anions, in general, are better plasticizers for PEO. The semi-crystalline nature of LiDFSI/PEO and LiTFSI/PEO are further characterized by X-ray diffraction (XRD, see **Figure 3.11b**), where two diffraction peaks at 2θ = 19.3° and 23.7° assigned to the crystalline PEO phase are observed. As seen in **Figure 3.13a** the total ionic conductivity (σ_{total}) of both electrolytes increases substantially at approximately 60 °C upon the heating scan, testifying the occurrence of melting transitions of semi-crystalline PEO phases.

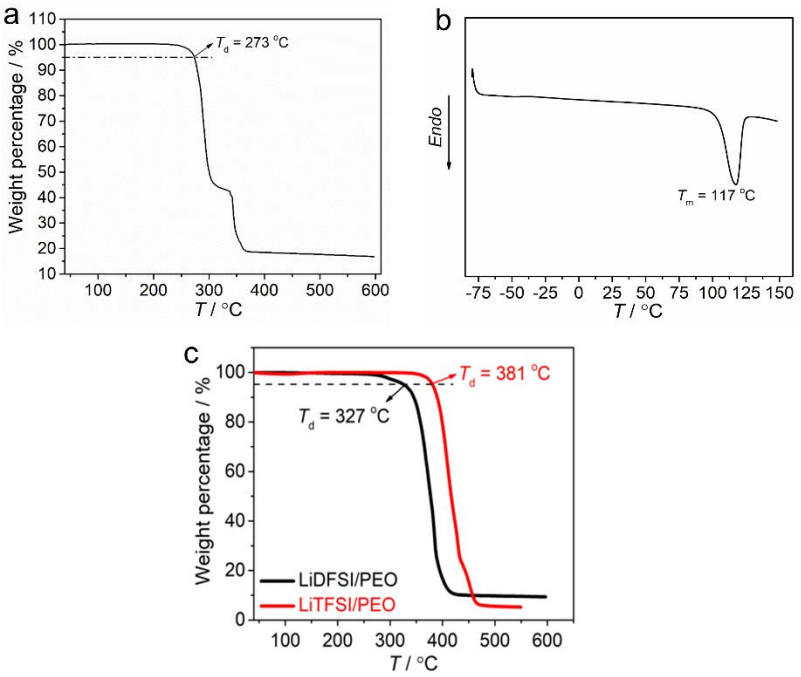

Figure 3.10. (a) Thermogravimetric analysis (TGA) and (b) differential scanning calorimetry analysis (DSC) of the neat LiDFSI salt. (c) TGA of the PEO-based SPEs. Reproduced with permission from Ref. [25].

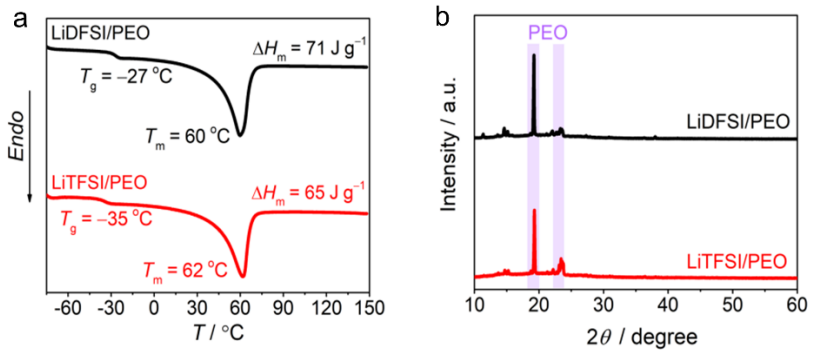

Figure 3.11. (a) DSC and (b) X-Ray diffraction (XRD) of the PEO-based SPEs. Reproduced with permission from Ref. [25].

Table 3.2. Characterization data for the phase behaviours of the LiX/PEO (X = DFSI or TFSI) electrolytes. Reproduced with permission from Ref. [25].

Samples	T_g [a] / °C	T_m [b] / °C	ΔH_m [c] / J g^{-1}	χ_c [d] / %
LiDFSI/PEO (64)	−38	70	115	64
LiDFSI/PEO (32)	−33	66	96	58
LiDFSI/PEO (20)	−27	60	71	47
LiDFSI/PEO (8)	−32	69	53	46
LiTFSI/PEO (20)	−35	62	65	44

[a] Glass transition temperature (°C); [b] melting point (°C); [c] enthalpy of melting (J g^{-1}); [d] the crystallinity of the polymer electrolytes is calculated by ($\Delta H_m/\Delta H_{PEO} f_{PEO}$) × 100%, where ΔH_m is the melting enthalpy of the electrolytes, and ΔH_{PEO} is the value of 196.4 J g^{-1} for PEO perfect crystals reported in literature[51] for the melting enthalpy of 100% crystalline PEO, and f_{PEO} is the PEO weight fraction of the electrolyte samples.

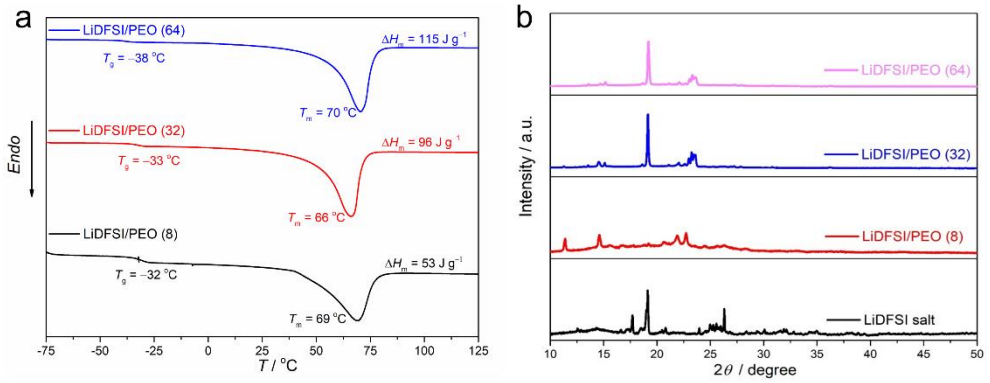

Figure 3.12. (a) DSC and (b) XRD of these two PEO-based SPEs at different ratios. Reproduced with permission from Ref. [25].

Increasing the salt concentration from EO/Li = 64 to EO/Li = 20 for LiDFSI/PEO, the T_g value progressively increases from −38 °C to −27 °C and the χ_c values decrease from 64% to 47%; however, further increase in salt concentration results in marginal changes in both T_g and χ_c, as seen in **Table 3.2** and **Figure 3.12a**. The XRD pattern of LiDFSI/PEO (EO/Li = 8) displays multiple new diffraction peaks originated neither from un-dissolved LiDFSI nor crystalline PEO phase (**Figure 3.12b**), which might indicate the formation of LiDFSI-PEO complexes [e.g., $P(EO)_6$LiDFSI]. As a result of the trade-off between the charge carriers number and their ionic diffusivity, the LiDFSI-based SPEs show the highest σ_{total} at the ratio of EO/Li = 20 (**Figure 3.13b**).[35, 52]

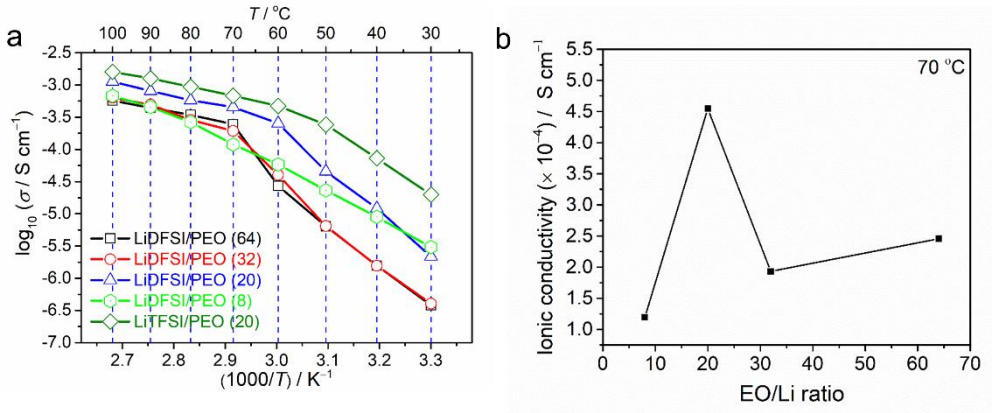

Figure 3.13. (a) Arrhenius plots of ionic conductivity of the electrolytes. (b) Concentration dependence of total ionic conductivity for the LiDFSI/PEO electrolytes at 70 °C. Reproduced with permission from Ref. [25].

Throughout the measured temperature range, the σ_{total} values of LiDFSI/PEO are lower than that of LiTFSI/PEO (**Figure 3.13a**), due to slightly lower segmental mobility in the former electrolyte, as indicated by its higher T_g value observed in **Figure 3.11a**. However, the Li-ion transference number (T_{Li}^+) of LiDFSI/PEO is 0.39 (EO/Li = 20 at 70 °C), which is higher than that of the LiTFSI-based one (i.e., T_{Li}^+ = 0.20; **Figure 3.14** and **Table 3.3**), suggesting that the hydrogen-bond interactions stemming from the selective replacement of F atoms with H atoms in $TFSI^-$ could effectively restrict the mobility of anionic species. Consequently, the LiDFSI-based SPE exhibits a slightly higher Li-ion conductivity ($\sigma_{Li}^+ = \sigma_{total} \times T_{Li}^+$) as compared to that of the LiTFSI-based one (i.e., 1.8×10^{-4} S cm^{-1} vs. 1.4×10^{-4} S cm^{-1} at 70 °C, EO/Li = 20; **Table 3.4**). The higher Li-ion conductivity reduces the concentration gradient and the internal cell polarization, and thus enhancing the cyclability of LMP batteries.[35]

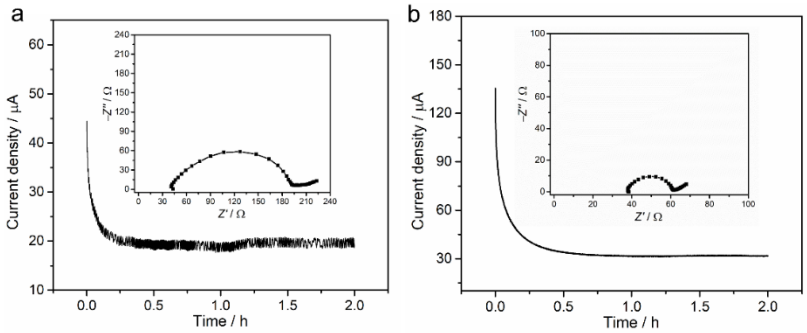

Figure 3.14. Polarization profiles and impedance before polarization (inset) of the Li° symmetric cells using the (a) LiDFSI/PEO (20) and (b) LiTFSI/PEO (20) electrolytes at 70 °C. Reproduced with permission from Ref. [25].

Table 3.3. Calculated values of lithium-ion transference numbers (T_{Li}^+) of the LiDFSI- and LiTFSI-based SPEs at 70 °C. Reproduced with permission from Ref. [25].

Samples	I_{ss} [a] / μA	R_{cell} [b] / Ω	ΔV [c] / mV	T_{Li}^+ [d]
LiDFSI/PEO (20)	20	196	10	0.39
LiTFSI/PEO (20)	32	63	10	0.20

[a] Steady-state current obtained from the DC polarization; [b] total resistances of Li° symmetric cell; [c] the DC voltage subjected to the polarization; [d] calculated by $T_{Li}^+ = R_{cell} / (\Delta V / I_{ss})$.[53]

Table 3.4. Calculated Li-ion conductivities of the LiDFSI- and LiTFSI-based SPEs at 70 °C. Reproduced with permission from Ref. [25].

Samples	σ_{total} [a] / S cm^{-1}	T_{Li}^+	σ_{Li}^+ [b] / S cm^{-1}
LiDFSI/PEO (20)	4.6×10^{-4}	0.39	1.8×10^{-4}
LiTFSI/PEO (20)	6.8×10^{-4}	0.20	1.4×10^{-4}

[a] Total ionic conductivity; [b] Li-ion conductivity calculated by $\sigma_{Li}^+ = \sigma_{total} \times T_{Li}^+$.

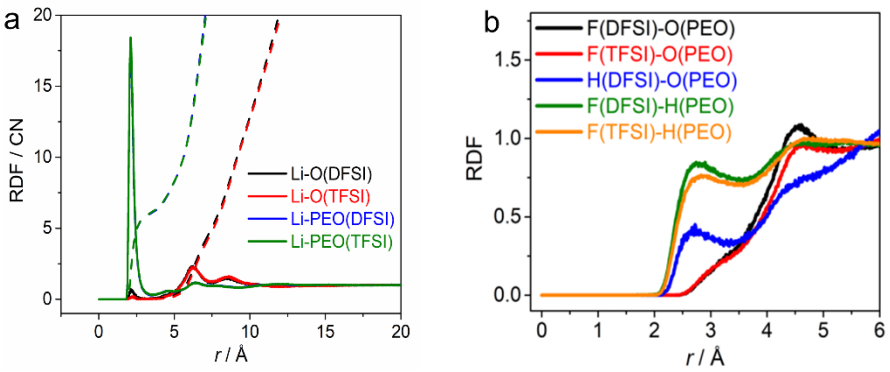

Figure 3.15. (a) Radial distribution function (RDF, solid line) between Li and O from either anions or PEO, as well as their coordination number (CN, dotted line). (b) RDF between H and O from either anions or PEO. Reproduced with permission from Ref. [25].

To shed further light on the ionic transport differences between the LiDFSI- and LiTFSI-based SPEs, molecular dynamic (MD) simulations were carried out. As depicted in the radial distribution function (RDF) and distance-dependent coordination number (CN) in **Figure 3.15a**, the Li^+ cations closely interact with oxygen atoms of PEO as usually observed in PEO-based SPEs.[54-55] As shown in **Figure 3.15b**, both $DFSI^-$ and $TFSI^-$ interact with the hydrogen atoms of PEO through the fluorine atoms (RDF peak within the range 2–3 Å), yet the average distance in the case of $DFSI^-$ is slightly shorter (i.e., stronger interaction) than in $TFSI^-$. More importantly, when spotlighting on the oxygen atoms of PEO an additional RDF peak around 2–3 Å appears in the case of $DFSI^-$, which clearly indicates the formation of hydrogen-bonding between $DFSI^-$ and oxygens in PEO. This additional attractive interaction is directly reflected in the mean square displacement (MSD) shown in **Figure 3.16**. MSD is a proxy of ion motion

and reveals that the mobility of F-containing species (i.e., anions) drops remarkably when replacing —CF_3 with —CF_2H, indicating a lower diffusivity of $DFSI^-$ than that of $TFSI^-$. Yet, the mobility decrease of Li species tends to be less pronounced. These results further reinforce the conclusion that hydrogen-bonding interaction between $DFSI^-$ and PEO-based SPEs benefits the selective transport of Li^+ cations by hindering the anions motion.

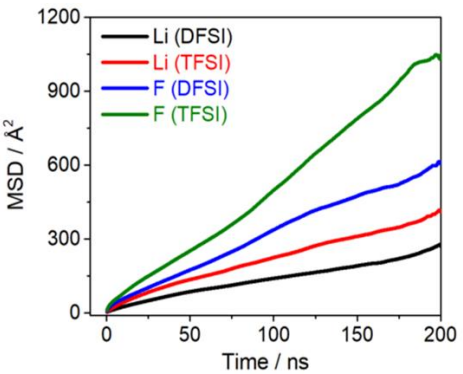

Figure 3.16. Mean-square displacement (MSD) of Li^+ and F atoms in anions zoomed in the first 80 ns of the whole simulation. Reproduced with permission from Ref. [25].

In addition, to access the intrinsic anodic stability of the H-containing anion, a diluted solution of 0.1 M LiDFSI in propylene carbonate (PC, known to be electrochemically stable up to ca. 6 V vs. Li/Li^+)[4] was investigated by linear sweep voltammetry (LSV) using Pt as a working electrode, and the LiTFSI/PC solution was analyzed under the same condition for comparison (**Figure 3.17a**). The LiDFSI-based electrolyte exhibits a lower anodic stability than that of the LiTFSI-based one [i.e., 5.4 V (LiDFSI/PC) vs. 5.9 V (LiTFSI/PC) vs. Li/Li^+], ascribed to the

replacement of two strong electron-withdrawing F atoms with the electron-donating H atoms.[35] Yet such stability above 5 V would be amply enough for pairing the LiDFSI-based liquid solution with most of the reported electrode materials. Shifting from the PC-based liquid electrolyte to the PEO-based SPEs, the oxidation currents assigned to the decomposition of PEO at ca. 4.0 V vs. Li/Li^+ are observed prior to the breakdown of both anions (**Figure 3.17b**); *a fortiori*, both SPEs are acceptable for < 4 V LMP batteries such as $LiFePO_4$ or sulfur cathode materials.

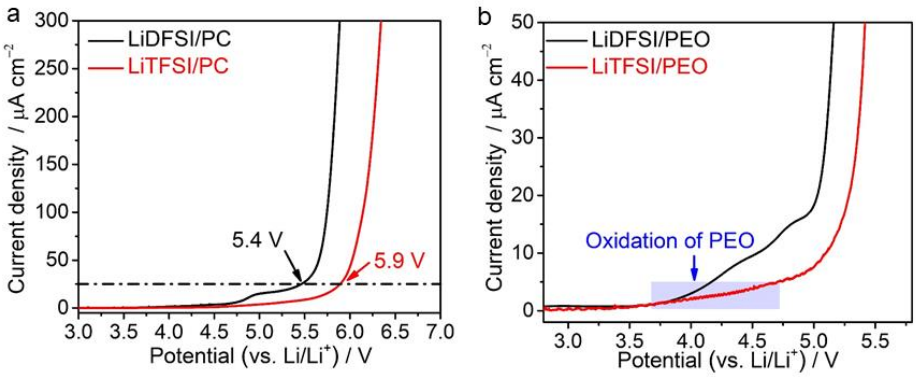

Figure 3.17. (a) Linear sweep voltammetry (LSV) profiles of the 0.1 M LiX/PC (X = DFSI or TFSI) solutions measured on a Pt electrode at room temperature. (b) LSV profiles of the LiX/PEO (X = DFSI or TFSI, EO/Li^+ = 20) SPEs measured on stainless steel (SS) electrode at 70 °C. Reproduced with permission from Ref. [25].

3.3.3. Interfacial compatibility with Li° electrode

Dendrite-free and highly reversible cycling of Li° electrode, being largely determined by the quality of Li° electrode/SPE interphase layer, is a prerequisite for attaining LMP batteries with prolonged cycle life and good rate capability. **Figure 3.18a** shows the cyclic voltammetry (CV) profiles

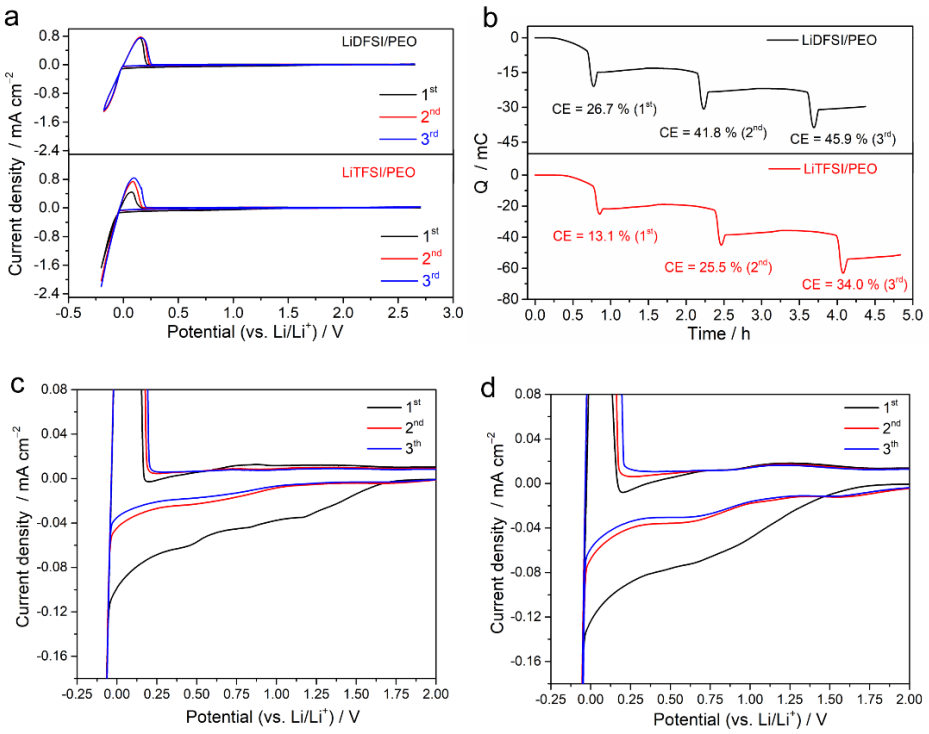

Figure 3.18. (a) Cyclic voltammetry (CV) and (b) Coulombic efficiencies (CEs) of LiX/PEO (X= DFSI or TFSI) based cells measured on Cu electrode using a scan rate of 1 mV s^{-1} at 70 °C. Zoomed-in CV plots of different electrolytes: (c) LiDFSI/PEO, and (d) LiTFSI/PEO. Reproduced with permission from Ref. [25].

measured on Cu electrode using LiDFSI/PEO and LiTFSI/PEO. In the potential range of −0.5 to 0.5 V vs. Li/Li^+, characteristic redox peaks of Li deposition and dissolution are observed. Interestingly, the cumulative Coulombic charges of Li deposition processes are closer to those of Li dissolution ones for the LiDFSI-based system (**Figure 3.18b**), suggesting higher Coulombic efficiencies (CEs) and better electrochemical reversibility of Li redox reaction in such electrolyte. Taking a closer look on the CV

profiles (**Figure 3.18c** and **d**), one may note that the LiDFSI-based electrolyte shows minor reductive currents at ca. 1.6–2.0 V at the first downwards scan before a second reduction step at ca. 0.5 V (vs. Li/Li$^+$). This first event may be related to the reduction of DFSI$^-$ due to the presence of acidic C—H bonds in the anionic structure.

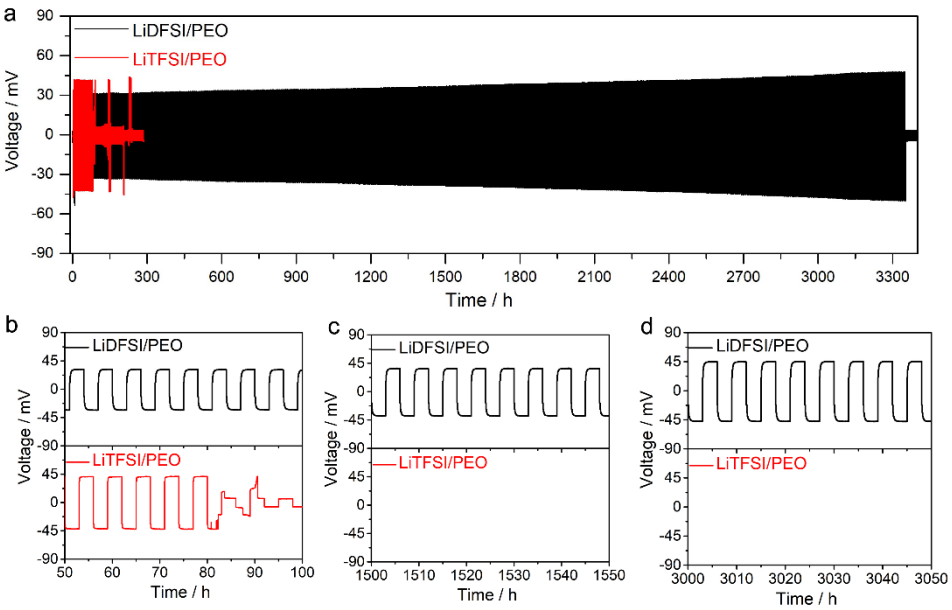

Figure 3.19. (a) Galvanostatic cycling of Li° anode in PEO-based electrolytes at 70 °C (current density: 0.1 mA cm^{-2}; duration of half-cycle: 3 h). (b-d) Zoomed-in plots of the Li° symmetric cells in the range of (b) 50−100 h, (c) 1500−1550 h, and (d) 3000−3050 h. Reproduced with permission from Ref. [25].

The interfacial stabilities with Li° electrode were characterized by galvanostatic cycling of Li° symmetric cells using both PEO-based SPEs (**Figure 3.19a**) and 1,2-dimethoxyethane (DME)-based LEs (**Figure 3.20**). Despite the difference in molecular weight, DME and PEO are chemical

analogues with very similar coordinating/solvating abilities to Li^+ cations; while DME-based LEs allow the reliable recovery of cycled Li° electrode for post-mortem analyses [e.g., SEM, Raman, X-ray photoelectron spectroscopy (XPS)] which are particularly necessary for unrevealing the alluring anion chemistry on the interphases of Li° electrode.

Table 3.5. Performance of state-of-the-art of the SPE-based Li° symmetric cells. Reproduced with permission from Ref. [25].

Entry	Electrolyte [a]	Current density / mA cm^{-2}	Areal capacity [b] / mAh cm^{-2}	C_d [c] / mAh cm^{-2}	Overpotential / mV	Ref.
1	P(SSPSILi-*alt*-MA)/PEO	0.01	0.04	12	100	56
2	LiFTFSI/PEO	0.1	0.2	20	30	57
3	LiEFA/PEO	0.1	0.3	25	30	58
4	$LiClO_4$/PVA-UPy-PEG	0.05	0.15	25	200	59
5	LiTFPFB/P(PO-*co*-EM)	0.1	0.05	50	43	60
6	LiTFSI/POSS/P(EO-*co*-PO)	0.1	0.1	50	250	61
7	LiTFSI/GP	0.1	0.1	60	40	62
8	LiDFOB/PEO/cPTFBC	0.2	0.2	60	90	63
9	*hb*PS-*star*-PPEGMA	0.05	0.05	70	100	64
10	LiTFSI/PEO	0.2	0.2	3	160	65
11	LiTFSI/$CsClO_4$/PEO	0.2	0.2	100	185	65
12	LiTFSI/PEO	0.2	0.2	10	138	66
13	LiFSI/FPE/PEO	0.1	0.2	100	40	67
14	LiTFSI/BCP	0.2	0.4	140	120	49
15	LiFSI/PVDF	0.1	0.05	200	50	68
16	LiTFSI/PEO	0.1	0.1	0.5	50	69
17	**LiDFSI/PEO**	**0.1**	**0.3**	**330**	**48**	**This work**

[a] The abbreviations are listed as below: BCP (Jeffamine-based block copolymer), cPTFBC [poly(2,2,3,3-tetrafluoro butyl carbonate) with cyano ends], FPE

(Jeffamine®-based flowable polymer electrolyte), GP (grafted polyrotaxanes), *hb*PS (hyperbranched polystyrene), LiDFSI [lithium bis(difluoromethanesulfonyl)imide], LiEFA [lithium (trifluoromethanesulfonyl)(*N*-bis(methoxyethyl)sulfonyl)imide], LiDFOB [lithium difluoro(oxalato)borate], LiFSI [lithium bis(fluorosulfonyl)imide], LiFTFSI [lithium (fluorosulfonyl)(trifluoromethanesulfonyl)imide], LiTFPFB [lithium trifluoro(perfluoro-*tert*-butyloxyl)borate], LiTFSI [lithium bis(trifluoromethanesulfonyl)imide], PEO [poly(ethylene oxide)], PEG [poly(ethylene glycol)], P(EO-*co*-PO) [poly(ethylene oxide-*co*-polypropylene oxide)], POSS (polyhedral oligomeric silsesquioxane), PPEGMA {poly[poly(ethylene glycol) methyl ether methacrylate]}, P(PO-*co*-EM) {poly[propylene oxide-*co*-2-(2-methoxyethoxy)ethyl]}, PVA [poly(vinyl alcohol)], PVDF [poly(vinylidene difluoride)], UPy (ureidopyrimidinone), P(SSPSILi-*alt*-MA) {poly[lithium 4-styrenesulfonyl(phenylsulfonyl)imide-*alt*-maleic anhydride]}; [b] areal capacity of half cycle; [c] the reported charge that had passed through the cell.

As seen in **Figure 3.19a**, the Li° symmetric cell using LiTFSI/PEO encounters internal short-circuit after only ca. 100 h (**Figure 3.19b**), being close to those reported in literature (see Entry 10[65] and Entry 12[66] in **Table 3.5**). In sharp contrast, the LiDFSI/PEO-based one significantly improves the cycle life, sustaining more than 3300 h and simultaneously allowing the passage of 330 mAh cm^{-2} of charges before encountering an internal short-circuit (see **Figure 3.19b-d** for the zoomed-in plots). Indeed, the CF_3-free anion, $DFSI^-$, outperforms most of the reported anions in terms of cycle life of Li° symmetric cells (**Table 3.5**). In the liquid configuration, the cells with LiDFSI/DME present a stable and lower voltage profile (45 mV) for more than 4200 h; however, the LiTFSI-based cell shows erratic voltage oscillations only after 200 h (**Figure 3.20a-c**) and a drastically increased overvoltage (e.g., 109 mV at 700 h, **Figure 3.20d**). In addition, it can be

found from **Figure 3.21** that the interfacial resistance (R_i) of the LiDFSI-based cell is much lower than that of the LiTFSI-based one [e.g., R_i = 60 Ω cm^2 (LiDFSI) vs. R_i = 457 Ω cm^2 (LiTFSI)] after galvanostatic cycling as shown in **Figure 19a**. The markedly improved cyclability and reduced overvoltage for the LiDFSI-based liquid and solid cells strongly suggest the formation of more stable and conductive SEI layers on the Li° electrodes.

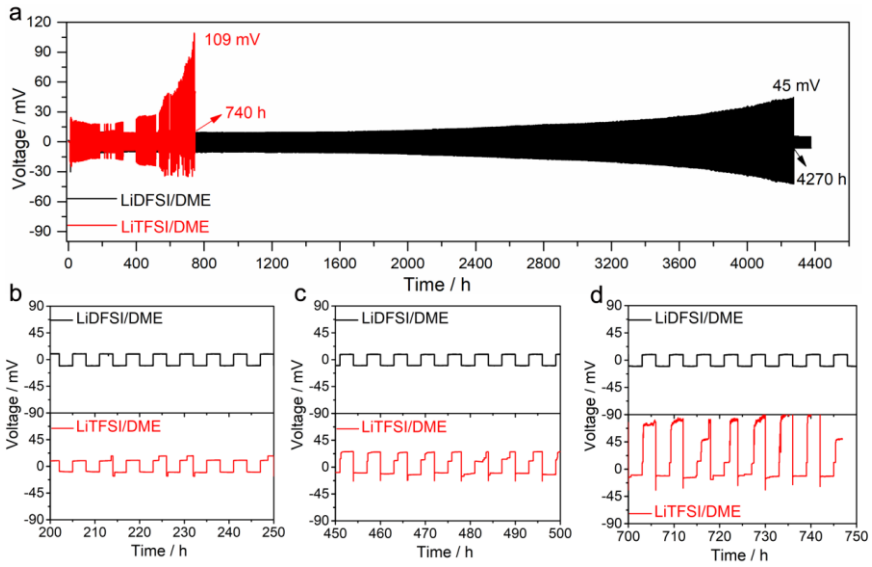

Figure 3.20. (a) Galvanostatic cycling of Li° anode in the DME-based electrolytes at room temperature, and (b-d) zoomed-in plots of the Li° symmetric cells in the range of (b) 200−250 h, (c) 450−500 h, (d) 700−750 h. Reproduced with permission from Ref. [25].

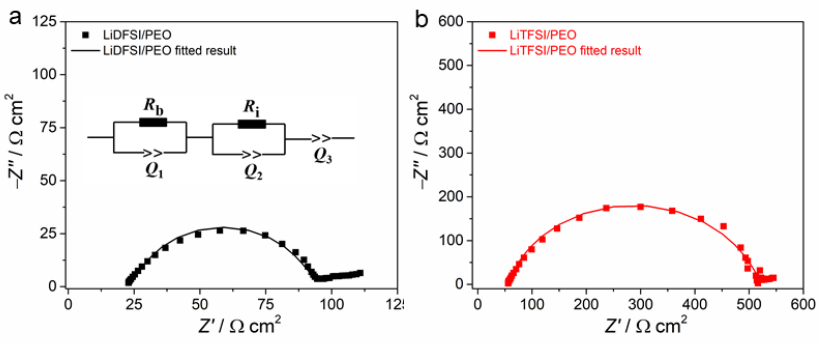

Figure 3.21. Impedance spectra of the Li° symmetric cells in Figure 3.19a after cycling. The inset shows the equivalent circuit adapted from Ref.[70] for fitting the raw EIS spectra and the fitted results are plotted as lines. Reproduced with permission from Ref. [25].

To unravel the unique role of anionic structure on the properties of SEI layers, the morphology of Li° deposits and the chemical compositions of SEI layers were investigated by SEM, XPS, and Raman spectroscopy, possible decomposition mechanism of salt anions is assessed by computational approaches and chemical simulations using organic radicals. **Figure 3.22a** shows the physical appearances and micro-sized morphologies of Li° deposits on a Cu substrate using the LiDFSI and LiTFSI-based LEs. Li° deposits formed in the LiDFSI-based LE show better coverage and homogeneity, in marked contrast to those formed in the LiTFSI-based one (**Figure 3.22a**, i and ii), accompanied by a much lesser extent of voids and needle-like Li° dendrites, as shown in the top view (**Figure 3.22a**, iii and iv) and cross-sectional SEM images (**Figure 3.22a**, v and vi). As noted in previous work,[71] controlling the morphology of Li° deposits by reducing the amount of dead lithium (i.e., non-electrochemically active Li°) and dendritic lithium could largely ameliorate the cycling efficiency and cycle life of

SSLMBs. Our results suggest that the hydrogen-containing salt LiDFSI favors the formation of energetically stable and less reactive Li° deposits.

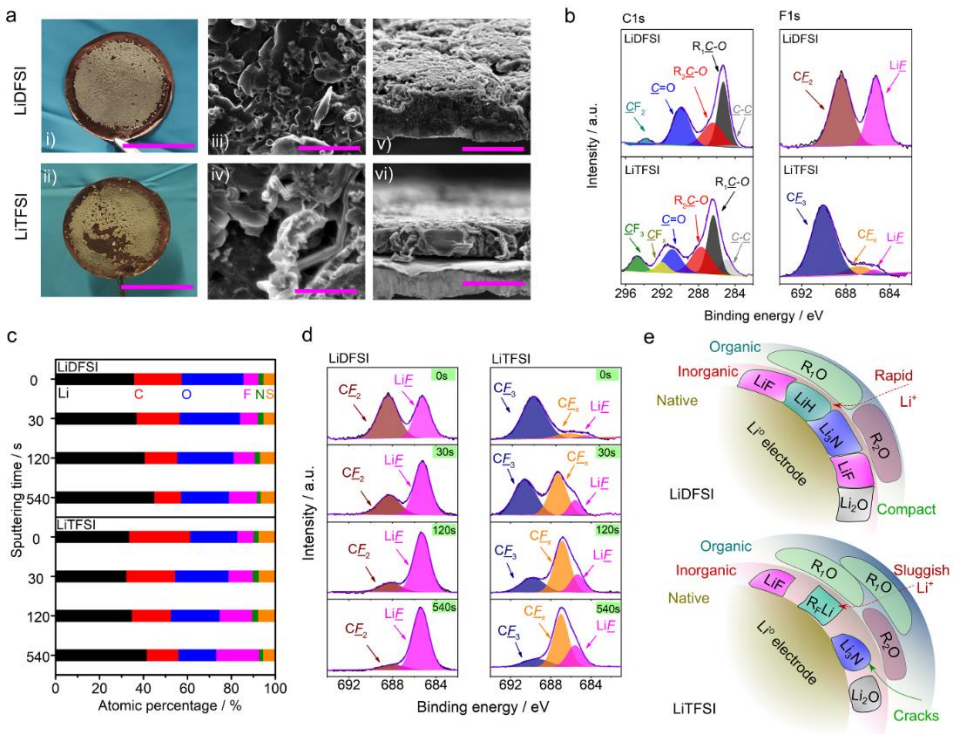

Figure 3.22. The role of salt anion on the surface of Li° electrode. (a) Optical and SEM images of Li° deposits on a Cu substrate recovered from the LiDFSI- and LiTFSI-based solutions. The scale bars in optical (left), top view (middle), cross-sectional (right) images are 10 mm, 20 µm, and 50 µm, respectively. (b) XPS spectra of C1s and F1s collected from the surface of Li° deposits. (c) The evolution of atomic percentage vs. sputtering time for the LiDFSI- and LiTFSI-based samples. (d) F1s spectra after various sputtering times for the LiDFSI- and LiTFSI-based samples. In Figure 3.22b and d, the purple and black lines represent the raw data and fitted results. (e) Schematic illustration of SEI formed in the LiDFSI- and LiTFSI-based electrolytes. Reproduced with permission from Ref. [25].

Figure 3.22b shows the XPS C1s and F1s spectra gathered from the outer surface of Li° deposits, the survey spectra and assignment of the peaks are provided **Figure 3.23** and **Table 3.6**. As seen in the C1s spectra of **Figure 3.22b**, non-fluorine containing organic species such as $R_1\underline{C}$—O (e.g., $\underline{C}H_3$—O—, ~286 eV) and $R_2\underline{C}$—O (e.g., —H$\underline{C}$—O—CH_3, ~287 eV) resulting from the decomposition of the solvent DME are found to be predominant SEI components, in addition to the *C*—F containing compounds engendered from the chemical and electrochemical reduction of salt anions on electronegative Li° deposits (e.g., $\underline{C}F_3$ at ~295 eV, $\underline{C}F_2$ at ~294 eV, $\underline{C}F_x$ at ~290 eV). Besides confirming the presence of these *C*—F containing compounds (e.g., C$\underline{F}_3$ at ~691 eV, C$\underline{F}_2$ at ~689 eV, C$\underline{F}_x$ at 688–687 eV), the F1s spectra (**Figure 3.22b**) also shows that the amount of Li$\underline{F}$ (~685 eV) in the LiDFSI-based LE weighs over that in the LiTFSI-based one, implying the formation of LiF-richer SEI layers in the former electrolyte possibly due to the facile decomposition of —CF_2H group in $DFSI^-$ vs. —CF_3 group in $TFSI^-$.

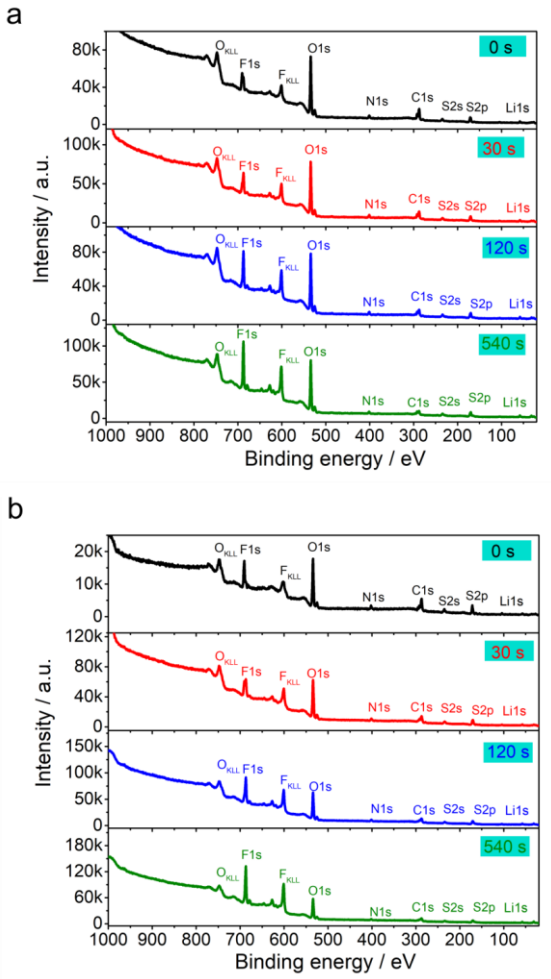

Figure 3.23. XPS survey spectra for the Li° deposits obtained from the Li° || Cu cell using 1 M LiX/DME [X = DFSI (a) or TFSI (b)] at different sputtering times. Reproduced with permission from Ref. [25].

Table 3.6. XPS data of main SEI components as reported in literature.[a)] Reproduced with permission from Ref. [25].

Compound	Li1s	C1s	O1s	F1s	S2p3/2	N1s
Li	52.3					
Li_2O	54.0		528.7			
LiF	56.0, 56.4			686.5		
				685−686		
				686.4−686.8		
LiH	55.5		531.9			
LiOH	55.5					
R-CH_2OLi		288	532			
		290.1				
		286.3				
		286				
$ROCO_2Li$	55	289−291	532.5			
		288−292	532.2			
		287.6	531.8			
		290.1, 286.7	533			
PEO (C−O−C)		286.2, 286.5	532.8			
$(CH_2OCO_2Li)_2$		286−287	553			
LiTFSI	56.6	289	533	688.6	169.4	399.6
		293	533.9	689.9	170.2	
		295			168.5−170	
LiDFSI (this work)	56.6	294	533.2	688.5	170	399.7
		290				

[a)] For comparison, the values of binding energy of some typical SEI components summarized in Ref.[46] are shown.

By subjecting Li° deposits to Ar^+ ion sputtering, the elemental information of SEI layers beneath the outmost surface could be further exposed by XPS measurement. **Figure 3.22c** presents the atomic percentage of each element with the variation of sputtering time. For both LiDFSI- and LiTFSI-based electrolytes, the Li and F contents gradually increase and the C and O contents progressively decrease by extending the sputtering times, e.g., 12.7% (540s sputtering) vs. 6.9% (pristine) in the LiDFSI-based system and 19.5% (540s) vs. 7.4% (pristine) in the LiTFSI-based system in the case of F content. This suggests that the inner parts of SEI layers formed in both cases are mainly composed of thermodynamically stable inorganic species (e.g., LiF, Li_2O, etc…). **Figure 3.22d** compares the F1s spectra of Li° deposits obtained from the LiDFSI- and LiTFSI-based electrolytes. The peak intensity of LiF (~685 eV) substantially increases with prolonged Ar^+ sputtering for Li° deposits recovered from the LiDFSI-based LE [e.g., 42% (pristine) vs. 84% (120s sputtering)]; however, for the TFSI-based one, the CF_y content becomes predominant SEI specie under the same condition (e.g., 57% after 120s sputtering), in spite of a steady increase of the LiF content [e.g., 13% (pristine) vs. 18% (120s sputtering)]. This implies that the reduction of $DFSI^-$ tends to be more complete compared to that of $TFSI^-$ after the replacement of one fluorine atom in —CF_3 group with hydrogen atom.

Interesting to note is that the decomposition of —CF_2H group might result in the formation of lithium hydride (LiH) which has a moderate Li^+ conductivity of 10^{-10} S cm^{-1} at room temperature, as reported by Ikeya.[72]

The de-convolution of Li1s spectra tends to be relatively difficult due to the presence of a large number of Li-containing species originating from the complete/incomplete decomposition of salt and solvent on Li° electrode, and H1s is too light to be determined by XPS. Hence, Raman spectroscopy was employed to monitor the chemical composition of SEI layers. As seen in **Figure 3.24**, the broad peak located at ca. 500 cm^{-1} is assigned to LiH, as evidenced in previous reports.[73] The intensity of LiH increases more significantly after being cycled in the LiDFSI-based electrolyte than in the LiTFSI-based one, indicating the likely formation of LiH via the decomposition of $DFSI^-$.

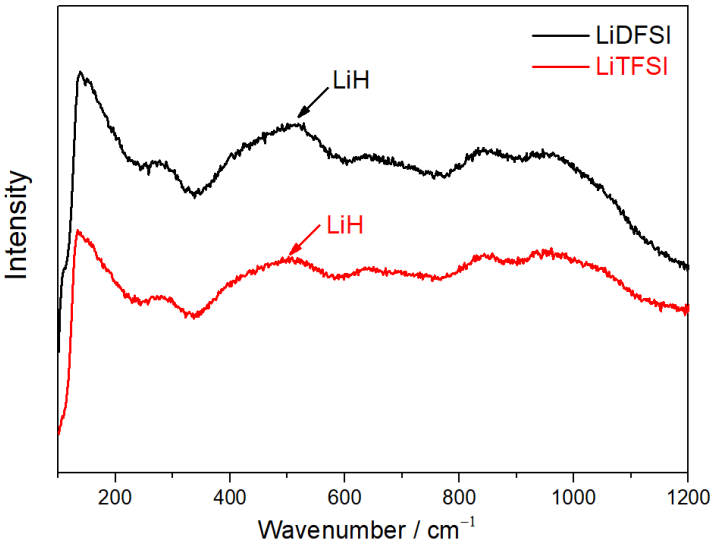

Figure 3.24. XPS survey spectra for the Li° deposits obtained from the Li° || Cu cell using 1 M LiX/DME [X = DFSI (a) or TFSI (b)] at different sputtering times. Reproduced with permission from Ref. [25].

To substantiate the above observations and anticipations, a series of computational models and chemical simulations via organic radicals which are analogous to Li/Li^+ redox were carried out. As shown in **Figure 3.25**, DFT calculation shows that the lowest unoccupied molecular orbital (LUMO) of $DFSI^-$ is located at a lower energy than that of $TFSI^-$ [i.e., 3.17 eV ($DFSI^-$) vs. 3.68 eV ($TFSI^-$), see **Figure 3.25a**], and the injection of one electron in $DFSI^-$ requires less energy compared to $TFSI^-$ [−68 kJ mol^{-1}, see **Figure 3.25b**), which suggests that the reduction of $DFSI^-$ is more energetically favourable. In addition, the LUMO of $DFSI^-$ is centered on the C—H bond which is occupied by the newly added electron in $DFSI^{2-}$, as shown in **Figure 3.25c** of the molecular orbital analysis. This is clearly consistent with the electron affinity of the Lewis acid H in $DFSI^-$, which may be subjected to subsequent decomposition during electrochemical processes.

On the other side, chemical simulations (**Figure 3.26**) show that $DFSI^-$ is chemically reduced in the presence of naphthalene radical anion which possesses a potential of ~1 V (vs. Li/Li^+)[46], while $TFSI^-$ remains stable under the same conditions, further reinforcing the hypothesis that $DFSI^-$ is less resistive against reduction. On the basis of the above experimental evidences and fundamental principles of imide chemistry, we tentatively suggest the decomposition mechanism of LiDFSI via three potential routes: 1) the cleavage of labile C—H bond, leading to the formation of Li-ion conducive LiH and thermodynamically unstable $C^{(-)}F_2LiSO_2N^{(-)}SO_2CF_2H$, which decomposes further to LiF and other Li-containing species (**Scheme 3.1a**); 2) the breakdown of S—N bond, yielding —SO_2NLi and —SO_2Li (**Scheme 3.1b**).

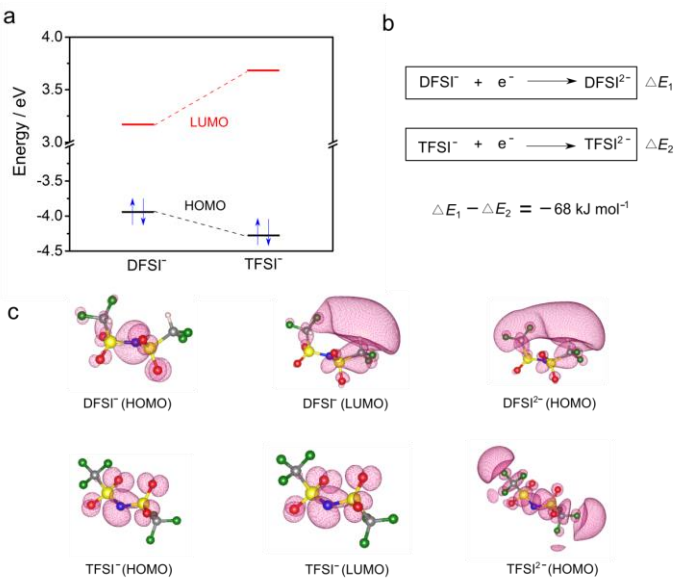

Figure 3.25. (a-c) DFT calculation on $DFSI^-$ and $TFSI^-$. (a) Energy of HOMO and LUMO. (b) Energy difference between two anions when injecting one electron. (c) Visualized HOMO and LUMO of $DFSI^-$ and $TFSI^-$ and their reduced form (i.e., $DFSI^{2-}$, $TFSI^{2-}$). The light pink, grey, blue, red, green, and yellow balls signify H, C, N, O, F, and S atoms, respectively. Reproduced with permission from Ref. [25].

To sum up, the SEI layers covering the surface of Li° deposits mainly comprise the native layer, inorganic-rich and organic-rich layers as schematically shown in **Figure 3.22e**. With respect to the LiDFSI-based system, the complete reduction of $DFSI^-$ results in a compact and dense inner layer with Li-ion conductive Li_3N and LiH. In comparison, for the LiTFSI-based system, the incomplete decomposition of $TFSI^-$ causes a poor coverage of inner layer with bulky R_FLi (e.g., CF_3SO_2Li, $CF_3SO_2NLi_2$) species with lesser Li-ion conductivity. The remaining exposed Li° which is highly chemically/electrochemically reactive induces the aggressive decomposition of ether-based solvents (e.g., DME), generating a thicker

organic layer. Therefore, the SEI layers formed in LiDFSI-based electrolyte are less resistive, more stable and robust, enabling the long-term cycling of Li° electrode as shown in **Figure 3.19** and **Figure 3.20**.

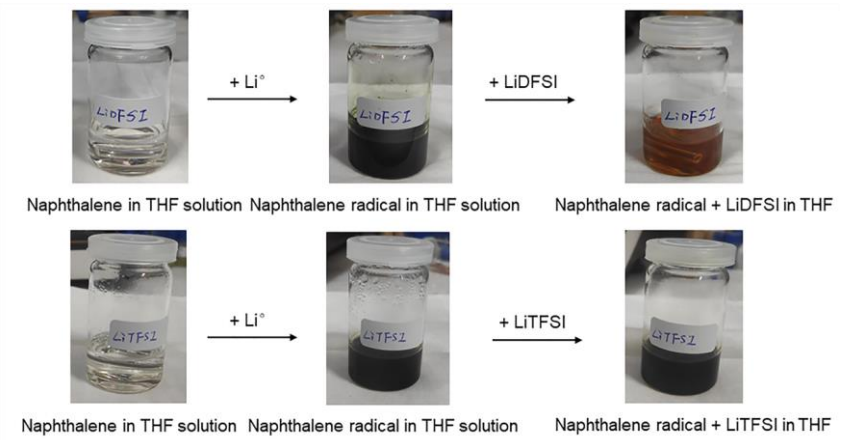

Figure 3.26. Chemical stabilities of LiDFSI and LiTFSI towards chemical reduction in the presence of naphthalene radical in tetrahydrofuran (THF) solutions. Reproduced with permission from Ref. [25].

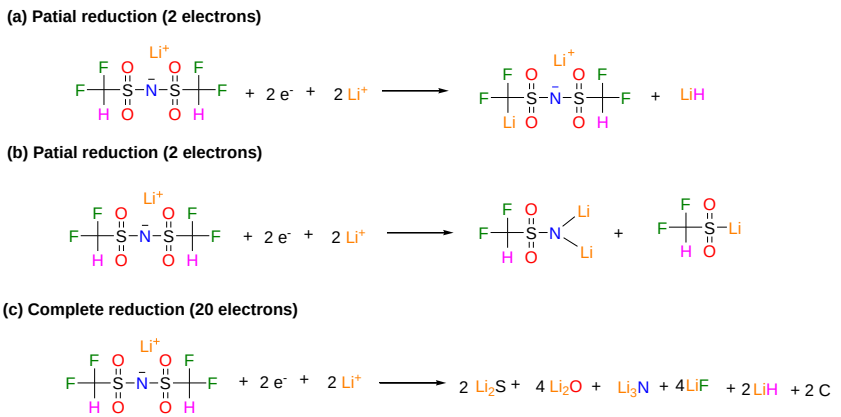

Scheme 3.1. Possible reduction mechanism of the $DFSI^-$ anion on the surface of Li° electrode. Reproduced with permission from Ref. [25].

3.3.4. Cell performance

To explore the potential application of the DFSI-based SPEs, long-term cycling performance of Li° || $LiFePO_4$ cells with LiX/PEO (X = DFSI or TFSI, EO/Li = 20) were evaluated at 70 °C. As shown in **Figure 3.27a-c**, the LiDFSI-based cell shows a stable charge/discharge profile with lower internal polarization for more than 140 cycles; however, the LiTFSI-based cell presents prolonged charging process beyond the 12^{th} cycles, which is attributed to the formation of soft dendrites on Li° anode.[67, 74] The poor cyclability of LiTFSI-based cells was also observed by other groups using bare Li° anode without any protection and conventional PEO-based electrolytes, e.g., 5 cycles for Li | LiTFSI/PEO | $LiFePO_4$ at 60 °C reported by Sun et al.[65] (see Entry 1, **Table 3.7**); and 30 cycles for Li | LiTFSI/PEO | $LiFePO_4$ at 60 °C reported by Yao et al.[75] (see Entry 2, **Table 3.7**). **Figure 3.27c** shows the specific capacity and Coulombic efficiency (CE) vs. cycle number for both LiDFSI- and LiTFSI-based cells at 70 °C. It is found that the initial discharge capacities of the cells using LiDFSI/PEO and LiTFSI/PEO at a current rate of C/5 are 104 and 129 mAh g^{-1}, respectively. The lower initial capacities of the both cells might be due to the poor contact between the SPEs and electrodes. After several formation cycles, this LiTFSI-based cell shows a higher capacity of ca. 170 mAh g^{-1} compared to that of LiDFSI-based one (e.g., ca. 120–130 mAh g^{-1}), which might be associated with inferior wettability of the LiDFSI-based electrolyte compared to that of LiTFSI-based one in the composite $LiFePO_4$ cathode, as discussed in previous work for FSI-based electrolytes which tend to show poor wettability towards $LiFePO_4$ cathode.[76] More importantly, the LiDFSI-based cell could deliver a high capacity of 123 mAh g^{-1} even after 140

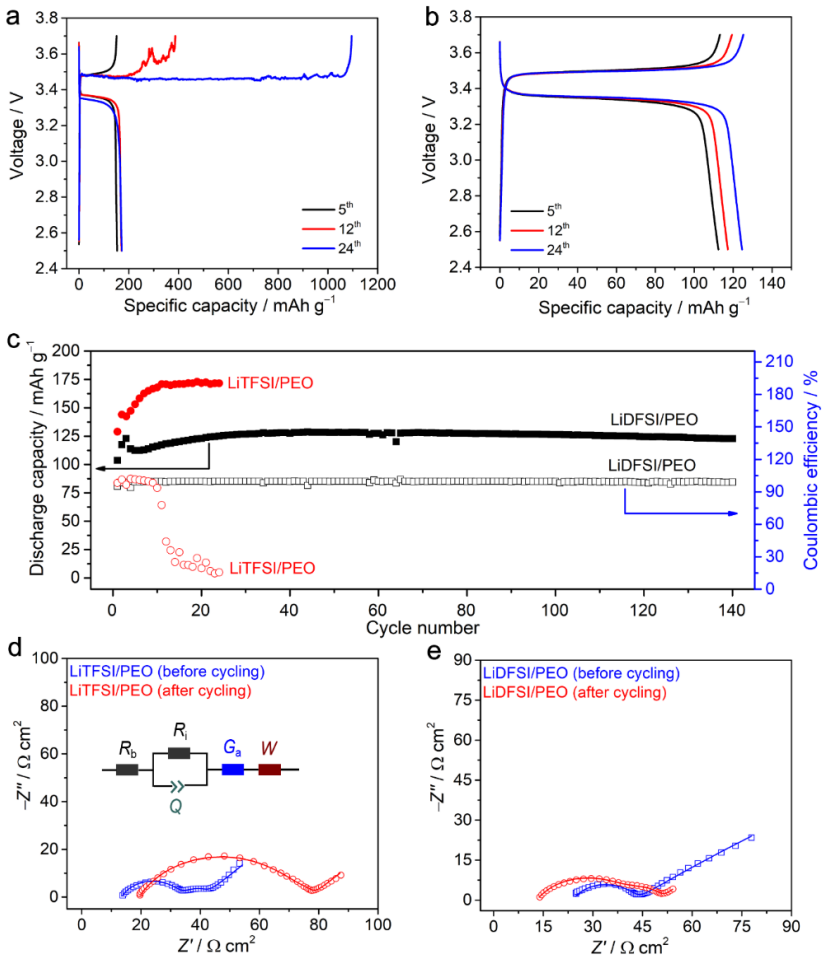

Figure 3.27. Cycling performance of solid-state lithium metal polymer cells using LiX/PEO (X = DFSI or TFSI, EO/Li = 20). (a, b) Discharge/charge profiles of the Li° || $LiFePO_4$ cells at 70 °C: (a) LiTFSI/PEO, and (b) LiDFSI/PEO. (c) Long-term cycling performance of the Li° || $LiFePO_4$ cells (three formation cycles at rate of C/5 and then constant cycling at C/3). (d, e) The impedance plots of the cells before and after cycling: (d) LiDFSI/PEO, and (e) LiTFSI/PEO. The equivalent circuit (inset in Figure 3.27d) adapted from Ref.[70] is used for fitting the raw EIS spectra, and the fitted results are plotted as lines. Reproduced with permission from Ref. [25].

Table 3.7. Performance of the state-of-the-art of conventional PEO-based Li° || $LiFePO_4$ cells. Reproduced with permission from Ref. [25].

Entry	Electrolyte [a]	M_w (PEO) / g mol^{-1}	CD [b] / mA g^{-1}	T [c] / °C	AML [d] / mg cm^{-2}	Cycling performance	Ref.
1	LiTFSI/PEO	1000000	85	60	Not reported	~130 mAh g^{-1} at the 5th cycle (short circuit)	65
2	LiTFSI/PEO	600000	17	60	2.0	Capacity retention of 76% and areal capacity of 0.26 mAh cm^{-2} at 30th cycle (short circuit)	75
3	LiTFSI/PEO	1000000	85	60	Not reported	~130 mAh g^{-1} at the 10th cycle (short circuit)	66
4	$LiClO_4$/PEO/LAGP	200000	34	55	3.6	Capacity retention of 92% and areal capacity of 0.44 mAh cm^{-2} at the 100th cycle	77
5	LiTFSI/PEO	500000	170	60	1.5	Capacity retention of 29% and areal capacity of 0.06 mAh cm^{-2} at the 20th cycle	78
6	LiTFSI/PEO	Not reported	17	70	5.9	Capacity retention of 93% and areal capacity of 0.74 mAh cm^{-2} at the 18th cycle (short circuit)	79
7	LiFSI/PEO	Not reported	17	70	5.9	Areal capacity of 0.89 mAh cm^{-2} at 15th cycle (short circuit)	79
8	LiEFA/PEO	5000000	57	70	Not reported	~140 mAh g^{-1} at the 25th cycle	58
9	LiTNFSI/PEO	6000000	170	60	1.5	Capacity retention of 64% and areal capacity of 0.14 mAh cm^{-2} at the 300th cycle	80
10	LiTFSI/PEO	Not reported	170	60	1.2	Capacity retention of 43% and areal capacity of 0.07 mAh cm^{-2} at the 200th cycle	62
11	LiBOB/PEO/SiO_2	Not reported	8	60	1.5	Capacity retention of 83% and areal capacity of 0.19 mAh cm^{-2} at the 75th cycle	81
12	LiTFSI/PEO	600000	85	60	3.2	Capacity retention of 10% and areal capacity of 0.04 mAh cm^{-2} at the 50th cycle	82
13	**LiDFSI/PEO**	**5000000**	**57**	**70**	**4.0**	**Capacity retention of 96% and areal capacity of 0.49 mAh cm^{-2} at the 140th cycle**	**This work**

[a] The abbreviations are listed as below: LAGP [lithium aluminium germanium phosphate ($Li_{1+x}Al_xGe_{2-x}(PO_4)_3$)], LiBOB [lithium bis(oxalate) borate], LiTNFSI

[lithium (trifluoromethanesulfonyl)(*N*-nonafluorobutanesulfonyl)imide]; [b] current density; [c] temperature; [d] active material loading.

cycles, strongly suggesting the excellent interfacial compatibility of the LiDFSI-based SPE towards to the Li° and $LiFePO_4$ electrodes (see **Table 3.7** for detailed comparison with the state-of-the-art results of conventional PEO-based Li° || $LiFePO_4$ cells).

To better understand the enhanced performance of the LiDFSI-based cell, the electrochemical impedance spectra (EIS) of both cells were collected before and after cycling (see **Figure 3.27d** and **e**). Generally, the high-frequency intercept of the spectra is associated to the bulk resistance (R_b), and the medium-frequency semicircles corresponds to interfacial resistance (R_i). The equivalent circuit of the spectra is shown as an inset in **Figure 3.27d** and the fitted values of EIS spectra are collected in **Table 3.8**. The initial R_b of the LiDFSI-based cell is higher than that of the LiTFSI-based cells (e.g., 24 Ω cm^2 vs. 13 Ω cm^2) which is due to the relatively lower ionic conductivity of the former one. However, the R_i of the LiTFSI-based cell increases substantially after 24 cycles [i.e., 53 Ω cm^2 (after 24 cycles) vs. 19 Ω cm^2 (before), **Table 3.8**] while the R_i of the LiDFSI-based one remains relatively stable even after 140 cycles [i.e., 26 Ω cm^2 (after 140 cycles) vs. 19 Ω cm^2 (before), **Table 3.8**]. The minimal increase of R_i for the LiDFSI-based cell compared to the LiTFSI-based one indicates again that an excellent SEI layer is formed on Li° electrode due to the reduction of $DFSI^-$ during cycling, as supported by the in-depth investigations on the Li° symmetric cells (**Figure 3.22**).

Table 3.8. The fitted R_b and R_i results of the Li° || $LiFePO_4$ cells based on different SPEs. Reproduced with permission from Ref. [25].

Electrolyte	R_b / Ω cm^{-2}		R_i / Ω cm^{-2}	
	Before	After	Before	After
LiDFSI/PEO (20)	24	13	19	26
LiTFSI/PEO (20)	13	19	19	53

3.4. Conclusion

Weakly-coordinating nature of anions is prerequisite for facilely dissociating Li^+ cation and thereby offering sufficient Li-ion mobility, this is generally attained by introducing strong electron-withdrawing perfluorinated groups (e.g., —CF_3, —C_2F_5, —C_4F_9). Yet, perfluorinated groups could not be easily degraded via chemical and/or biochemical routes and possess negligible interactions with PEO-based polymer matrices (i.e., "slippery" anion), thus moving much faster than the counter-charges. Inheriting the flexible sulfonimide center from $TFSI^-$ but eliminating the poorly degradable —CF_3, the newly conceived $DFSI^-$ is adaptive and pliable after dissolving in PEO, as shown by very close values of T_g for LiDFSI/PEO and LiTFSI/PEO. Very interestingly, $DFSI^-$ with two defluorinated —CF_2H moieties could be easily hydrolyzed under mild basic conditions, and is likely non-persistent in the environment. However, the stability in neutral/acidic aqueous environment is sufficient for an easy reclaiming of the salts when recycling the batteries, contributing to the circular economy.

Experimental and computational results suggest that the H-bonding interactions originated from —CF_2H moieties and EO units slow down the migration of the anions under electric field, leading to a remarkable

improvement in T_{Li}^{+}. Though —CF_2H moiety slightly decreases the anodic stability (~0.5 V lower than $TFSI^-$), $DFSI^-$ remains stable towards oxidation in contact with the quasi totality of the commercial electrode materials. The superior electrochemical performance of Li° electrode in LiDFSI-based cells is associated with the unique chemistry of the salt anion, leading to the likely formation of ionically conductive LiH and mechanically stable LiF as SEI-building species on Li° electrode. As a result, the prototype Li° || $LiFePO_4$ cell using LiDFSI/PEO could be cycled for more than 140 cycles with minimal capacity decay, suggesting the feasibility of $DFSI^-$ as conducting salt for SPE-based SSLMBs.

To conclude, the innovative chemistry of —CF_2H moiety demonstrated in this work could not only provide promising electrolyte candidates to SSLMBs but also inspire the design of suitable battery materials for other kind of batteries such as sodium and potassium batteries.

3.5 References

1. Zhang, H.; Li, C.; Eshetu, G. G.; Laruelle, S.; Grugeon, S.; Zaghib, K.; Julien, C.; Mauger, A.; Guyomard, D.; Rojo, T., From Solid‐Solution Electrodes and the Rocking‐Chair Concept to Today's Batteries. *Angewandte Chemie* **2020,** *132* (2), 542-546.

2. Mauger, A.; Julien, C. M.; Goodenough, J. B.; Zaghib, K., Tribute to Michel Armand: from rocking chair–Li-ion to solid-state lithium batteries. *Journal of The Electrochemical Society* **2019,** *167* (7), 070507.

3. Tarascon, J. M.; Armand, M., Issues and challenges facing rechargeable lithium batteries. *Nature* **2001,** *414* (6861), 359-367.

4. Xu, K., Electrolytes and interphases in Li-ion batteries and beyond. *Chemical reviews* **2014,** *114* (23), 11503-11618.

5. Yang, Z.; Zhang, J.; Kintner-Meyer, M. C. W.; Lu, X.; Choi, D.; Lemmon, J. P.; Liu, J., Electrochemical energy storage for green grid. *Chemical reviews* **2011,** *111* (5), 3577-3613.

6. Schmuch, R.; Wagner, R.; Hörpel, G.; Placke, T.; Winter, M., Performance and cost of materials for lithium-based rechargeable automotive batteries. *Nature Energy* **2018,** *3* (4), 267-278.

7. Aurbach, D.; Zinigrad, E.; Cohen, Y.; Teller, H., A short review of failure mechanisms of lithium metal and lithiated graphite anodes in liquid electrolyte solutions. *Solid state ionics* **2002,** *148* (3-4), 405-416.

8. Wang, L.; Chen, B.; Ma, J.; Cui, G.; Chen, L., Reviving lithium cobalt oxide-based lithium secondary batteries-toward a higher energy density. *Chemical Society Reviews* **2018,** *47* (17), 6505-6602.

9. Cheng, X.-B.; Zhang, R.; Zhao, C.-Z.; Zhang, Q., Toward safe lithium metal anode in rechargeable batteries: a review. *Chemical reviews* **2017,** *117* (15), 10403-10473.

10. Lin, D.; Liu, Y.; Cui, Y., Reviving the lithium metal anode for high-energy batteries. *Nature nanotechnology* **2017,** *12* (3), 194.

11. Di Noto, V.; Lavina, S.; Giffin, G. A.; Negro, E.; Scrosati, B., Polymer electrolytes: Present, past and future. Elsevier: 2011.

12. Hallinan Jr, D. T.; Balsara, N. P., Polymer electrolytes. *Annual review of materials research* **2013,** *43*, 503-525.

13. Zhang, H.; Li, C.; Piszcz, M.; Coya, E.; Rojo, T.; Rodriguez-Martinez, L. M.; Armand, M.; Zhou, Z., Single lithium-ion conducting solid polymer electrolytes: advances and perspectives. *Chemical Society Reviews* **2017,** *46* (3), 797-815.

14. Zhou, Q.; Ma, J.; Dong, S.; Li, X.; Cui, G., Intermolecular Chemistry in Solid Polymer Electrolytes for High-Energy-Density Lithium Batteries. *Advanced Materials* **2019,** *31* (50), 1902029.

15. Fenton, D. E.; Parker, J. M.; Wright, P. V., Complexes of alkali metal ions with poly(ethylene oxide). *Polymer* **1973,** *14* (11), 589.

16. M. Armand; J. M. Chabagno; M. J. Duclot, The 2nd International conference on solid electrolyte. **1978**.

17. https://www.bollore.com/en/activites-et-participations-2/stockage-delectricite-et-systemes/.

18. Liu, J.; Bao, Z.; Cui, Y.; Dufek, E. J.; Goodenough, J. B.; Khalifah, P.; Li, Q.; Liaw, B. Y.; Liu, P.; Manthiram, A., Pathways for practical high-energy long-cycling lithium metal batteries. *Nature Energy* **2019,** *4* (3), 180-186.

19. Tikekar, M. D.; Choudhury, S.; Tu, Z.; Archer, L. A., Design principles for electrolytes and interfaces for stable lithium-metal batteries. *Nature Energy* **2016,** *1* (9), 1-7.

20. Hallinan Jr, D. T.; Mullin, S. A.; Stone, G. M.; Balsara, N. P., Lithium metal stability in batteries with block copolymer electrolytes. *Journal of The Electrochemical Society* **2013,** *160* (3), A464.

21. Stone, G. M.; Mullin, S. A.; Teran, A. A.; Hallinan Jr, D. T.; Minor, A. M.; Hexemer, A.; Balsara, N. P., Resolution of the modulus versus adhesion dilemma in solid polymer electrolytes for rechargeable lithium metal batteries. *Journal of The Electrochemical Society* **2011,** *159* (3), A222.

22. Croce, F.; Appetecchi, G. B.; Persi, L.; Scrosati, B., Nanocomposite polymer electrolytes for lithium batteries. *Nature* **1998,** *394* (6692), 456-458.

23. Liu, W.; Lee, S. W.; Lin, D.; Shi, F.; Wang, S.; Sendek, A. D.; Cui, Y., Enhancing ionic conductivity in composite polymer electrolytes with well-aligned ceramic nanowires. *Nature energy* **2017,** *2* (5), 1-7.

24. Liu, W.; Liu, N.; Sun, J.; Hsu, P.-C.; Li, Y.; Lee, H.-W.; Cui, Y., Ionic conductivity enhancement of polymer electrolytes with ceramic nanowire fillers. *Nano letters* **2015,** *15* (4), 2740-2745.

25. Qiao, L.; Oteo, U.; Zhang, Y.; Peña, S. R.; Martínez-Ibañez, M.; Santiago, A.; Cid, R.; Meabe, L.; Manzano, H.; Carrasco, J.; Zhang, H.; Armand, M., Trifluoromethyl-free anion for highly stable lithium metal polymer batteries. *Energy Storage Materials* **2020**.

26. M. Armand; W. Gorecki; R. Andreani, Proceedings of the 2nd International Meeting on Polymer Electrolytes (Ed.: B. Scrosati). *Elsevier, London* **1989**, p. 91.

27. Zhang, H.; Oteo, U.; Judez, X.; Eshetu, G. G.; Martinez-Ibañez, M.; Carrasco, J.; Li, C.; Armand, M., Designer Anion Enabling Solid-State Lithium-Sulfur Batteries. *Joule* **2019**.

28. Neumann, J.; Cho, C.-W.; Steudte, S.; Köser, J.; Uerdingen, M.; Thöming, J.; Stolte, S., Biodegradability of fluoroorganic and cyano-based ionic liquid anions under aerobic and anaerobic conditions. *Green chemistry* **2012,** *14* (2), 410-418.

29. Wells, A. S.; Coombe, V. T., On the freshwater ecotoxicity and biodegradation properties of some common ionic liquids. *Organic Process Research & Development* **2006,** *10* (4), 794-798.

30. Banks, R. E.; Smart, B. E.; Tatlow, J. C., *Organofluorine chemistry: principles and commercial applications*. Springer Science & Business Media: 2013.

31. Blum, V.; Gehrke, R.; Hanke, F.; Havu, P.; Havu, V.; Ren, X.; Reuter, K.; Scheffler, M., Ab initio molecular simulations with numeric atom-centered orbitals. *Computer Physics Communications* **2009,** *180* (11), 2175-2196.

32. Havu, V.; Blum, V.; Havu, P.; Scheffler, M., Efficient O (N) integration for all-electron electronic structure calculation using numeric basis functions. *Journal of Computational Physics* **2009,** *228* (22), 8367-8379.

33. Lee, C.; Yang, W.; Parr, R. G., Development of the Colle-Salvetti correlation-energy formula into a functional of the electron density. *Physical review B* **1988,** *37* (2), 785.

34. Becke, A. D., Density‐functional thermochemistry. III. The role of exact exchange. *The Journal of Chemical Physics* **1993,** *98* (7), 5648-5652.

35. Zhang, H.; Oteo, U.; Zhu, H.; Judez, X.; Martinez-Ibañez, M.; Aldalur, I.; Sanchez-Diez, E.; Li, C.; Carrasco, J.; Forsyth, M., Enhanced Li‐ion conductivity

of polymer electrolytes with selective introduction of hydrogen in the anion. *Angewandte Chemie* **2019**.

36. Momma, K.; Izumi, F., VESTA 3 for three-dimensional visualization of crystal, volumetric and morphology data. *Journal of applied crystallography* **2011,** *44* (6), 1272-1276.

37. Pronk, S.; Páll, S.; Schulz, R.; Larsson, P.; Bjelkmar, P.; Apostolov, R.; Shirts, M. R.; Smith, J. C.; Kasson, P. M.; van der Spoel, D., GROMACS 4.5: a high-throughput and highly parallel open source molecular simulation toolkit. *Bioinformatics* **2013,** *29* (7), 845-854.

38. Watkins, E. K.; Jorgensen, W. L., Perfluoroalkanes: Conformational analysis and liquid-state properties from ab initio and Monte Carlo calculations. *The Journal of Physical Chemistry A* **2001,** *105* (16), 4118-4125.

39. Rizzo, R. C.; Jorgensen, W. L., OPLS all-atom model for amines: resolution of the amine hydration problem. *Journal of the American Chemical Society* **1999,** *121* (20), 4827-4836.

40. Price, M. L. P.; Ostrovsky, D.; Jorgensen, W. L., Gas‐phase and liquid‐state properties of esters, nitriles, and nitro compounds with the OPLS‐AA force field. *Journal of Computational Chemistry* **2001,** *22* (13), 1340-1352.

41. McDonald, N. A.; Jorgensen, W. L., Development of an all-atom force field for heterocycles. Properties of liquid pyrrole, furan, diazoles, and oxazoles. *The Journal of Physical Chemistry B* **1998,** *102* (41), 8049-8059.

42. Kaminski, G. A.; Friesner, R. A.; Tirado-Rives, J.; Jorgensen, W. L., Evaluation and reparametrization of the OPLS-AA force field for proteins via comparison with accurate quantum chemical calculations on peptides. *The Journal of Physical Chemistry B* **2001,** *105* (28), 6474-6487.

43. Jorgensen, W. L.; McDonald, N. A., Development of an all-atom force field for heterocycles. Properties of liquid pyridine and diazenes. *Journal of Molecular Structure: THEOCHEM* **1998,** *424* (1-2), 145-155.

44. Jorgensen, W. L.; Maxwell, D. S.; Tirado-Rives, J., Development and testing of the OPLS all-atom force field on conformational energetics and properties of organic liquids. *Journal of the American Chemical Society* **1996,** *118* (45), 11225-11236.

45. Martinez‐Ibañez, M.; Sanchez‐Diez, E.; Qiao, L.; Zhang, Y.; Judez, X.; Santiago, A.; Aldalur, I.; Carrasco, J.; Zhu, H.; Forsyth, M., Unprecedented Improvement of Single Li‐Ion Conductive Solid Polymer Electrolyte Through Salt Additive. *Advanced Functional Materials* **2020,** *30* (16), 2000455.

46. Zhang, H.; Oteo, U.; Judez, X.; Eshetu, G. G.; Martinez-Ibanez, M.; Carrasco, J.; Li, C.; Armand, M., Designer anion enabling solid-state lithium-sulfur batteries. *Joule* **2019,** *3* (7), 1689-1702.

47. Volel, M.; Armand, M.; Gorecki, W., Influence of Sample History on the Morphology and Transport Properties of PEO− Lithium Salt Complexes. *Macromolecules* **2004,** *37* (22), 8373-8380.

48. Hagiwara, R.; Tamaki, K.; Kubota, K.; Goto, T.; Nohira, T., Thermal properties of mixed alkali bis (trifluoromethylsulfonyl) amides. *Journal of Chemical & Engineering Data* **2008,** *53* (2), 355-358.

49. Aldalur, I.; Martinez‐Ibañez, M.; Piszcz, M.; Zhang, H.; Armand, M., Self‐Standing Highly Conductive Solid Electrolytes Based on Block Copolymers for Rechargeable All‐Solid‐State Lithium‐Metal Batteries. *Batteries & Supercaps* **2018,** *1* (4), 149-159.

50. Magistris, A.; Mustarelli, P.; Quartarone, E.; Tomasi, C., Transport and thermal properties of (PEO) n–LiPF6 electrolytes for super-ambient applications. *Solid state ionics* **2000,** *136*, 1241-1247.

51. Stolwijk, N. A.; Heddier, C.; Reschke, M.; Wiencierz, M.; Bokeloh, J.; Wilde, G., Salt-concentration dependence of the glass transition temperature in PEO–NaI and PEO–LiTFSI polymer electrolytes. *Macromolecules* **2013,** *46* (21), 8580-8588.

52. Lascaud, S.; Perrier, M.; Vallee, A.; Besner, S.; Prud'Homme, J.; Armand, M., Phase diagrams and conductivity behavior of poly (ethylene oxide)-molten salt rubbery electrolytes. *Macromolecules* **1994,** *27* (25), 7469-7477.

53. Suo, L.; Hu, Y.-S.; Li, H.; Armand, M.; Chen, L., A new class of solvent-in-salt electrolyte for high-energy rechargeable metallic lithium batteries. *Nature communications* **2013,** *4* (1), 1-9.

54. Diddens, D.; Heuer, A.; Borodin, O., Understanding the lithium transport within a rouse-based model for a PEO/LiTFSI polymer electrolyte. *Macromolecules* **2010,** *43* (4), 2028-2036.

55. Borodin, O.; Smith, G. D., Mechanism of ion transport in amorphous poly (ethylene oxide)/LiTFSI from molecular dynamics simulations. *Macromolecules* **2006,** *39* (4), 1620-1629.

56. Cao, C.; Li, Y.; Feng, Y.; Peng, C.; Li, Z.; Feng, W., A solid-state single-ion polymer electrolyte with ultrahigh ionic conductivity for dendrite-free lithium metal batteries. *Energy Storage Materials* **2019,** *19*, 401-407.

57. Eshetu, G. G.; Judez, X.; Li, C.; Martinez-Ibañez, M.; Gracia, I.; Bondarchuk, O.; Carrasco, J.; Rodriguez-Martinez, L. M.; Zhang, H.; Armand, M., Ultrahigh performance all solid-state lithium sulfur batteries: salt anion's chemistry-induced anomalous synergistic effect. *Journal of the American chemical society* **2018,** *140* (31), 9921-9933.

58. Zhang, H.; Chen, F.; Lakuntza, O.; Oteo, U.; Qiao, L.; Martinez‐Ibañez, M.; Zhu, H.; Carrasco, J.; Forsyth, M.; Armand, M., Suppressed Mobility of Negative Charges in Polymer Electrolytes with an Ether‐Functionalized Anion. *Angewandte Chemie* **2019,** *131* (35), 12198-12203.

59. Jo, Y. H.; Zhou, B.; Jiang, K.; Li, S.; Zuo, C.; Gan, H.; He, D.; Zhou, X.; Xue, Z., Self-healing and shape-memory solid polymer electrolytes with high mechanical strength facilitated by a poly (vinyl alcohol) matrix. *Polymer Chemistry* **2019,** *10* (48), 6561-6569.

60. Wang, Q.; Cui, Z.; Zhou, Q.; Shangguan, X.; Du, X.; Dong, S.; Qiao, L.; Huang, S.; Liu, X.; Tang, K., A supramolecular interaction strategy enabling high-performance all solid state electrolyte of lithium metal batteries. *Energy Storage Materials* **2020,** *25*, 756-763.

61. Hsu, S.-T.; Tran, B. T.; Subramani, R.; Nguyen, H. T. T.; Rajamani, A.; Lee, M.-Y.; Hou, S.-S.; Lee, Y.-L.; Teng, H., Free-standing polymer electrolyte for all-solid-state lithium batteries operated at room temperature. *Journal of Power Sources* **2020,** *449*, 227518.

62. Imholt, L.; Dörr, T. S.; Zhang, P.; Ibing, L.; Cekic-Laskovic, I.; Winter, M.; Brunklaus, G., Grafted polyrotaxanes as highly conductive electrolytes for lithium metal batteries. *Journal of power sources* **2019,** *409*, 148-158.

63. Wang, Q.; Liu, X.; Cui, Z.; Shangguan, X.; Zhang, H.; Zhang, J.; Tang, K.; Li, L.; Zhou, X.; Cui, G., A fluorinated polycarbonate based all solid state polymer electrolyte for lithium metal batteries. *Electrochimica Acta* **2020,** *337*, 135843.

64. Chen, Y.; Shi, Y.; Liang, Y.; Dong, H.; Hao, F.; Wang, A.; Zhu, Y.; Cui, X.; Yao, Y., Hyperbranched PEO-based hyperstar solid polymer electrolytes with simultaneous improvement of ion transport and mechanical strength. *ACS Applied Energy Materials* **2019,** *2* (3), 1608-1615.

65. Yang, X.; Sun, Q.; Zhao, C.; Gao, X.; Adair, K.; Zhao, Y.; Luo, J.; Lin, X.; Liang, J.; Huang, H.; Zhang, L.; Lu, S.; Li, R.; Sun, X., Self-healing electrostatic shield enabling uniform lithium deposition in all-solid-state lithium batteries. *Energy Storage Materials* **2019,** *22*, 194-199.

66. Yang, X.; Gao, X.; Zhao, C.; Sun, Q.; Zhao, Y.; Adair, K.; Luo, J.; Lin, X.; Liang, J.; Huang, H.; Zhang, L.; Lu, S.; Li, R.; Sun, X., Suppressed dendrite formation realized by selective Li deposition in all-solid-state lithium batteries. *Energy Storage Materials* **2020,** *27*, 198-204.

67. Aldalur, I.; Martinez-Ibañez, M.; Krztoń-Maziopa, A.; Piszcz, M.; Armand, M.; Zhang, H., Flowable polymer electrolytes for lithium metal batteries. *Journal of Power Sources* **2019,** *423*, 218-226.

68. Zhang, X.; Wang, S.; Xue, C.; Xin, C.; Lin, Y.; Shen, Y.; Li, L.; Nan, C. W., Self-Suppression of Lithium Dendrite in All-Solid-State Lithium Metal Batteries with Poly(vinylidene difluoride)-Based Solid Electrolytes. *Advanced Materials* **2019,** *31* (11).

69. Cui, Y.; Wan, J.; Ye, Y.; Liu, K.; Chou, L.-Y.; Cui, Y., A fireproof, lightweight, polymer–polymer solid-state electrolyte for safe lithium batteries. *Nano letters* **2020,** *20* (3), 1686-1692.

70. Wurster, V.; Engel, C.; Graebe, H.; Ferber, T.; Jaegermann, W.; Hausbrand, R., Characterization of the Interfaces in LiFePO4/PEO-LiTFSI Composite Cathodes and to the Adjacent Layers. *Journal of The Electrochemical Society* **2019,** *166* (3), A5410.

71. Fang, C.; Li, J.; Zhang, M.; Zhang, Y.; Yang, F.; Lee, J. Z.; Lee, M.-H.; Alvarado, J.; Schroeder, M. A.; Yang, Y., Quantifying inactive lithium in lithium metal batteries. *Nature* **2019,** *572* (7770), 511-515.

72. Ikeya, M., Electrical properties of lithium hydride. *Journal of the Physical Society of Japan* **1977,** *42* (1), 168-174.

73. Stowe, A. C.; Smyrl, N., Raman spectroscopy of lithium hydride corrosion: Selection of appropriate excitation wavelength to minimize fluorescence. *Vibrational Spectroscopy* **2012,** *60*, 133-136.

74. Aldalur, I.; Martinez-Ibañez, M.; Piszcz, M.; Rodriguez-Martinez, L. M.; Zhang, H.; Armand, M., Lowering the operational temperature of all-solid-state lithium polymer cell with highly conductive and interfacially robust solid polymer electrolytes. *Journal of Power Sources* **2018,** *383*, 144-149.

75. Zhu, Z.; Lu, L.-L.; Yin, Y.; Shao, J.; Shen, B.; Yao, H.-B., High Rate and Stable Solid-State Lithium Metal Batteries Enabled by Electronic and Ionic Mixed Conducting Network Interlayers. *ACS applied materials & interfaces* **2019,** *11* (18), 16578-16585.

76. Aldalur, I.; Wang, X.; Santiago, A.; Goujon, N.; Echeverria, M.; Martinez-Ibanez, M.; Piszcz, M.; Howlett, P. C.; Forsyth, M.; Armand, M., Nanofiber-reinforced polymer electrolytes toward room temperature solid-state lithium batteries. *Journal of Power Sources* **2020,** *448*, 227424.

77. Jung, Y.-C.; Lee, S.-M.; Choi, J.-H.; Jang, S. S.; Kim, D.-W., All solid-state lithium batteries assembled with hybrid solid electrolytes. *Journal of The Electrochemical Society* **2015,** *162* (4), A704.

78. Tao, C.; Gao, M.-H.; Yin, B.-H.; Li, B.; Huang, Y.-P.; Xu, G.; Bao, J.-J., A promising TPU/PEO blend polymer electrolyte for all-solid-state lithium ion batteries. *Electrochimica Acta* **2017,** *257*, 31-39.

79. Judez, X.; Piszcz, M.; Coya, E.; Li, C.; Aldalur, I.; Oteo, U.; Zhang, Y.; Zhang, W.; Rodriguez-Martinez, L. M.; Zhang, H., Stable cycling of lithium metal electrode in nanocomposite solid polymer electrolytes with lithium bis (fluorosulfonyl) imide. *Solid State Ionics* **2018,** *318*, 95-101.

80. Ma, Q.; Qi, X.; Tong, B.; Zheng, Y.; Feng, W.; Nie, J.; Hu, Y.-S.; Li, H.; Huang, X.; Chen, L.; Zhou, Z., Novel Li[(CF3SO2)(n-C4F9SO2)N]-Based Polymer Electrolytes for Solid-State Lithium Batteries with Superior Electrochemical Performance. *ACS Applied Materials & Interfaces* **2016,** *8* (43), 29705-29712.

81. Huang, K. C.; Li, H. H.; Fan, H. H.; Guo, J. Z.; Xing, Y. M.; Hu, Y. P.; Wu, X. L.; Zhang, J. P., An in situ‐Fabricated Composite Polymer Electrolyte Containing Large‐Anion Lithium Salt for All‐Solid‐State LiFePO4/Li Batteries. *ChemElectroChem* **2017,** *4* (9), 2293-2299.

82. Li, A.; Liao, X.; Zhang, H.; Shi, L.; Wang, P.; Cheng, Q.; Borovilas, J.; Li, Z.; Huang, W.; Fu, Z., Nacre‐Inspired Composite Electrolytes for Load‐Bearing Solid‐State Lithium‐Metal Batteries. *Advanced Materials* **2020,** *32* (2), 1905517.

Chapter 4

A benzene-conjugated anion for all-solid-state lithium-metal batteries

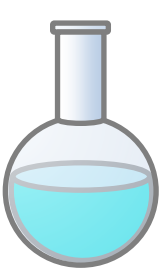

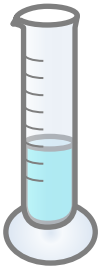

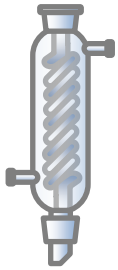

Chapter 4:

A benzene-conjugated anion for all-solid-state lithium-metal batteries

4.1. Introduction

With the increasing demand of energy storage devices for utilization in portable electronics, electric vehicles (EVs) and large-format grid storage systems, the existing state-of-the-art lithium-ion batteries (LIBs) have fallen far behind the drastic requirements owing to their relatively low energy storage (e.g., 250 Wh kg^{-1}).[1-2] On the other hand, the intrinsic flammability and instability of organic liquid electrolytes for current LIBs may trigger safety concerns such as fire or even exploration under abuse conditions, impeding their combination with high-capacity lithium metal (Li°) anode, which possesses nearly 10 times higher theoretical capacity compared with widely used graphite anode [e.g., 3860 mAh g^{-1} (Li°) versus 372 mAh g^{-1} (graphite)].[3-6]

Solid polymer electrolytes (SPEs) with flexibility, processability and excellent interfacial compatibility with the Li° anode have been regarded as a promising alternative to enhance the energy density and safety of current LIBs from both academic and industrial aspects.[7-8] The practical feasibility of SPEs-based Li° metal batteries (LMBs) have been demonstrated successfully via the implementation of the Bluecar® or Bluebus® launched by Bollore in several cities.[9] However, most of the SPEs-based LMBs exhibit low lithium transference number (σ_{Li^+}) due to the utilization of the dual-ion conducting salts [e.g., lithium bis(trifluoromethanesulfonyl)imide (LiTFSI)] as Li^+ sources, which could lead to concentration polarization and premature failure of the cells.[10]

To suppress the mobility of the anionic species and enhance the lithium-ion conductivity for minimizing cell polarization and eliminating cell

premature failures in SPEs, currently, several strategies have been employed during the past decades, including 1) tethering salt anions to organic long-chain backbone; 2) introducing anionic traps to confine anions movement and 3) incorporation of inorganic particles to retard the anions mobility.[10-11] However, all these methods mentioned above are either involved in arduous modifications or with the sacrifice of the total ionic conductivities.

The structural modification of the salt anions has been proposed as a facile and efficient strategy to tune the electrochemical properties of the SPEs. Several new salts have been proposed in our previous works to improve the physicochemical and electrochemical properties of the SPEs, i.g., lithium (difluoromethanesulfonyl)(trifluoromethanesulfonyl)imide (LiDFTFSI),[12-13] lithium (trifluoromethanesulfonyl)(*N*-bis(methoxyethyl)sulfonyl)imide (LiEFA),[11] which resulted in significant improvement of lithium-ion conductivities in PEO-based SPEs. In this Chapter, a benzene-based salt lithium benzenesulfonyl (trifluoromethanesulfonyl)imide (abbreviated as LiBTFSI) was synthesized for high-performance PEO-based SPEs with aim of further improving the lithium-ion conductivity. In contrast to the abundantly used lithium LiTFSI, LiBTFSI-based SPEs present good interfacial stability toward Li° anode, extremely high lithium-ion transference number, very high discharge capacities, high Coulombic efficiencies as well as excellent long-term cyclability. These results demonstrate the importance of the molecular structure of anions in SPEs and shed light on a way for future advancement and development high-performance SPEs-based LMBs.

4.2. Materials

Benzenesulfonyl chloride (98%, Sigma-Aldrich), lithium bis(trifluoromethanesulfonyl)imide (LiTFSI, 99%, Sigma-Aldrich), deuterium oxide (D_2O, Eurisotop, 99.8 wt% D), potasium hydroxide (KOH, reagent grade, Scharlab), hydrochloric acid (37%, extra pure, Scharlab), acetonitrile (ACN, 99%, Scharlab), toluene (99.3%, Scharlab), triethylamine (99.5%, Sigma-Aldrich), and poly(ethylene oxide) (PEO, M_w = 5 × 10^6 g mol^{-1}, Sigma-Aldrich) were used as purchased. Lithium perchlorate ($LiClO_4$, 99.5%, Sigma-Aldrich) was dried at 50 °C under vacuum overnight before use. Trifluoromethanesulfonamide ($CF_3SO_2NH_2$) was a generous gift from Solvay.

4.3. Synthesis and characterization of the neat salt

4.3.1. Synthesis of the neat salt

The synthetic route for the potassium benzenesulfonyl (trifluoromethanesulfonyl)imide (KBTFSI) and lithium benzenesulfonyl (trifluoromethanesulfonyl)imide (LiBTFSI) is shown in **Scheme 4.1**, and detailed synthesis process of the salts is given as below. Firstly, the staring material benzenesulfonyl chloride (17.67 g, 100 mmol) was dissolved in 150 mL ACN and then the stoichiometric potassium trifluoromethanesulfonamide (18.67g, 100 mol) in 100 mL ACN was added slowly into the benzenesulfonyl chloride/ACN solution under Argon flow. After that, triethylamine (15 mL, 200 mmol) was added and the solution was left for stirring and refluxing at room temperature overnight with Argon protection.

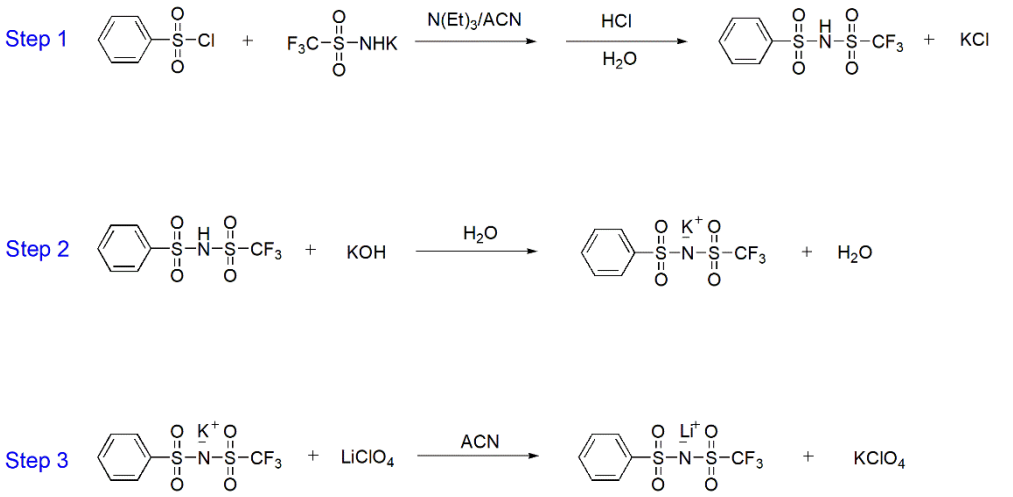

Scheme 4.1. Synthetic route of the potassium and lithium salt.

Then, ACN solvent was removed under vacuum and the obtained crude product was acidified by dilute (ca. 5 wt%) HCl aqueous solution and extracted with toluene. The removal of solvents gave benzenesulfonyl (trifluoromethanesulfonyl)imide acid as a viscous liquid. Lastly, this acid was readily transformed by slow neutralization procedure with KOH in water. The recrystallization of the crude product using toluene/acetone mixture afforded KBTFSI as a white powder (15.6 g; yield: 54%). The LiBTFSI was synthesized by cation exchange via the reaction between KBTFSI and $LiClO_4$ in ACN (**Scheme 4.1)**. Nuclear magnetic resonance (NMR) was used to characterize the structure of the lithium salt, and some abbreviations (e.g., s, singlet; d, doublet; m, multiplet) are used to describe the multiplicity in NMR spectra. ^{1}H NMR (300 MHz, D_2O, ppm): δ = 7.97 (d, 2H), δ = 7.72 (m, 1H), δ = 7.76 (m, 2H). ^{19}F NMR (282 MHz, D_2O, ppm):

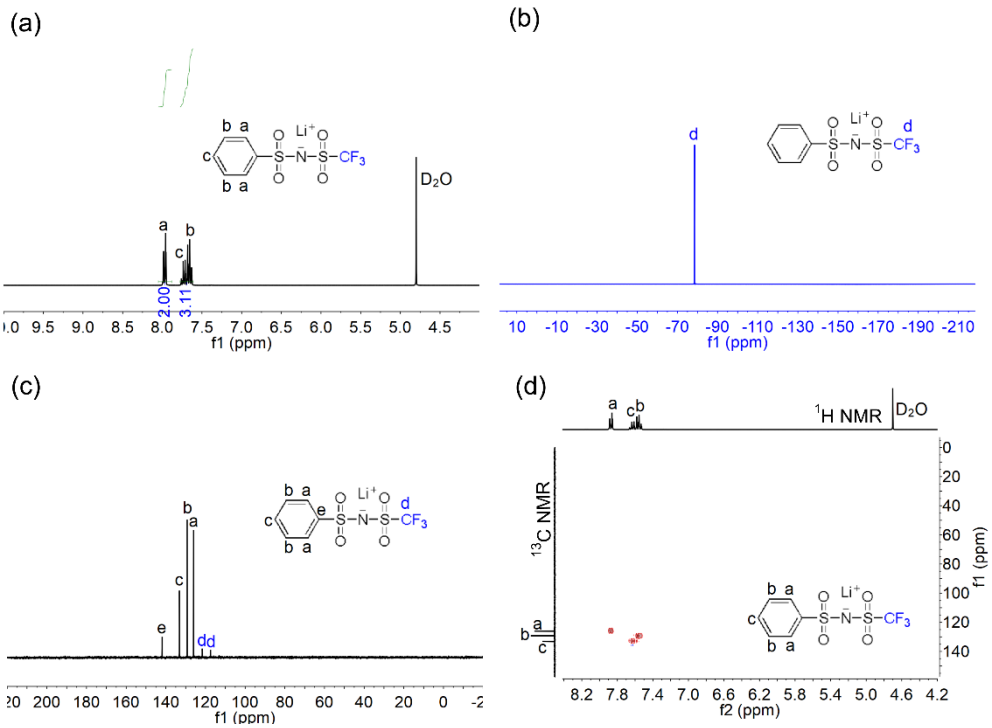

Figure 4.1. Nuclear magnetic resonance (NMR) spectra of the synthesized LiBTFSI salt: (a) ^{1}H NMR, (b) ^{19}F NMR, (c) ^{13}C NMR and (c) edited 2D heteronuclear single quantum coherence (HSQC).

δ = –78.55 (3F). ^{13}C NMR (75.5 MHz, D_2O, ppm): δ = 121.65 (t, 1C), δ = 126.02 (s, 1C), δ = 129.22 (s, 1C), δ = 133.14 (s, 1C), δ = 141.81 (s, 1C). The characterization spectra are shown in **Figure 4.1**.

4.3.2. Characterization of the neat salt

4.3.2.1. Nuclear magnetic resonance spectra

In this Chapter, the lithium salt LiBTFSI was synthesized by cation exchange using the KBTFSI and $LiClO_4$ in ACN, and the processes of the

synthesis of the salts are presented in details in the synthesis part. The structure of LiBTFSI salt was characterized by NMR spectra. As shown in **Figure 4.1a**, characteristic peaks in the range of δ = 7.63–7.99 ppm related to the protons in the benzene ring are observed in the ^{1}H NMR spectrum. Moreover, the characteristic peak of CF_3 group is observed at δ = –78.55 ppm in the ^{19}F NMR, which is also detected in the ^{13}C NMR spectrum at δ = 121.65 ppm (**Figure 4.1b, c)**, indicating that the CF_3SO_2N– moiety is successfully grafted onto the benzene-based moiety. More importantly, the heteronuclear single quantum coherence spectroscopy (HSQC, **Figure 4.1d**) shows an unambiguous correlation between the carbon atoms and their corresponding hydrogen atoms. All these results indicate that the LiBTFSI salt is successful synthesized in this work.

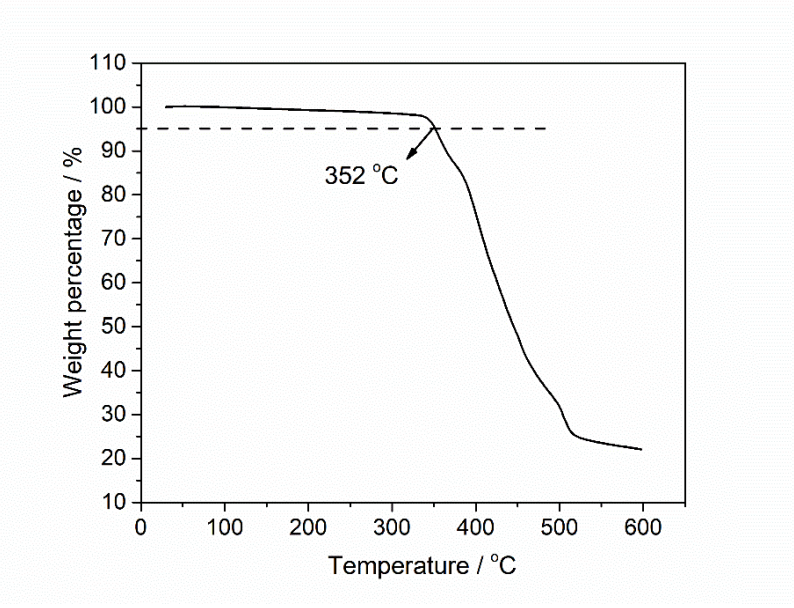

Figure 4.2. Thermogravimetric analysis (TGA) of the synthesized LiBTFSI salt.

4.3.2.2. Thermal stability

Thermal stability of lithium salts is an important parameter that can determine the safety of a battery. Thermogravimetric analysis (TGA) of the synthesized LiBTFSI salt is shown in **Figure 4.2**, it can be seen from **Figure 4.2** that although the decomposition temperature (T_d) of the LiBTFSI salt is slightly lower than thar of the commonly used lithium bis(trifluoromethanesulfonyl)imide (LiTFSI) salt (i.e., 352 ℃ for LiBTFSI vs. 384 ℃ for LiTFSI),[14] which still is capable to be used as a conducting salt for poly (ethylene oxide) (PEO)-based lithium metal batteries whose operating temperature is around 70 ℃.

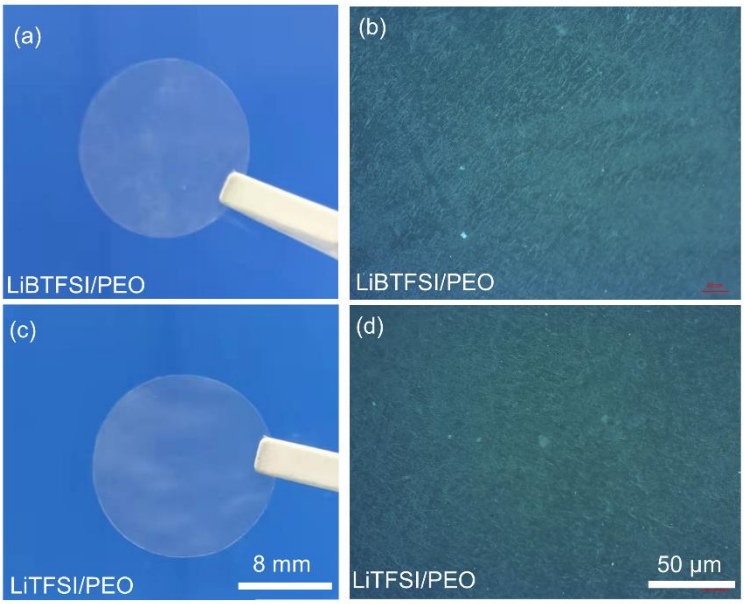

Figure 4.3. Digital and optical images of SPEs. (a,b) LiBTFSI-based SPEs. (c,d) LiTFSI-based SPEs. ($EO/Li^+ = 20$)

4.4. SPEs characterization

4.4.1. Morphological characterization of SPEs

SPEs comprising of the synthesized LiBTFSI or LiTFSI and PEO matrix were prepared by the conventional solvent casting method using acetonitrile (ACN) as secondary solvent, and the details of the electrolyte preparation are described in the experimental section in Chapter 2. As shown in **Figure 4.3a** and **c**, both the LiBTFSI and LiTFSI-based SPEs are self-standing and transparent membranes with good toughness, which can facilitate to suppress the notorious lithium dendrites growth on the lithium metal anode upon repeated chare/discharge process.

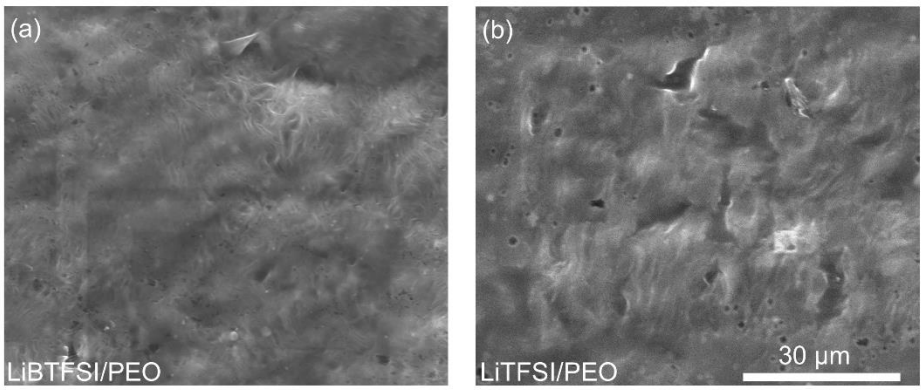

Figure 4.4. Scanning electron microscope (SEM) images of SPEs. (a) LiBTFSI-based SPEs, (b) LiTFSI-based SPEs. ($EO/Li^+ = 20$)

When subjected to micro scale, it can be seen from the optical images (**Figure 4.3b** and **d**) that both of these two SPEs possess uniform and homogenous surface morphology, which strongly demonstrates that both the LiBTFSI and LiTFSI salts are facilely dissolved in PEO matrix. In addition, surface morphology of these two PEO-based SPEs are also detected by the scanning electron microscope (SEM), as displayed in **Figure 4.4**, uniform

and smooth surfaces are observed although micro holes scatter on the surfaces due to the electron impact when carrying out the measurements.

4.4.2. Thermogravimetric analysis (TGA)

The state-of-the-art lithium-ion batteries (LIBs) have been suffering from the safety issue stemmed from the application of flammable organic liquid electrolytes which can get fire or even explosion under abuse conditions. Replacing liquid electrolytes with SPEs possessing better thermal stability could definitely boost the safety of lithium batteries. In this chapter, thermal stabilities of the PEO-based SPEs (i.e., LiBTFSI/PEO and LiTFSI/PEO) are evaluated by thermogravimetric analysis (TGA), the TGA traces of these two SPEs are shown in **Figure 4.5**. The decomposition temperature (T_d) of the LiTFSI/PEO-based SPE is 385 ℃ which is well consistent previous reported literature.[15] The LiBTFSI/PEO-based SPE presents a slightly lower T_d of 378 ℃ compared with the LiTFSI/PEO-based one, which could be explained by the lower T_d of the neat LiBTFSI salt than that of the neat LiTFSI salt (see **Figure 4.2**). Indeed, both of these two SPEs possess excellent thermal stability with high T_d > 300 ℃, which are suitable for the PEO-based all-solid-state lithium-metal batteries (ASSLMBs) where the operating temperatures are lower than 100 ℃.

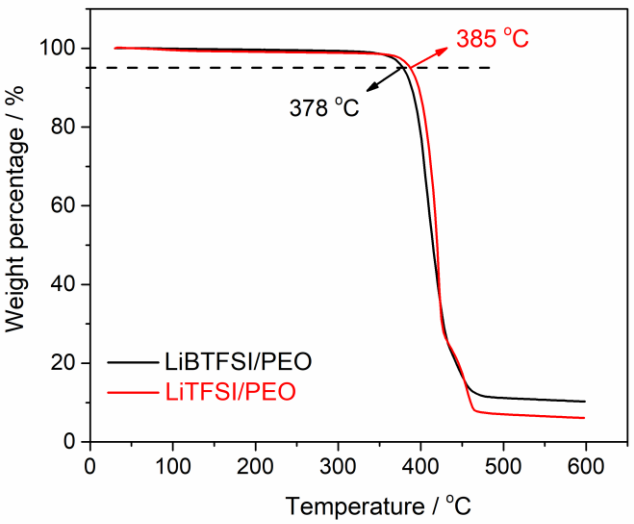

Figure 4.5. Thermogravimetric analysis (TGA) of the PEO-based LiBTFSI and LiTFSI SPEs (EO/Li^+ = 20).

4.4.3. Differential scanning calorimetry analysis (DSC)

The flexibility of SPEs is of great importance for facilitating the ionic migration in AASLMBs, and the flexibility of a SPEs could be partially revealed by the glass transition behaviour of the SPEs from differential scanning calorimetry analysis (DSC) result. As shown in **Figure 4.6**, obvious endothermic peaks in the DSC traces at ca. 60 °C, generating from the melting transitions of PEO matrices, which clearly confirms the existence of crystalline phases in these two PEO-based electrolytes. In addition, the LiBTFSI/PEO-based electrolyte displays higher glass transition temperature (T_g; i.e., T_g = –21 °C for LiBTFSI/PEO vs. T_g = –40 °C for LiTFSI/PEO) and higher crystallinities (χ_c; i.e., χ_c = 51 for LiBTFSI/PEO vs. χ_c = 48 for LiTFSI/PEO, **Table 4.1**) compared to LiTFSI/PEO-based

electrolyte. This might be ascribed to the inferior plasticizing effect of benzene moiety in the LiBTFSI salt.

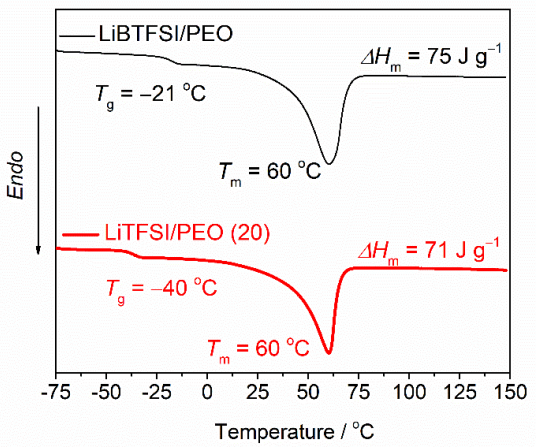

Figure 4.6. Differential scanning calorimetry analysis (DSC) of the PEO-based LiBTFSI and LiTFSI SPEs (EO/Li^+ = 20).

Table 4.1. Characterization data for the phase behaviours of the LiX/PEO (X = BTFSI or TFSI) electrolytes.

Samples	T_g [a] / °C	T_m [b] / °C	ΔH_m [c] / J g^{-1}	χ_c [d] / %
LiBTFSI/PEO (20)	−21	60	75	51
LiTFSI/PEO (20)	−40	60	71	48

[a] Glass transition temperature (°C); [b] melting point (°C); [c] enthalpy of melting (J g^{-1}); [d] the crystallinity of the polymer electrolytes is calculated by ($\Delta H_m/\Delta H_{PEO} f_{PEO}$) × 100%, where ΔH_m is the melting enthalpy of the electrolytes, and ΔH_{PEO} is the value of 196.4 J g^{-1} for PEO perfect crystals reported in literature[16] for the melting enthalpy of 100% crystalline PEO, and f_{PEO} is the PEO weight fraction of the electrolyte samples.

4.4.4. X-ray diffraction analysis (XRD)

The crystallinities of these two SPEs are also evaluated by X-ray diffractometer analysis (XRD). Normally, the neat PEO has two characteristic diffraction peaks at 19.36° and 23.72° with high density, which reflects the crystalline chain structure of the PEO host (set of planes (120) and (112)].[17] The peaks of PEO shifted to lower 2θ values after introducing LiTFSI and LiBTFSI (e.g., 2θ = 19.09, 23.41 for LiTFSI/PEO; 2θ = 19.10, 23.50 23.41 for LiBTFSI/PEO; **Figure 4.7**), which indicates the interaction between the Li^+ ions with ether oxygen of PEO. No other peaks appear in the XRD spectra of the SPEs, which suggests that the complete dissolution of lithium salt in the SPEs.[18] This also further confirms the complex formation between lithium salts and PEO matrices.[19] Noticeably, the peak intensity of the LiBTFSI/PEO is stronger compared to the LiTFSI/PEO electrolyte, meaning the stronger plasticizing effect of the two $–SO_2CF_3$ moieties in the $TFSI^–$ than that of the $BTFSI^–$ anion comprising only one $–SO_2CF_3$ moiety.

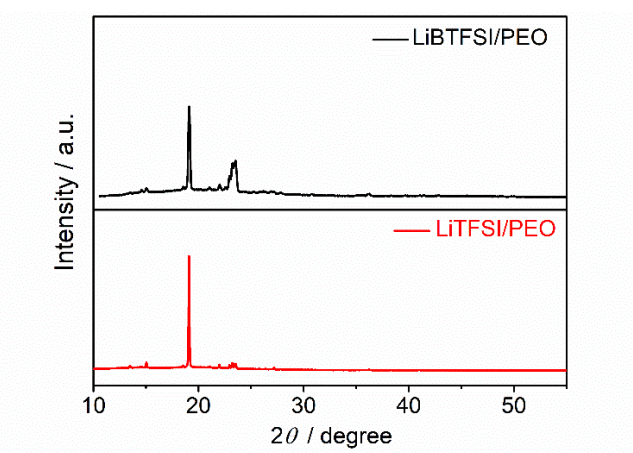

Figure 4.7. XRD patterns of the PEO-based LiBTFSI and LiTFSI SPEs (EO/Li^+ = 20).

4.4.5. Ionic conductivity

Ionic conductivities (σ_{total}) of these two SPEs are measured using symmetric stainless steel (SS | SPEs | SS) by the electrochemical impedance spectroscopy (EIS) on a VMP3 potentiostat (Biologic), the cell configuration and the experimental details of this measurement are displayed in Chapter 2. The ionic conductivities values of these two SPEs change obviously at around 60 ℃ due to the melting of the excess PEO matrices, which is well in agreement with DSC results shown in **Figure 4.6**. Arrhenius plots of ionic conductivities for these two SPEs are presented **Figure 4.8**, the ionic conductivity of LiBTFSI/PEO is lower than that of the LiTFSI/PEO based one over the whole temperature range, which might be due to its weaker plasticizing effect of the $BTFSI^-$ anion. Nevertheless, the LiBTFSI/PEO shows an acceptable σ_{total} of 3.6×10^{-4} S cm^{-1} at 70 ℃ which is still suitable for AASLMBs although the σ_{total} is lower compared with that of LiTFSI/PEO (i.e., $\sigma_{total} = 6.8 \times 10^{-4}$ S cm^{-1} at 70 ℃).

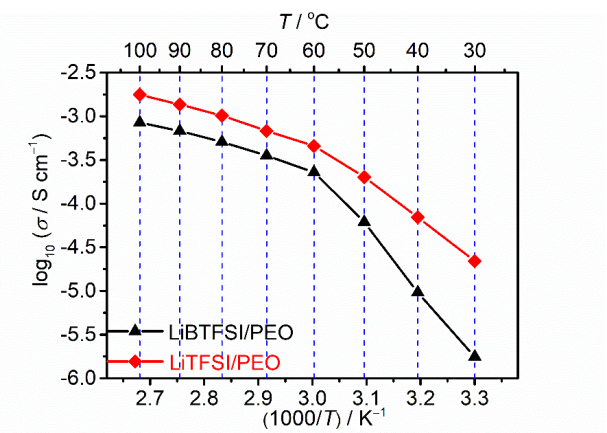

Figure 4.8. Arrhenius plots of ionic conductivity for PEO-based LiBTFSI and LiTFSI SPEs ($EO/Li^+ = 20$).

4.4.6. Lithium-ion transference number

Li^+ conduction in polymer electrolytes is associated with the segmental motion of the polymer matrix such as PEO in the amorphous phase, in which the Li^+ ions interact with the ether oxygen atoms by the Lewis acid-base interactions.[20] However, the counter anions interact more weakly with the ether oxygen atoms than that of Li^+ in the polymer, hence transporting much easier compared to Li^+ ions.[21] Consequently, a major problem of dual ionic conduction in polymer electrolytes is the low Li^+ ion transference number (T_{Li^+}) which can lead to deleterious salt concentration gradients.[20] The occurrence of salt concentration gradients can further trigger a concentration polarization and thus bring about some poor performances of the lithium ion batteries, such as voltage loss, high internal resistances, dendrites and unexpected side reactions, which can cause premature failures of the batteries.[22] Electrochemical T_{Li^+} of these two SPEs were obtained using a VMP3 potentiostat (Biologic) and a combination of alternating-current (AC) EIS and direct-current (DC) polarization methods suggested by Hu *et al.*[23] The T_{Li^+} were calculated by Equation [4.1]:

$$T_{\mathrm{Li}}^{+} = \frac{V_{\mathrm{DC}}}{I_{\mathrm{DC}} \times R_{\mathrm{cell}}} \qquad [4.1]$$

Where, V_{DC} is the DC polarization voltage (10 mV), I_{DC} is the stable current (I_{DC}, in mA) after the polarization process and R_{cell} is the total resistance of the Li° | SPEs | Li°. The temperature was accurately controlled and set to 70 ^{o}C (± 1 ^{o}C) for all measurements using an electro-thermostatic oven (Lan technics, Model DHG).

Table 4.2. Calculated values of lithium-ion transference numbers (T_{Li^+}) of the LiBTFSI-based SPEs at 70 ℃.

Samples (LiBTFSI/PEO)	I_{ss} [a] / μA	R_{cell} [b] / Ω	ΔV [c] / mV	T_{Li^+} [d]
Cell A	28.16	244	10	0.687
Cell B	17.54	391	10	0.686
Cell C	16.15	427	10	0.690
Cell D	17.58	391	10	0.687

[a] Steady-state current obtained from the DC polarization; [b] total resistances of Li° symmetric cell; [c] the DC voltage subjected to the polarization; [d] calculated by Equation [4.1].

As shown in **Table 4.2**, the LiBTFSI/PEO exhibits a much higher T_{Li^+} of 0.69 compared with that of the LiTFSI/PEO-based SPE (i.e., T_{Li^+} = 0.20 for LiTFSI/PEO at 70 ℃),[24] which might be due to the larger volume of the $BTFSI^-$ anion and stronger intermolecular/intramolecular interactions, e.g., intermolecular π–π stacking of the $BTFSI^-$ anion, intramolecular H bonds between $BTFSI^-$ anion and PEO matrix.

Enhancing the mobility of lithium cations in polymer electrolytes is essential for mitigating the concentration gradient and internal cell polarization, and thereby improving the stability and cycle life of rechargeable lithium metal batteries. The lithium-ion conductivity (σ_{Li^+}) of the PEO-based SPE is calculated by Equation [4.2]:

$$\sigma_{Li}^{+} = \sigma_{total} \times T_{Li}^{+} \qquad [4.2]$$

Wherein, the σ_{Li^+}, σ_{total}, and T_{Li^+} are the lithium-ion conductivity, total ionic conductivity and lithium-ion transference number of a SPE, respectively.

Table 4.3. Calculated values of lithium-ion conductivity (σ_{Li^+}) for the LiBTFSI/PEO and LiTFSI/PEO-based SPEs at 70 ℃.

Samples	σ_{total} [a] / S cm^{-1}	T_{Li^+} [b]	σ_{Li^+} [c] / S cm^{-1}
LiBTFSI/PEO	3.60×10^{-4}	0.69	2.48×10^{-4}
LiTFSI/PEO	6.80×10^{-4}	0.20	1.38×10^{-4}

[a] Total ionic conductivity of the SPEs; [b] lithium-ion transference number of the SPEs; [c] lithium-ion conductivity of the SPEs, which is calculated by Equation [4.2]. The T_{Li^+} value of LiTFSI/PEO is reproduced from our previous literature Ref. [24]

Benefiting from its higher T_{Li^+}, the LiBTFSI/PEO-based SPE shows a higher lithium-ion conductivity (σ_{Li^+}) than that of the LiTFSI/PEO-based SPE, e.g., $\sigma_{Li^+} = 2.48 \times 10^{-4}$ S cm^{-1} (LiBTFSI/PEO) vs. $\sigma_{Li^+} = 1.38 \times 10^{-4}$ S cm^{-1} (LiTFSI/PEO at 70 ℃), as shown in **Table 4.3**.

4.4.7. Electrochemical stability

The electrochemical stability window (ESW) of an electrolyte is measured as the voltage domain between the onset of reduction and that of oxidation. The ESW is a fundamental parameter for choosing SPEs as solid electrolytes in ASSLMBs. To meet the practical application, the SPEs for ASSLMBs should possess a high oxidation potential to appropriately and compatibly couple with high-voltage cathode materials.

4.4.7.1. Anodic stability

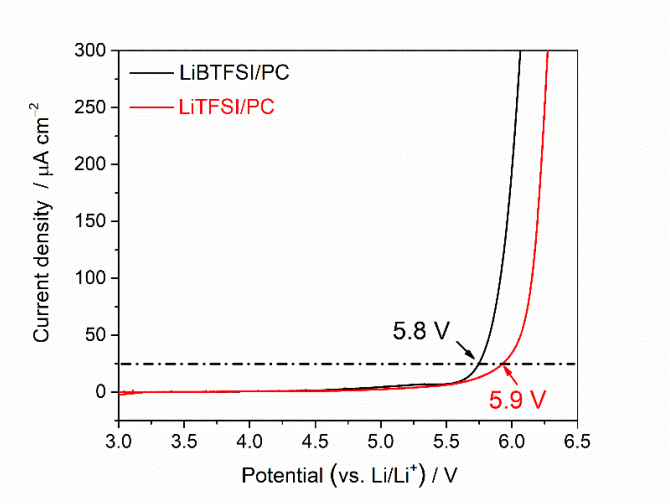

Figure 4.9. Linear sweep voltammogram (LSV) of the 0.1 M LiX/PC (X= BTFSI or TFSI) electrolytes.

Anodic stabilities of the electrolytes in this chapter are determined by linear sweep voltammogram (LSV) measurement using a VMP3 potentiostat (Biologic). To determine the anodic stability of the salts, LSV experiments were performed in both liquid-based electrolyte at 25 °C and PEO-based electrolytes at 70 °C, respectively. For the liquid electrolytes, propylene carbonate (PC) was used as the solvent for this measurement as it possesses high anodic stability that can help to determine the stability of the anions of dissolved lithium salts without the interference of solvent oxidation.[25] [12] Therefore, 0.1 M LiX/PC (X= BTFSI or TFSI) electrolytes were prepared in an Argon-filled glove box with H_2O and O_2 content less than 0.1 ppm. In addition, a three-electrode cell with platinum (surface area: 0.0314 cm^{-2}) as working electrode, Li° disks as both counter and reference electrodes were

used to perform this LSV measurement. The LSV of profiles of these two 0.1 M LiX/PC (X= BTFSI or TFSI) electrolytes are displayed in **Figure 4.9**, the LiBTFSI/PC exhibits a slightly lower anodic stability compared to the LiTFSI/PC electrolyte, e.g., 5.8 V Li/Li^+ for LiBTFSI/PC vs. 5.9 V Li/Li^+ for LiTFSI/PC, which might to due to the lower delocalized of the $BTFSI^-$ anion compared to the $TFSI^-$ anion.

For PEO-based SPEs, a two-electrode cell using Li° | SPEs | SS (surface area: 0.0707 cm^{-2}) was adopted. Obvious onsets of current density at ca. 4.0 V Li/Li^+ attributed to the oxidation of PEO chains were observed for both LiBTFSI/PEO and LiTFSI/PEO-based SPEs (see in **Figure 4.10**), which is well consistent with previous reports.[11] [26-27] Nevertheless, both of these two PEO-based SPEs are suitable for < 4 V-class ASSLMBs, such as Li° || $LiFePO_4$ and Li° || S batteries.

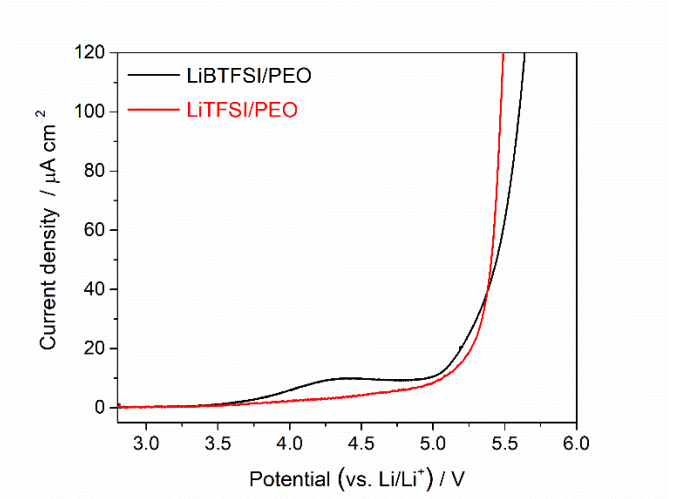

Figure 4.10. LSV profiles of the PEO-based LiBTFSI and LiTFSI SPEs at 70 ℃ (EO/Li^+ = 20).

4.4.7.2. Cathodic stability

Electrochemical cathodic stability of the SPEs was determined by cyclic voltammetry (CV) in a VMP3 potentiostat (Biologic). A CR2032 type Li ||° Cu coin cell was used comprising copper disk (surface area: 0.0707 cm^{-2}) as working electrode and Li° disk as both counter and reference electrodes. As shown in **Figure 4.11**, both electrolytes show clear redox currents that are associated with Li^+ plating/stripping on Cu electrodes. However, the current density of the LiTFSI/PEO-based cell is much higher than that of the LiBTFSI/PEO, which might due to its higher ionic conductivity as discussed above (e.g., σ_{total} = 6.8 × 10^{-4} S cm^{-1} for LiTFSI/PEO vs. σ_{total} = 3.6 × 10^{-4} S cm^{-1} for LiBTFSI/PEO at 70 °C).

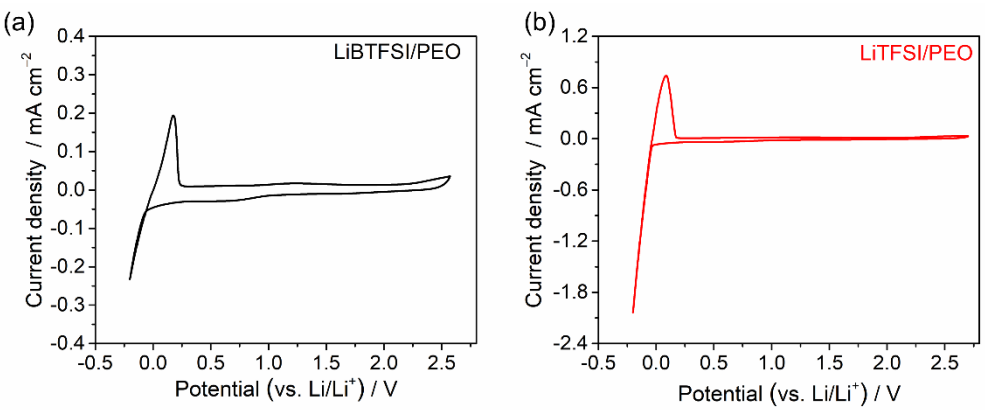

Figure 4.11. Cyclic voltammetry (CV) profiles of the PEO-based LiBTFSI (a) and LiTFSI SPEs (b) at 70 °C at a scan rate of 1 mV s^{-1}.

4.5. Cell performance

4.5.1. Li° || Li° cells

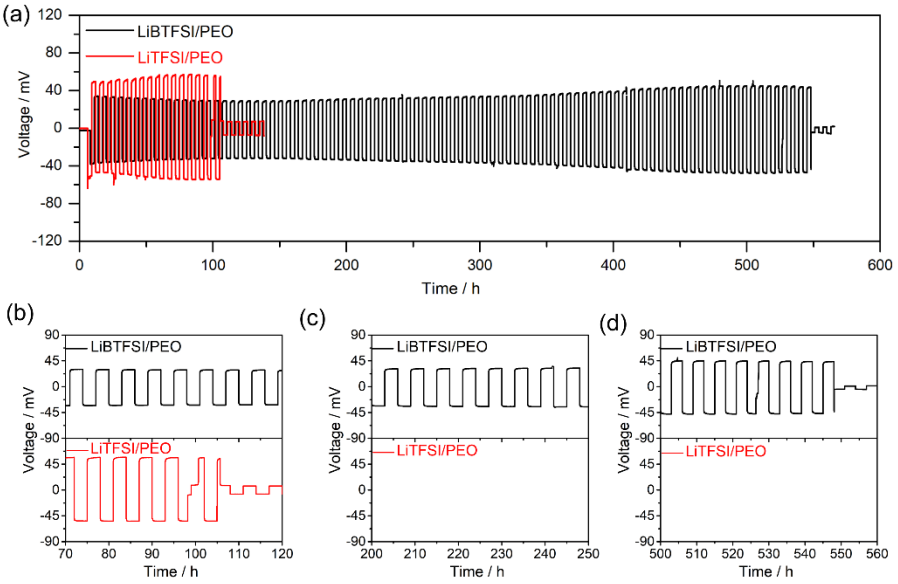

Figure 4.12. (a) Galvanostatic cycling of Li° anode in PEO-based electrolytes at 70 ℃ (current density: 0.1 mA cm^{-2}; duration of half-cycle: 3 h). (d–f) Zoomed-in plots of the Li° symmetric cells in the range of (d) 70–120 h, (e) 200–250 h, and (f) 500–560 h.

For the SPEs-based Li° || Li° cells, galvanostatic cycling of Li° symmetrical cells (areal of Li° disk: 1.54 cm^{-2}) are carried out using Neware® battery testers at a current density of 0.1 mA cm^{-2}. The duration of each half-cycle is 3 h for the measurement. The lithium plating and stripping performance of these two SPEs is shown in **Figure 4.12**, under an electrochemical condition, the Li° || Li° symmetric cells using the LiTFSI/PEO SPE encounter short-circuit after around 100 h owing to the generation of dendritic Li° (**Figure 4.12b**), which could penetrate through the SPE membrane and cause cell premature failure.[28] This result is well consistent with our previous published works as well as literature published

by other groups.[24, 29-30] As for comparison, the LiBTFSI/PEO-based cell could stably operate for more than 540 h with absence of voltage fluctuation under the same conditions (**Figure 4.12**), indicating that the solid electrolyte interface (SEI) formed on the Li° anode in the LiBTFSI/PEO-based cell seems to be more robust and compact, which could inhibit the continuous Li° dendrites growth and thus enable the cell a long-life cycle. In addition, the higher T_{Li^+} of the LiBTFSI/PEO based SPEs may also help to reduce the nucleation of dendrites.[31]

4.5.2. Li° || LFP cells

On account of above-mentioned attractive physicochemical and electrochemical of the LiBTFSI/PEO SPE, the feasibility of LiBTFSI/PEO as an electrolyte for ASSLMBs is eventually evaluated in a full Li° || LFP cell configuration. The LFP electrodes with a high areal loading of 4.0 mg cm^{-2} were prepared by conventional casting method, and all the Li° || LFP cells are assembled in an argon-filled glovebox. Afterwards, these cells are subjected to three formation cycles at a rate of C/5 and then charged and discharged with a constant *C*-rate of C/3 for constant cycling in a voltage range (2.5-3.7 V), and the corresponding charge/discharge performance is shown in **Figure 4.13**. It can be clearly seen that the LiBTFSI/PEO-based cell displayed superior performance compared with that of the LiTFSI/PEO-based cell, as reflected by the initial capacity as well as cycle life. The LiTFSI/PEO-based cell delivered an initial discharge capacity of 114 mAh g^{-1} and showed a seriously overcharging process at 11^{th} cycle (see **Figure 4.13c**) due to the formation of soft dendrites on Li° anode under a high LFP

loading or high current density, which is well consistent with previous reported literature.[29-30]

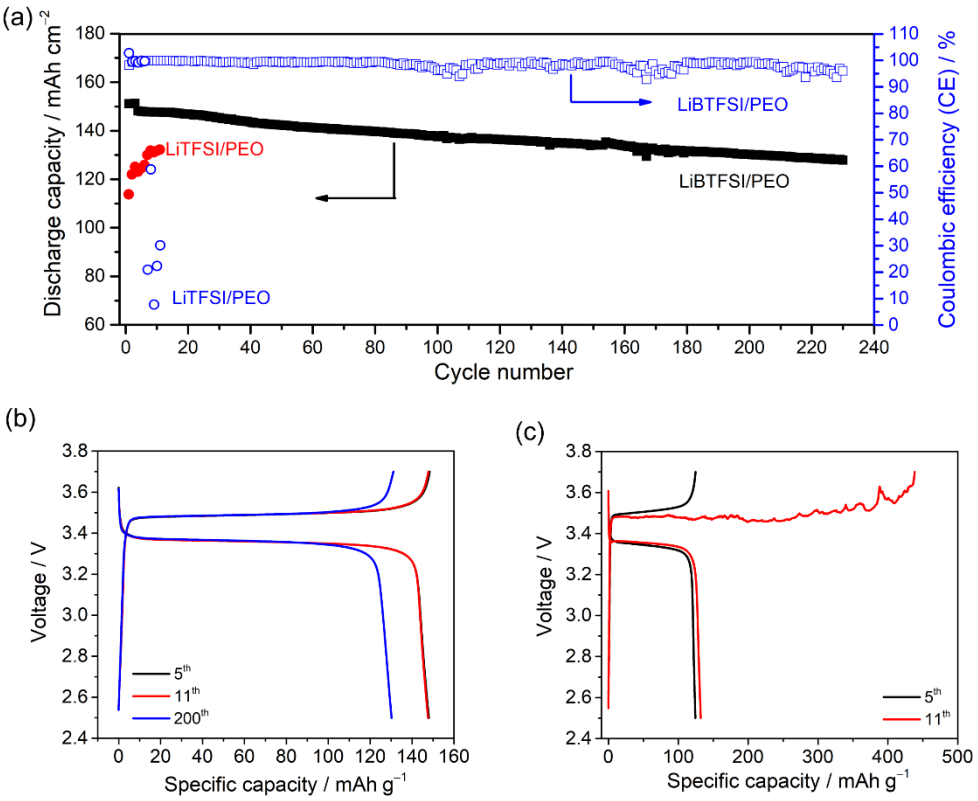

Figure 4.13. Cycling performance of solid-state lithium metal polymer cells using LiBTFSI/PEO SPE. (a) Long-term cycling performance of the Li° || $LiFePO_4$ (LFP) cells (three formation cycles at rate of C/5 and then constant cycling at C/3). (b, c) Discharge/charge profiles of the Li° || LFP cells at 70 °C: (b) LiBTFSI/PEO and (c) LiTFSI/PEO.

Notably, replacement of the high areal loading of LFP with a lower one (e.g., decrease from 4.0 mg cm^{-2} to 2.65 mg cm^{-2}) can significantly improve the cycling performance LiTFSI-based Li° || LFP cells. As shown in **Figure**

4.14a, the LiTFSI-based Li° || LFP cell could be operated for 150 cycles with a high discharge capacity of 146 mAh g^{-1} without short-circuits phenomena. In addition, the LiTFSI-based Li° || LFP cell exhibits stable charge/discharge profiles (**Figure 4.14b**), and more importantly, there is no overcharging process is observed, which indicates that the overcharging phenomenon happens in a high LFP areal capacity cell with the LiTFSI/PEO SPE is attributed to the lithium dendrites growth under a high current density.

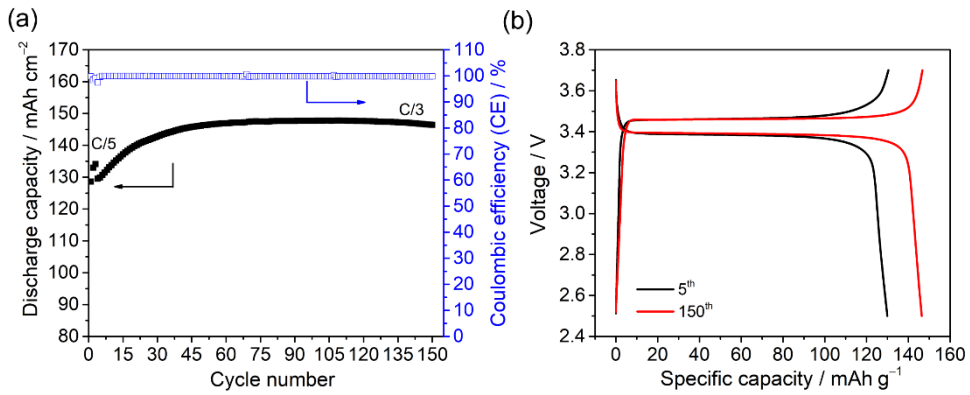

Figure 4.14. Cycling performance of solid-state lithium metal polymer cells using LiTFSI/PEO SPE with a low LFP areal loading of 2.65 mg cm^{-2} (EO/Li = 20). (a) Long-term cycling performance of the Li° || $LiFePO_4$ (LFP) cell with LiTFSI/PEO SPE. (b) Discharge/charge profiles of LiTFSI/PEO-based Li° || LFP cells with a low LFP areal loading.

The rate capability of these two PEO-based SPEs were evaluated at different *C*-rate and the results are shown in **Figure 4.15**. The LiBTFSI/PEO-based Li° || LFP cell could be operated at different *C*-rate (e.g., from C/5 to 1C) with good Coulombic efficiency close to 100% and stable charge and discharge plateaus (**Figure 4.15a** and **c**). The discharge capacities of the LiBTFSI/PEO-based Li° || LFP cell at different *C*-rate are

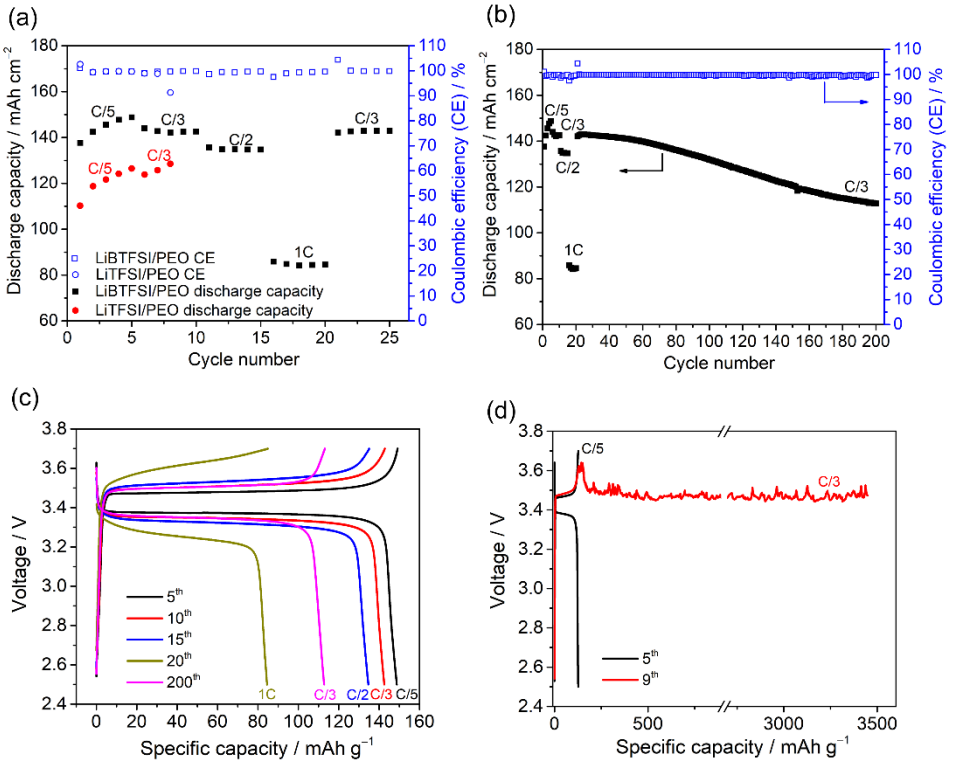

Figure 4.15. Rate performance of solid-state lithium metal polymer cells using LiX/PEO (X = BTFSI or TFSI, EO/Li = 20). (a) Rate capability of these two PEO-based Li° || LFP cells under different currents. (b) Cyclability of these two cells after *C*-rate tests. (c, d) Discharge/charge profiles of the Li° || LFP cells at 70 °C and different current densities: (c) LiBTFSI/PEO and (d) LiTFSI/PEO.

148.8 mAh g^{-1} (C/5), 142.6 mAh g^{-1} (C/3), 134.7 mAh g^{-1} (C/2) and 84.5 mAh g^{-1} (1C), respectively. In sharp contrast, the overcharge process occurs in the LiTFSI/PEO-based Li° || LFP cell (see the overcharged profile in **Figure 4.15d**) and the cell could be only cycled at C/5 under this higher areal LFP loading. More importantly, the LiBTFSI/PEO-based Li° || LFP cells exbibit excellent cycling performance over 200 cycles when the current density returns to C/3, as shown in **Figure 4.15b**. All these results mentioned

above demonstrate that the $BTFSI^-$ possesses superior compatibility with both Li° anode and LFP cathode, which testifies that the anions play a pivotal role in dictating the electrochemical properties of PEO-based Li° || LFP cells.

4.6. Conclusion

In summary, we report a highly lithium-ion conductive PEO-based SPE using a novel benzene-based lithium salt (LiBTFSI). As a result, the LiBTFSI-based SPE shows three times higher lithium-ion transference number and higher lithium-ion conductivity compared with the conventional LiTFSI-based SPEs. This could be attributed to the strong intermolecular and intramolecular interactions between the $BTFSI^-$ anion and PEO matrices and with itself. More importantly, the LiBTFSI/PEO-based SPE presents excellent compatibility with lithium anode as shown in the prolonged cycled Li° || Li° cells, which also enables the solid-state Li° || $LiFePO_4$ cell with superior cycling performance. This work provides an efficient and facile strategy for attaining highly lithium-ion conductive and Li° electrode compatible SPEs, which sheds light on future exploration directions towards high-performance solid-state lithium batteries and other rechargeable batteries.

4.7 References

1. Tarascon, J. M.; Armand, M., Issues and challenges facing rechargeable lithium batteries. *Nature* **2001,** *414* (6861), 359-367.

2. Armand, M.; Tarascon, J. M., Building better batteries. *Nature* **2008,** *451* (7179), 652-657.

3. Lin, D.; Liu, Y.; Cui, Y., Reviving the lithium metal anode for high-energy batteries. *Nature nanotechnology* **2017,** *12* (3), 194.

4. Mauger, A.; Armand, M.; Julien, C. M.; Zaghib, K., Challenges and issues facing lithium metal for solid-state rechargeable batteries. *Journal of Power Sources* **2017,** *353*, 333-342.

5. Park, S.; Lee, J.-I.; Song, G.; Cho, S.; Han, D.-Y., Lithium Metal Interface Modification for High-Energy Batteries: Approaches and Characterization. *Batteries & Supercaps* **2020,** *n/a* (n/a).

6. Wang, R.; Cui, W.; Chu, F.; Wu, F., Lithium metal anodes: Present and future. *Journal of Energy Chemistry* **2020,** *48*, 145-159.

7. Zhang, H.; Armand, M., History of Solid Polymer Electrolyte ‐ Based Solid ‐ State Lithium Metal Batteries: A Personal Account. *Israel Journal of Chemistry* **2021,** *61* (1-2), 94-100.

8. Zhang, H.; Chen, Y.; Li, C.; Armand, M., Electrolyte and anode-electrolyte interphase in solid-state lithium metal polymer batteries: A perspective. *SusMat* **2021,** *n/a* (n/a).

9. Zhang, H.; Oteo, U.; Judez, X.; Martinez-Ibanez, M.; Aldalur, I.; Sanchez-Diez, E.; Li, C.; Carrasco, J.; Armand, M.; Zhu, H.; Forsyth, M., Enhanced Lithium-Ion Conductivity of Polymer Electrolytes by Selective Introduction of Hydrogen into the Anion. *Angew Chem Int Ed Engl* **2019,** *58* (23), 7829-7834.

10. Zhang, H.; Li, C.; Piszcz, M.; Coya, E.; Rojo, T.; Rodriguez-Martinez, L. M.; Armand, M.; Zhou, Z., Single lithium-ion conducting solid polymer electrolytes: advances and perspectives. *Chemical Society Reviews* **2017,** *46* (3), 797-815.

11. Zhang, H.; Chen, F.; Lakuntza, O.; Oteo, U.; Qiao, L.; Martinez ‐ Ibañez, M.; Zhu, H.; Carrasco, J.; Forsyth, M.; Armand, M., Suppressed mobility of negative charges in polymer electrolytes with an ether ‐ functionalized anion. *Angewandte Chemie* **2019,** *131* (35), 12198-12203.

12. Zhang, H.; Oteo, U.; Zhu, H.; Judez, X.; Martinez-Ibañez, M.; Aldalur, I.; Sanchez-Diez, E.; Li, C.; Carrasco, J.; Forsyth, M., Enhanced Li ‑ ion conductivity of polymer electrolytes with selective introduction of hydrogen in the anion. *Angewandte Chemie* **2019**.

13. Zhang, H.; Oteo, U.; Judez, X.; Eshetu, G. G.; Martinez-Ibanez, M.; Carrasco, J.; Li, C.; Armand, M., Designer anion enabling solid-state lithium-sulfur batteries. *Joule* **2019,** *3* (7), 1689-1702.

14. Hagiwara, R.; Tamaki, K.; Kubota, K.; Goto, T.; Nohira, T., Thermal Properties of Mixed Alkali Bis(trifluoromethylsulfonyl)amides. *Journal of Chemical & Engineering Data* **2008,** *53* (2), 355-358.

15. Eshetu, G. G.; Judez, X.; Li, C.; Martinez-Ibañez, M.; Gracia, I.; Bondarchuk, O.; Carrasco, J.; Rodriguez-Martinez, L. M.; Zhang, H.; Armand, M., Ultrahigh Performance All Solid-State Lithium Sulfur Batteries: Salt Anion's Chemistry-Induced Anomalous Synergistic Effect. *Journal of the American Chemical Society* **2018,** *140* (31), 9921-9933.

16. Stolwijk, N. A.; Heddier, C.; Reschke, M.; Wiencierz, M.; Bokeloh, J.; Wilde, G., Salt-concentration dependence of the glass transition temperature in PEO–NaI and PEO–LiTFSI polymer electrolytes. *Macromolecules* **2013,** *46* (21), 8580-8588.

17. Dey, A.; Karan, S.; De, S. K., Effect of nanofillers on thermal and transport properties of potassium iodide–polyethylene oxide solid polymer electrolyte. *Solid State Communications* **2009,** *149* (31), 1282-1287.

18. Polu, A. R.; Rhee, H.-W., The effects of LiTDI salt and POSS-PEG (n= 4) hybrid nanoparticles on crystallinity and ionic conductivity of PEO based solid polymer electrolytes. *Science of Advanced Materials* **2016,** *8* (5), 931-940.

19. Polu, A. R.; Kumar, R.; Rhee, H.-W., Magnesium ion conducting solid polymer blend electrolyte based on biodegradable polymers and application in solid-state batteries. *Ionics* **2015,** *21* (1), 125-132.

20. Armand, M., The history of polymer electrolytes. *Solid State Ionics* **1994,** *69* (3-4), 309-319.

21. Guhathakurta, S.; Min, K., Lithium sulfonate promoted compatibilization in single ion conducting solid polymer electrolytes based on lithium salt of sulfonated polysulfone and polyether epoxy. *Polymer* **2010,** *51* (1), 211-221.

22. Sun, X.-G.; Kerr, J. B., Synthesis and characterization of network single ion conductors based on comb-branched polyepoxide ethers and lithium bis (allylmalonato) borate. *Macromolecules* **2006,** *39* (1), 362-372.

23. Suo, L.; Hu, Y.-S.; Li, H.; Armand, M.; Chen, L., A new class of solvent-in-salt electrolyte for high-energy rechargeable metallic lithium batteries. *Nature communications* **2013,** *4* (1), 1-9.

24. Qiao, L.; Oteo, U.; Zhang, Y.; Peña, S. R.; Martínez-Ibañez, M.; Santiago, A.; Cid, R.; Meabe, L.; Manzano, H.; Carrasco, J.; Zhang, H.; Armand, M., Trifluoromethyl-free anion for highly stable lithium metal polymer batteries. *Energy Storage Materials* **2020**.

25. Xu, K., Nonaqueous liquid electrolytes for lithium-based rechargeable batteries. *Chemical reviews* **2004,** *104* (10), 4303-4418.

26. Aldalur, I.; Martinez-Ibañez, M.; Piszcz, M.; Rodriguez-Martinez, L. M.; Zhang, H.; Armand, M., Lowering the operational temperature of all-solid-state lithium polymer cell with highly conductive and interfacially robust solid polymer electrolytes. *Journal of Power Sources* **2018,** *383*, 144-149.

27. Mindemark, J.; Lacey, M. J.; Bowden, T.; Brandell, D., Beyond PEO—Alternative host materials for Li+-conducting solid polymer electrolytes. *Progress in Polymer Science* **2018,** *81*, 114-143.

28. Cheng, X.-B.; Zhang, R.; Zhao, C.-Z.; Zhang, Q., Toward Safe Lithium Metal Anode in Rechargeable Batteries: A Review. *Chemical Reviews* **2017,** *117* (15), 10403-10473.

29. Yang, X.; Sun, Q.; Zhao, C.; Gao, X.; Adair, K.; Zhao, Y.; Luo, J.; Lin, X.; Liang, J.; Huang, H.; Zhang, L.; Lu, S.; Li, R.; Sun, X., Self-healing electrostatic shield enabling uniform lithium deposition in all-solid-state lithium batteries. *Energy Storage Materials* **2019,** *22*, 194-199.

30. Zhu, Z.; Lu, L.-L.; Yin, Y.; Shao, J.; Shen, B.; Yao, H.-B., High Rate and Stable Solid-State Lithium Metal Batteries Enabled by Electronic and Ionic Mixed Conducting Network Interlayers. *ACS Applied Materials & Interfaces* **2019,** *11* (18), 16578-16585.

31. Lu, Y.; Tikekar, M.; Mohanty, R.; Hendrickson, K.; Ma, L.; Archer, L. A., Stable Cycling of Lithium Metal Batteries Using High Transference Number Electrolytes. *Advanced Energy Materials* **2015,** *5* (9), 1402073.

Chapter 5

Solid polymer electrolytes comprising camphor-derived chiral salts for solid-state batteries

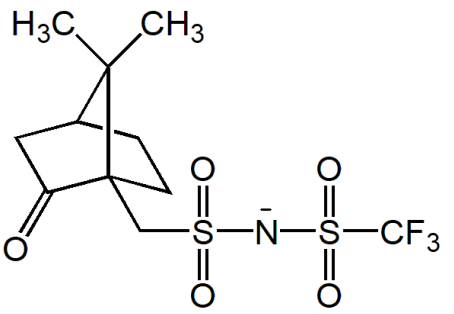

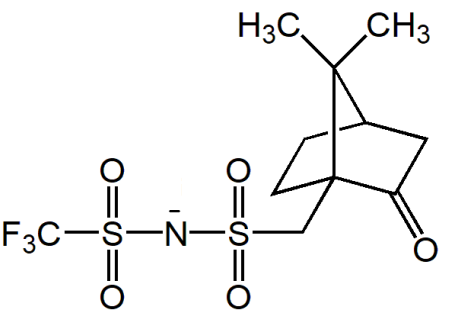

Chapter 5:

Solid polymer electrolytes comprising camphor-derived chiral salts for solid-state batteries

5.1. Introduction

With an ever-increasing demand of portable electronics and electric vehicles which both are essential elements for electrifying the modern society, rechargeable batteries with high safety and long cycle life have been highlighted in recent years.[1] Among all the existing technologies, lithium-ion batteries (LIBs) have been widely employed as power sources owing to their higher energy density and efficiency over traditional batteries (*e.g.*, lead-acid, nickel-metal hydride).[2-3] However, conventional LIBs containing organic liquid electrolytes suffer from safety concerns such as flammability, thermal runaway and even explosion under abusive conditions.[4] In addition, LIBs composed of graphite anodes and lithium transition metal oxide cathodes have more or less reached their theoretical limits in terms of specific and gravimetric energy densities.[5]

Solid polymer electrolytes (SPEs) have attracted great attention in the development of practical solid-state lithium metal (Li°) batteries (SSLMBs) ever since the perceptive proposal of using SPEs for rechargeable batteries by Armand in 1978.[6-10] Amongst the various polymer matrices suggested, poly(ethylene oxide) (PEO) possesses flexibility, processability, and excellent solvating ability toward a wide variety of salts, and has therefore been abundantly used as host material.[9] [11] The technological feasibility of PEO-based SPEs has been demonstrated by the implementation of Bluecar® and Bluebus® powered by Li° | SPEs | $LiFePO_4$ batteries in different cities and countries (*i.e.* Lyon, Bordeaux, Indianapolis, and Singapore).[12] Indeed, the chemistry of the lithium salt employed plays a pivotal role in dictating the physico-chemical and electrochemical performance of any SPE, and thus

also influences the performance of SSLMBs. The lithium bis(trifluoromethanesulfonyl)imide (LiTFSI) salt, first suggested as salt for SPEs in 1986,[13] possesses low lattice energy and the TFSI anion has a large structural flexibility, both due to the anion's highly delocalized negative charge and flexible center [*e.g.*, $–SO_2–N^{(–)}–SO_2–$][14] and has therefore been commonly used for SPE-based SSLMBs.[10] However, low lithium-ion transference number (T_{Li^+}) and poor solid electrolyte interphase (SEI) creating properties result in severe cell polarization and simultaneously notorious dendritic growth on the Li° anode.[15] Therefore, several new salts such as lithium (difluoromethanesulfonyl)(trifluoromethanesulfonyl)imide (LiDFTFSI)[16] and lithium (trifluoromethanesulfonyl)[*N*-bis(methoxyethyl)sulfonyl]imide (LiEFA)[17] have recently been proposed for SPE-based SSLMBs, both providing better transport numbers, cyclability, and interfacial compatibility. Yet, these SPEs do not really meet the stringent requirements for practical solid-state batteries, especially considering their relatively low ionic conductivities at ambient temperatures (*ca.* 10^{-4} S cm^{-1} at 40 °C).

Here we instead turn to investigate chiral Li-salts to create more performant SPEs. Chirality at the molecular level is ubiquitous in the natural world, *e.g.*, chiral amino acids and some natural sugars. Additionally, chiral compounds have attracted significant attention in a variety of fields such as photonics, biosensing, catalysis, medicine, and nanotechnology.[18-28] For example, Williams *et al.*[29] reported that a spiroborate with a chiral anion could be a promising candidate for chiral resolution. In addition, conducting chiral polymers such as polypyrrole (PPy), polythiophene (PTh), and

polyaniline (PAN) have demonstrated promise in electrochemical chiral sensing and electrochemical asymmetric synthesis.[30]

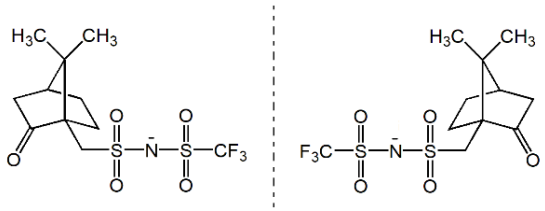

Scheme 5.1. Chemical structures of the chiral anions, RCTFSI and SCTFSI, synthesized from camphorsulfonic acid. Reproduced with permission from Ref. [31].

However, to date little attention has been paid to chiral salts and their impact on fundamental physico-chemical properties, *e.g.*, phase behavior, ionic conductivity, T_{Li^+}, *etc.*, of SPEs. In 2002, Béranger *et al.*[32] reported on SPEs using camphor-based chiral potassium salts synthesized from a commercially available camphorsulfonic acid *i.e.*, (R,S)-(±)-10-camphorsulfonic acid. The authors observed a slight difference in the ionic conductivities between the SPEs based on the R and the S enantiomers, RCTFSI and SCTFSI, respectively (**Scheme 5.1**), which basically should be impossible. Yet, PEO tends to adopt, both in pristine state and when wrapping around a cation, as in many SPEs, helical structure[33] and helices are chiral.[34] The question thus arises whether a chiral salt may induce a net chiral turn of the helices. In such a case, if the R and S enantiomers are expected to give identical ionic conductivities, there may be an effect, either enhancement or depression, when an artificial racemic mixture is used.[33 35 36 37-38 39] To verify or dismiss this hypothesis is only possible using very stringent ionic conductivity measurements – since the semi-crystalline PEO may influence the physical contact between the electrolyte and the

electrode(s), causing considerable experimental uncertainties.[40-41] In this work, we revisit this intriguing topic using the same anions but expand the type of cation from potassium to lithium. The fundamental properties of the neat salts and PEO-based SPEs are comprehensively investigated, aiming to elucidate the impact of chirality – if any.

5.2. Experimental

5.2.1 Materials

(1R)-(−)-10-camphorsulfonic acid (98%, > 96% enantiomeric excess, Sigma-Aldrich), (1S)-(+)-10-camphorsulfonic acid (98%, > 96% enantiomeric excess, Sigma-Aldrich), thionyl chloride ($SOCl_2$, 97%, Sigma-Aldrich), deuterium oxide (D_2O, Eurisotop, 99.8 wt% D), potassium carbonate (K_2CO_3, 99%, Sigma-Aldrich), dichloromethane (CH_2Cl_2, 99%, Fisher Chemical), acetonitrile (ACN, 99%, Scharlab), toluene (99.3%, Scharlab), triethylamine (99.5%, Sigma-Aldrich), and poly(ethylene oxide) (PEO, M_w = 5 × 10^6 g mol^{-1}, Sigma-Aldrich) were used as purchased. Lithium perchlorate ($LiClO_4$, 99.5%, Sigma-Aldrich) was dried at 50 °C under vacuum overnight before use. Trifluoromethanesulfonamide ($CF_3SO_2NH_2$) was a generous gift from Solvay.

5.2.2. Structural characterization

Nuclear magnetic resonance (NMR) spectra of the chiral salts were performed on Bruker (300 MHz for ^1H, 75.5 MHz for ^{13}C, and 282 MHz for ^{19}F NMR) using D_2O as deuterated solvent. Chemical shifts (δ) of the products are reported in ppm relative to residual solvent signals (D_2O, 4.80

ppm for ^{1}H-NMR). Some abbreviations (e.g., s, singlet; d, doublet; m, multiplet) are used to describe the multiplicity in NMR spectra.

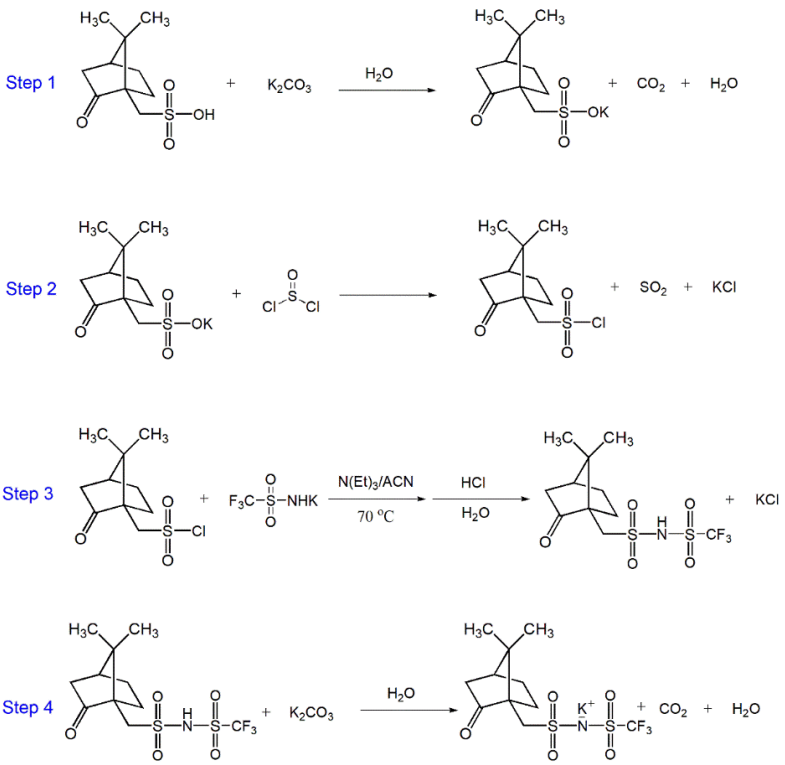

Scheme 5.2. The synthesis route of chiral potassium salts. Reproduced with permission from Ref. [31].

Raman and Fourier-transform infrared (FTIR) spectra of the neat salts and SPEs were measured on a Renishaw inVia confocal Raman spectrometer (serial number 16H981) and a Fourier-transform infrared spectrometer (Bruker vertex 70), respectively. The abbreviations given below are used to intensity of the bands in Raman and FTIR spectra: s, strong; m, medium; w, weak. All the preparation and measurement procedures were followed according to our previous works.[7, 42]

5.2.3. Synthesis and characterization of the neat salts

The synthesis route of chiral potassium salts is shown in **Scheme 5.2**. The detailed procedures for synthesizing potassium [(1R)-(−)-10-camphor sulfonyl](trifluoromethanesulfonyl)imide {$K[N(SO_2C_{10}H_{15}O)(SO_2CF_3)]$, KRCTFSI} are given as below. Firstly, to a solution of (1R)-(−)-10-camphorsulfonic acid ($RCSO_3H$, 23 g, 100 mmol) in 100 mL H_2O, K_2CO_3 (6.9 g, 50 mmol) was added slowly at 0 ^oC. The reaction was kept stirring at ambient temperature for 4 h. The solvent was removed under vacuum and potassium (1R)-(−)-10-camphorsulfonic ($RCSO_3K$) was obtained as a white solid (26 g; yield: 96 %). Secondly, $SOCl_2$ (27 mL, 384 mmol) was added slowly to the as-prepared $RCSO_3K$ (26 g, 96 mmol) in a flask under argon protection at 0 ^oC. The reaction was left stirring for 12 h at room temperature. Excess of $SOCl_2$ was quenched with water/ice, and the resulting mixture was extracted with CH_2Cl_2 (3 × 100 mL) and the collected organic phase was washed by deionized water for 3 times. The evaporation of CH_2Cl_2 gave a white, crystalline solid of (1R)-(−)-10-camphorsulfonyl chloride ($RCSO_2Cl$; 21 g; yield: 87 %). Thirdly, to a solution of $RCSO_2Cl$ (21 g, 84 mmol) in ACN (100 mL), a solution of potassium trifluoromethanesulfonamide (15.7 g, 84 mmol) and triethylamine (35 mL, 252 mmol) in ACN (150 mL) was added dropwise under argon atmosphere at 0 ^oC. The reaction was stirred and refluxed at 70 ^oC overnight under Argon flow. Then, ACN solvent was removed under vacuum and the obtained crude product was acidified by dilute (ca. 5 wt%) HCl aqueous solution and extracted with toluene. The removal of solvents gave [(1R)-(−)-10-camphor sulfonyl](trifluoromethanesulfonyl)imide acid (HRCTFSI) as a yellowish viscous liquid. Lastly, KRCTFSI was readily obtained by the neutralization

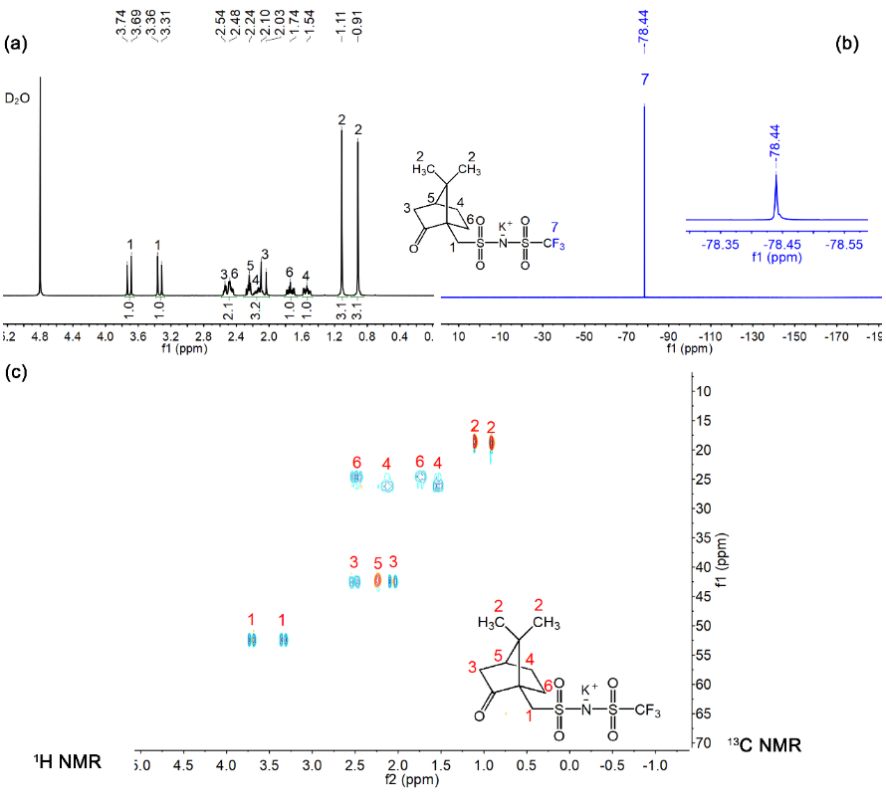

Figure 5.1. NMR spectra of the as-prepared KRCTFSI salt: (a) ^{1}H NMR, (b) ^{19}F NMR and (c) edited 2D HSQC. Reproduced with permission from Ref. [31].

of HRCTFSI with K_2CO_3 in water. The recrystallization of the crude product using toluene/ethanol mixture afforded KRCTFSI as a white powder (18.6 g; yield: 48%). ^{1}H NMR (300 MHz, D_2O, ppm): δ = 3.72 (d, J = 15.1 Hz, 1H), δ = 3.34 (d, J = 15.1 Hz, 1H), δ = 2.51 (m, 17.0 Hz, 2H), δ = 2.24 (m, 1H), δ = 2.07 (m, 19.0 Hz, 2H), δ = 1.74 (m, 1H), δ = 1.54 (d, 1H), δ = 1.11 (s, 3H), δ = 0.91 (s, 3H). ^{19}F NMR (282 MHz, D_2O, ppm): δ = –78.44 (s, 3F). FTIR (cm^{-1}): 1730 (s), 1332 (s), 1185 (w), 1078 (m), 807 (w), 764 (m), 729 (m), 604 (s), 518 (s). Raman (cm^{-1}): 1733 (w), 1470 (w), 1418 (w), 1236 (w), 734

(s), 588 (m), 400 (w), 308 (s). The characterization spectra and assignments of corresponding peaks are shown in **Figures 5.1.**, **5.4.**, **5.5** and **Table 5.1**, **5.2**.

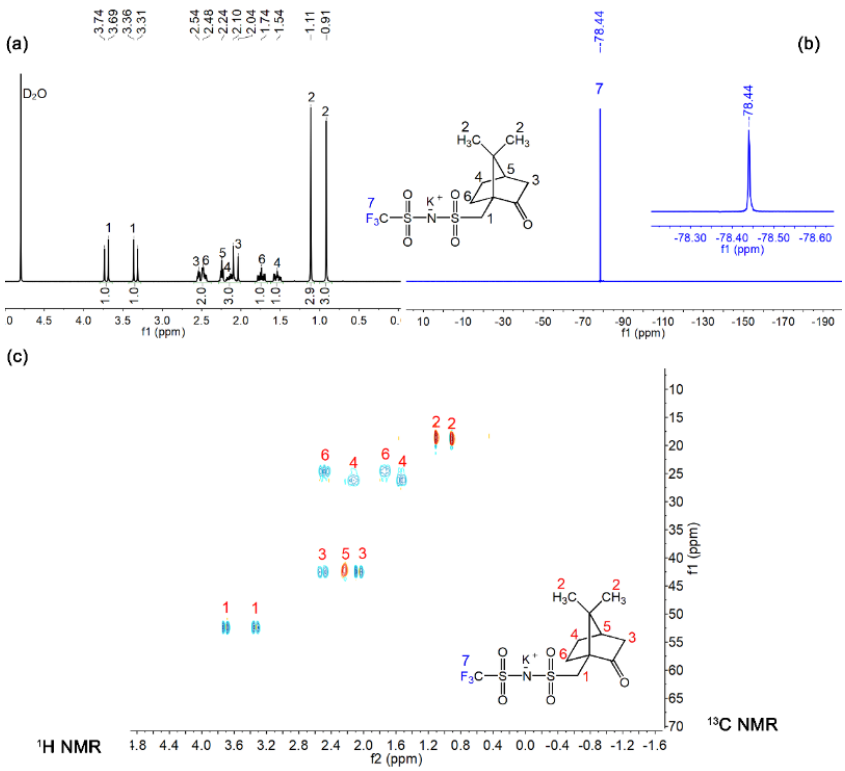

Figure 5.2. NMR spectra of the as-prepared KSCTFSI salt: (a) ^{1}H NMR, (b) ^{19}F NMR and (c) edited 2D HSQC. Reproduced with permission from Ref. [31].

The same synthetic procedures were followed for the potassium [(1S)-(+)-10-camphor sulfonyl](trifluoromethanesulfonyl)imide salt {$K[N(SO_2C_{10}H_{15}O)(SO_2CF_3)]$, KSCTFSI; yield: 52%} except using (1S)-(+)-10-camphorsulfonic acid as a starting material. ^{1}H NMR (300 MHz, D_2O, ppm): δ = 3.71 (d, J = 15.1 Hz, 1H), δ = 3.34 (d, J = 15.1 Hz, 1H), δ = 2.51 (m, J = 18.1 Hz, 2H), δ = 2.24 (m, 1H), δ = 2.07 (m, J = 19.0 Hz, 2H), δ =

1.74 (m, 1H), δ = 1.54 (d, 1H), δ = 1.11 (s, 3H), δ = 0.91 (s, 3H). ^{19}F NMR (282 MHz, D_2O, ppm): δ = –78.44 (s, 3F). FTIR (cm^{-1}): 1730 (s), 1332 (s), 1185 (w), 1078 (m), 807 (w), 764 (m), 729 (m), 604 (s), 518 (s). Raman (cm^{-1}): 1733 (w), 1470 (w), 1418 (w), 1236 (w), 734 (s), 588 (m), 400 (w), 308 (s). The characterization spectra and assignments of corresponding peaks are shown in **Figures 5.2**, **5.4**, **5.5** and **Tables 5.1**, **5.2**.

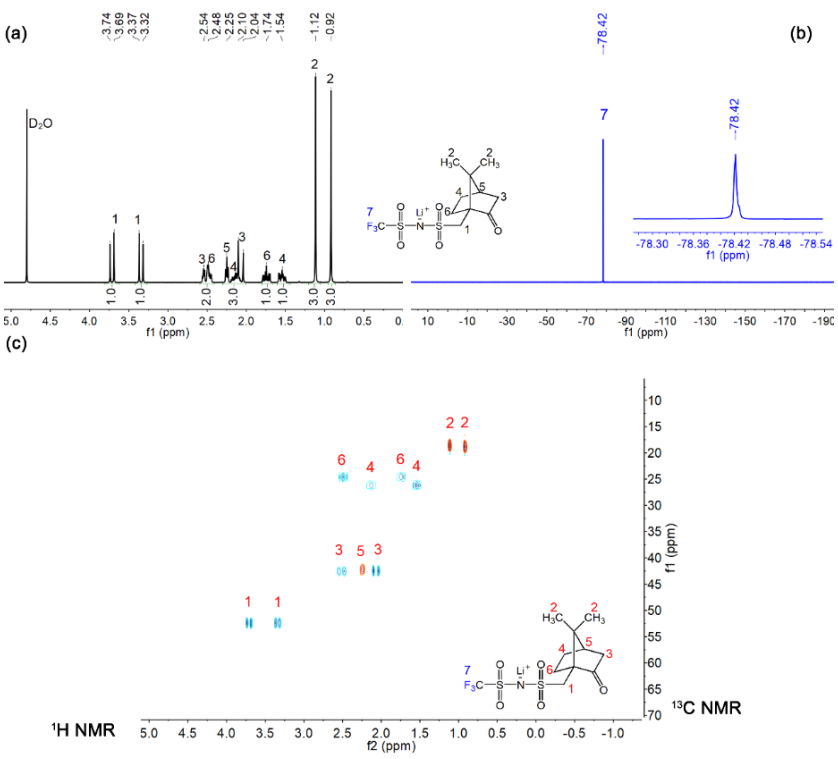

Figure 5.3. NMR spectra of the as-prepared LiSCTFSI salt: (a) ^{1}H NMR, (b) ^{19}F NMR and (c) edited 2D HSQC. Reproduced with permission from Ref. [31].

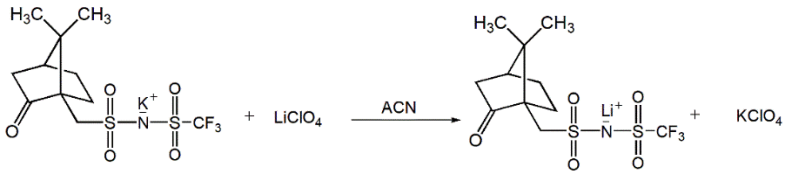

Scheme 5.3. The synthesis route of chiral lithium salts. Reproduced with permission from Ref. [31].

The corresponding chiral lithium salts were prepared by cation exchange of the as-prepared potassium salts with $LiClO_4$ in ACN according to previous work[10] and the synthetic route is shown in **Scheme 5.3.** Consequently, a white solid of the lithium [(1R)-(−)-10-camphorsulfonyl](trifluoromethanesulfonyl)imide salt {$Li[N(SO_2C_{10}H_{15}O)(SO_2CF_3)]$,LiRCTFSI} was obtained after recrystallization in ACN (yield: 89%). ^{1}H NMR (300 MHz, D_2O, ppm): δ = 3.71 (d, J = 54.3 Hz, 1H), δ = 3.34 (d, J = 15.1 Hz, 1H), δ = 2.51 (m, J = 17.9 Hz, 2H), δ = 2.24 (m, 1H), δ = 2.06 (m, 2H), δ = 1.74 (m, 1H), δ = 1.54 (d, 1H), δ = 1.11 (s, 3H), δ = 0.91 (s, 3H). ^{19}F NMR (282 MHz, D_2O, ppm): δ = –78.44 (s, 3F). FTIR (cm^{-1}): 1750 (m), 1332 (s), 1185 (s), 1078 (s), 807 (w), 764 (w), 729 (w), 604 (m), 518 (m). Raman (cm^{-1}): 1757 (m), 1470 (w), 1418 (w), 1236 (w), 734 (s), 588 (m), 400 (w), 308 (w). The characterization spectra and assignments of corresponding peaks are shown in **Figure 5.4-6** and **Tables 5.3**, **5.4**.

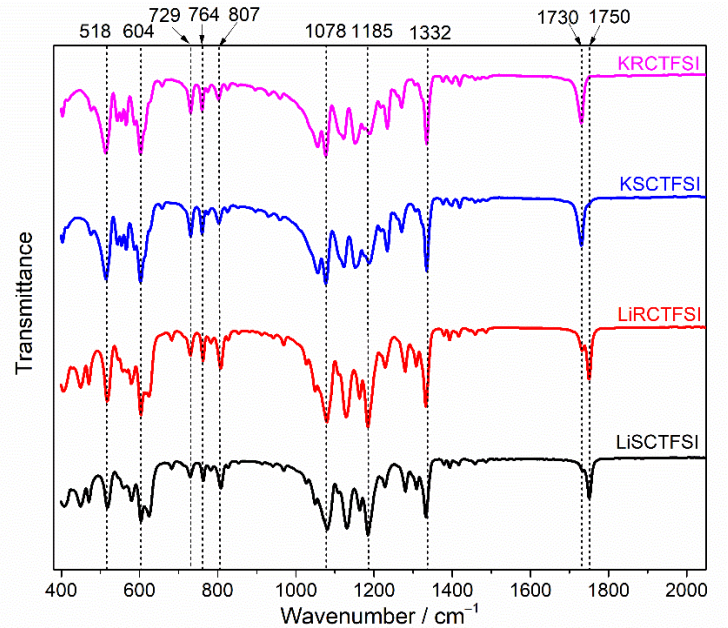

Figure 5.4. FTIR spectra of the as-prepared chiral salts. Reproduced with permission from Ref. [31].

The same synthesis procedures were followed for the lithium [(1S)-(+)-10-camphor sulfonyl](trifluoromethanesulfonyl)imide salt {Li[N($SO_2C_{10}H_{15}O$)(SO_2CF_3)], LiSCTFSI} except using (1S)-(+)-10-camphorsulfonic acid as a starting material, affording LiSCTFSI as a white solid (yield: 87%). ^{1}H NMR (300 MHz, D_2O, ppm): δ = 3.72 (d, J = 15.1 Hz, 1H), δ = 3.35 (d, J = 15.1 Hz, 1H), δ = 2.51 (m, J = 17.9 Hz, 2H), δ = 2.25 (m, 1H), δ = 2.07 (m, J = 19.0 Hz, 2H), δ = 1.74 (m, 1H), δ = 1.54 (d, 1H), δ = 1.12 (s, 3H), δ = 0.92 (s, 3H). ^{19}F NMR (282 MHz, D_2O, ppm): δ = –78.42 (s, 3F). FTIR (cm^{-1}): 1750 (m), 1332 (s), 1185 (s), 1078 (s), 807 (w), 764 (w), 729 (w), 604 (m), 518 (m). Raman (cm^{-1}): 1757 (m), 1470 (w), 1418 (w), 1236 (w), 734 (s), 588 (m), 400 (w), 308 (w). The characterization

spectra and assignments of corresponding bands are shown in **Figures 5.3-5.5**, **Tables 5.3** and **5.4**.

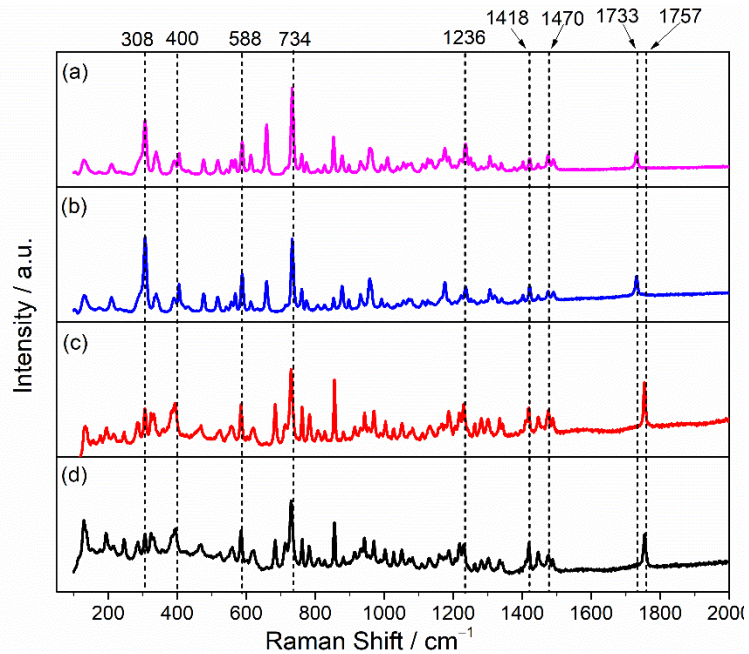

Figure 5.5. Raman spectra of the as-prepared (a) KRSCTFSI, (b) KSCTFSI, (c) LiRCTFSI and (d) LiSCTFSI salts, respectively. Reproduced with permission from Ref. [31].

5.2.4. Ionic conductivity

The ionic conductivities of the as-prepared SPEs were obtained by electrochemical impedance spectroscopy (EIS) on a VMP3 potentiostat (Biologic). CR2032 type coin cells (SS | SPEs | SS) comprising two stainless steel (SS) blocking electrodes and Teflon O-ring (see **Figure 2.1** for schematic illustration) were assembled in an argon filled glovebox (M Braun, H_2O < 0.1 ppm, O_2 < 0.1 ppm) for ionic conductivity tests. The cells were

subjected to EIS in a frequency range 10^4 to 10^{-1} Hz from 30 °C to 100 °C and the temperature was controlled by using an electro-thermostatic oven (± 1 °C, Lan technics, Model DHG). The ionic conductivities were obtained by Equation [5.1]:

$$\sigma_{\text{total}} = L/(S \times R_{\text{bulk}}) \qquad [5.1]$$

wherein, σ_{total} (in S cm^{-1}) is the total ionic conductivity of the SPE, L (in cm) is the thickness of the SPE, S (in cm^2) is the contact area between the SPE and the electrode and R_{bulk} (in Ω) is the bulk resistance of the SPE. To minimize experimental uncertainties at least four repetitions were made for each SPE. The standard deviation (σ_{SD}) and fractional uncertainty (f_{FN}) of the ionic conductivities were calculated using Equation [5.2] and Equation [5.3],[43] respectively:

$$\sigma_{\text{SD}} = \sqrt{\sum(\sigma_{\text{i}} - \bar{\sigma})^2 /(N-1)} \qquad [5.2]$$

$$f_{\text{FN}} = \sigma_{\text{SD}}/(\sqrt{N} \times \bar{\sigma}) \times 100\% \qquad [5.3]$$

In Equation [5.2] and Equation [5.3], σ_{i} is the ionic conductivity of sample i, $\bar{\sigma}$ is the mean value of all the measured samples, and N is the number of measurements. All the ionic conductivities herein are reported as $\bar{\sigma} + \sigma_{\text{SD}}$, representing a 68% confidence limit.[43]

Table 5.1. Mode assignment of typical bands observed by FTIR spectroscopy of the chiral potassium salts. Reproduced with permission from Ref. [31].

FTIR wavenumber / cm^{-1}	Assignment
1730	C=O stretching vibration
1332	$–SO_2–$ stretching vibration
1185	$–SO_2–$ stretching vibration
1078	$–SO_2–$ bending vibration
604	$–SO_2–$ bending vibration
807	C–H bending vibration
764	C–H bending vibration
729	C–H bending vibration
518	$–CF_3$ bending vibration

Table 5.2. Mode assignment of typical bands observed by Raman spectroscopy of the chiral potassium salts. Reproduced with permission from Ref. [31].

Raman shift / cm^{-1}	Assignment
1733	C=O stretching vibration
1740	$–CH_2–$ or $–CH_3$ asymmetric bending vibration
1418	$–CH_2–$ or $–CH_3$ asymmetric bending vibration
1236	$–CF_3$ symmetric stretching vibration
734	$–CF_3$ symmetric bending vibration
588	$–SO_2–$ bending vibration
400	$–SO_2–$ wagging vibration
308	$–SO_2–$ rocking vibration

Table 5.3. Mode assignment of typical bands observed by FTIR spectroscopy of the chiral lithium salts. Reproduced with permission from Ref. [31].

FTIR wavenumber / cm^{-1}	Assignment
1750	C=O stretching vibration
1332	$–SO_2–$ stretching vibration
1185	$–SO_2–$ stretching vibration
1078	$–SO_2–$bending vibration
604	$–SO_2–$ bending vibration
807	C–H bending vibration
764	C–H bending vibration
729	C–H bending vibration
518	$–CF_3$ bending vibration

Table 5.4. Mode assignment of typical bands observed by Raman spectroscopy of the chiral lithium salts. Reproduced with permission from Ref. [31].

Raman shift / cm^{-1}	Assignment
1757	C=O stretching vibration
1740	$–CH_2–$ or $–CH_3$ asymmetric bending vibration
1418	$–CH_2–$ or $–CH_3$ asymmetric bending vibration
1236	$–CF_3$ symmetric stretching vibration
734	$–CF_3$ symmetric bending vibration
588	$–SO_2–$ bending vibration
400	$–SO_2–$ wagging vibration
308	$–SO_2–$ rocking vibration

5.3. Results and discussion

5.3.1 Synthesis and structural characterization

The chirality of the as-prepared salts is inherited from the chiral precursors (R,S)-(±)-10-camphorsulfonic acid and the synthetic routes only modifies the anionic center from $–SO_3^-$ to $–SO_2N^{(-)}SO_2CF_3$, where the latter's negative charge is more delocalized, a critical feature for high SPE ionic conductivity.[9, 44] The chemical structures of the chiral salts have been characterized by multiple techniques, enlisting NMR, FTIR, and Raman spectroscopies.

As seen in **Figure 5.6**, taking LiRCTFSI as an example, the characteristic peaks assigned to the camphor-based moiety in the range 3.73–0.91 ppm are observed in the ^{1}H-NMR spectrum (**Figure 5.6a**) and a sharp peak at around −78.4 ppm corresponding to the $–CF_3$ group appears in the ^{19}F NMR spectrum (**Figure 5.6b**). The 2D heteronuclear single quantum coherence spectroscopy (HSQC, **Figure 5.6c**) shows an unambiguous correlation between the carbon atoms and their corresponding hydrogen atoms. Altogether, these results clearly suggest that the trifluoromethanesulfonamide group has been successfully grafted onto the camphor-based moiety. This is further reinforced by the corresponding signals in the FTIR and Raman spectra (**Figures. 5.4**, **5.5** and **Tables 5.3-5.4**). For example, the band at 1750 cm^{-1} characteristic of the asymmetric stretching of C=O in a camphor moiety concurrently appears together with that at 518 cm^{-1} belonging to the typical bending vibration of the $–CF_3$ group in the FTIR spectrum (**Figure 5.4**, **Table 5.3**). The band at 734 cm^{-1}, also assigned to the symmetric bending vibration of the $–CF_3$ group, is observed in the corresponding Raman spectrum (**Figure 5.5**, **Table 5.4**). All these spectroscopic results indicate that the LiRCTFSI salt with good purity has been synthesized successfully. The chemical structures of the other three

salts, *i.e.*, KRCTFSI, KSCTFSI, and LiSCTFSI, are also confirmed by the same characterization techniques (see **Figures 5.1-5**, **Tables 5.1-4**).

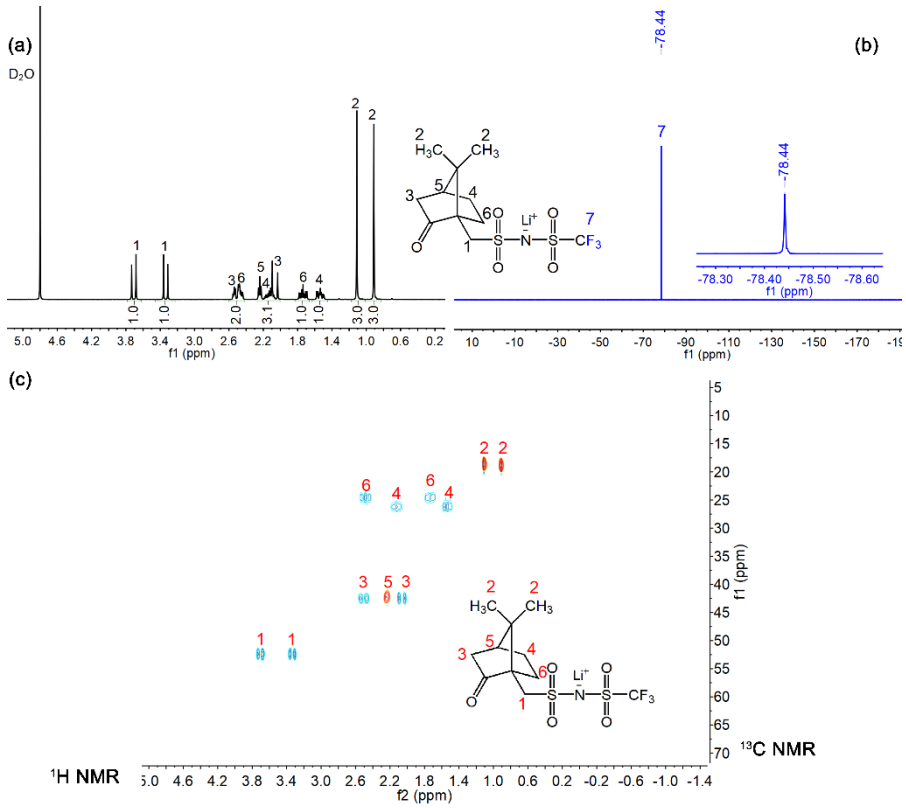

Figure 5.6. NMR spectra of the as-prepared LiRCTFSI salt: (a) ^{1}H NMR, (b) ^{19}F NMR, and (c) edited 2D HSQC. Reproduced with permission from Ref. [31].

5.3.2 Thermal stability

Thermal stability of electrolyte components is of vital importance to enable scalable processing of SPEs, *e.g.*, extrusion, without detrimental decomposition.[45] The neat salts (**Figure 5.7a**, **b**), for either K^+ or Li^+ as cations, show TGA traces quasi-superimposed for the RCTFSI and SCTFSI

enantiomers, without any differences in the decomposition temperatures, *e.g.*, T_d = 360 °C for KRCTFSI and KSCTFSI and 318 °C for LiRCTFSI and LiSCTFSI. Thus chirality has no measurable impact on the thermal stability of the neat salts, but the potassium salts are more stable than the corresponding lithium salts, likely related to the stronger affinity of the lithium cation (hard acid) for the fluorine atoms (hard base) in the anions according to the "Hard and Soft Acids and Bases (HSAB)" concept,[46] promoting the formation of lithium fluoride (LiF) at relatively lower temperatures by pyrolysis.[46]

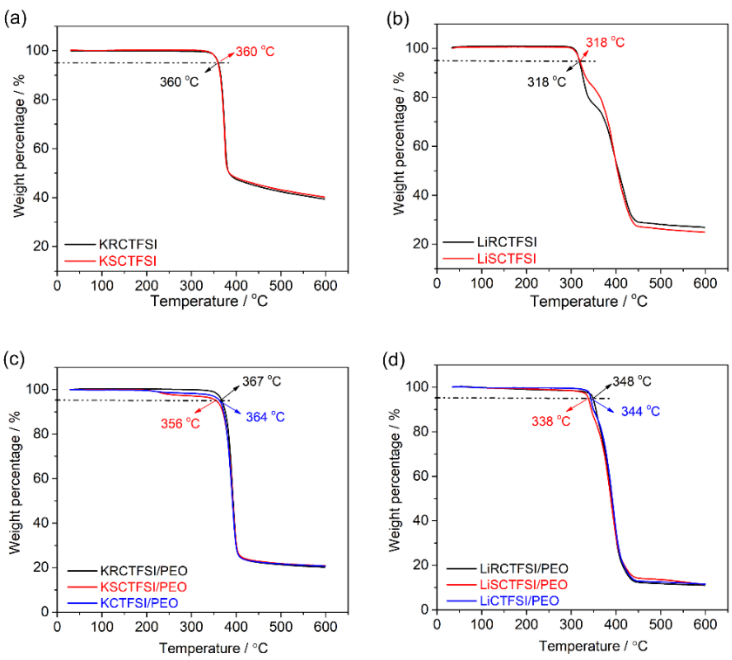

Figure 5.7. Thermal stabilities of (a, b) the neat camphor-derived chiral salts and (c, d) the PEO-based SPEs. Reproduced with permission from Ref. [31].

For the SPEs (**Figure 5.7c**, **d**), for a given cation, there are slight variations in the TGA traces between 200 °C to 400 °C observable for the

three choices of anions *i.e.*, RCTFSI, SCTFSI and CTFSI. The SCTFSI-based SPEs tend to be slightly less thermally stable, *e.g.*, KSCTFSI/PEO (T_d = 356 °C) < KCTFSI/PEO (T_d = 364 °C) < KRCTFSI/PEO (T_d = 367 °C), **Figure 5.7c**; LiSCTFSI/PEO (T_d = 338 °C) < LiCTFSI/PEO (T_d = 344 °C) < LiRCTFSI/PEO (T_d = 348 °C), **Figure 5.7d**. This could be associated with trace amounts of impurities which may trigger decomposition of PEO.[47] Using the same data, we find that, just as for the neat salts – and in principle controlled by their behavior as itself PEO decomposes at a temperature of no less than *ca.* 360 °C,[48] for a given anion, the SPEs based on the potassium salts unquestionably present better resistance toward pyrolysis compared to those based on the lithium salts. Notwithstanding, all the SPEs exhibit good thermal stabilities, > 300 °C, and are thus more than stable enough to be employed as electrolytes for SSLMBs.

5.3.3 Phase transition

The migration of ionic species in SPEs usually takes place in the amorphous phase of these often semi-crystalline systems and a higher segmental mobility of the polymer backbones allows for faster ionic transport.[9] Therefore, the phase behavior including glass and melting transitions are useful measures for SPEs and the DSC data are presented in **Figure 5.8** and **Table 5.5**.

In the series of neat salts, as shown in **Figure 5.8a** and **b**, for a given cation, both the RCTFSI-based and SCTFSI-based salts exhibit the same melting temperatures (T_m) and melting enthalpies (ΔH_m), *e.g.*, T_m = 272 °C and ΔH_m = 90 J g^{-1} for KRCTFSI vs. T_m = 272 °C and ΔH_m = 91 J g^{-1} for KSCTFSI; T_m = 234 °C and ΔH_m = 7 J g^{-1} for LiRCTFSI vs. T_m = 234 °C

and ΔH_m = 7 J g^{-1} for LiSCTFSI. Again, the chirality has as expected no impact on the phase behavior of the neat salts, but also points to accurate preparation and purity as well as sample preparation. The same has been observed for other camphor-based derivatives; *e.g.*, T_m = 225 °C for R-(−)/S-(+)-10-(camphorsulfonyl)imine[49] and T_m = 174 °C for R-(−)/S-(+)-[(8,8-dichlorocamphoryl)sulfonyl]imine.[49]

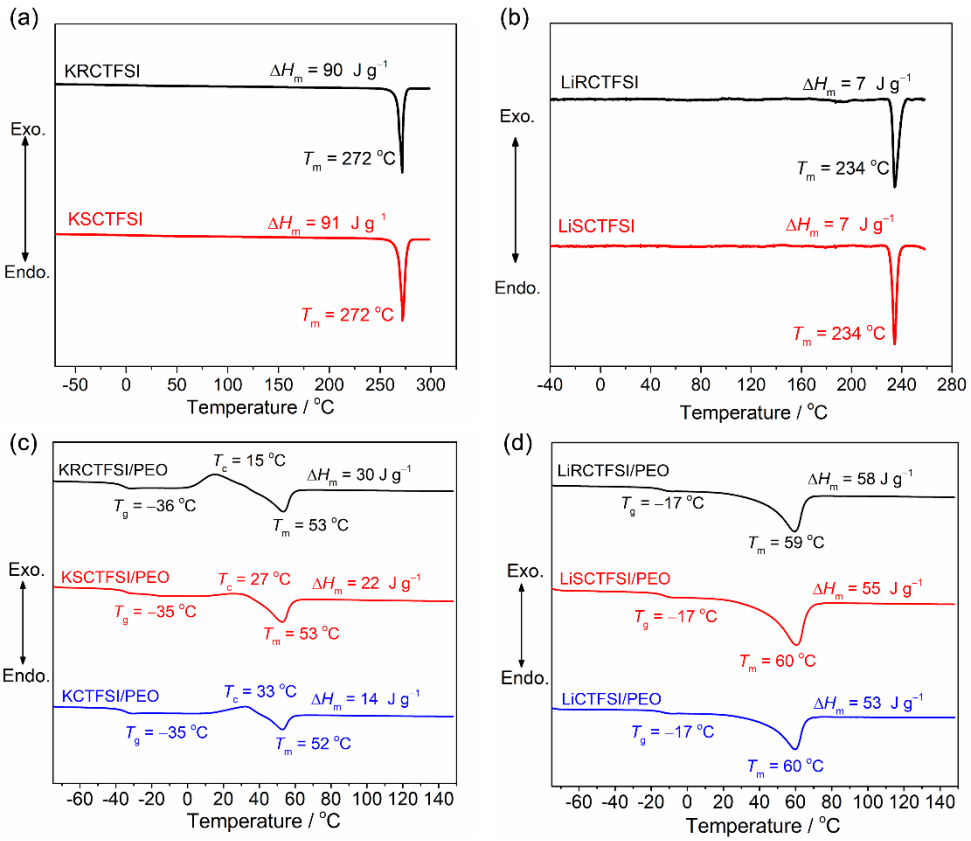

Figure 5.8. Differential scanning calorimetry (DSC) traces of the salts and SPEs: (a) potassium salts, (b) lithium salts, (c) K-based SPEs and (d) Li-based SPEs. The DSC traces of the neat salts and SPEs are obtained from the first and second heating scans, respectively. Reproduced with permission from Ref. [31].

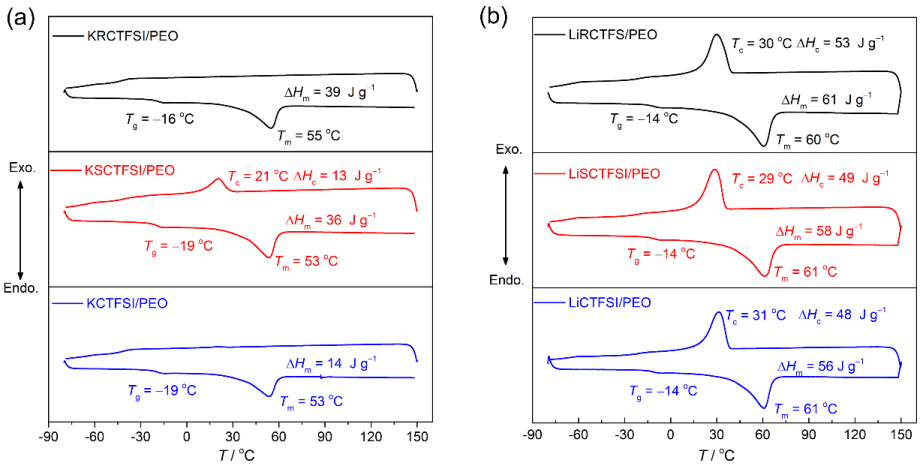

Figure 5.9. DSC traces of different SPEs during the first heating and cooling scans. Reproduced with permission from Ref. [31].

Again, the same as the TGA T_d data, for a given anion, the lithium salts possess lower T_m as compared to the corresponding potassium salts. This diverges from the TFSI salts, where KTFSI has a lower T_m (199 °C) than LiTFSI (233 °C)[50] and can be rationalized by the different lattice energies, originating from the greatly complicated electrostatic interactions of these bulky organic anions with different cations, as previously observed for other sulfonimide salts, *e.g.*, for salts of the (fluorosulfonyl)(pentafluoroethanesulfonyl)imide (FPFSI) anion, where LiFPFSI has a T_m = 152 °C and KFPFSI is more high melting (T_m = 173 °C).[51]

In the series of SPEs, for a constant cation, both T_g and T_m are very close for the RCTFSI, SCTFSI and CTFSI based, *e.g.*, T_g = −36 °C and T_m = 53 °C for KRCTFSI/PEO vs. T_g = −35 °C and T_m = 53 °C for KSCTFSI/PEO vs. T_g = −35 °C and T_m = 52 °C for KCTFSI/PEO; T_g = −17 °C and T_m = 59

°C for LiRCTFSI/PEO vs. T_g = −17 °C and T_m = 60 °C for LiSCTFSI/PEO vs. T_g = −17 °C and T_m = 60 °C for LiCTFSI/PEO (**Figure 5.8** and **Table 5.5**). Once again this indicates that the chirality of the salt anion has no impact.

Table 5.5. Physico-chemical data for phase behavior of the SPEs. Reproduced with permission from Ref. [31].

Samples	T_g [a] / °C	T_m [b] / °C	ΔH_m [c] / J g^{-1}	χ_c [d] / %
KRCTFSI/PEO	−36	53	30	24
KSCTFSI/PEO	−35	53	22	18
KCTFSI/PEO	−25	52	14	11
LiRCTFSI/PEO	−17	59	58	45
LiSCTFSI/PEO	−17	60	55	43
LiCTFSI/PEO	−17	60	53	41

[a] Glass transition temperature (°C); [b] melting point (°C); [c] enthalpy of melting (J g^{-1}); [d] the crystallinity as calculated by ($\Delta H_m/\Delta H_{PEO}f_{PEO}$) × 100%, wherein, ΔH_m is the melting enthalpy of the SPEs and ΔH_{PEO} is 196.4 J g^{-1} – the melting enthalpy of 100% crystalline PEO,[52] and f_{PEO} is the PEO weight fraction.

Similar to the neat salts, the cations, *i.e.*, Li^+ and K^+, play a determining role in dictating the phase transitions of the SPEs. In contrast to the Li-based SPEs, all the K-based SPEs display a noticeable crystallization temperature (T_c) (**Figure 5.8c**) during the second heating scan. This is due to their slower crystallization kinetics, which is manifested by the absent/negligible re-crystallization during the first cooling scan (**Figure 5.9**). Additionally, using the data above, we find that both T_g and T_m are lower for the K-based SPEs than for the Li-based SPEs, which might be due to the larger volume and lower polarizing power of K^+ as compared to Li^+, reducing the extent and

strength of dynamic cross-linking and hence less impacting on the PEO chain flexibility[53] and thereby slowing down the formation of lamellar structures of PEO, *i.e.*, crystallization, in the K-based SPEs.[54] Increased T_g for the Li-based SPEs has also been observed for TFSI-based and DFTFSI-based SPEs.

All of the above demonstrate that the cations of the salts have an important role in dictating the thermal properties of both the neat salts and SPEs, but that the impact of anion chirality is very limited.

5.3.4 Ionic conductivity

Ionic conductivity is one of the most critical properties for a SPE aimed at SSLMB application.[10] It is generally accepted that the ion transport in traditional semi-crystalline SPEs occurs mainly in the amorphous phase through polymer chain segmental motions, and this is also why a low T_g is so important (see above). Béranger *et al.* [32] [32]showed that the chirality of salt anions influenced the ionic conduction in PEO-based SPEs as electrolytes containing artificial racemic salts, *i.e.*, an equimolar mixture of KRCTFSI and KSCTFSI, showed slightly lower ionic conductivities. However, PEO-based SPEs with moderate salt contents (EO/Li > 12) are usually semi-crystalline, which causes poor interfacial contact with the SS electrodes, rendering pronounced uncertainties, in particular below T_m (<60 °C). Therefore, we employed four repetitions for each sample (**Figures 5.10** and **5.11**), where **Figure 5.10a** displays the overall total ionic conductivity (σ_{total}) for the K-based SPEs and the zoomed-in plots of the area A (30–60 °C) and area B (70–100 °C) in **Figure 5.10a** are shown in **Figure 5.10b** and **Figure 5.10c**, respectively. In addition, the standard deviations (σ_{SD}) of log σ_{total}

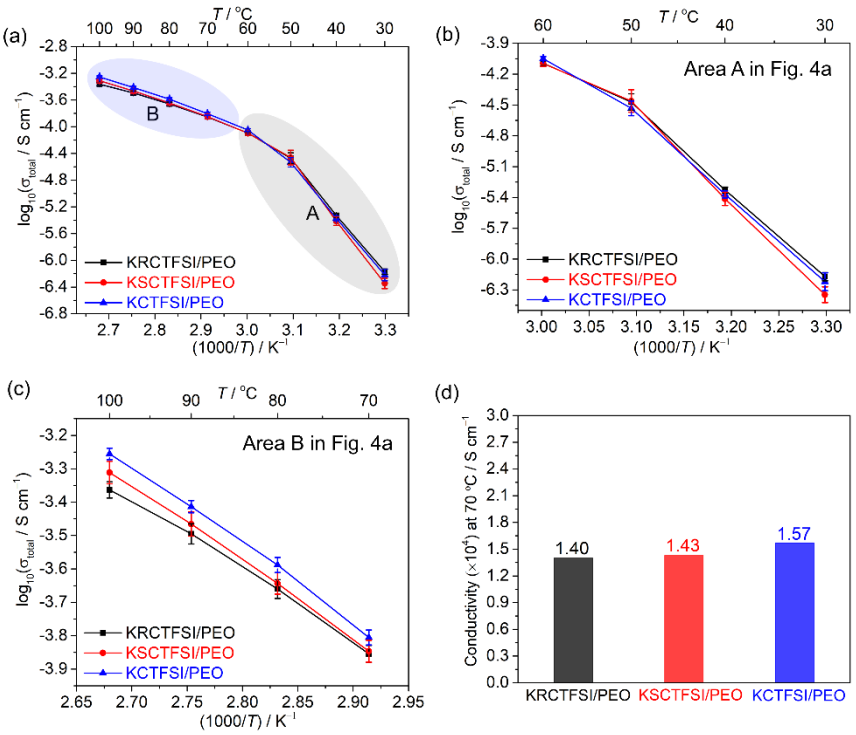

Figure 5.10. (a-c) Temperature dependence of ionic conductivity (standard deviation as error bar) for the K-based SPEs: (a) temperatures ranging from 30–100 °C, (b) zoomed-in plot of area A in Figure 5.10a ($5.0 \times 10^{-7} < \sigma_{total} < 1.0 \times 10^{-4}$ S cm^{-1}) and (c) zoomed-in plot of area B in Figure 5.10a ($1.4 \times 10^{-4} < \sigma_{total} < 5.0 \times 10^{-4}$ S cm^{-1}). (d) Ionic conductivity of the PEO-based electrolytes at 70 °C. Reproduced with permission from Ref. [31].

values are also included in **Figure 5.10a-c**, and the corresponding linear values are tabulated in **Table 5.6**. All the SPEs exhibit uncertainties in ionic conductivities and the relative uncertainties tend to be more pronounced at low temperatures (30–60 °C), *e.g.*, 3.2% (40 °C) vs. 2.9% (70 °C) for KRCTFSI/PEO; 7.3% (40 °C) vs. 3.8% (70 °C) for KSCTFSI/PEO; 3.8% (40 °C) vs. 2.6% (70 °C) for KCTFSI/PEO (**Table 5.6**). This corroborates

well with our hypothesis that the semi-crystallinity and the sample history affects the interfacial contact. [41] A similar behavior was also reported by Marzantowicz *et al.*;[40] a partial loss of contact between the SPE and the electrodes tended to cause an apparent decrease in ionic conductivity.

The σ_{total} changes remarkably at *ca.* 60 ºC, *e.g.*, (3.42 ± 0.58) × 10^{-5} S cm^{-1} (50 ºC) vs. (1.40 ± 0.08) × 10^{-4} S cm^{-1} (70 ºC) for KRCTFSI/PEO, likely due to the melting of the semi-crystalline PEO polymer matrix,[9] as supported also by the DSC data (**Figure 5.8c**). A close look on the ionic conductivities within the two distinct temperature regions area A and area B, show negligible differences in σ_{total} for the three K-based SPEs; *e.g.*, (1.40 ± 0.08) × 10^{-4} S cm^{-1} for KRCTFSI/PEO vs. (1.43 ± 0.10) × 10^{-4} S cm^{-1} for KSCTFSI/PEO vs. (1.57 ± 0.08) × 10^{-4} S cm^{-1} for KCTFSI/PEO at 70 ºC (**Figure 5.10d**). This clearly contradicts the previous results by Béranger *et al.*[32] and this is largely ascribed to the above mentioned uncertainties in the ionic conductivity measurements. Hence, we conclude that the chirality in these camphor-based salt anions has nothing but a minimal impact on the total ionic conductivities of the PEO-based SPEs.

Along the same lines, σ_{total} of the Li-based SPEs (**Figure 5.11** and **Table 5.7**) show similar relative uncertainties at lower temperatures (30–60 ºC), *e.g.*, 12.0% (40 ºC) vs. 1.8% (70 ºC) for LiRCTFSI/PEO; 12.2% (40 ºC) vs. 3.3% (70 ºC) for LiSCTFSI/PEO; and 4.6% (40 ºC) vs. 4.3% (70 ºC) for LiCTFSI/PEO. Also here the crystaline phase of PEO influences the accuracy and there is an abrupt increase in ionic conductivity above 60 ºC correlating with the DSC data (**Figure 5.8d**).[9] Again all three Li-based SPEs

Table 5.6. The specific σ_{total} (σ_i) from 4 repetitions and the corresponding average σ_{total} ($\bar{\sigma}$), standard deviation (σ_{SD}) and functional uncertainty (f_{FN}) for the K-based SPEs at different temperatures. Reproduced with permission from Ref. [31].

	σ_1 (Sample 1) / S cm^{-1}	σ_2 (Sample 2) / S cm^{-1}	σ_3 (Sample 3) / S cm^{-1}	σ_4 (Sample 4) / S cm^{-1}	$\bar{\sigma}$ / S cm^{-1}	σ_{SD} / S cm^{-1}	f_{FN} / %
KRCTFSI/PEO							
30 °C	7.00×10^{-7}	5.87×10^{-7}	7.19×10^{-7}	7.03×10^{-7}	6.77×10^{-7}	6.06×10^{-8}	4.5
40 °C	4.27×10^{-6}	4.80×10^{-6}	4.89×10^{-6}	4.91×10^{-6}	4.72×10^{-6}	3.02×10^{-7}	3.2
50 °C	2.59×10^{-5}	3.51×10^{-5}	3.63×10^{-5}	3.94×10^{-5}	3.42×10^{-5}	5.82×10^{-6}	8.5
60 °C	7.61×10^{-5}	8.48×10^{-5}	8.37×10^{-5}	7.77×10^{-5}	8.06×10^{-5}	4.31×10^{-6}	2.7
70 °C	1.29×10^{-4}	1.41×10^{-4}	1.42×10^{-4}	1.48×10^{-4}	1.40×10^{-4}	8.02×10^{-6}	2.9
80 °C	2.04×10^{-4}	2.10×10^{-4}	2.28×10^{-4}	2.34×10^{-4}	2.19×10^{-4}	1.42×10^{-5}	3.2
90 °C	2.93×10^{-4}	3.16×10^{-4}	3.27×10^{-4}	3.46×10^{-4}	3.21×10^{-4}	2.23×10^{-5}	3.5
100 °C	4.07×10^{-4}	4.21×10^{-4}	4.48×10^{-4}	4.59×10^{-4}	4.34×10^{-4}	2.41×10^{-5}	2.8
KSCTFSI/PEO							
30 °C	5.71×10^{-7}	3.74×10^{-7}	4.32×10^{-7}	4.45×10^{-7}	4.55×10^{-7}	8.27×10^{-8}	9.1
40 °C	3.54×10^{-6}	3.27×10^{-6}	4.37×10^{-6}	4.38×10^{-6}	3.89×10^{-6}	5.71×10^{-7}	7.3
50 °C	2.83×10^{-5}	2.73×10^{-5}	4.27×10^{-5}	4.33×10^{-5}	3.54×10^{-5}	8.77×10^{-6}	12.4
60 °C	7.51×10^{-5}	7.81×10^{-5}	8.05×10^{-5}	8.75×10^{-5}	8.03×10^{-5}	5.28×10^{-6}	3.3
70 °C	1.32×10^{-4}	1.53×10^{-4}	1.35×10^{-4}	1.51×10^{-4}	1.43×10^{-4}	1.08×10^{-5}	3.8
80 °C	2.18×10^{-4}	2.40×10^{-4}	2.09×10^{-4}	2.43×10^{-4}	2.28×10^{-4}	1.67×10^{-5}	3.7
90 °C	3.30×10^{-4}	3.54×10^{-4}	3.12×10^{-4}	3.77×10^{-4}	3.43×10^{-4}	2.87×10^{-5}	4.2
100 °C	4.70×10^{-4}	4.95×10^{-4}	4.51×10^{-4}	5.41×10^{-4}	4.89×10^{-4}	3.87×10^{-5}	4.0
KCTFSI/PEO							
30 °C	5.02×10^{-7}	6.97×10^{-7}	5.14×10^{-7}	7.36×10^{-7}	6.12×10^{-7}	1.22×10^{-7}	9.9
40 °C	4.48×10^{-6}	3.79×10^{-6}	4.37×10^{-6}	4.46×10^{-6}	4.27×10^{-6}	3.27×10^{-7}	3.8
50 °C	3.51×10^{-5}	2.36×10^{-5}	3.04×10^{-5}	2.93×10^{-5}	2.96×10^{-5}	4.73×10^{-6}	8.0
60 °C	8.67×10^{-5}	8.56×10^{-5}	9.03×10^{-5}	9.50×10^{-5}	8.94×10^{-5}	4.23×10^{-6}	2.4
70 °C	1.52×10^{-4}	1.49×10^{-4}	1.60×10^{-4}	1.67×10^{-4}	1.57×10^{-4}	8.17×10^{-6}	2.6
80 °C	2.45×10^{-4}	2.49×10^{-4}	2.67×10^{-4}	2.73×10^{-4}	2.58×10^{-4}	1.35×10^{-5}	2.6
90 °C	3.85×10^{-4}	3.74×10^{-4}	3.75×10^{-4}	4.10×10^{-4}	3.86×10^{-4}	1.65×10^{-5}	2.1
100 °C	5.48×10^{-4}	5.29×10^{-4}	5.71×10^{-4}	5.75×10^{-4}	5.56×10^{-4}	2.15×10^{-5}	1.9

Table 5.7. The specific σ_{total} (σ_i) from 4 repetitions and the corresponding average σ_{total} ($\bar{\sigma}$), standard deviation (σ_{SD}) and functional uncertainty (f_{FN}) for the Li-based SPEs at different temperatures. Reproduced with permission from Ref. [31].

	σ_1 (Sample 1) / S cm^{-1}	σ_2 (Sample 2) / S cm^{-1}	σ_3 (Sample 3) / S cm^{-1}	σ_4 (Sample 4) / S cm^{-1}	$\bar{\sigma}$ / S cm^{-1}	σ_{SD} / S cm^{-1}	f_{FN} / %
LiRCTFSI/PEO							
30 °C	2.11×10^{-7}	3.01×10^{-7}	3.37×10^{-7}	2.50×10^{-7}	2.74×10^{-7}	5.55×10^{-8}	10.1
40 °C	1.50×10^{-6}	2.07×10^{-6}	2.66×10^{-6}	2.51×10^{-6}	2.19×10^{-6}	5.25×10^{-7}	12.0
50 °C	1.70×10^{-5}	1.93×10^{-5}	1.92×10^{-5}	1.76×10^{-5}	1.83×10^{-5}	1.14×10^{-6}	3.1
60 °C	8.33×10^{-5}	8.49×10^{-5}	7.75×10^{-5}	6.76×10^{-5}	7.83×10^{-5}	7.84×10^{-6}	5.0
70 °C	1.37×10^{-4}	1.49×10^{-4}	1.42×10^{-4}	1.46×10^{-4}	1.43×10^{-4}	5.13×10^{-6}	1.8
80 °C	2.00×10^{-4}	2.31×10^{-4}	2.12×10^{-4}	2.37×10^{-4}	2.20×10^{-4}	1.70×10^{-5}	3.9
90 °C	2.90×10^{-4}	3.36×10^{-4}	2.94×10^{-4}	3.28×10^{-4}	3.12×10^{-4}	2.35×10^{-5}	3.8
100 °C	3.93×10^{-4}	4.64×10^{-4}	3.80×10^{-4}	3.82×10^{-4}	4.05×10^{-4}	3.98×10^{-5}	4.9
LiSCTFSI/PEO							
30 °C	2.26×10^{-7}	2.46×10^{-7}	2.55×10^{-7}	2.40×10^{-7}	2.42×10^{-7}	1.20×10^{-8}	2.5
40 °C	1.33×10^{-6}	2.34×10^{-6}	2.24×10^{-6}	2.44×10^{-6}	2.09×10^{-6}	5.09×10^{-7}	12.2
50 °C	1.94×10^{-5}	2.46×10^{-5}	2.69×10^{-5}	3.03×10^{-5}	2.53×10^{-5}	4.58×10^{-6}	9.1
60 °C	7.96×10^{-5}	9.55×10^{-5}	8.81×10^{-5}	8.86×10^{-5}	8.79×10^{-5}	6.48×10^{-6}	3.7
70 °C	1.34×10^{-4}	1.57×10^{-4}	1.48×10^{-4}	1.45×10^{-4}	1.46×10^{-4}	9.62×10^{-6}	3.3
80 °C	2.07×10^{-4}	2.37×10^{-4}	2.24×10^{-4}	2.36×10^{-4}	2.26×10^{-4}	1.41×10^{-5}	3.1
90 °C	3.03×10^{-4}	3.39×10^{-4}	2.94×10^{-4}	3.24×10^{-4}	3.15×10^{-4}	2.03×10^{-5}	3.2
100 °C	3.44×10^{-4}	4.14×10^{-4}	3.68×10^{-4}	3.91×10^{-4}	3.79×10^{-4}	3.01×10^{-5}	4.0
LiCTFSI/PEO							
30 °C	1.64×10^{-7}	2.50×10^{-7}	2.27×10^{-7}	2.14×10^{-7}	2.14×10^{-7}	3.66×10^{-8}	8.6
40 °C	2.02×10^{-6}	2.28×10^{-7}	2.44×10^{-7}	2.49×10^{-6}	2.31×10^{-6}	2.13×10^{-7}	4.6
50 °C	1.64×10^{-5}	1.95×10^{-5}	2.10×10^{-5}	2.49×10^{-5}	2.04×10^{-5}	3.54×10^{-6}	8.7
60 °C	8.21×10^{-5}	7.84×10^{-5}	8.92×10^{-5}	7.73×10^{-5}	8.17×10^{-5}	5.37×10^{-6}	3.3
70 °C	1.36×10^{-4}	1.36×10^{-4}	1.61×10^{-4}	1.37×10^{-4}	1.42×10^{-4}	1.23×10^{-5}	4.3
80 °C	1.98×10^{-4}	2.14×10^{-4}	2.41×10^{-4}	1.58×10^{-4}	2.03×10^{-4}	3.48×10^{-5}	8.6
90 °C	2.98×10^{-4}	2.98×10^{-4}	3.40×10^{-4}	3.06×10^{-4}	3.10×10^{-4}	1.99×10^{-5}	3.2
100 °C	3.85×10^{-4}	3.97×10^{-4}	3.93×10^{-4}	4.04×10^{-4}	3.95×10^{-4}	7.97×10^{-6}	1.0

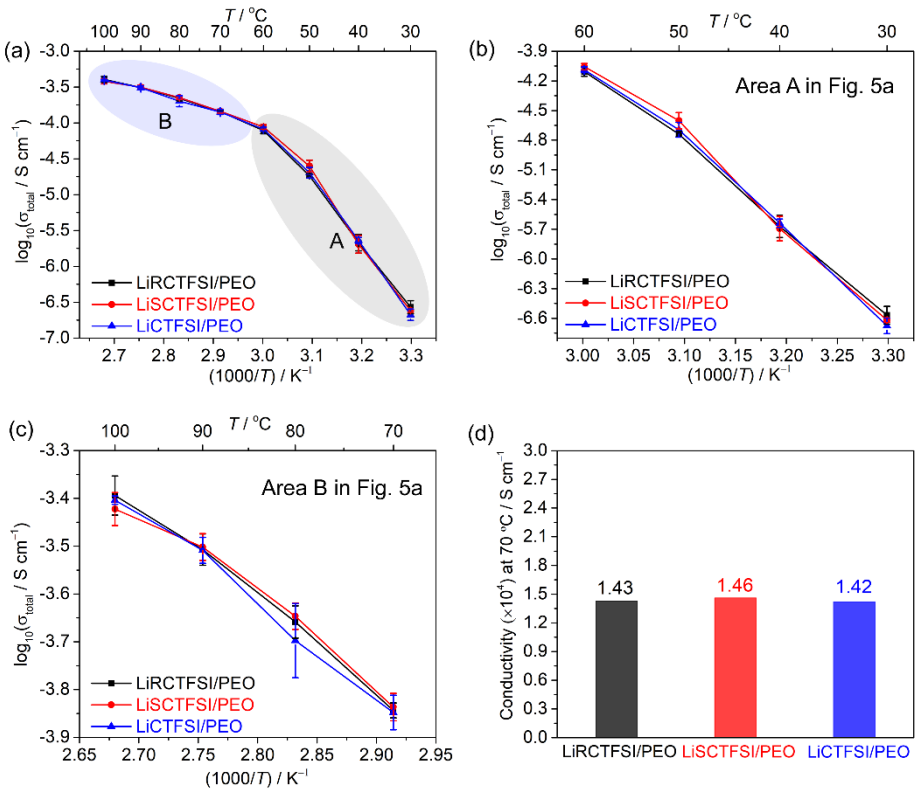

Figure 5.11. (a-c) Temperature dependence of ionic conductivity (standard deviation as error bar) for the Li-based SPEs: (a) temperatures ranging from 30–100 °C, (b) zoomed-in plot of area A in Figure 5.11a ($2.5 \times 10^{-7} < \sigma_{total} < 1.0 \times 10^{-4}$ S cm^{-1}) and (c) zoomed-in plot of area B in Figure 5.11a ($1.4 \times 10^{-4} < \sigma_{total} < 4.0 \times 10^{-4}$ S cm^{-1}). (d) Ionic conductivity of the PEO-based electrolytes at 70 °C. Reproduced with permission from Ref. [31].

have comparable σ_{total}, *e.g.*, $(1.43 \pm 0.05) \times 10^{-4}$ S cm^{-1} for LiRCTFSI/PEO vs. $(1.46 \pm 0.10) \times 10^{-4}$ S cm^{-1} for LiSCTFSI/PEO vs. $(1.42 \pm 0.12) \times 10^{-4}$ S cm^{-1} for LiCTFSI/PEO at 70 °C (**Figure 5.11d**). Altogether this further

supports the statement above – no visible impact of the camphor anion chirality on the ion transportation in PEO-based SPEs.

5.3.5 FTIR and Raman spectroscopy characterization

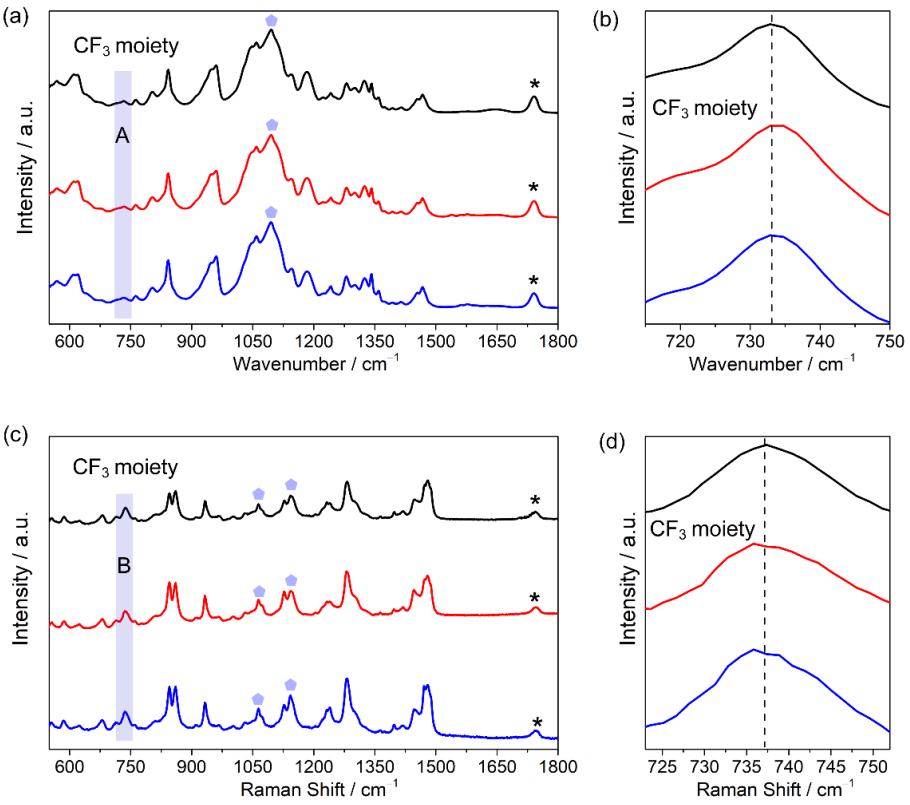

Figure 5.12. (a) FTIR and (c) Raman spectra of the different Li-based SPEs. (b) and (d) Zoomed-in profiles of the area A and area B shown in Figs. 5.12a and c, respectively. The black, red and blue lines represent LiRCTFSI/PEO, LiSCTFSI/PEO and LiCTFSI/PEO, respectively. Reproduced with permission from Ref. [31].

To further elaborate on the possible impact of anion chirality on physico-chemical properties for the different SPEs, the Li-based SPEs were characterized by FTIR and Raman spectroscopy. The spectra are shown in **Figure 5.12** and the band assignments are provided in **Tables 5.8** and **5.9**. For the FTIR spectra (**Figure 5.12a**) the bands are nearly superimposed for the three SPEs, *e.g.*, the asymmetric stretching of C=O bond from the chiral anion at 1740 cm^{-1} (asterisk) and the combined C–O–C bending and C–O stretching vibration of PEO at 1100 cm^{-1} (pentagon).[55-56] In addition, the bending vibrations of the $–CF_3$ moiety at 730–740 cm^{-1} (area A in **Figure 5.12a**), often used to assess the extent of ion-ion interactions, *i.e.*, ion pairs, solvated ions, *etc.*,[57] present very similar behavior (zoomed-in plots in **Figure 5.12b**). Thus, also at the molecular level, all the SPEs are very similar and the chirality of the camphor anions has a negligible impact.

Table 5.8. Mode assignment of typical bands observed by FTIR spectroscopy of the Li-based SPEs.[56 55] Reproduced with permission from Ref. [31].

FTIR wavenumber / cm^{-1}	Assignment
1740	C=O stretching vibration
1470	$–CH_2–$ bending vibration
962	$–CH_2–$ bending vibration
1300–1400	C–H wagging vibration
1100	C–O–C stretching vibration
844	$–CH_2–$ rocking vibration
730–740	expansion/contraction mode of $–CF_3$ moiety
613	$–SO_2–$ asymmetric blending vibration

Table 5.9. Mode assignment of typical bands observed by Raman spectroscopy of the Li-based SPEs.[7] Reproduced with permission from Ref. [31].

Raman shift / cm^{-1}	Assignment
1740	C=O stretching vibration
1478	$–CH_2–$ bending vibration
1278	$–CH_2–$ bending vibration
1142	C–O–C stretching vibration
1064	C–O–C stretching vibration
730–734	$–CF_3$ symmetric bending vibration

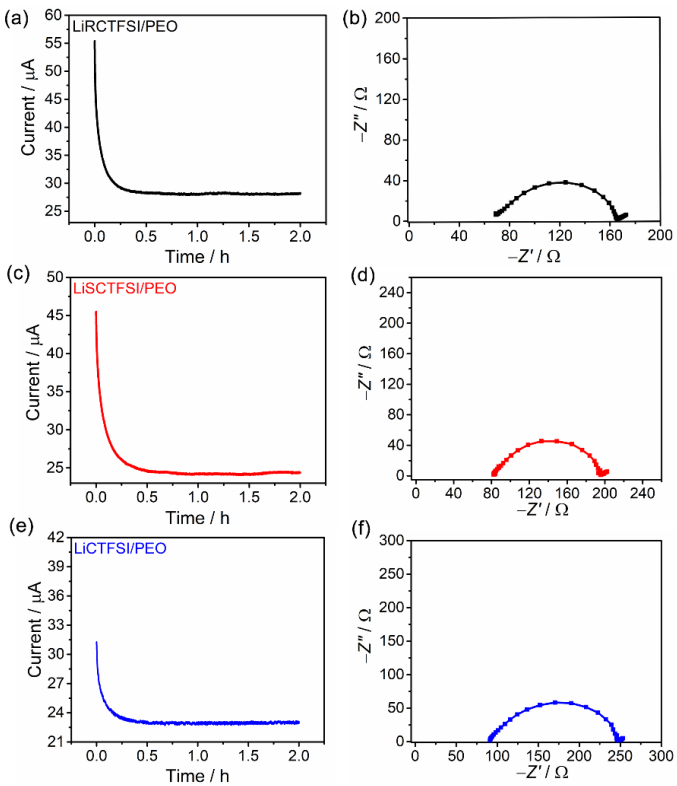

Figure 5.13. (a, c, e) Polarization profiles and (b, d, f) electrochemical impedance spectra before polarization of the Li° || Li° cells using different SPEs. Reproduced with permission from Ref. [31].

The Raman spectra show more or less the same overlap for the asymmetric stretching at ca. 1740 cm^{-1}, the combined bending and stretching vibration at ca. 1142 cm^{-1} and ca. 1064 cm^{-1} as well as for the $–CF_3$ feature (**Figure 5.12c** and **d**). The unambiguous FTIR and Raman spectral data combined strongly suggest that the local environment of the Li^+ ions and the chiral anions are quite similar for all three SPEs.

5.3.6 Lithium-ion transference number

Though only a marginal difference in σ_{total} (**Figure 5.11**) appears present, it is still possible with an impact of chiral anions on the selectivity of ion transport, *i.e.*, the $T_{Li}{}^+$. This would have a large impact in practice since only Li-ion migration under electric field is required for SSLMB application and a higher $T_{Li}{}^+$ would better mitigate concentration gradients and reduce internal cell polarization upon cell charge/discharge.[9]

Table 5.10. Data used to calculate lithium-ion transference numbers ($T_{Li}{}^+$) for the Li-based SPEs at 70 °C. Reproduced with permission from Ref. [31].

Samples	I_{DC} [a] / mA	R_{cell} [b] / Ω	V_{DC} [c] / mV	$T_{Li}{}^+$ [d]
LiRCTFSI/PEO	0.028	167	10	0.47
LiSCTFSI/PEO	0.024	195	10	0.48
LiCTFSI/PEO	0.023	248	10	0.57

[a] Steady-state current obtained from the DC polarization; [b] total resistances of Li° symmetric cell before DC polarization; [c] the DC voltage subjected to the polarization; [d] the $T_{Li}{}^+$ is calculated by Eq. [4].[58]

For the three Li-based SPEs, the $T_{Li}{}^+$ are very comparable, 0.47 for LiRCTFSI/PEO vs. 0.48 for LiSCTFSI/PEO vs. 0.57 for LiCTFSI/PEO at 70

°C (**Figure 5.13**, **Table 5.10**), and thus little changes in the Li-ion transport mechanism, where the Li^+ cations are solvated by the PEO chains and the anions interact little with neither PEO nor Li^+.[42] The anion chirality does not result in any accelerated diffusion/migration of Li^+ through ordered helices, but on the other hand these Li-based SPEs with camphor-derived chiral salts all show much higher T_{Li^+} as compared to conventional PEO-based SPEs with other sulfonimide salts, *e.g.*, LiFSI (T_{Li^+} = 0.14)[59] and LiTFSI (T_{Li^+} = 0.18),[59] presumably due to the larger anionic volume of the former anions.

5.4 Conclusion

The impact of chiral salts synthesized from camphor sulfonic acid on PEO-based SPEs show that the cation plays an important role in dictating not only the physico-chemical properties *e.g.*, T_d and T_m of the neat salts, but also for the PEO-based SPEs. The Li-based SPEs using chiral anions exhibit acceptable ionic conductivities (*ca.* 10^{-4} S cm^{-1}) with high T_{Li^+} (*ca.* 0.5) at 70 °C, which could fulfill the requirements of SSLMBs. That the R and S ionic conductivities are still not totally superimposable despite the extreme care taken in sample preparation and statistics applied, rather points to the difficulties of reliable ionic conductivity measurements in PEO electrolytes (≤ 8% dispersion) in particular at lower temperatures (< 60 °C), where probably the sample history plays a significant role. This goes together with the observation by Maurel *et al.*[41] of a strong dependence of the electrode geometry and the role of electrolyte stretching.[60] The expected induced order by using a single anion enantiomer, R or S, shows no marked improvement in ionic conductivity vs. applying the racemic mixture, for the camphor-based salts. Nonetheless, tailoring the chemical structure of anions to attain

long-range order of SPEs remains an intriguing strategy for facilitating fast ion transport. In the SPEs created here the chirality is localized in a part of the anion that plays no significant role with respect to solvation/dissociation. However, the effect might be more pronounced for intrinsically chiral anionic centers, like in borates or extended charge delocalized imides. We hope the insights provided here in terms of experimental accuracy needed may assist and also inspire further research on the design of new salts much needed for high-performant SPE-based SSLMBs.

5.5 References

1. Zhang, H.; Li, C.; Eshetu, G. G.; Laruelle, S.; Grugeon, S.; Zaghib, K.; Julien, C.; Mauger, A.; Guyomard, D.; Rojo, T., From Solid ‐ Solution Electrodes and the Rocking ‐ Chair Concept to Today's Batteries. *Angewandte Chemie* **2020,** *132* (2), 542-546.

2. Armand, M.; Tarascon, J. M., Building better batteries. *nature* **2008,** *451* (7179), 652-657.

3. Tarascon, J. M.; Armand, M., Issues and challenges facing rechargeable lithium batteries. *Nature* **2001,** *414* (6861), 359-367.

4. Feng, X.; Ren, D.; He, X.; Ouyang, M., Mitigating thermal runaway of lithium-ion batteries. *Joule* **2020,** *4* (4), 743-770.

5. Xu, K., Electrolytes and interphases in Li-ion batteries and beyond. *Chemical reviews* **2014,** *114* (23), 11503-11618.

6. Zhou, Q.; Ma, J.; Dong, S.; Li, X.; Cui, G., Intermolecular Chemistry in Solid Polymer Electrolytes for High-Energy-Density Lithium Batteries. *Advanced Materials* **2019,** *31* (50), 1902029.

7. Martinez ‐ Ibañez, M.; Sanchez ‐ Diez, E.; Qiao, L.; Zhang, Y.; Judez, X.; Santiago, A.; Aldalur, I.; Carrasco, J.; Zhu, H.; Forsyth, M., Unprecedented Improvement of Single Li ‐ Ion Conductive Solid Polymer Electrolyte Through Salt Additive. *Advanced Functional Materials* **2020,** *30* (16), 2000455.

8. Mauger, A.; Julien, C. M.; Goodenough, J. B.; Zaghib, K., Tribute to Michel Armand: from rocking chair–Li-ion to solid-state lithium batteries. *Journal of The Electrochemical Society* **2019,** *167* (7), 070507.

9. Zhang, H.; Li, C.; Piszcz, M.; Coya, E.; Rojo, T.; Rodriguez-Martinez, L. M.; Armand, M.; Zhou, Z., Single lithium-ion conducting solid polymer electrolytes: advances and perspectives. *Chemical Society Reviews* **2017,** *46* (3), 797-815.

10. Zhang, H.; Oteo, U.; Zhu, H.; Judez, X.; Martinez‐Ibañez, M.; Aldalur, I.; Sanchez‐Diez, E.; Li, C.; Carrasco, J.; Forsyth, M., Enhanced Lithium‐Ion Conductivity of Polymer Electrolytes by Selective Introduction of Hydrogen into the Anion. *Angewandte Chemie International Edition* **2019,** *58* (23), 7829-7834.

11. Qiao, L.; Judez, X.; Rojo, T.; Armand, M.; Zhang, H., Polymer Electrolytes for Sodium Batteries. *Journal of The Electrochemical Society* **2020,** *167* (7), 070534.

12. https://www.bollore.com/en/activites-et-participations-2/stockage-delectricite-et-systemes/.

13. M. Armand; W. Gorecki; R. Andreani, Proceedings of the 2nd International Meeting on Polymer Electrolytes (Ed.: B. Scrosati). *Elsevier, London* **1989**, p. 91.

14. Johansson, P.; Gejji, S. P.; Tegenfeldt, J.; Lindgren, J., The imide ion: potential energy surface and geometries. *Electrochimica acta* **1998,** *43* (10-11), 1375-1379.

15. Judez, X.; Zhang, H.; Li, C.; González-Marcos, J. A.; Zhou, Z.; Armand, M.; Rodriguez-Martinez, L. M., Lithium bis (fluorosulfonyl) imide/poly (ethylene oxide) polymer electrolyte for all solid-state Li–S cell. *The journal of physical chemistry letters* **2017,** *8* (9), 1956-1960.

16. Zhang, H.; Oteo, U.; Judez, X.; Eshetu, G. G.; Martinez-Ibanez, M.; Carrasco, J.; Li, C.; Armand, M., Designer anion enabling solid-state lithium-sulfur batteries. *Joule* **2019,** *3* (7), 1689-1702.

17. Zhang, H.; Chen, F.; Lakuntza, O.; Oteo, U.; Qiao, L.; Martinez-Ibañez, M.; Zhu, H.; Carrasco, J.; Forsyth, M.; Armand, M., Suppressed Mobility of Negative Charges in Polymer Electrolytes with an Ether-Functionalized Anion. *Angewandte Chemie International Edition* **2019,** *58* (35), 12070-12075.

18. Ariga, K.; Ji, Q.; Mori, T.; Naito, M.; Yamauchi, Y.; Abe, H.; Hill, J. P., Enzyme nanoarchitectonics: organization and device application. *Chemical Society Reviews* **2013,** *42* (15), 6322-6345.

19. Ariga, K.; Vinu, A.; Yamauchi, Y.; Ji, Q.; Hill, J. P., Nanoarchitectonics for mesoporous materials. *Bulletin of the Chemical Society of Japan* **2012,** *85* (1), 1-32.

20. Buda, A. B.; der Heyde, T. A.; Mislow, K., On quantifying chirality. *Angewandte Chemie International Edition in English* **1992,** *31* (8), 989-1007.

21. Cahard, D.; Xu, X.; Couve-Bonnaire, S.; Pannecoucke, X., Fluorine & chirality: how to create a nonracemic stereogenic carbon–fluorine centre? *Chemical Society Reviews* **2010,** *39* (2), 558-568.

22. Hembury, G. A.; Borovkov, V. V.; Inoue, Y., Chirality-sensing supramolecular systems. *Chemical reviews* **2008,** *108* (1), 1-73.

23. Khan, M. K.; Giese, M.; Yu, M.; Kelly, J. A.; Hamad, W. Y.; MacLachlan, M. J., Flexible mesoporous photonic resins with tunable chiral nematic structures. *Angewandte Chemie* **2013,** *125* (34), 9089-9092.

24. Kopeček, J.; Yang, J., Smart self‐assembled hybrid hydrogel biomaterials. *Angewandte Chemie International Edition* **2012,** *51* (30), 7396-7417.

25. Liu, Y.; Goebl, J.; Yin, Y., Templated synthesis of nanostructured materials. *Chemical Society Reviews* **2013,** *42* (7), 2610-2653.

26. Nguyen, T. D.; Hamad, W. Y.; MacLachlan, M. J., CdS quantum dots encapsulated in chiral nematic mesoporous silica: new iridescent and luminescent materials. *Advanced Functional Materials* **2014,** *24* (6), 777-783.

27. Zhang, J.-H.; Xie, S.-M.; Zhang, M.; Zi, M.; He, P.-G.; Yuan, L.-M., Novel inorganic mesoporous material with chiral nematic structure derived from nanocrystalline cellulose for high-resolution gas chromatographic separations. *Analytical chemistry* **2014,** *86* (19), 9595-9602.

28. Zhou, L.; Xu, G.; Mahmood, Q.; Lv, C.; Wang, X.; Sun, X.; Guo, K.; Wang, Q., N-Heterocyclic olefins and thioureas as an efficient cooperative catalyst system for ring-opening polymerization of δ-valerolactone. *Polymer Chemistry* **2019,** *10* (14), 1832-1838.

29. Wong, L. W. Y.; Kan, J. W. H.; Nguyen, T.-h.; Sung, H. H. Y.; Li, D.; Au-Yeung, A. S. F.; Sharma, R.; Lin, Z.; Williams, I. D., Bis (mandelato) borate: an effective, inexpensive spiroborate anion for chiral resolution. *Chemical Communications* **2015,** *51* (87), 15760-15763.

30. Kane-Maguire, L. A. P.; Wallace, G. G., Chiral conducting polymers. *Chemical Society Reviews* **2010,** *39* (7), 2545-2576.

31. Lixin, Q.; Alexander, S.; Yan, Z.; Maria, M.-I.; Eduardo, S.-D.; Elias, L.; Marcel, T.; Patrik, J.; Heng, Z.; Michel, A., Solid Polymer Electrolytes Comprising Camphor-Derived Chiral Salts for Solid-State Batteries. *Journal of the Electrochemical Society* **2020**.

32. Béranger, S.; Fortier, M.-H.; Baril, D.; Armand, M. B., Inducing order in polymer. *Solid State Ionics* **2002,** *148* (3-4), 437-441.

33. Takahashi, Y.; Tadokoro, H., Structural studies of polyethers,(-(CH2) mO-) n. X. Crystal structure of poly (ethylene oxide). *Macromolecules* **1973,** *6* (5), 672-675.

34. Ho, R.-M.; Chiang, Y.-W.; Lin, S.-C.; Chen, C.-K., Helical architectures from self-assembly of chiral polymers and block copolymers. *Progress in polymer science* **2011,** *36* (3), 376-453.

35. M. Armand; J. M. Chabagno; M. J. Duclot, The 2nd International conference on solid electrolyte. **1978**.

36. Armand, M. B., Polymer electrolytes. *Annual Review of Materials Science* **1986,** *16* (1), 245-261.

37. Armand, M., Polymers with ionic conductivity. *Advanced Materials* **1990,** *2* (6‐7), 278-286.

38. Chatani, Y.; Okamura, S., Crystal structure of poly (ethylene oxide)—sodium iodide complex. *Polymer* **1987,** *28* (11), 1815-1820.

39. Chanda, M., *Plastics technology handbook*. CRC press: 2017.

40. Marzantowicz, M.; Dygas, J. R.; Krok, F., Impedance of interface between PEO: LiTFSI polymer electrolyte and blocking electrodes. *Electrochimica Acta* **2008,** *53* (25), 7417-7425.

41. Maurel, A.; Armand, M.; Grugeon, S.; Fleutot, B.; Davoisne, C.; Tortajada, H.; Courty, M.; Panier, S.; Dupont, L., Poly (Ethylene Oxide)− LiTFSI Solid Polymer Electrolyte Filaments for Fused Deposition Modeling Three-Dimensional Printing. *Journal of The Electrochemical Society* **2020,** *167* (7), 070536.

42. Zhang, H.; Chen, F.; Lakuntza, O.; Oteo, U.; Qiao, L.; Martinez‐Ibañez, M.; Zhu, H.; Carrasco, J.; Forsyth, M.; Armand, M., Suppressed Mobility of Negative Charges in Polymer Electrolytes with an Ether‐Functionalized Anion. *Angewandte Chemie* **2019,** *131* (35), 12198-12203.

43. Cohen, E. R., An introduction to error analysis: The study of uncertainties in physical measurements. IOP Publishing: 1998.

44. Ma, Q.; Zhang, H.; Zhou, C.; Zheng, L.; Cheng, P.; Nie, J.; Feng, W.; Hu, Y. S.; Li, H.; Huang, X., Single lithium‐ion conducting polymer electrolytes based on a super‐delocalized polyanion. *Angewandte Chemie International Edition* **2016,** *55* (7), 2521-2525.

45. Wang, Y.; Zhong, W. H., Development of Electrolytes towards Achieving Safe and High‐Performance Energy‐Storage Devices: A Review. *ChemElectroChem* **2015,** *2* (1), 22-36.

46. Pinter, B.; Nagels, N.; Herrebout, W. A.; De Proft, F., Halogen bonding from a hard and soft acids and bases perspective: investigation by using density functional theory reactivity indices. *Chemistry–A European Journal* **2013,** *19* (2), 519-530.

47. Cameron, G. G.; Ingram, M. D.; Qureshi, M. Y.; Gearing, H. M.; Costa, L.; Camino, G., The thermal degradation of poly (ethylene oxide) and its complex with NaCNS. *European polymer journal* **1989,** *25* (7-8), 779-784.

48. Zhang, H.; Judez, X.; Santiago, A.; Martinez-Ibañez, M.; Muñoz-Márquez, M. Á.; Carrasco, J.; Li, C.; Eshetu, G. G.; Armand, M., Fluorine-Free Noble Salt Anion for High-Performance All-Solid-State Lithium–Sulfur Batteries. *Advanced Energy Materials* **2019,** *0* (0), 1900763.

49. Cermak, S. C.; Wiemer, D. F., Synthesis of derivatives of (1R)-(-)-and (1S)-(+)-10-camphorsulfonic acid. *Journal of chemical education* **1999,** *76* (12), 1715.

50. Hagiwara, R.; Tamaki, K.; Kubota, K.; Goto, T.; Nohira, T., Thermal properties of mixed alkali bis (trifluoromethylsulfonyl) amides. *Journal of Chemical & Engineering Data* **2008,** *53* (2), 355-358.

51. Zhang, H.; Feng, W.; Nie, J.; Zhou, Z., Recent progresses on electrolytes of fluorosulfonimide anions for improving the performances of rechargeable Li and Li-ion battery. *Journal of Fluorine Chemistry* **2015,** *174*, 49-61.

52. Stolwijk, N. A.; Heddier, C.; Reschke, M.; Wiencierz, M.; Bokeloh, J.; Wilde, G., Salt-concentration dependence of the glass transition temperature in PEO–NaI and PEO–LiTFSI polymer electrolytes. *Macromolecules* **2013,** *46* (21), 8580-8588.

53. Ratner, M. A.; Johansson, P.; Shriver, D. F., Polymer electrolytes: ionic transport mechanisms and relaxation coupling. *Mrs Bulletin* **2000,** *25* (3), 31-37.

54. Di Marco, G.; Bartolotta, A.; Carini, G., Size effect of the alkali cation on the structure and the molecular mobility of solid polymeric electrolytes. *Journal of applied physics* **1992,** *71* (12), 5834-5840.

55. Anilkumar, K. M.; Jinisha, B.; Manoj, M.; Jayalekshmi, S., Poly (ethylene oxide)(PEO)–Poly (vinyl pyrrolidone)(PVP) blend polymer based solid electrolyte membranes for developing solid state magnesium ion cells. *European Polymer Journal* **2017,** *89*, 249-262.

56. Narita, A.; Shibayama, W.; Ohno, H., Structural factors to improve physico-chemical properties of zwitterions as ion conductive matrices. *Journal of Materials Chemistry* **2006,** *16* (15), 1475-1482.

57. Sun, B.; Mindemark, J.; Morozov, E. V.; Costa, L. T.; Bergman, M.; Johansson, P.; Fang, Y.; Furó, I.; Brandell, D., Ion transport in polycarbonate based solid polymer electrolytes: experimental and computational investigations. *Physical Chemistry Chemical Physics* **2016,** *18* (14), 9504-9513.

58. Suo, L.; Hu, Y.-S.; Li, H.; Armand, M.; Chen, L., A new class of solvent-in-salt electrolyte for high-energy rechargeable metallic lithium batteries. *Nature communications* **2013,** *4* (1), 1-9.

59. Zhang, H.; Liu, C.; Zheng, L.; Xu, F.; Feng, W.; Li, H.; Huang, X.; Armand, M.; Nie, J.; Zhou, Z., Lithium bis (fluorosulfonyl) imide/poly (ethylene oxide) polymer electrolyte. *Electrochimica Acta* **2014,** *133*, 529-538.

60. Golodnitsky, D.; Livshits, E.; Peled, E. In *Highly conductive oriented PEO‐based polymer electrolytes*, 2003; Wiley Online Library: pp 27-46.

Chapter 6

Conclusion

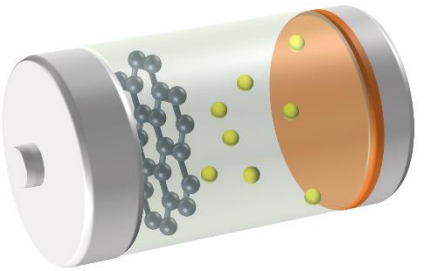

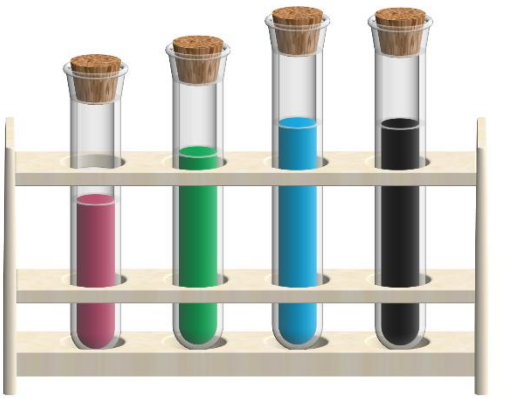

Chapter 6: Conclusion

6.1 Conclusion

PEO-based solid polymer electrolytes (SPEs) with flexibility, processability, and excellent solvating ability toward a wide variety of salts have been widely in solid-state lithium metal batteries (SSLMBs). Actually, the chemistry of the lithium salt employed in PEO-based SPEs plays a pivotal role in dictating the physico-chemical and electrochemical performance of any SPE, and thus also influences the performance of SSLMBs. The lithium bis(trifluoromethanesulfonyl)imide (LiTFSI) salt, first suggested as salt for SPEs in 1986, possesses low lattice energy and the $TFSI^-$ anion has an extensive structural flexibility, both due to the anion's highly delocalized negative charge and flexible center [*e.g.*, $–SO_2–N^{(-)}–SO_2–$] and has therefore been commonly used for SPE-based SSLMBs. However, the low lithium-ion transference number (T_{Li^+}) and poor solid electrolyte interphase-creating properties (SEI) result in severe cell polarization and simultaneously notorious dendritic growth on the Li° anode.

The main objective of this work is to design and synthesize new lithium salts with suppressed anionic mobility to enhance lithium-ion transference number (T_{Li^+}) without sacrificing significantly the ionic conductivity, and simultaneously with the aim of forming an excellent SEI layers at the Li° anode to improve interfacial compatibility and stability towards Li° anode.

Several novel lithium salts with different properties were synthesized and employed as conductive salts in PEO-based SPEs in this thesis, the structures of the lithium salts are shown in **Scheme 6.1**. The fundamental

properties of the neat salts and PEO-based SPEs are comprehensively characterized, in terms of surface morphology, thermal stability, phase transition, ionic conductivity, and electrochemical stability, etc. In addition, different lithium cells such as lithium symmetric Li° || Li° cells and Li° || LFP cells were assembled to systematically evaluate the feasibility of these lithium salts-based SPEs.

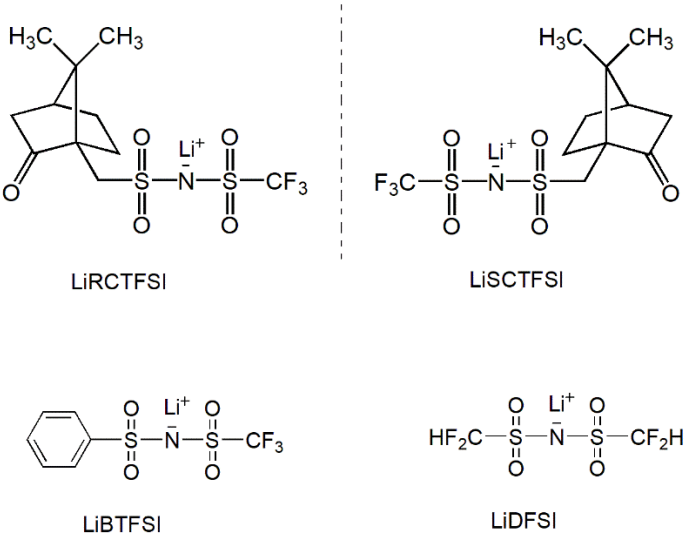

Scheme 6.1. The structures of the synthesized salts in this thesis.

Among these SPEs, the benzene-based lithium salt, lithium benzenesulfonyl(trifluoromethanesulfonyl)imide (LiBTFSI)-based SPE shows the highest T_{Li^+} of ca. 0.69 with a measured ionic conductivity of 3.6 × 10^{-4} S cm^{-1} at 70 °C. This high T_{Li^+} might be due to the larger volume of the $BTFSI^-$ anion and stronger intermolecular/intramolecular interactions, e.g., intermolecular π–π stacking of the $BTFSI^-$ anion, intramolecular H bonds between $BTFSI^-$ anion and PEO matrix. Besides, the $LiFePO_4$ || Li° cells assembled with the LiBTFSI-based SPEs show a superior long-term

cyclability with excellent Coulombic efficiencies as well as high discharge capacities. In another work, the chiral salts-based SPEs also exhibit a high T_{Li}^{+} around 0.50 at 70 °C, however, these SPEs present the lowest ionic conductivity of 1.5×10^{-4} S cm^{-1} (**Figure 6.1**) among the salts tested, which might be ascribed to the low migration kinetics of the bulky camphor-based anion.

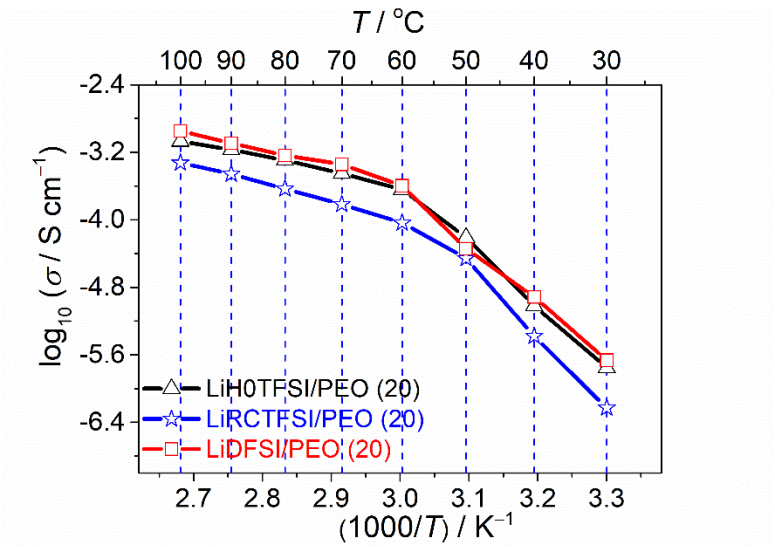

Figure 6.1. Temperature dependence of ionic conductivities of different solid polymer electrolytes (SPEs).

Not surprisingly, the trifluoromethyl-free salt, lithium bis(difluoromethanesulfonyl)imide (LiDFSI)-based SPEs show the highest ionic conductivity of 4.6×10^{-4} S cm^{-1} at 70 °C compared with the other two SPEs, as shown in **Figure 6.1**. In addition, the LiDFSI-based SPEs display a decent T_{Li}^{+} of 0.39 owing to the H-bonding interactions between $–CF_2H$ moieties and EO units. It is generally accepted that the widely used LiTFSI salt that contains two trifluoromethyl ($–CF_3$) groups has a very low chemical

and biochemical degradability, despite its strong electron-withdrawing ability which is essential for the dissolution and transport of ions in SPEs. This raises considerable risks to environment and human health once the salts or their decomposition products leak out of the battery pack or are poorly disposed of. In contrast to LiTFSI, the $–CHF_2$ moieties of LiDFSI-based salt shows a rapid chemical degradation under a mild basic solution. More importantly, the LiDFSI-based cells show a superior electrochemical performance towards Li° electrode which is associated with the formation of ionically conductive LiH and mechanically stable LiF-rich SEI-building species on Li° electrode. As a result, the prototype Li° || $LiFePO_4$ cell using LiDFSI/PEO could be cycled for more than 140 cycles with minimal capacity decay, suggesting the feasibility of $DFSI^-$ as conducting salt for SPE-based SSLMBs.

In conclusion, the results obtained are well in agreement with the objectives defined at the beginning of this thesis. Among the salts synthesized in this thesis, the innovative LiDFSI salt with the highest ionic conductivities and excellent SEI formation as well as the good chemical degradation property is the most promising salt candidate to SSLMBs.

Appendix

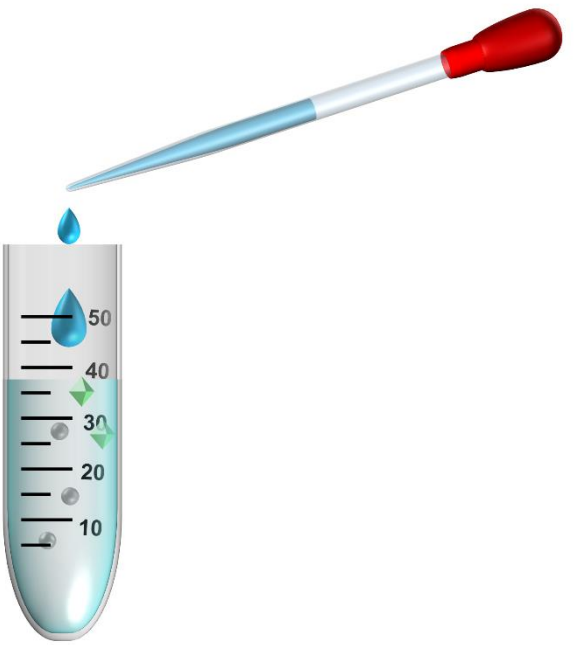

Appendix:

Appendix

A.1. List of abbreviations

σ_{Li^+}	Li-ion conductivity
σ_{SD}	Standard deviation
σ_{total}	Total ionic conductivity
ACN	Acetonitrile
AFM	Atomic force microscopy
CEs	Coulombic efficiencies
CEI	Cathode electrode interface
CPEs	Composite polymer electrolytes
CV	Cyclic voltammogram
DEC	Diethyl carbonate
DMC	Dimethyl carbonate
DME	1,2-dimethoxyethane
DSC	Differential scanning calorimetry
EC	Ethylene carbonate
EDLCs	Electric double layer capacitors
EFA	Ether-functionalized anion

EIS	Electrochemical impedance spectroscopy
EMC	Ethyl methyl carbonate
ESW	Electrochemical stability window
EO	Ethylene oxide
EVs	Electric vehicles
f_{FN}	Fractional uncertainty
FTIR	Fourier-transform infrared spectroscopy
GPEs	Gel polymer electrolytes
HCs	Hybrid capacitors
HOMO	Highest occupied molecular orbital
ILs	Ionic liquids
LEs	Liquid electrolytes
$LiAsF_6$	Lithium hexafluoroarsenate
LiBETI	Lithium bis (perfluoroethanesulfonyl)imide
$LiBF_4$	Lithium tetrafluoroborate
LiBOB	Lithium bis(oxalato)borate
LiBTFSI	Lithium benzenesulfonyl (trifluoromethanesulfonyl)imide

$LiCF_3SO_3$/LiTf	Lithium trifluoromethanesulfonate
$LiC_2F_5SO_3$	Lithium perfluoroethanesulfonate
$LiC_4F_9SO_3$	Lithium perfluorobutanesulfonate
$LiClO_4$	Lithium perchlorate
$LiCoO_2$/LCO	Lithium cobalt oxide
LiDCTA	Lithium-4,5-dicyano-1,2,3-triazolate
LiDFOB	Lithium difluoro(oxalato)borate
LiDFTFSI	Lithium (difluoromethanesulfonyl)(trifluoromethanesulfonyl)imide
LiFAP	Lithium tris(perfluuoroethyl)trifluorophosphate
LiFNFSI	Lithium (fluorosulfonyl)(*n*-nonafluorobutanesulfonyl)imide
LFP	$LiFePO_4$
LiFPFSI	Lithium (fluorosulfonyl)(pentafluoroethanesulfonyl)imide
LiFSI	Lithium bis(fluorosulfonyl)imide
LiFTFSI	Lithium (fluorosulfonyl)(trifluoromethanesulfonyl)imide
LIBs	Lithium-ion batteries

LiDFSI	Lithium bis(difluoromethanesulfonyl)imide
LMBs	Lithium metal (Li°) batteries
LiPDI	Lithium-4,5-dicyano-2-(pentafluoroethyl)imidazole
$LiPF_6$	Lithium hexafluorophosphate
LiRCTFSI	Lithium [(1R)-(−)-10-camphorsulfonyl](trifluoromethanesulfonyl)imide
LiSCN	Lithium thiocyanate
LiSCTFSI	Lithium [(1S)-(+)-10-camphorsulfonyl](trifluoromethanesulfonyl)imide
$LiSbF_6$	Lithium hexafluoroantimonate
LisTFSI	Lithium [trifluoromethane(*S*-trifluoromethanesulfonylimino)sulfonyl]-(trifluoromethanesulfonyl)imide
LiTCM	Lithium tricyanomethanide
LiTDI	Lithium 2-trifluoromethyl-4,5-dicyanoimidazolate
LiTFPFB	Lithium trifluoro(perfluoro-tert-butyloxyl)borate
LiTNFSI	Lithium (trifluoromethanesulfonyl)(*n*-nonafluorobutanesulfonyl)imide
LiTFSI	Lithium bis(trifluoromethanesulfonyl)imide

LSV	Linear sweeping voltammogram
LUMO	Lowest unoccupied molecular orbital
Ni-Cd	Nickel-cadmium batteries
Ni-MH	Nickel-metal hybrid batteries
NO_x	Nitrogen oxides
NMR	Nuclear magnetic resonance spectroscopy
PAN	Polyacrylonitrile
PC	Propylene carbonate
PCs	Pseudo-capacitors
PEO	Poly(ethylene oxide)
PMMA	Poly(methylmethacrylate)
P(PO/EM)	Poly[propylene oxide-co-2-(2-methoxyethoxy)ethyl glycidyl ether]
PVA	Poly(vinyl alcohol)
PVC	Poly(vinyl chloride)
PVDF-HFP	Poly(vinylidene fluoride-*co*-hexafluoropropylene)
R_b	Bulk resistance

RLMBs	Rechargeable lithium metal batteries
R_i	Interfacial resistance
S	Sulfur
SEI	Solid electrolyte interface
SEM	Scanning electron microscope
SHE	Standard hydrogen electrode
SIBs	Sodium-ion batteries
SO_x	Sulfur species sulfides
SPEs	Solid polymer electrolytes
SS	Stainless steel
SSEs	Solid-state electrolytes
SSRLMBs	Solid-state based RLMBs
T_c	Crystallization temperature
T_{Li^+}	Lithium-ion transference number
T_g	Glass transition temperature
TGA	Thermogravimetric analysis
THF	Tetrahydrofuran

T_m	Melting temperature
XPS	X-ray photoelectron spectroscopy

A.2. List of figures

electrolyte (GE) or ceramic electrolyte (CE) | $LiFePO_4$ and Na° | GE or CE | $NaFePO_4$ cells are denoted as GE (CE)-LMB and GE (CE)-SMB, respectively. Notice that the volumetric energy densities of glassy and ceramic electrolyte-based cells are superimposed in Figure 1.8c.

Figure 1.9. (a) The theoretical capacity of graphite and various metal anodes. (b) Reduction potential of various metal anodes. (c) The elemental abundance in earth crust.

Figure 1.10. (a) Scheme of dilemma for Li° anode in rechargeable batteries Reproduced with permission from Ref. [95]. (b). Correlations among the different challenges in the Li° anode, originating from high reactivity and infinite relative volume change.

Figure 1.11. Historical overview on the development of solid polymer electrolytes (SPEs)-based solid-state lithium metal batteries.

Figure 1.12. Mechanism of ion transport in PEO-based polymers.

Figure 1.13. Schematic view of organic/inorganic composites with different microstructures and various Li^+ transportation pathways.

Figure 2.1. Schematic illustration of SPEs preparation by conventional solvent casting method.

Figure 2.2. Schematic illustration of the coin cell used for ionic conductivity measurements.

Figure 3.1. Comparison between the chemistry of CF_2H- and CF_3-containing compounds inside and outside a lithium metal cell. The light grey, grey, red, and light blue balls represent H, C, O, and F atoms, respectively.

Figure. 3.2. NMR spectra of the as-prepared LiDFSI salt: (a) ^{1}H NMR, (b) ^{19}F NMR without decoupling, (c) ^{19}F NMR decoupling, (d) ^{13}C NMR, and (e) edited 2D correlation heteronuclear single quantum coherence spectroscopy (HSQC).

Figure 3.3. Raman spectrum of the LiDFSI salt.

Figure 3.4. Hydrolysis tests of the lithium salts. (a) ^{1}H NMR and (b) ^{19}F NMR spectra of LiDFSI/D_2O, and (c) ^{19}F NMR spectra of LiTFSI/D_2O after different storage times under neutral condition. (d) ^{1}H NMR and (e) ^{19}F NMR spectra of LiDFSI/D_2O, and (f) ^{19}F NMR spectra of LiTFSI/D_2O after different storage times under basic condition.

Figure 3.5. Hydrolysis of lithium salts under basic condition. (a-c) ^{19}F NMR spectra of LiDFSI/D_2O and LiTFSI/D_2O: (a) 0 h, (b) 3 h, and (c) 720 h. (d) Molar percentage of residual lithium salt vs. storage time.

Figure 3.6. The digital camera images (scale bar: 16 mm) of LiDFSI/PEO and LiTFSI/PEO electrolytes. (a) LiDFSI/PEO (EO/Li^+ = 20), (b) LiTFSI/PEO (EO/Li^+ = 20), (c) LiDFSI/PEO (EO/Li^+ = 64), (d) LiDFSI/PEO (EO/Li^+ = 32) and (e) LiDFSI/PEO (EO/Li^+ = 8).

Figure 3.7. Scanning electron microscopy (SEM) and optical microscope images of the (a,c) LiDFSI/PEO (20), and (b,d) LiTFSI/PEO (20) electrolytes.

Figure 3.8. Atomic force microscopy (AFM) images of the (a,c) LiDFSI/PEO (20) and (b,d) LiTFSI/PEO (20) electrolytes. (a,b) phase images and (c,d) topography images.

Figure 3.9. AFM phase images of the (a) LiDFSI/PEO (20) and (b) LiTFSI/PEO (20) electrolytes, as well as (c) the dependence of phase on a given axis indicated by cyan lines.

Figure 3.10. (a) Thermogravimetric analysis (TGA) and (b) differential scanning calorimetry analysis (DSC) of the neat LiDFSI salt. (c) TGA of the PEO-based SPEs.

Figure 3.11. (a) DSC and (b) X-Ray diffraction (XRD) of the PEO-based SPEs.

Figure 3.12. (a) DSC and (b) XRD of these two PEO-based SPEs at different ratios.

Figure 3.13. (a) Arrhenius plots of ionic conductivity of the electrolytes. (b) Concentration dependence of total ionic conductivity for the LiDFSI/PEO electrolytes at 70 ℃.

Figure 3.14. Polarization profiles and impedance before polarization (inset) of the Li° symmetric cells using the (a) LiDFSI/PEO (20) and (b) LiTFSI/PEO (20) electrolytes at 70 ℃.

Figure 3.15. (a) Radial distribution function (RDF, solid line) between Li and O from either anions or PEO, as well as their coordination number (CN, dotted line). (b) RDF between H and O from either anions or PEO.

Figure 3.16. Mean-square displacement (MSD) of Li^+ and F atoms in anions zoomed in the first 80 ns of the whole simulation.

Figure 3.17. (a) Linear sweep voltammetry (LSV) profiles of the 0.1 M LiX/PC (X = DFSI or TFSI) solutions measured on a Pt electrode at room temperature. (b) LSV profiles of the LiX/PEO (X = DFSI or TFSI, EO/Li = 20) SPEs measured on stainless steel (SS) electrode at 70 ℃.

Figure 3.18. (a) Cyclic voltammetry (CV) and (b) Coulombic efficiencies (CEs) of LiX/PEO (X= DFSI or TFSI) based cells measured on Cu electrode using a scan rate of 1 mV s^{-1} at 70 ℃. Zoomed-in CV plots of different electrolytes: (c) LiDFSI/PEO (20), and (d) LiTFSI/PEO (20).

Figure 3.19. (a) Galvanostatic cycling of Li° anode in PEO-based electrolytes at 70 ^oC (current density: 0.1 mA cm^{-2}; duration of half-cycle: 3 h). (b-d) Zoomed-in plots of the Li° symmetric cells in the range of (b) 50−100 h, (c) 1500−1550 h, and (d) 3000−3050 h.

Figure 3.20. (a) Galvanostatic cycling of Li° anode in the DME-based electrolytes at room temperature, and (b-d) zoomed-in plots of the Li° symmetric cells in the range of (b) 200−250 h, (c) 450−500 h, (d) 700−750 h.

Figure 3.21. Impedance spectra of the Li° symmetric cells in Figure 3.19a after cycling. The inset shows the equivalent circuit adapted from Ref. [70] for fitting the raw EIS spectra and the fitted results are plotted as lines.

Figure 3.22. The role of salt anion on the surface of Li° electrode. (a) Optical and SEM images of Li° deposits on a Cu substrate recovered from the LiDFSI- and LiTFSI-based solutions. The scale bars in optical (left), top

view (middle), cross-sectional (right) images are 10 mm, 20 μm, and 50 μm, respectively. (b) XPS spectra of C1s and F1s collected from the surface of Li° deposits. (c) The evolution of atomic percentage vs. sputtering time for the LiDFSI- and LiTFSI-based samples. (d) F1s spectra after various sputtering times for the LiDFSI- and LiTFSI-based samples. In Figure 3.22b and d, the purple and black lines represent the raw data and fitted results. (e) Schematic illustration of SEI formed in the LiDFSI- and LiTFSI-based electrolytes.

Figure 3.23. XPS survey spectra for the Li° deposits obtained from the Li° || Cu cell using 1 M LiX/DME [X = DFSI (a) or TFSI (b)] at different sputtering times.

Figure 3.24. XPS survey spectra for the Li° deposits obtained from the Li° || Cu cell using 1 M LiX/DME [X = DFSI (a) or TFSI (b)] at different sputtering times.

Figure 3.25. (a-c) DFT calculation on $DFSI^-$ and $TFSI^-$. (a) Energy of HOMO and LUMO. (b) Energy difference between two anions when injecting one electron. (c) Visualized HOMO and LUMO of $DFSI^-$ and $TFSI^-$ and their reduced form (i.e., $DFSI^{2-}$, $TFSI^{2-}$). The light pink, grey, blue, red, green, and yellow balls signify H, C, N, O, F, and S atoms, respectively.

Figure 3.26. Chemical stabilities of LiDFSI and LiTFSI towards chemical reduction in the presence of naphthalene radical in tetrahydrofuran (THF) solutions.

Figure 3.27. Cycling performance of solid-state lithium metal polymer cells using LiX/PEO (X = DFSI or TFSI, EO/Li = 20). (a, b)

Discharge/charge profiles of the Li° || $LiFePO_4$ cells at 70 °C: (a) LiTFSI/PEO, and (b) LiDFSI/PEO. (c) Long-term cycling performance of the Li° || $LiFePO_4$ cells (three formation cycles at rate of C/5 and then constant cycling at C/3). (d, e) The impedance plots of the cells before and after cycling: (d) LiDFSI/PEO, and (e) LiTFSI/PEO. The equivalent circuit (inset in Figure 3.27d) adapted from Ref. [70] is used for fitting the raw EIS spectra, and the fitted results are plotted as lines.

Figure 4.1. Nuclear magnetic resonance (NMR) spectra of the as-prepared LiBTFSI salt: (a) ^{1}H NMR, (b) ^{19}F NMR, (c) ^{13}C NMR and (c) edited 2D heteronuclear single quantum coherence (HSQC).

Figure 4.2. Thermogravimetric analysis (TGA) of the synthesized LiBTFSI salt.

Figure 4.3. Digital and optical images of SPEs. (a,b) LiBTFSI-based SPEs. (c,d) LiTFSI-based SPEs. ($EO/Li^+ = 20$)

Figure 4.4. Scanning electron microscope (SEM) images of SPEs. (a) LiBTFSI-based SPEs, (b) LiTFSI-based SPEs. ($EO/Li^+ = 20$)

Figure 4.5. Thermogravimetric analysis (TGA) of the PEO-based LiBTFSI and LiTFSI SPEs ($EO/Li^+ = 20$).

Figure 4.6. Differential scanning calorimetry analysis (DSC) of the PEO-based LiBTFSI and LiTFSI SPEs ($EO/Li^+ = 20$).

Figure 4.7. XRD patterns of the PEO-based LiBTFSI and LiTFSI SPEs ($EO/Li^+ = 20$).

Figure 4.8. Arrhenius plots of ionic conductivity for PEO-based LiBTFSI and LiTFSI SPEs ($EO/Li^+ = 20$).

Figure 4.9. Linear sweep voltammogram (LSV) of the 0.1 M LiX/PC (X= BTFSI or TFSI) electrolytes.

Figure 4.10. LSV profiles of the PEO-based LiBTFSI and LiTFSI SPEs at 70 °C ($EO/Li^+ = 20$).

Figure 4.11. Cyclic voltammetry (CV) profiles of the PEO-based LiBTFSI (a) and LiTFSI SPEs (b) at 70 °C ($EO/Li^+ = 20$).

Figure 4.12. (a) Galvanostatic cycling of Li° anode in PEO-based electrolytes at 70 °C (current density: 0.1 mA cm^{-2}; duration of half-cycle: 3 h). (d–f) Zoomed-in plots of the Li° symmetric cells in the range of (d) 70–120 h, (e) 200–250 h, and (f) 500–560 h.

Figure 4.13. Cycling performance of solid-state lithium metal polymer cells using LiBTFSI/PEO SPE. (a) Long-term cycling performance of the Li° || $LiFePO_4$ (LFP) cells (three formation cycles at rate of C/5 and then constant cycling at C/3). (b, c) Discharge/charge profiles of the Li° || LFP cells at 70 °C: (b) LiBTFSI/PEO and (c) LiTFSI/PEO.

Figure 4.14. Cycling performance of solid-state lithium metal polymer cells using LiTFSI/PEO SPE with a low LFP areal loading of 2.65 mg cm^{-2} (EO/Li = 20). (a) Long-term cycling performance of the Li° || $LiFePO_4$ (LFP) cell with LiTFSI/PEO SPE. (b) Discharge/charge profiles of LiTFSI/PEO-based Li° || LFP cells with a low LFP areal loading.

Figure 4.15. Rate performance of solid-state lithium metal polymer cells using LiX/PEO (X = BTFSI or TFSI, EO/Li = 20). (a) Rate capability of these two PEO-based Li° || LFP cells under different currents. (c, d) Discharge/charge profiles of the Li° || LFP cells at 70 °C and different current densities: (c) LiBTFSI/PEO and (d) LiTFSI/PEO.

Figure 5.1. NMR spectra of the as-prepared KRCTFSI salt: (a) ^{1}H NMR, (b) ^{19}F NMR and (c) edited 2D HSQC.

Figure 5.2. NMR spectra of the as-prepared KSCTFSI salt: (a) ^{1}H NMR, (b) ^{19}F NMR and (c) edited 2D HSQC.

Figure 5.3. NMR spectra of the as-prepared LiSCTFSI salt: (a) ^{1}H NMR, (b) ^{19}F NMR and (c) edited 2D HSQC.

Figure 5.4. FTIR spectra of the as-prepared chiral salts.

Figure 5.5. Raman spectra of the as-prepared (a) KRSCTFSI, (b) KSCTFSI, (c) LiRCTFSI and (d) LiSCTFSI salts, respectively.

Figure 5.6. NMR spectra of the as-prepared LiRCTFSI salt: (a) ^{1}H NMR, (b) ^{19}F NMR, and (c) edited 2D HSQC.

Figure 5.7. Thermal stabilities of (a, b) the neat camphor-derived chiral salts and (c, d) the PEO-based SPEs.

Figure 5.8. Differential scanning calorimetry (DSC) traces of the salts and SPEs: (a) potassium salts, (b) lithium salts, (c) K-based SPEs and (d) Li-based SPEs. The DSC traces of the neat salts and SPEs are obtained from the first and second heating scans, respectively.

Figure 5.9. DSC traces of different SPEs during the first heating and cooling scans.

Figure 5.10. (a-c) Temperature dependence of ionic conductivity (standard deviation as error bar) for the K-based SPEs: (a) temperatures ranging from 30–100 ºC, (b) zoomed-in plot of area A in Figure 5.10a ($5.0 \times 10^{-7} < \sigma_{total} < 1.0 \times 10^{-4}$ S cm^{-1}) and (c) zoomed-in plot of area B in Figure 5.10a ($1.4 \times 10^{-4} < \sigma_{total} < 5.0 \times 10^{-4}$ S cm^{-1}). (d) Ionic conductivity of the PEO-based electrolytes at 70 ℃.

Figure 5.11. (a-c) Temperature dependence of ionic conductivity (standard deviation as error bar) for the Li-based SPEs: (a) temperatures ranging from 30–100 ºC, (b) zoomed-in plot of area A in Figure 5.11a ($2.5 \times 10^{-7} < \sigma_{total} < 1.0 \times 10^{-4}$ S cm^{-1}) and (c) zoomed-in plot of area B in Figure 5.11a ($1.4 \times 10^{-4} < \sigma_{total} < 4.0 \times 10^{-4}$ S cm^{-1}). (d) Ionic conductivity of the PEO-based electrolytes at 70 ℃.

Figure 5.12. (a) FTIR and (c) Raman spectra of the different Li-based SPEs. (b) and (d) Zoomed-in profiles of the area A and area B shown in Figs. 5.12a and c, respectively. The black, red and blue lines represent LiRCTFSI/PEO, LiSCTFSI/PEO and LiCTFSI/PEO, respectively.

Figure 5.13. (a, c, e) Polarization profiles and (b, d, f) electrochemical impedance spectra before polarization of the Li° || Li° cells using different SPEs.

Figure 6.1. Temperature dependence of ionic conductivities of different solid polymer electrolytes (SPEs).

A.3. List of tables

Table 4.3. Calculated values of lithium-ion conductivity (σ_{Li^+}) for the LiBTFSI/PEO and LiTFSI/PEO-based SPEs at 70 ℃.

Table 5.1. Mode assignment of typical bands observed by FTIR spectroscopy of the chiral potassium salts.

Table 5.2. Mode assignment of typical bands observed by Raman spectroscopy of the chiral potassium salts.

Table 5.3. Mode assignment of typical bands observed by FTIR spectroscopy of the chiral lithium salts.

Table 5.4. Mode assignment of typical bands observed by Raman spectroscopy of the chiral lithium salts.

Table 5.5. Physico-chemical data for phase behavior of the SPEs.

Table 5.6. The specific σ_{total} (σ_i) from 4 repetitions and the corresponding average σ_{total} ($\bar{\sigma}$), standard deviation (σ_{SD}) and functional uncertainty (f_{FN}) for the K-based SPEs at different temperatures.

Table 5.7. The specific σ_{total} (σ_i) from 4 repetitions and the corresponding average σ_{total} ($\bar{\sigma}$), standard deviation (σ_{SD}) and functional uncertainty (f_{FN}) for the Li-based SPEs at different temperatures.

Table 5.8. Mode assignment of typical bands observed by FTIR spectroscopy of the Li-based SPEs.

Table 5.9. Mode assignment of typical bands observed by Raman spectroscopy of the Li-based SPEs.

Table 5.10. Data used to calculate lithium-ion transference numbers (T_{Li^+}) for the Li-based SPEs at 70 ºC.

A.4. List of schemes

A.5. List of contributions

A.5.1 List of publications

1. Judez, X.; Qiao, L.; Armand, M.; Zhang, H., Energy Density Assessment of Organic Batteries. *ACS Applied Energy Materials* **2019**.

2. Zhang, H.; Chen, F.; Lakuntza, O.; Oteo, U.; Qiao, L.; Martinez-Ibañez, M.; Zhu, H.; Carrasco, J.; Forsyth, M.; Armand, M., Suppressed Mobility of Negative Charges in Polymer Electrolytes with an Ether-Functionalized Anion. *Angewandte Chemie International Edition* **2019,** *58* (35), 12070-12075.

3. Gyabeng, D.; Qiao, L.; Zhang, H.; Oteo, U.; Armand, M.; Forsyth, M.; Chen, F.; O'Dell, L. A., Anion-cation interactions in novel ionic liquids based on an asymmetric sulfonimide anion observed by NMR and MD simulations. *Journal of Molecular Liquids* **2020**, 114879.

4. Lixin, Q.; Alexander, S.; Yan, Z.; Maria, M.-I.; Eduardo, S.-D.; Elias, L.; Marcel, T.; Patrik, J.; Heng, Z.; Michel, A., Solid Polymer Electrolytes Comprising Camphor-Derived Chiral Salts for Solid-State Batteries. *Journal of the Electrochemical Society* **2020**.

5. Martinez-Ibañez, M.; Sanchez-Diez, E.; Qiao, L.; Meabe, L.; Santiago, A.; Zhu, H.; O'Dell, L. A.; Carrasco, J.; Forsyth, M.; Armand, M.; Zhang, H., Weakly coordinating fluorine-free polysalt for single lithium-ion conductive solid polymer electrolytes. *Batteries & Supercaps* **2020,** *n/a* (n/a).

6. Martinez-Ibañez, M.; Sanchez-Diez, E.; Qiao, L.; Zhang, Y.; Judez, X.; Santiago, A.; Aldalur, I.; Carrasco, J.; Zhu, H.; Forsyth, M.; Armand, M.; Zhang, H., Unprecedented Improvement of Single Li-Ion Conductive Solid Polymer Electrolyte Through Salt Additive. *Advanced Functional Materials* **2020,** *n/a* (n/a), 2000455.

7. Qiao, L.; Judez, X.; Rojo, T.; Armand, M.; Zhang, H., Polymer Electrolytes for Sodium Batteries. *Journal of The Electrochemical Society* **2020,** *167* (7), 070534.

8. Qiao, L.; Oteo, U.; Zhang, Y.; Peña, S. R.; Martínez-Ibañez, M.; Santiago, A.; Cid, R.; Meabe, L.; Manzano, H.; Carrasco, J.; Zhang, H.; Armand, M., Trifluoromethyl-free anion for highly stable lithium metal polymer batteries. *Energy Storage Materials* **2020**.

9. Santiago, A.; Judez, X.; Castillo, J.; Garbayo, I.; Sáenz de Buruaga, A.; Qiao, L.; Baraldi, G.; Coca-Clemente, J. A.; Armand, M.; Li, C.; Zhang, H., Improvement of Lithium Metal Polymer Batteries through a Small Dose of Fluorinated Salt. *The Journal of Physical Chemistry Letters* **2020**, 6133-6138.

10. Santiago, A.; Castillo, J.; Garbayo, I.; Saenz de Buruaga, A.; Coca Clemente, J. A.; Qiao, L.; Cid Barreno, R.; Martinez-Ibañez, M.; Armand, M.; Zhang, H.; Li, C., Salt Additives for Improving Cyclability of Polymer-Based All-Solid-State Lithium–Sulfur Batteries. *ACS Applied Energy Materials* **2021**.

A.5.2 List of the oral presentation

Qiao, L.; Zhang, H.; Armand, M., Chiral Salts for Solid-State Lithium-Metal Batteries. *2021 Virtual MRS Spring Meeting.*